

UC San Diego

UC San Diego Electronic Theses and Dissertations

Title

Nano-scale positioning, control and motion planning in hard disk drives

Permalink

<https://escholarship.org/uc/item/9h08n8sn>

Author

Boettcher, Uwe

Publication Date

2011

Peer reviewed|Thesis/dissertation

UNIVERSITY OF CALIFORNIA, SAN DIEGO

**Nano-scale Positioning, Control and Motion Planning in Hard Disk
Drives**

A dissertation submitted in partial satisfaction of the
requirements for the degree
Doctor of Philosophy

in

Engineering Sciences (Mechanical Engineering)

by

Uwe Boettcher

Committee in charge:

Professor Frank E. Talke, Chair
Professor Raymond A. de Callafon, Co-Chair
Professor Robert R. Bitmead
Professor Kenneth Kreutz-Delgado
Professor Vitaliy Lomakin

2011

Copyright

Uwe Boettcher, 2011

All rights reserved.

The dissertation of Uwe Boettcher is approved, and it is acceptable in quality and form for publication on micro-film and electronically:

Co-Chair

Chair

University of California, San Diego

2011

DEDICATION

To my parents, Heidi and Helmut Böttcher,
and my paternal grandparents, Hilde and Manfred Böttcher.

TABLE OF CONTENTS

Signature Page	iii
Dedication	iv
Table of Contents	v
List of Acronyms	ix
List of Symbols	xiii
List of Figures	xix
List of Tables	xxii
Acknowledgements	xxiii
Vita and Publications	xxvii
Abstract of the Dissertation	xxix
1 An introduction to storage technology	1
1.1 Information storage in human history	1
1.2 Current and emerging storage technologies	7
1.2.1 Overview	7
1.2.2 Hard disk drives	9
1.2.3 Tape storage devices	10
1.2.4 Optical storage	12
1.2.5 Emerging non-volatile memory	13
1.3 Future storage trends	15
2 Introduction to hard disk drives	18
2.1 Mechanical aspects	18
2.2 Magnetic aspects	20
2.2.1 Recording principle	20
2.2.2 Longitudinal and perpendicular recording	22
2.2.3 Reading data	24
2.3 Tribological aspects	25
2.3.1 The head-disk interface	26
2.3.2 Air bearing slider and head-gimbal assembly	28
2.4 Signal processing aspects	30
2.5 Electro-mechanical aspects: actuators in a hard disk drive	32
2.5.1 Spindle motor	32
2.5.2 Voice coil motor	35

2.5.3	Micro-actuator	38
2.5.4	Flying height actuator	41
2.6	Control aspects	43
2.6.1	Servo sectors for position estimation	45
2.6.2	Track following	48
2.6.3	Track seeking	49
2.7	Geometric aspects	52
2.7.1	Bit aspect ratio, linear density and areal density	52
2.7.2	Zone bit recording	53
2.7.3	Skew angle	53
2.8	Ongoing challenges and trends in hard disk drives	55
2.8.1	Miniaturization	55
2.8.2	Form factors	58
2.8.3	Economic challenges	59
2.9	Physical limits and possible solutions	60
2.9.1	Thermal stability and super paramagnetic limit	60
2.9.2	Patterned and discrete-track recording	60
2.9.3	Energy assisted magnetic recording	62
2.9.4	Shingle recording	63
2.10	Further reading	64
2.11	Contribution and organization of this dissertation	65
2.12	Acknowledgement	67
3	Modeling and control of a dual-stage actuator hard disk drive	69
3.1	Introduction	69
3.2	Modeling and system identification	70
3.3	Controller design	75
3.3.1	General overview	75
3.3.2	Sensitivity decoupling method	77
3.3.3	H_∞ loop shaping controller design	78
3.3.4	Controller evaluation	80
3.4	Controller implementation	82
3.5	Conclusion	84
3.6	Acknowledgement	86
4	Reference signal shaping for seeking in hard disk drives	89
4.1	Introduction	89
4.2	Defining the system	95
4.2.1	Specifications of closed-loop signals	95
4.2.2	Explicit solution of the closed-loop system	98
4.3	Convex optimization	101
4.3.1	Constraints on the closed-loop signals	101
4.3.2	Constraints on reference signals	103

4.3.3	Combined constraints in linear form	105
4.3.4	Feasibility check for time-optimal solution	105
4.3.5	Quadratic programming	107
4.3.6	Semidefinite programming	109
4.3.7	Solution to LP, QP and SDP problems	110
4.4	Experimental verification: seeking in a hard disk drive	111
4.4.1	Experimental set-up	111
4.4.2	Closed-loop dynamic modeling of the servo mechanism . . .	113
4.4.3	Results	116
4.5	Conclusions	123
4.6	Appendix - selected matrix dimensions	124
4.7	Acknowledgment	124
5	Analytical read back signal modeling in magnetic recording	125
5.1	Introduction	125
5.2	Media contribution	127
5.3	Head sensitivity	134
5.4	Simulation example	135
5.5	Conclusions	136
5.6	Acknowledgement	136
6	Servo signal processing for flying height control in hard disk drives	141
6.1	Introduction	141
6.2	Flying height estimation	142
6.2.1	Available techniques	142
6.2.2	Servo signal based flying height estimation	143
6.2.3	Simulated off-track characteristics	145
6.3	Experimental results	148
6.3.1	Experimental set-up and methodology	148
6.3.2	Verification of proposed flying height estimation scheme . . .	150
6.3.3	Off-track characteristics	151
6.3.4	Voltage step measurements	152
6.3.5	Data based dynamic modeling of the heater response	154
6.4	Conclusions	156
6.5	Acknowledgement	158
7	Dynamic flying height adjustment in hard disk drives through feedforward control	159
7.1	Introduction	159
7.2	Experimental set-up	161
7.3	Dynamic modeling of the heater response	163
7.3.1	Modeling based on physical principles	163
7.3.2	Data-based modeling approach	164
7.3.3	Modeling algorithm applied to experimental data	169

7.4	Computing optimal power profile	179
7.4.1	Development of the optimization algorithm	179
7.4.2	Optimization algorithm applied to experimental set-up . . .	182
7.5	Conclusions	184
8	Summary	187
	Bibliography	192

LIST OF ACRONYMS

AC	Alternating current
a.u.	Arbitrary units
BLDC	Brushless direct current (motor)
BPM	Bit-patterned media
CD	Compact disc
CPU	Central processing unit
DAQ	Data acquisition system
DC	Direct current
DISO	Dual-input single-output
DRAM	Dynamic random-access memory
DSA	Dual-stage actuator
DSP	Digital signal processing
DVD	Digital versatile disc
EB	Exabyte, $1\text{EB} = 10^{18}$ bytes
ECC	Error correction code
EMF	Electromotive force
FDB	Fluid dynamic bearing
FIR	Finite impulse response
FRF	Frequency response function
Gb	Gigabit, $1\text{Gb} = 10^9$ bits

GB	Gigabyte, $1\text{GB} = 10^9$ bytes
GMR	Giant magnetoresistance
GRA	Generalized realization algorithm
GS	Giga samples (10^9 samples)
HAMR	Heat-assisted magnetic recording
HDD	Hard disk drive
HGA	Head gimbal assembly
HMS	Head-medium spacing
IDFT	Inverse discrete Fourier transform
ITI	Inter-track interference
kb	Kilobit, $1\text{kb} = 10^3$ bits
kB	Kilobyte, $1\text{kB} = 10^3$ bytes
ktpi	Kilo tracks per inch
LDV	Laser Doppler vibrometer
LMI	Linear matrix inequality
LMR	Longitudinal magnetic recording
LP	Linear programming
LQG	Linear-quadratic-Gaussian (control)
LTI	Linear time invariant (system)
LTR	Loop transfer recovery (control)
Mb	Megabit, $1\text{Mb} = 10^6$ bits

MB	Megabyte, $1\text{MB} = 10^6$ bytes
MEMS	Microelectromechanical systems
MIMO	Multi-input multi-output
MOSFET	Metal-oxide-semiconductor field-effect transistor
MR	Magnetoresistive
MRAM	Magnetoresistive random access memory
NAND	NOT AND (logic operator)
NRRO	Non-repeatable run out
OPA	Operational amplifier
PB	Petabyte, $1\text{PB} = 10^{15}$ bytes
PES	Position error signal
PID	Proportional-integral-derivative (controller)
PMR	Perpendicular magnetic recording
PTOS	Proximate time-optimal servomechanism
PZT	Piezoelectric transducer
QP	Quadratic programming
RMS	Root mean square
rpm	Revolutions per minute
RRO	Repeatable run out
SDM	Sensitivity decoupling method
SDP	Semidefinite programming

SNR	Signal-to-noise ratio
SRAM	Static random-access memory
SISO	Single-input single-output
STOS	Shaped time-optimal servomechanism
SVD	Singular value decomposition
TAA	Track average amplitude
TAR	Thermally assisted recording
Tb	Terabit, $1\text{Tb} = 10^{12}$ bits
TB	Terabyte, $1\text{TB} = 10^{12}$ bytes
TFC	Thermal flying height control
TMR	Track misregistration
TMR	Tunnel magnetoresistance
TOC	Time-optimal control
VCM	Voice coil motor
ZB	Zettabyte, $1\text{ZB} = 10^{21}$ bytes

LIST OF SYMBOLS

Symbol	Description	Unit
A	System matrix (state space form)	
B	Input matrix (state space form)	
B	Bandwidth	Hz
\vec{B}	Magnetic flux density	Vs/m ²
C	Output matrix (state space form)	
C	Channel capacity	Hz
C	Controller	
C_{DS}	Dual-stage controller	
C_{PZT}	Micro-actuator controller	
C_{VCM}	Voice coil motor controller	
C_W	Weighted controller	
c	(viscous) damping coefficient	Pa · s
δ	Damping ratio	1
δu_G	Input signal rate to actuator	
$\underline{\delta u_G}, \overline{\delta u_G}$	Lower and upper amplitude constraint on δu_G	
δr	Reference signal rate	
$\underline{\delta r}, \overline{\delta r}$	Lower and upper amplitude constraint on δr	
Δd	Thermal actuator protrusion	m

Δt	Time difference	s
Δz	Flying height change	m
Δz_0	Spacing parameter	m
d	Disturbances	
D	Feed-through term (state space form)	
ϵ	Tolerance	
e	Error	
F	Force	N
G	Dynamic model of a plant	
G_{VCM}	Dynamic model of a voice coil motor	
G_{PZT}	Dynamic model of a micro-actuator	
G_W	Weighted plant model	
\hat{G}_{PZT}	Simplified micro-actuator model	
g_{PZT}	DC gain of micro-actuator	
g	Shield gap	m
h	Spacing	m
h	Relative step height	1
H	Magnetic field strength	A/m
H_C	Coercivity	A/m
I	Current	A
k	Sample number	1

k	Spring constant	N/m
k	Wave number	1/m
k_1	Feedback gain of position	
k_2	Feedback gain of velocity	
k^*	Transition sample number	1
k_{min}^*	Minimum sample number	1
K	Coupling factor	1
K	Gain	
\vec{l}	Coil vector	m
λ	Mean free path of gas molecules	m
λ	Wavelength	m
L	Length	m
L_0	Length scale of problem	m
μ	Viscosity	Pa · s
m	Mass	kg
m	Number of outputs	1
M	Magnetization	A/m
M	Control horizon	1
M_r	Remanent magnetization	A/m
M_s	Saturation magnetization	A/m
n	Matrix rank and model order	1

N	Noise power	W
N	Number of samples	1
M	Optimization horizon	1
ω	Angular frequency	rad/s
ω_0	Angular natural frequency	rad/s
ω_d	Damped angular natural frequency	rad/s
Φ	Harmonic amplitude of readback signal	
Φ	Magnetic flux	Vs
p	Pressure	Pa
p	Number of inputs	1
P, P_{in}, P_{step}	Input/step input power	W
PES	Position error signal	1
\bar{Q}	Correction term	1
r	Reference signal	
\underline{r}, \bar{r}	Lower and upper amplitude constraint on r	
r_1	Reference signal	
r_2	Reference (feed-forward) signal	
r_s	Residual reference signal	
R	Resistance	Ω
R_g	Relative gain	1
σ	Standard deviation	

σ	Spacing parameter	m
s	Complex angular frequency	rad/s
S	Signal power	W
S	Sensitivity function	
S_{PZT}	Sensitivity function micro-actuator loop	
S_{VCM}	Sensitivity function voice coil motor loop	
τ	Time constant	
t	Time	s
t	Thickness	m
T	Closed-loop transfer function	
T	Thickness	m
u	Input signal	
u_G	Input signal to actuator	
$\underline{u}_G, \overline{u}_G$	Lower and upper amplitude constraint on u_G	
v	Voltage	V
W	Width	m
W_{PZT}	Weighting filter micro-actuator	
W_{VCM}	Weighting filter voice coil motor	
x	Displacement	m
x	State	
x_C	Controller state	

x_G	Actuator state
x_M	Measurement state
y	Output
y_C	Controller output
y_G	Output of actuator
y_t	Target output
$\underline{y}_1, \overline{y}_1$	Lower and upper amplitude constraint during targeting stage
$\underline{y}_2, \overline{y}_2$	Lower and upper amplitude constraint during settling stage

LIST OF FIGURES

Figure 1.1:	Gutenberg press of the 15th century (artist unknown)	2
Figure 1.2:	Phonograph next to its inventor T.A. Edison	3
Figure 1.3:	The first digital tape recording systems	5
Figure 1.4:	The first hard disk drive as part of the IBM RAMAC	6
Figure 1.5:	Memory hierarchy in modern computer architecture	8
Figure 1.6:	Functional principle of a hard disk drive	10
Figure 1.7:	Functional principle of a tape drive	11
Figure 1.8:	Functional principle of a CD player	12
Figure 1.9:	Schematic of magnetoresistive random access memory	14
Figure 1.10:	Market share of storage media by storage capacity	16
Figure 1.11:	Consumer storage usage	17
Figure 2.1:	Schematic of the mechanical components of a hard disk drive. . .	19
Figure 2.2:	Schematic of suspension, slider and gimbal.	20
Figure 2.3:	Typical hysteresis loop in magnetic recording	21
Figure 2.4:	Principle of longitudinal and perpendicular magnetic recording .	23
Figure 2.5:	Side view on head-disk interface showing layered structure . . .	27
Figure 2.6:	Converging fluid channel in a slider bearing system	28
Figure 2.7:	Head-gimbal assembly in a dual-stage actuator hard disk drive .	29
Figure 2.8:	Evolution of the size of the slider	30
Figure 2.9:	Schematic of data storage system with error correction codes . .	31
Figure 2.10:	Ideal and realistic data tracks	33
Figure 2.11:	Fluid dynamic bearing and ball bearing in a spindle motor . . .	34
Figure 2.12:	Main principle of inner rotor brushless DC motor	35
Figure 2.13:	Spindle motor connection	36
Figure 2.14:	Two form factor 5.25" hard disk drives	36
Figure 2.15:	Main functional principle of rotary voice coil motor	37
Figure 2.16:	Methods for non-operational head positioning	38
Figure 2.17:	Piezo-electric push/pull actuated suspension	41
Figure 2.18:	Thermal flying height control slider	43
Figure 2.19:	Common closed loop control structure	44
Figure 2.20:	Disk with servo and data sectors	46
Figure 2.21:	Typical amplitude based servo pattern	47
Figure 2.22:	Readback signal for head position 1-4 from Fig. 2.21	48
Figure 2.23:	Time optimal and proximate time-optimal control	50
Figure 2.24:	Schematic of shaped time-optimal servomechanism	52
Figure 2.25:	Bit geometry definition	52
Figure 2.26:	Schematic of zone bit recording with 5 different zones	54
Figure 2.27:	Effect of skew angle on read/write offset and read/write delay .	55
Figure 2.28:	Bit shape recorded at 0 and 15° skew angle	56
Figure 2.29:	Areal density increase	57

Figure 2.30: Different form factors of recent hard disk drives	58
Figure 2.31: Evolution of price per gigabyte of hard drive storage since 1980.	59
Figure 2.32: Patterned media, discrete-track media and conventional media	61
Figure 2.33: Principle of heat assisted magnetic recording	63
Figure 2.34: Principle of shingle magnetic recording	64
Figure 3.1: Close-up image of the piezoelectric microactuator	70
Figure 3.2: Experimental set-up to determine frequency response function	71
Figure 3.3: FRF measurement and estimated 15th order VCM model	75
Figure 3.4: FRF measurement and estimated 20th order PZT model	76
Figure 3.5: Control structure of sensitivity decoupling method	77
Figure 3.6: H_∞ loop shaping control structure	79
Figure 3.7: Comparison SDM and H_∞ loop shaping controller	81
Figure 3.8: Comparison of sensitivity functions	82
Figure 3.9: Simulation of step responses	83
Figure 3.10: Simulated displacement for VCM and PZT	84
Figure 3.11: Implemented SDM controller	85
Figure 3.12: Head position and control signals for SDM controller	86
Figure 3.13: Implemented H_∞ loop shaping controller	87
Figure 3.14: Head position and control signals for H_∞ loop shaping controller	88
Figure 4.1: Mass-spring-damper system	89
Figure 4.2: Input shaping example: force input and displacement output	90
Figure 4.3: Closed loop LTI system with constraints on closed-loop signals	93
Figure 4.4: Definition of the output constraints	102
Figure 4.5: Optimization algorithm	107
Figure 4.6: Computational steps and scheme of the experimental set-up	112
Figure 4.7: Experimental set-up	112
Figure 4.8: Measured and simulated actuator and controller outputs	114
Figure 4.9: Bode plot of estimated model and FRF measurement	115
Figure 4.10: Optimized signals for fixed step size	119
Figure 4.11: Optimized signals for fixed seek time	120
Figure 4.12: Loose and tight output boundaries for a 10 track seek	121
Figure 4.13: 100 track step for fixed seek time and time-optimal solution	122
Figure 5.1: Defining the coordinate system	128
Figure 5.2: Magnetic field components for longitudinal recording	131
Figure 5.3: Modeling perpendicular recording	132
Figure 5.4: Magnetic field components for perpendicular recording	133
Figure 5.5: Assumed TMR head sensitivity function	134
Figure 5.6: Normalized longitudinal read back signal	138
Figure 5.7: Normalized perpendicular read back signal	139
Figure 5.8: Measured read back signal of a 16T pattern	140

Figure 6.1:	Definition of burst spacing for a dual servo pattern	146
Figure 6.2:	Off-track dependence of measurement for LMR and PMR	147
Figure 6.3:	Experimental set-up	149
Figure 6.4:	Circumferential flying height modulation	150
Figure 6.5:	Measured cross-track behavior at 10mW heater input	152
Figure 6.6:	Flying height modulation for step inputs	153
Figure 6.7:	Relative steps (Fig. 6.6-Fig. 6.4) and identified first order models	154
Figure 6.8:	Variance in relative flying height	155
Figure 6.9:	Estimated gain K and time constant τ from Fig. 6.7	156
Figure 6.10:	Static flying height change for different heater input power levels	157
Figure 7.1:	Network model of the resistance heater element	163
Figure 7.2:	Schematic of thermal actuator and flying height sensor	165
Figure 7.3:	Dependence of the heater resistance on the input power level . . .	170
Figure 7.4:	Step response measured at 15.36 kHz	171
Figure 7.5:	Step response measured at 380 kHz	172
Figure 7.6:	Bode response of ZOH equivalent continuous-time models	173
Figure 7.7:	Touch down experiment	175
Figure 7.8:	Measured read back signal of the data sector	176
Figure 7.9:	Spin stand measurement: step response	178
Figure 7.10:	Singular values of the weighted Hankel matrix	179
Figure 7.11:	Spin stand measurement: optimized input and output	183

LIST OF TABLES

Table 3.1: Comparison SDM and H_∞ loop shaping controller	81
Table 4.1: Bisection algorithm	106
Table 5.1: Coefficients	131
Table 7.1: Parameter of 2nd order discrete-time models	174

ACKNOWLEDGEMENTS

First and foremost, I would like to express my deepest gratitude to my advisor Professor Frank Talke for his continuous support, guidance and trust. He has been extremely helpful and supportive in countless situations during the almost four years that I have been part of his research group. I greatly enjoyed working with him and I also thank him for encouraging me to pursue the Ph.D. degree.

Second, I wish to thank my co-advisor Professor Raymond de Callafon for giving valuable suggestions and directions and for his support throughout the years. He has been a great teacher and guide in many aspects during my Ph.D. research and has accelerated the progress tremendously.

Next, I would like to thank former Talkelab members Prof. Bart Raeymaekers for introducing me to the topic of information storage in disk and tape drives and for countless discussions and Dr. Ralf Brunner for many helpful suggestions and much help inside and outside the lab. The former and current group members, in particular, Dr. Melanie Gauvin, Dr. Andrey Ovcharenko, Dr. Longqiu Li and fellow graduate student Hao Zheng are greatly acknowledged for many fruitful discussions. I would like to express my gratitude to Dirk Fetzner for much help with performing the experiments used in chapter 4 of this dissertation. For many very helpful discussions, Dr. Fred Spada is gratefully acknowledged.

Professor Lienig from Dresden University of Technology encouraged me to do an internship in San Diego and made it possible for me to work on my "Diplom"

thesis at UCSD as well. I wish to thank him for that. Professor Lienig, Prof. de Callafon and Prof. Talke encouraged and supported my application for graduate studies at UCSD.

Special thanks to Prof. Izhak Etsion from the Technion, Izrael Institute of Technology in Haifa for helpful suggestions/discussions and motivation during his many visits to San Diego.

I would also like to thank former and current members of the System Identification and Control Laboratory (SICL), in particular, Dr. Charles Kinney, Dr. Alexander Simpkins and Younghee Han for their helpful suggestions with control theory related problems. Moreover, I wish to thank Ray Descoteaux for enormous help and many suggestions with experimental set-up and lab equipment. In addition, Steve Roberts, Chris Cassidy and Jack Philhower are acknowledged for their technical support and advice.

I would like to thank our industry partners for many helpful discussions, providing parts and collaboration. In particular, I wish to thank Edmund Fanslau of NHK International Corporation, Dr. Alexei Sacks of Seagate Technology, Dr. Bernhard Knigge of Western Digital Corporation, Dr. Hui Li of Hitachi Asia Limited. Special thanks to Dr. Gregory Kimball of Texas Instruments for donating the spin stand, and, Tom Crittenden, and Dr. Christopher Lacey of Microphysics, Inc. and Dr. John Contreras of Hitachi Global Storage Technologies, Ltd. for their help with setting up the spin stand. Without them, a significant part of this dissertation would not have been possible in the present form.

Many thanks to Iris Villanueva, Betty Manoulian and Jan Neumann for their assistance with many different administrative matters.

My friends here and back home overseas deserve a special "thank you" for being a great help in many different ways throughout the years. In addition, I thank the friendly Southern Californians who made my stay in San Diego extraordinarily enjoyable.

Finally, I would like to thank my parents, Heidi und Helmut, my grandparents, Hilde and Manfred, my siblings, Kerstin and Ralf and my extended family, all of whom supported me mentally and financially during my stay in San Diego. My lovely girlfriend Jeanette has been a strong support and a great source of encouragement for the past two years and I wish to thank her for that.

Chapter 2 and 3, in part, are a reprint of the material as it appears in "Modeling and Control of a Dual-Stage Actuator Hard Disk Drive", Boettcher U., de Callafon R.A., Talke F.E., *Journal of Advanced Mechanical Design, Systems, and Manufacturing*, Volume 4, Issue 1, pp. 107-118, 2010. The dissertation author was the primary investigator and author of this paper.

Chapter 4, in part, is a reprint of the material as it appears in "Reference Signal Shaping for Closed-loop Systems with Application to Seeking in Hard Disk Drives", Boettcher U., Fetzer D., Li H., de Callafon R.A., Talke F.E., submitted to *IEEE, Transactions on Control Systems Technology*. The dissertation author was the primary investigator and author of this paper.

Chapter 5, in part, is a reprint of the material as it appears in "Analytical

Read Back Signal Modeling in Magnetic Recording”, Boettcher U., Lacey C.A., Li H., Amemiya K., de Callafon R.A., Talke F.E., *Microsystem Technologies*, 2011.

The dissertation author was the primary investigator and author of this paper.

Chapter 2 and 6, in part, are a reprint of the material as it appears in ”Servo Signal Processing for Flying Height Control in Hard Disk Drives”, Boettcher U., Lacey C.A., Li H., Amemiya K., de Callafon R.A., Talke F.E., *Microsystem Technologies*, 2011. The dissertation author was the primary investigator and author of this paper.

Chapter 2 and 7, in part, are a reprint of the material as it appears in ”Dynamic Flying Height Adjustment in Hard Disk Drives through Feedforward Control”, Boettcher U., Li H., de Callafon R.A., Talke F.E., *IEEE, Transactions on Magnetics*, 2011. The dissertation author was the primary investigator and author of this paper.

In addition, chapter 2 and 3, in part, are a reprint of the material as it appears in the dissertation author’s ”Diplomarbeit” (Master’s thesis) at Dresden University of Technology. The Master’s thesis was done at UCSD/CMRR.

VITA

2003-2008	Study of Electrical Engineering at Dresden University of Technology, Dresden, Germany
2005	Vordiplom (pre-diplom degree), specialization in Precision Mechanics
2007	Visiting graduate student at the Center for Magnetic Recording Research, University of California, San Diego
2008	Dipl.-Ing. degree (equivalent to M.Sc. degree) in Electrical Engineering, Dresden University of Technology, Dresden, Germany
2008-2011	Graduate Research Assistant, University of California, San Diego
2010	Master of Science, University of California, San Diego, USA
2011	Doctor of Philosophy, University of California, San Diego

PUBLICATIONS

Journal Papers

- J1 Boettcher U, Raeymaekers B, de Callafon RA, Talke FE, "Dynamic Modeling and Control of a Piezo-Electric Dual-Stage Tape Servo Actuator", *IEEE Transactions on Magnetics*, 2009, Vol. 45(7), pp. 3017-3024
- J2 Boettcher U, de Callafon RA, Talke FE, "Modeling and Control of a Dual-Stage Actuator Hard Disk Drive", *Journal of Advanced Mechanical Design, Systems, and Manufacturing*, Vol. 4 (2010) , No. 1, pp. 107-118
- J3 Boettcher U, Lacey CA, Li H, Amemiya K, de Callafon RA, Talke FE, "Analytical Read Back Signal Modeling in Magnetic Recording", *Microsystems Technology*
- J4 Boettcher U, Lacey CA, Li H, Amemiya K, de Callafon RA, Talke FE, "Servo Signal Processing for Flying Height Control in Hard Disk Drives", *Microsystems Technology*
- J5 Boettcher U, Fetzer D, Li H, de Callafon RA, Talke FE, "Multiobjective Time Domain Input Shaping for Closed-Loop Discrete-Time Systems", *submitted to IEEE Control Systems Technology*

- J6 Boettcher U, Li H, de Callafon RA, Talke FE, "Optimal Feed Forward Profiles for Dynamic Flying Height Control in Hard Disk Drives" (invited paper), accepted for publication by *IEEE Transactions on Magnetics*

Conference Papers

- C1 Boettcher U, Raeymaekers B, de Callafon RA, Talke FE, "Dynamic Modeling and Control of a Piezo-Electric Dual-Stage Tape Servo Actuator", *Proceedings of ASME Conference on Engineering Systems Design and Analysis*, Haifa, Israel, 07-09 July 2008
- C2 Boettcher U, Raeymaekers B, de Callafon RA, Talke FE, "Design of a Dual-stage Actuator Tape Head Controller", *Proceedings of Information Storage and Processing Systems (ISPS) Conference*, Santa Clara, CA (USA), 16-17 June 2008
- C3 Boettcher U, de Callafon RA, Talke FE, "Modeling and Control of a dual-stage actuator hard disk drive", *JSME-IIP/ASME-ISPS Joint Conference on Micromechanics for Information and Precision Equipment (MIPE 2009)*, June 17-20, 2009, Tsukuba International Congress Center, Ibaraki, Japan
- C4 Boettcher U, de Callafon RA, Talke FE, "Data based modeling and control of a dual-stage actuator hard disk drive", *Proceedings of 48th IEEE Conference on Decision and Control*, December 16-18, 2009 in Shanghai, China
- C5 Boettcher U, de Callafon RA, Talke FE, "Multiobjective Time Domain Input Shaping for Closed-Loop Discrete-Time Systems" (invited paper), *5th IFAC Symposium on Mechatronic Systems (Mechatronics '10)*
- C6 Boettcher U, Lacey CA, de Callafon RA, Talke FE, "Servo Signal Data Processing for Flying Height Control in Hard Disk Drives", *20th ASME Annual Conference on Information Storage & Processing Systems (ISPS)*, Santa Clara, CA (USA), 14-15 June 2010
- C7 Boettcher U, de Callafon RA, Talke FE, "Closed-loop input shaping in discrete-time LTI systems", *20th ASME Annual Conference on Information Storage & Processing Systems (ISPS)*, Santa Clara, CA (USA), 14-15 June 2010
- C8 Boettcher U, Li H, de Callafon RA, Talke FE, "Optimal Feed Forward Profiles for Dynamic Flying Height Control in Hard Disk Drives" (invited paper), *accepted at the 18th IFAC World Congress*, (IFAC WC 2011)
- C9 Boettcher U, Lacey CA, Li H, Amemiya K, de Callafon RA, Talke FE, "Dynamic Modeling of the Resistance Heater Element in Thermal Flying Height Control Sliders and Optimal Feed-Forward Profiles" (invited paper), Asia-Pacific Magnetic Recording Conference (APMRC) 10-12 Nov 2010, Singapore

ABSTRACT OF THE DISSERTATION

Nano-scale Positioning, Control and Motion Planning in Hard Disk Drives

by

Uwe Boettcher

Doctor of Philosophy in Engineering Sciences (Mechanical Engineering)

University of California, San Diego, 2011

Professor Frank E. Talke, Chair
Professor Raymond A. de Callafon, Co-Chair

In this dissertation, we focus on optimization of cross-track and vertical positioning of the read/write element over the data track.

First, a data-based approach is presented for modeling and controller design of a dual-stage servo actuator in a hard disk drive. Based on discrete-time models, different dual-stage track-following controllers were designed using classic and H-infinity loop shaping techniques. The controllers were implemented in real-time.

Next, an input shaping algorithm based on convex optimization techniques is presented for closed-loop discrete-time linear time-invariant (LTI) system. The proposed algorithm allows closed-loop signals to be subjected to linear constraints on amplitude and rate of change. As an illustrative example the seeking process in a hard disk drive is investigated and experimentally verified.

To study the dependence of the read signal on cross-track and vertical motion, a straightforward analytical model for the read back signal is derived for perpendicular and longitudinal magnetic recording. The model captures the contribution of a single bit rather than the contribution of a bit transition which makes it applicable to patterned media as well as continuous media.

In addition, a novel method of measuring the relative head-medium spacing based on the measurement of the read back signal from servo sectors is developed. The spacing measurement is tested experimentally on a spin stand where the flying height is varied using the resistance heater element in a thermal flying height control slider. In addition, voltage step response measurements were obtained for data based modeling.

Finally, a dynamic model of the resistance heater in a thermal flying height control (TFC) slider is identified based on experimentally obtained step-input data. A generalized realization algorithm is used for identification of a discrete-time dynamic model of the resistance heater. Based on the identified model and convex optimization techniques, a computational scheme is proposed to obtain optimized feed forward input profiles to the heater element that minimize repeatable flying

height variations. The optimized input signals were applied to the heater and greatly reduced flying height variations were observed in spinstand experiments.

1 An introduction to storage technology

1.1 Information storage in human history

The time line of human history reveals several events that have triggered and accelerated the growth of societies and economies enormously. Many of those events are directly linked to the ability (and improvement) of storing, retrieving and distributing information. One of the main steps was unquestionably the invention of written language as a form of communication and information storage about 6,000-8,000 years ago [1]. This seems long ago but it can be considered relatively recent compared to approximately 250,000 years of Homo sapiens [2]. "Technical" inventions such as papyrus - the ancient form of paper - have made it easy to transport and store written information over generations. Libraries that assured access to the documents are presumably as old as written language itself. But it was not until the middle of the 15th century, when a mass production process for books based on movable types was invented by a German named Johannes Gutenberg.

The mass printing press (Fig. 1.1) made books affordable and accessible to the broad public, resulting in greatly reduced illiteracy in the population [3]. Prior to this invention, books were extremely pricey as it could take half a year to duplicate a book [3]. Within the first century of printing there were about 100,000



Figure 1.1: Gutenberg press of the 15th century (artist unknown - source: [4])

separate titles issued [5] and average editions at that time ranged from 200 to 1,000 copies [6]. One can note that inexpensive "storage" and distribution of written information was an important requirement for a further development towards our modern society. The period from the middle of the 16th through the middle of the 18th century is widely referred to as the "scientific revolution" [7]. Many important inventions, discoveries and improvements were made during this period

in disciplines such as astronomy, physics, and biology, to only name a few. However, as far as data storage is concerned, it was not until the industrial revolution of the 18th and 19th century when groundbreaking inventions were made: The first permanent photograph taken in 1826 [8] can be attributed to this period. Before that, any visual impression could only be captured on a painting or be described through written language. The first sound recording took also place during this period. The phonograph [9] (gramophone) of the late 19th century allowed the recording of arbitrary signals by mechanical means on a cylinder and later on a disk to make storage and reproduction easier (Fig. 1.2). Up to this point, recording



Figure 1.2: Phonograph next to its inventor T.A. Edison (source: [4])

and playback of sound was only possible by "automated instruments" similar to a

barrel organ.

For simple large-scale computing and storage purposes, punch cards gained popularity in the 1880s ¹. Punch cards can be considered the first digital data storage medium where the "bits" were characterized by a hole or the absence of a hole in stiff paper carton. The first large-scale application of punch cards was the US census in 1890 [10]. The computational tools were built by the *Tabulating Machine Company* that later merged with two other companies into *International Business Machines (IBM)*. Punch cards remained popular for some applications until the middle of the 20th century.

The idea of recording signals by magnetic means was first introduced by an American engineer named Oberlin Smith and published in a scientific journal in 1888 where he proposed to record on a metal string [11]. However, there is no evidence that he built a working prototype. The first functioning wire recorder was built a decade later by a Danish engineer named Valdemar Poulsen [12]. The invention received attention as a gold medal winner at the 1900 world exhibition in Paris, France [13]. However, during the following 20 years, attempts to commercialize the invention by Poulsen and his partners abroad failed and his company went bankrupt [13]. One reason for the failure was that electronic circuits had not been sophisticated enough, e.g. the vacuum tube amplifiers had not been invented yet [14]. Furthermore, the initial recording medium - steel - incorporated a number of disadvantages such as high weight and poor handling. The first

¹Punch cards had already been used for controlling musical instruments or textile looms throughout the 19th century.

practical working tape recorder was manufactured by the German company *Allgemeine Elektrizitäts-Gesellschaft (AEG)* and the corresponding tape was developed at *Badische Anilin- und Soda-Fabrik (BASF)*. This new device was presented to the public at the Berlin radio exhibition in 1935 [15]. The data storage world remained analog - with the exception of punch cards - until the early 1950s. In 1951, the first digital data was recorded on tape using the first commercial computer, the UNIVAC 1 [16]. Soon after, *IBM* introduced its first tape system, the IBM 726 Tape Drive in 1952 [17]. Both systems are shown in Fig 1.3. One further step



a)



b)

Figure 1.3: The first digital tape recording systems: a) The UNIVAC 1 and b) The IBM 726 Tape Drive (source: [18])

was the first random access memory in form of the first hard disk drive (HDD) where written data could be retrieved within a very short amount of time². IBM built this first HDD in its so-called "Random Access Method of Accounting and Control system", or short, RAMAC in 1956. The RAMAC (Fig. 1.4) stored 5 MB

²The average seek time of the 1956 RAMAC was 600 ms.

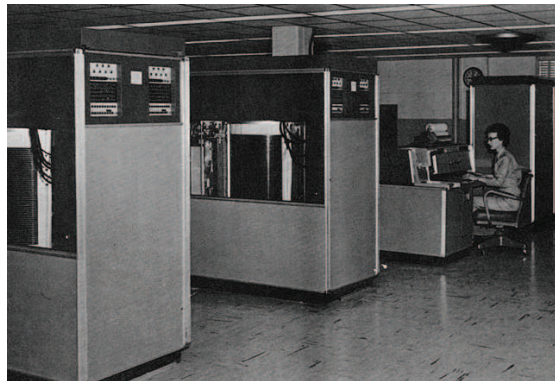


Figure 1.4: The first hard disk drive as part of the IBM RAMAC (source: [4])

of data on 50 two-foot diameter disks. It was not sold but could be rented for \$3,200 per month which would be equivalent to approximately \$25,000 in today's dollars³.

Tape drives and hard disk drives have started a new era in information storage and certainly laid the foundation for the information age (digital age) in which we currently live. The main technology is still in use today; in fact, the majority of data produced in today's world is stored magnetically using a similar functional principle as in the first products from 1952 and 1956, respectively. As a product they have improved tremendously in terms of storage density and cost per data unit volume over the past half a century as we will see in chapter 2 of this dissertation. Other competing storage technologies such as optical storage or solid state storage have arisen during this period. However, none of those newly developed technologies have yet been able to replace tape drives or hard disk

³according to the United States Department of Labor inflation calculator online available at: http://www.bls.gov/data/inflation_calculator.htm

drives as mass storage media but were only able to replace them in certain niche applications.

In the following subsections we will shortly introduce and discuss today's main available storage technologies. The focus will also be on economic aspects that have been shown to have great impact on whether or not a technology will succeed in the long term.

1.2 Current and emerging storage technologies

1.2.1 Overview

To review the different available storage technologies and their use it is important to understand that there is a memory hierarchy in modern computer architecture (Fig. 1.5). The ideal storage medium would be characterized by all the following attributes:

- high storage capacity
- fast writing of data
- high speed of (random) access to data
- low cost
- long-lasting data (non-volatile)
- low power consumption during operation

- ease of interchangeability

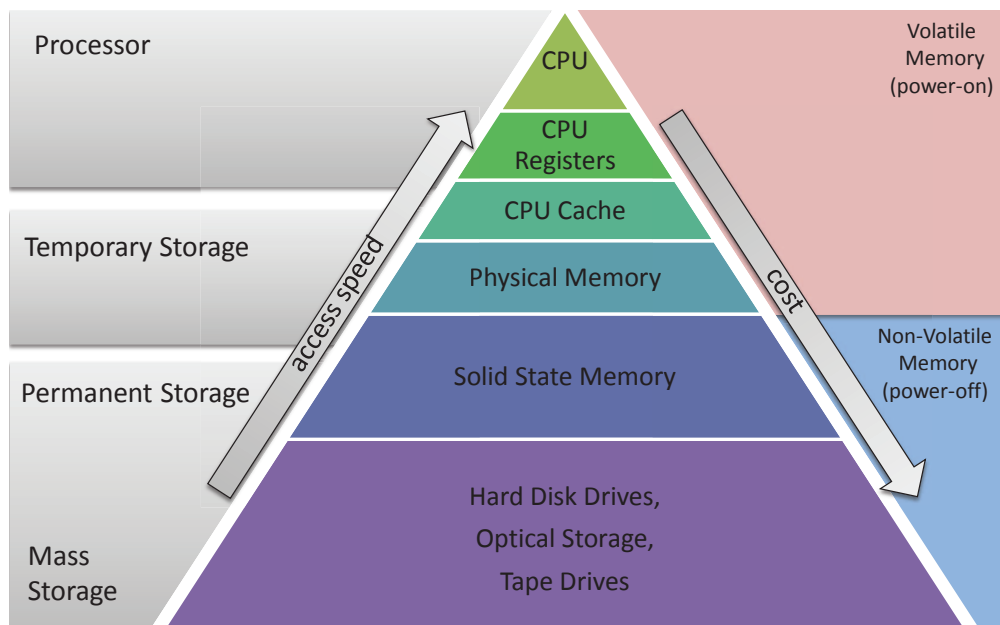


Figure 1.5: Memory hierarchy in modern computer architecture

In reality, there exists a trade off between the above attributes. The top of the storage hierarchy pyramid depicted in Fig. 1.5 is the central processing unit (CPU) with its multi-level registers. The CPU and register unit typically stores only a few bytes for an extremely short period of time. This memory is volatile, i.e., the information is lost after power is withdrawn. The CPU has the highest price per bit but also the highest speed. Relatively large physical (random access) memory blocks (DRAM, SRAM) exist today at relatively low cost. They are also volatile, much less expensive than the CPU but also much slower. For long-term storage we only consider non-volatile memory as shown at the bottom of the storage hierarchy pyramid in Fig. 1.5. Currently, hard disk drives represent

the best trade off between tape storage (inexpensive, long-lasting but slow access speed) and solid state storage (relatively expensive but fast and reliable). In the remainder of this chapter we will briefly introduce the current existing non-volatile storage technologies, discuss their main application and address future trends for their implementation.

1.2.2 Hard disk drives

Hard disk drives store the largest amount of today's data. They have been state-of-the-art technology for mass storage for more than 50 years now. Their storage capacity has increased from 5 MB in 1956 to 2 TB (2,000,000 MB) in 2011 and the price has decreased from \$1.5M⁴ per 5 MB to only \$90 per 2 TB. In 2010, an approximate number of 650 million hard disk drives was shipped worldwide. A simplified schematic of a hard disk drive is shown in Fig. 1.6. The data are stored magnetically on circumferential data tracks on a rotating disk. A servo actuator is used to adjust the radial position of the read/write element over the disk. The servo sectors indicated in Fig. 1.6 help to determine the off-track position of the read element with respect to the track center. This dissertation will focus on hard disk drives, in particular, on servo control related aspects of hard disk drives. The reader is referred to chapter 2 for a broad and detailed introduction to hard disk drive technology.

⁴This price is evaluated in today's dollars for a 5 year life span of a HDD considering rental cost of \$25,000 per month.

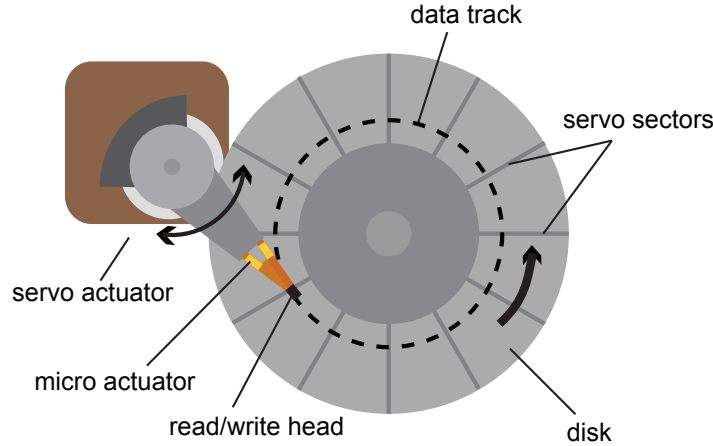


Figure 1.6: Simplified schematic of the functional principle of a hard disk drive

1.2.3 Tape storage devices

Magnetic tape seems to be an out-dated technology but it remains a preferred mass storage medium due to its low cost per unit storage capacity [19]. In particular, for back-up and archiving purposes where data are written once but read rarely (possibly never), it is a highly favorable solution. Today's tape drives are based upon the principle shown in Fig. 1.7. The tape moves from a so-called supply reel to the take-up reel at velocity v . Data are written on the tape and read from the tape by the read/write head. Since tape is a flexible medium it is exposed to many disturbances during reading and writing of data. Track densities are generally much lower compared to track densities in hard disk drives. The lateral position of the tape head is determined by means of a timing based servo pattern on the magnetic tape [20]. Similar to HDD technology, the off-track motion is adjusted by a servo actuator. The actuator rejects incoming disturbances

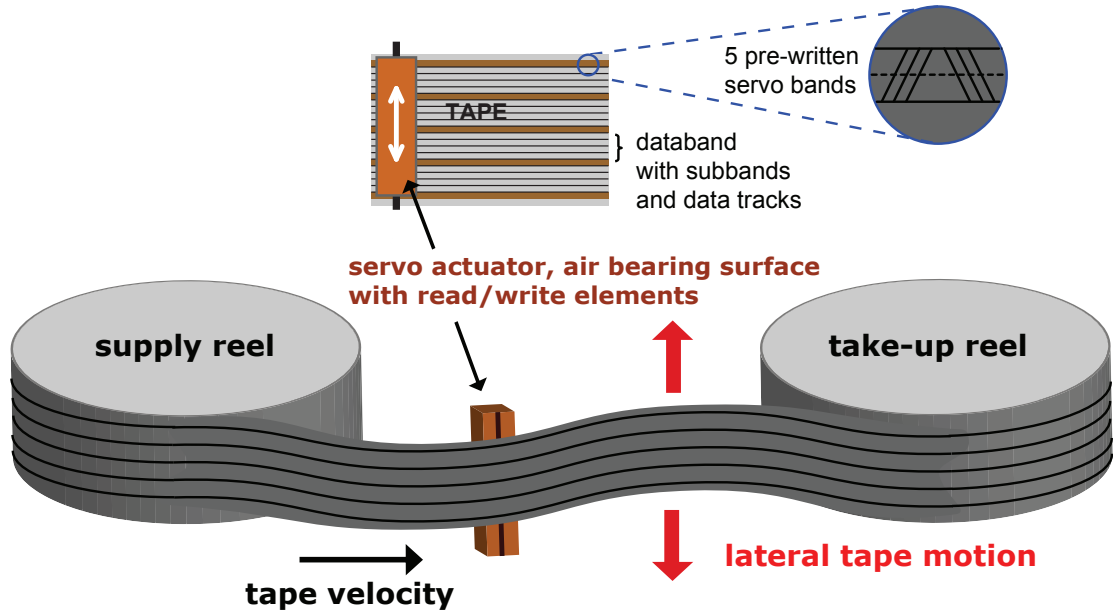


Figure 1.7: Simplified schematic of the functional principle of a tape drive

such as lateral tape motion which is defined as the motion of the tape perpendicular to the tape transport direction (see Fig. 1.7). Recently, it has been shown in a lab demo (IBM Zurich) that tape storage is still feasible at an areal density of 46 Mb/mm^2 (30 Gb/in^2) which is more than 10 times higher than what is currently implemented in commercial products [21]. One additional advantage of tape versus hard drives is the exchangeability of the medium. The cartridges can be stored in automated tape libraries that are accessed by a robot and data stored on tape has better long-term stability than data stored on a magnetic disk [22]. All these facts suggest that there will still be high demand for tape storage for years to come.

1.2.4 Optical storage

Optical storage technology became very popular during the mid 1980s mainly for audio recordings in form of compact disks (CD). The functional principle is illustrated in Fig. 1.8. The digital information is encoded in a pit pattern

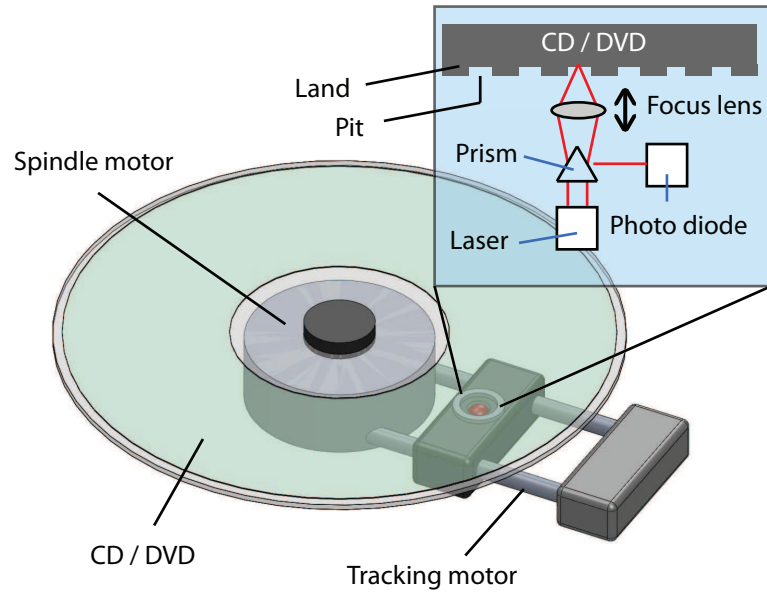


Figure 1.8: Simplified schematic of the functional principle of a CD player

on a rotating disk. A photo diode reads different amounts of reflected laser light depending on whether land or pit area is exposed to the laser light. The initial standard for CDs used a 780 nm (red) laser which was later reduced in wavelength for the "Digital Versatile (or Video) Disc" (DVD) to 650 nm (red-orange) [23]. A smaller wavelength allows the reading of smaller features on the disk. This has allowed an increase in storage capacity from 650 MB to 4.7 GB in the case of CDs and DVDs. A recent implementation of blue/violet lasers at a wavelength of

405 nm ("Blu-ray") can store up to 25 GB/layer [24]. CDs, DVDs and the emerging "Blu-ray" disks are characterized by inexpensive mass production and are widely-used for the distribution and storage of digital content such as audio, video and computer software.

1.2.5 Emerging non-volatile memory

Disk drives, tape drives and optical drives rely on moving parts. The storage medium moves along the read/write element so that different areas on the medium can be addressed. Solid state storage is based on a substantially different technology. The bit layout is pre-defined and each bit is accessed electrically rather than mechanically. This leads to a number of advantages of solid state storage over conventional mechanically accessed non-volatile memory such as disk drives and tape drives. However, so far the significant price difference and other issues such as e.g. the current lithography limits have prevented a replacement of hard drives and tape drives by solid state technology. The most popular solid state storage technology is NAND flash⁵. One of the main technical problems with Flash storage is that only a finite number of write cycles can be performed. This problem does not generally become apparent, however, during the typical lifetime of such a device [25].

New emerging technologies such as magnetoresistive random access memory (MRAM) are currently being developed. The main functional principle of MRAM

⁵The term "NAND" indicates that the transistors form a logic NOT AND configuration

is illustrated in Fig.1.9. The magnetic orientation of a free ferromagnetic layer

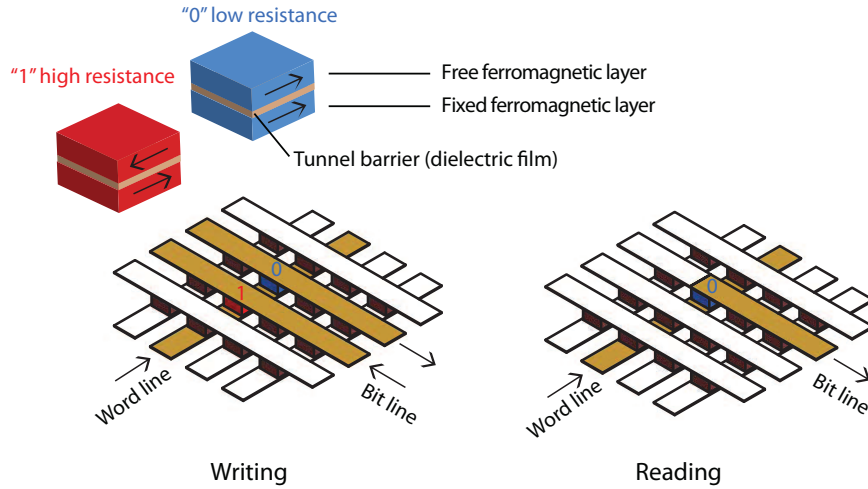


Figure 1.9: Simplified schematic of magnetoresistive random access memory (MRAM) - after [26]

can be switched, thereby changing its resistance. Thus, the resistance of the whole element has two distinct states. This effect is also used for read sensors in HDD technology as will be discussed in section 2.2.3. It has been suggested that MRAM might offer all the attributes listed in section 1.2.1 and that MRAM might become the "universal memory" [27].

Another promising emerging technology is the so-called phase change random access memory (PCRAM) [28]. Here, the actual interconnect device (bit) consists of a material that has at least two different phases: An amorphous phase characterized by high electrical resistance and a crystalline phase with low resistance [28]. Both, MRAM and PCRAM could be potential candidates to replace Flash storage which will likely face scalability problems in the near future [29].

There is a number of different new and also promising technologies that

are not addressed here. The interested reader is referred to [29] for an excellent overview and comparison.

1.3 Future storage trends

The continuous growth in storage capacity combined with an increasing number of storage devices shipped each year would not be possible without a growing demand for storage. This growth prevents the storage market from saturating. According to the market research and analysis firm International Data Corporation (IDC), the demand for data storage has exceeded the amount of available storage capacity in 2007 [30]. The supply-demand gap is expanding and in a more recent study it was suggested that the total "digital universe" will grow from 0.8 ZB⁶ in 2009 to 35 ZB in 2020 which is a 44-fold increase [31].

The way data is stored might be substantially different in the future considering current emerging concepts such as cloud storage and the increasing broadband access to the internet by many devices. Storage is increasingly outsourced to third party providers [32]. This might become a threat mainly to optical storage as it is widely used for distribution of data. However, mass storage products such as tape drives and hard disk drives will still be needed in large quantities. The number of hard disk drives shipped annually will exceed the inconceivable number of 1 billion within the next few years. The total amount of storage capacity that will be shipped on hard disk drives in the next two years will be larger than the

⁶1 zetabyte = 1 trillion gigabytes = 10^{21} bytes

total amount of hard disk drive storage capacity shipped within the past 20 years [33].

The current cost of HDD storage is at approximately \$0.05 per gigabyte and the price will continue to decline at a rate of approximately 25% to 30% per year [33]. For mass storage applications, solid state technology is currently on the order of 10 times more expensive than HDD storage. Hence, solid state technology has not been able to gain reasonable market share in terms of total storage volume (see Fig. 1.10). However, in some applications mostly related to

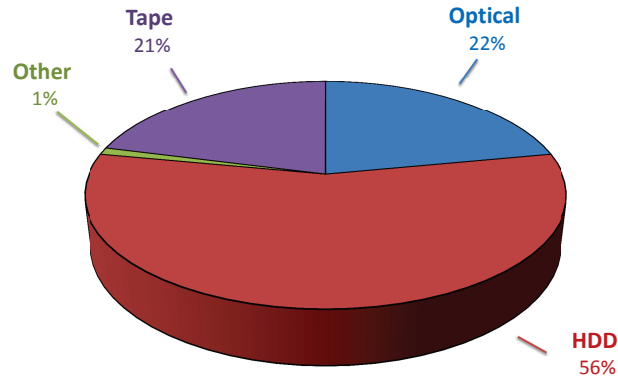


Figure 1.10: Market share of storage media by storage capacity shipped in 2007 according to [30]

consumer electronics, Flash applications could gain significant market share. This is indicated in Fig. 1.11. From Fig. 1.11 we also observe that the overall market is growing in an exponential manner. Hard disk drives will be replaced by solid state drives in applications where it is less expensive to do so. In the near future this will only be the case in low-end capacity products (below currently around 50 GB). Emerging hybrid drives that consist of a solid state cache and basic hard drive storage technology might offer a good compromise between price and performance.

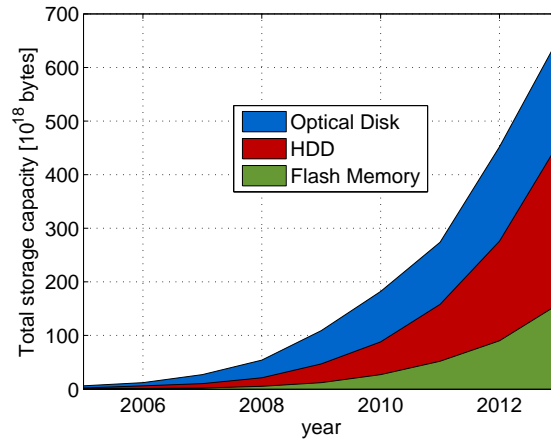


Figure 1.11: Consumer storage usage (home and portable): optical disc, hard drive, and flash (data from [34])

In the following chapter a comprehensive introduction to hard disk drive technology is given.

2 Introduction to hard disk drives

2.1 Mechanical aspects

Although hard disk drives have improved enormously in terms of storage capacity and data access time over the past decades, their main functional principle has not changed substantially. Figure 2.1 shows a schematic of the mechanical components of a typical commercially available hard disk drive (HDD) with its top cover removed. The data are written on circumferential tracks on the disk surfaces. The stack of disks¹ is spun by a spindle motor. Typically, data can be stored on each surface of the disk(s). The slider incorporates the read/write head located at the trailing edge of the slider (Fig.2.2). It flies on an air bearing at extremely close distance (on the order of nm) over the magnetic disk. The air bearing is designed in a way that the distance variation between the slider and the disk is kept at a minimum. Hence, the vertical run-out of the disks which is on

¹Typically between one and four disks

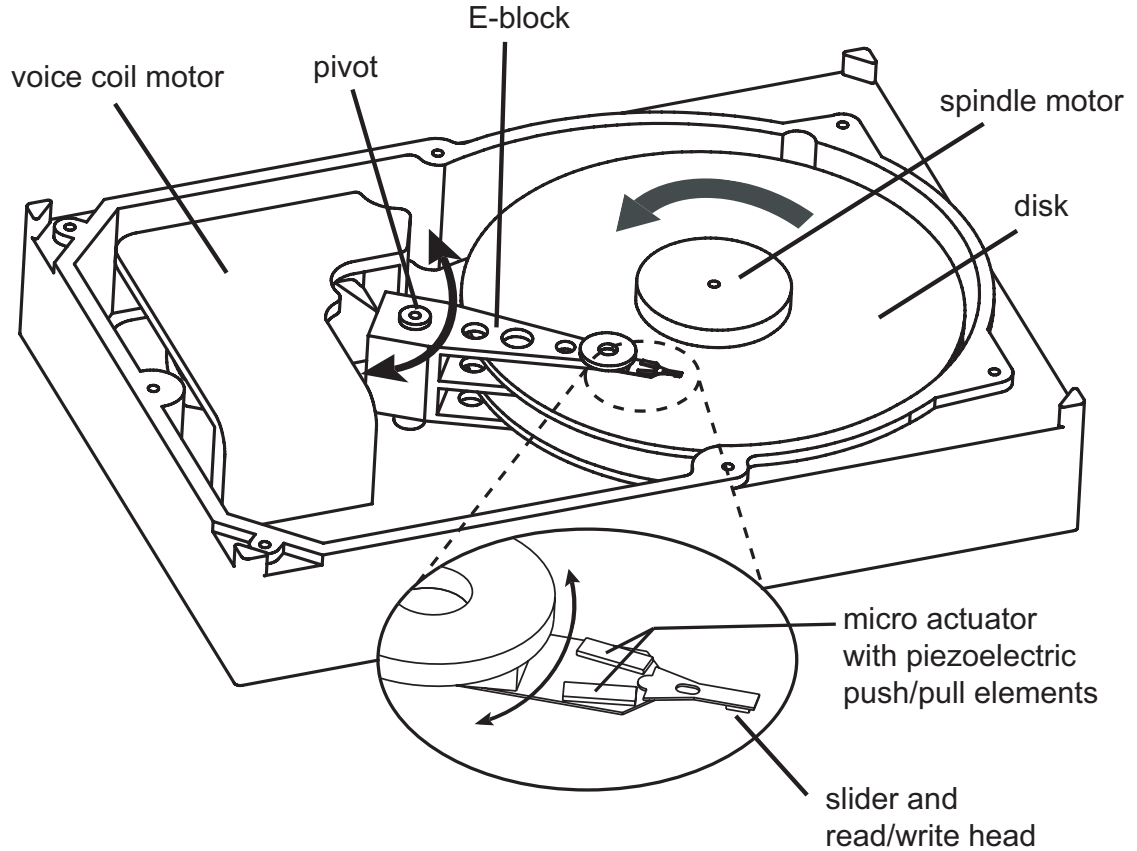


Figure 2.1: Schematic of the mechanical components of a hard disk drive.

the order of a few micrometers can be compensated.

As indicated in Fig. 2.2, the slider is mounted to a flexure (gimbal) which is attached to the suspension. The suspension provides pre-load in the vertical direction and is relatively stiff in the lateral (off-track) direction. The dimple is a spherical protrusion on the suspension and enables all the degrees of freedom indicated in Fig. 2.2 for the slider.

Each bit on the disk needs to be accessible by the read/write element. Therefore, all sliders and suspensions are inter-connected through a so-called E-

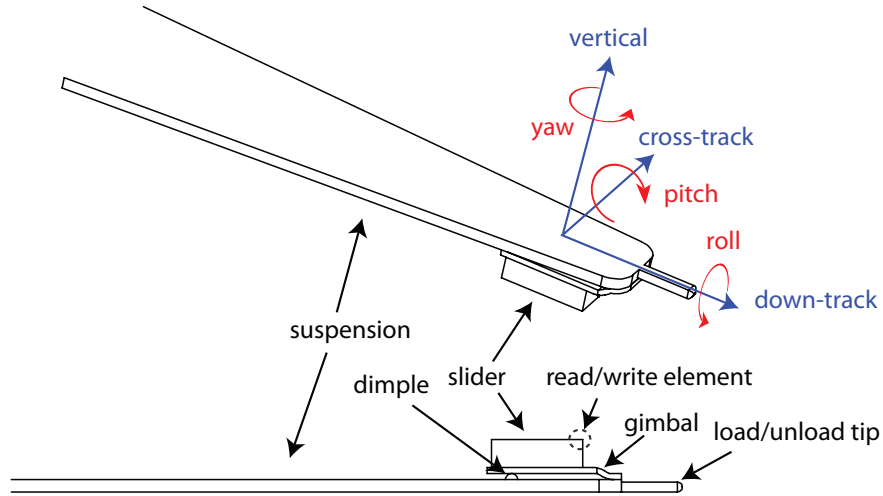


Figure 2.2: Schematic of suspension, slider and gimbal.

block which rotates around a pivot point (Fig. 2.1). This rotary actuator is driven by a so-called voice-coil-motor (VCM). Some hard drives have an additional micro-actuator to increase the positioning accuracy and closed-loop servo bandwidth.

The following subsections will explain various interdisciplinary aspects related to magnetics, tribology, signal processing, electro-mechanical and control engineering that are of great importance in today's hard disk drives.

2.2 Magnetic aspects

2.2.1 Recording principle

The main principle of magnetic recording is illustrated in the hysteresis loop shown in Fig.2.3. Several grains of the magnetic material in the recording layer form a bit (indicated by the gray rectangles in Fig.2.3). A bit forms the

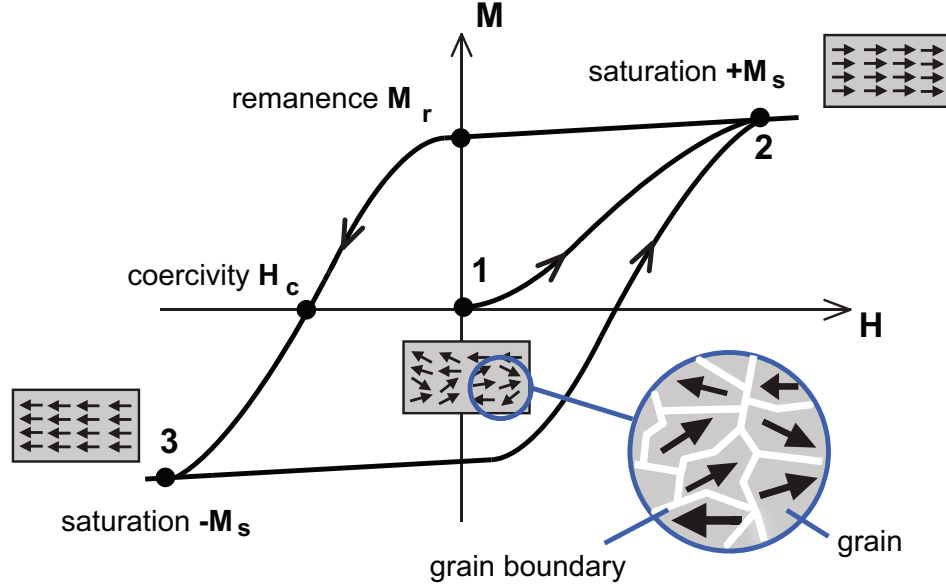


Figure 2.3: Typical hysteresis loop in magnetic recording

smallest undividable unit in digital storage and has two stable states. By applying a magnetic field H the grains can be aligned to remain a total directional magnetization M up to a saturation value $+M_s$ (point 1 to point 2). If the magnetic field is applied in the opposite direction a magnetization of $-M_s$ remains (point 3). These two possible states represent the basis for encoding digital information. The number of grains per bit have a high influence on the signal-to-noise ratio (SNR) during readback. The following relation holds [35]

$$\text{SNR}_{\text{media}} \propto \frac{V_{\text{bit}}}{V_{\text{grain}}} \quad (2.1)$$

where V_{bit} and V_{grain} are the bit and grain volume, respectively. From (2.1) we observe that several grains per bit are needed to maintain a high SNR. A decrease in bit size requires a decrease in grain size as well.

2.2.2 Longitudinal and perpendicular recording

There exist two different orientations in which the bits can be magnetized: horizontally and vertically which is referred to as longitudinal and perpendicular recording, respectively. The vast majority of early generation disk drives had longitudinal magnetic recording (LMR) technology implemented. There were only a few exceptions like e.g. a HDD by Censtor Corporation [36] that used perpendicular magnetic recording (PMR). The first successful commercial perpendicular hard disk drive was introduced in late 2004 by the Japanese company Toshiba [37]. However, the benefits of perpendicular versus longitudinal recording were discussed long before it was finally implemented [38, 39]. The main advantages of perpendicular over longitudinal recording are a much higher readback signal, a better defined bit transition and higher thermal stability [40]. The maximum achievable areal density is increased in perpendicular recording by approximately a factor of 10, from 150 Mb/mm^2 (100 Gb/in^2) to 1.5 Gb/mm^2 (1 Tb/in^2), in comparison with longitudinal recording [41]. Figure 2.4 shows schematically the fundamental differences between longitudinal (Fig. 2.4a) and perpendicular (Fig. 2.4b) recording. The write coil with several windings encloses a magnetic core. Depending on the write current direction and amplitude, the stray (fringe) field below the gap of the core magnetizes the recording media in a longitudinal manner as depicted in Fig. 2.4a. In case of perpendicular recording the write head has a slightly different geometry. One end of the core (monopole) has a relatively small area exposed to

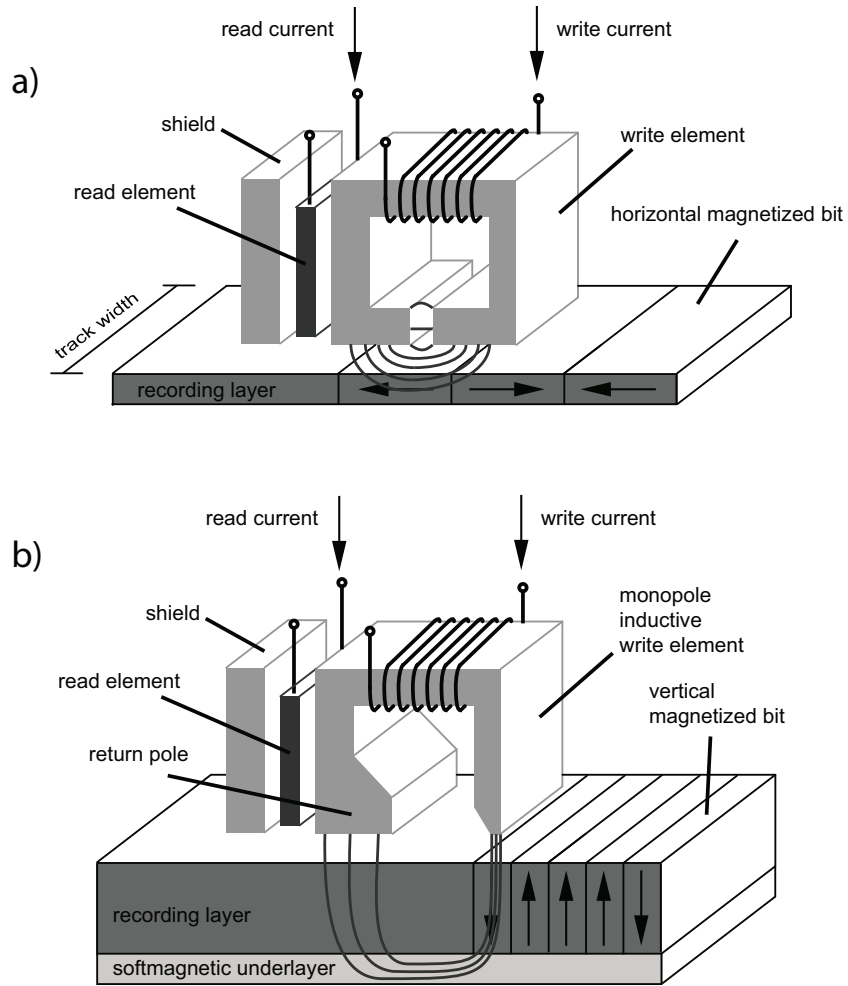


Figure 2.4: Principle of a) longitudinal and b) perpendicular magnetic recording.

the media and the return pole has a much larger area exposed. The magnetic flux generated in the magnetic core by the write coil closes through the recording layer and a soft magnetic underlayer as indicated by the flux lines in Fig. 2.4b. The soft magnetic underlayer has a relative permeability that is typically on the order of several hundred [42] and is essential in perpendicular recording as a return path of the magnetic flux. The grains below the monopole will be re-aligned depending on the direction and strength of the write current. Because of the larger foot print of

the return pole, the flux density is much smaller compared to the monopole and is therefore not sufficient to re-magnetize the media. Write heads have not changed much in today's products from their early versions except for a significant size reduction. Furthermore, early write heads incorporated coils made from wound wire that were replaced by thin film technology in the early 1980s [43].

2.2.3 Reading data

During the first decades of disk drive technology the read and write element was combined. The bit transition could be detected as a change in magnetic flux Φ in the ferrite core of the read/write head. According to Faraday's law, this flux change induces a voltage

$$V_{ind} = -N \frac{d\Phi}{dt} \quad (2.2)$$

in the coil where N is the number of windings. Starting in the early 1990s, a new technology based on magnetoresistive read elements was implemented. The read and write element were separated from each other as shown in Fig. 2.4. The magnetoresistive (MR) and giant magnetoresistive (GMR) element are multi-layered structures that change their overall resistance in the presence of a magnetic field. The sensitivity increase from inductive read elements to the (G)MR elements was enormous resulting in a sharp rise in areal density (see also Fig. 2.29 on page 57). With the advent of perpendicular recording, the GMR read elements were changed to tunnel magnetoresistance (TMR) heads. The principle of TMR is based on electron-tunneling that occurs with a certain probability in an extremely

thin insulating layer between two ferromagnetic layers. The structure of tunnel junctions is very similar to that of non-volatile MRAM memory shown in Fig. 1.9 on page 14. The free ferromagnetic layer changes its magnetization based on an external field (written bit on the disk). If the alignment of the magnetization of the free layer with the magnetization of the fixed layer increases, the probability of electrons tunneling through the insulator increases. Hence, the resistance of the TMR element changes dynamically depending on the external field. In chapter 5, a detailed derivation of an analytical approximation of the readback signal will be shown.

2.3 Tribological aspects

The word tribology was established by Prof. Peter Jost [44] and first introduced in 1966 in a report of the British Department of Education and defined as "the science and technology of interacting surfaces in relative motion, and of associated subjects and practices" [45]. In the disk drive as a paradigm of a mechatronic device, there are several "interacting surfaces in relative motion" which one needs to address. One aspect is the bearing in the spindle motor which will be discussed in section 2.5.1. Here, we will focus on the interface between the slider and the disk.

2.3.1 The head-disk interface

Since the slider incorporates the read/write element, it needs to be positioned in extremely close proximity to the disk to achieve a high signal-to-noise ratio (SNR) and high areal densities in recording. However, contact between the slider and the disk needs to be avoided as wear and damage to the head and the disk might occur. The flying height of sliders with respect to the disk surface in state-of-the-art HDDs is below 5 nanometers. This requires a very smooth disk. The root mean square (RMS) roughness of current disks is well in the sub-nanometer regime [46]. A thin carbon overcoat covers the slider and the disk. In addition, a thin lubricant layer on the disk reduces friction and helps to prevent wear at the interface. The layered structure of the slider and the disk is illustrated in Fig. 2.5. Since the distance between the recording layer and the read/write element needs to be minimized, the carbon overcoat and the lubricant are extremely thin layers.

The flying height is maintained by means of pressure distribution on the air bearing. The pressure distribution is generated by the high shear in the air film between the slider and the rotating disk. The pressure forces are in equilibrium with the suspension spring carrying the slider. During operation of the disk drive, the slider is supposed to "fly" over the disk without touching the disk.

The fundamental equation that is widely used to model the air bearing in a hard disk drive is the compressible Reynolds equation with rarefaction effects [47]

$$\frac{\partial}{\partial x} \left(\bar{Q} p h^3 \frac{\partial p}{\partial x} \right) + \frac{\partial}{\partial y} \left(\bar{Q} p h^3 \frac{\partial p}{\partial y} \right) = 6\mu \left(U \frac{\partial p h}{\partial x} + V \frac{\partial p h}{\partial y} \right) + 12\mu \frac{\partial p h}{\partial t} \quad (2.3)$$

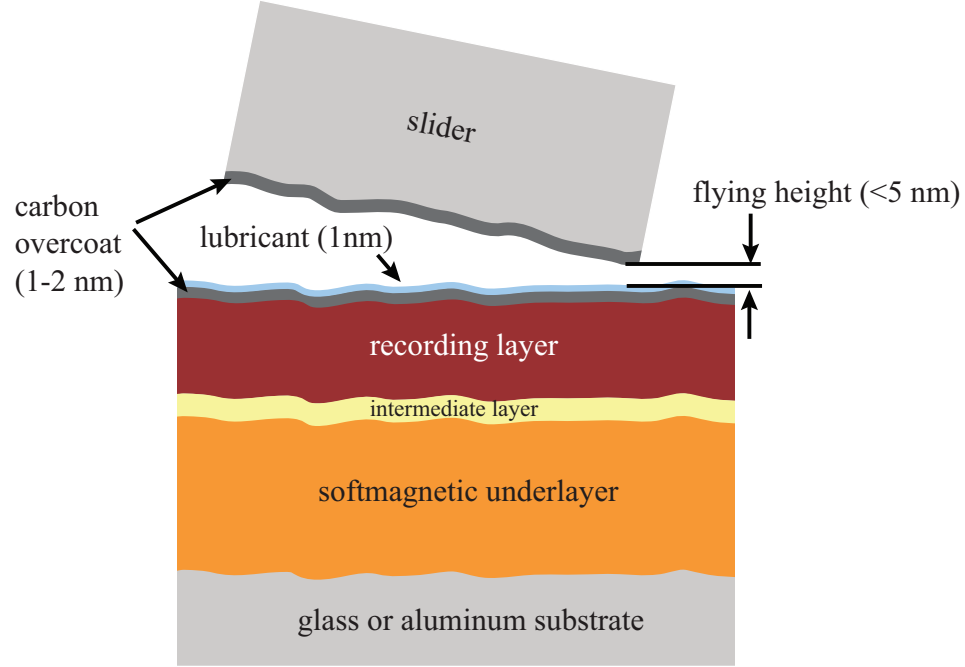


Figure 2.5: Side view on head-disk interface showing layered structure

where p is the local pressure, h is the spacing, μ the viscosity and U and V are x- and y- component of the disk velocity according to Fig.2.6. The Reynolds equation can be derived from the continuity and the Navier-Stokes equations in fluid dynamics. In (2.3), the pressure forces on the left hand side are balanced with the shear forces on the right hand side. The Reynolds equation assumes an ideal gas in the converging channel between the slider and the disk (Fig.2.6). Furthermore, laminar air flow and a constant viscosity are assumed.

Due to the rather complex air bearing geometry, numerical solutions of slider bearings must be obtained using (2.3). A solution of the 2^{nd} order partial differential equation in (2.3) is typically obtained using finite element [48] or finite

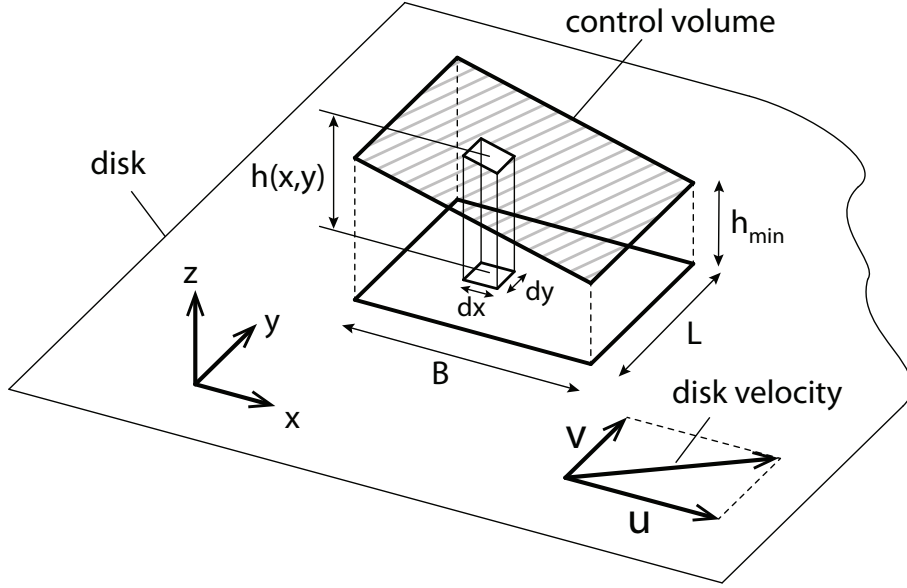


Figure 2.6: Coordinate system for the converging fluid channel in a slider bearing system (after [47])

difference methods [49]. In (2.3), \bar{Q} was introduced as a correction term for extremely low spacing [47]. $\bar{Q}(\text{Kn})$ is a function of the Knudson number $\text{Kn} = \lambda/L_0$ where λ is the mean free path of the gas molecules and L_0 represents the physical length scale of the problem. In the case of an air bearing, an appropriate length scale is the local spacing h . As the spacing between the slider and the disk reaches atomic distances, intermolecular adhesion forces [50] play an increasingly larger role.

2.3.2 Air bearing slider and head-gimbal assembly

Using the numerical means introduced in 2.3.1, one can design an air bearing for a pre-defined nominal flying height. Additional design parameters are: small flying height variations between inner and outer diameter of the disk [51], high

shock resistance [52], low power consumption and low sensitivity to operational and environmental variations [53].

The so-called head-gimbal assembly (HGA) refers to slider, read/write elements, gimbal and suspension. A typical HGA including a recently introduced

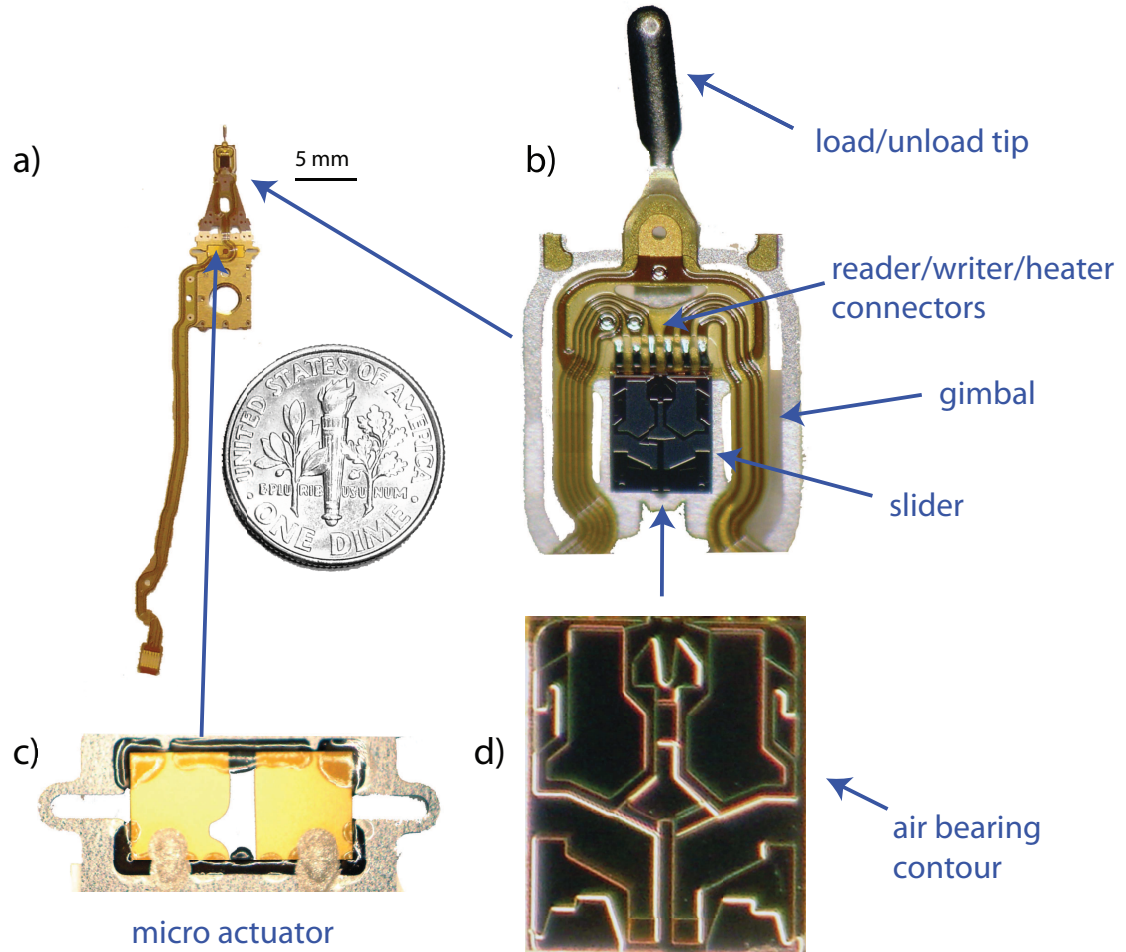


Figure 2.7: a) Head-gimbal assembly in a dual-stage actuator hard disk drive and magnified views of b) the tip of the head-gimbal assembly, c) micro actuator and d) air bearing surface

piezo-electric micro-actuator for achieving better tracking performance is shown in Fig. 2.7. In Fig. 2.7d we observe the complicated air bearing surface consisting of

several recessed surface depth levels and the so-called cavity. The different depth levels determine the pressure build-up over the air bearing.

The increase in storage density and the reduction in disk form factors have resulted in an enormous decrease of the size of sliders and suspensions. Figure 2.8 gives an overview of the decrease of slider size over the last few decades.

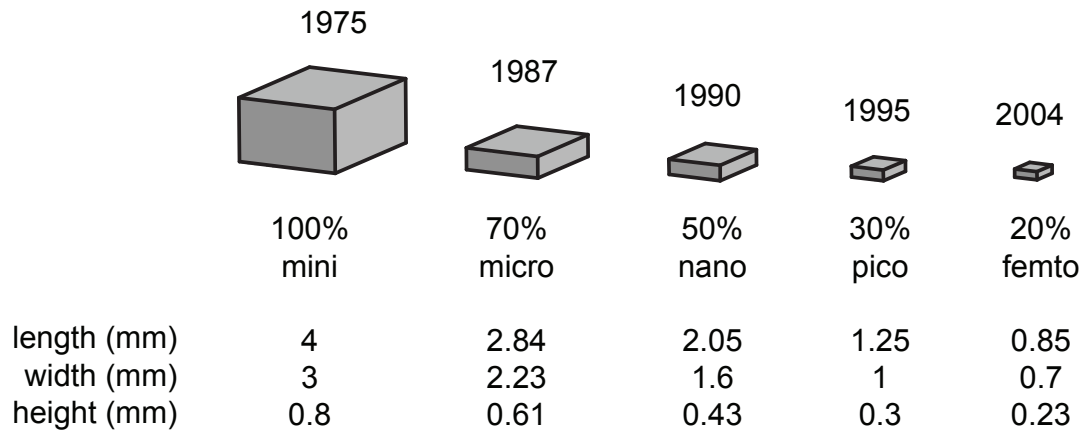


Figure 2.8: Evolution of the size of the slider. Data from [54] and [55]

2.4 Signal processing aspects

A hard drive would not be a successful product without extensive signal processing and so-called error correction codes (ECC). A simplified schematic of a magnetic data storage system is shown in Fig. 2.9. ECC is necessary to reduce errors due to measurement noise. Modulation coding is included for timing recovery and to enhance channel performance [56]. The ECC introduces a significant overhead of about 9% but by using sophisticated signal processing methods, one

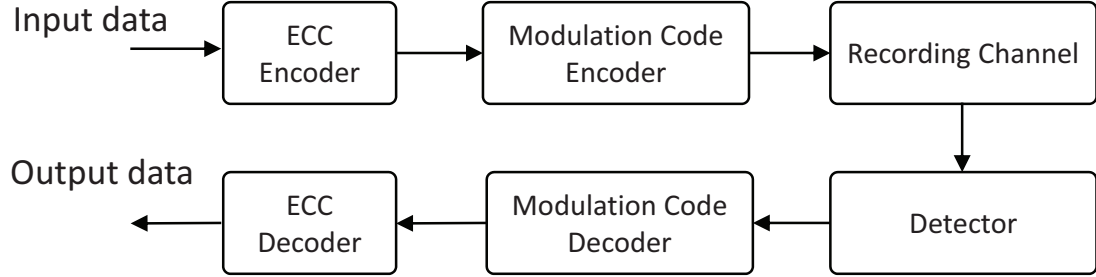


Figure 2.9: Schematic of data storage system with error correction codes (after [56])

can reduce the error rates from 10^{-5} to 10^{-11} [57]. Modern ECC such as the low-density parity check codes [58] perform very close to the theoretical channel capacity limit governed by the Shannon/Hartley theorem [59]

$$C = B \log_2 \left(1 + \frac{S}{N} \right) \quad (2.4)$$

where C is the channel capacity, B is the channel bandwidth, S is the signal power and N is the noise power.

In addition, enhanced signal processing algorithms could take advantage of inter-track interference (ITI) which is related to sensing signals from neighboring data tracks. One could potentially utilize two-dimensional recording in future products [60].

2.5 Electro-mechanical aspects: actuators in a hard disk drive

2.5.1 Spindle motor

The spindle motor in a hard disk drive has to function very precisely in many aspects. The spindle speed measured in revolutions per minute (RPM) has to be kept as constant as possible during operation in order to avoid jitter in the data read/write process [54]. Many different spindle speeds are used. Typically, 7200 rpm drives are used for desktop applications, while laptop HDDs typically run at 5400 rpm. High end and server products use spindle motor speeds up to 15000 rpm. Higher spindle speeds reduce the latency in the data read/write process but increase disturbances such as disk flutter [54].

Another important criteria is that the leakage of the magnetic field generated by the spindle motor should be very low in order to not affect reading or writing of data [61].

The spindle run-out is the motion of the spindle with respect to its center of rotation. It is distinguishable into repeatable (RRO) and non-repeatable (NRRO) run out [62]. RRO is not much of a concern as it is deterministic and could be compensated. If uncompensated, the RRO will result in not perfectly circular data tracks as indicated in Fig. 2.10. However, the NRRO needs to be kept as small as possible since it might lead to track misregistration (TMR).

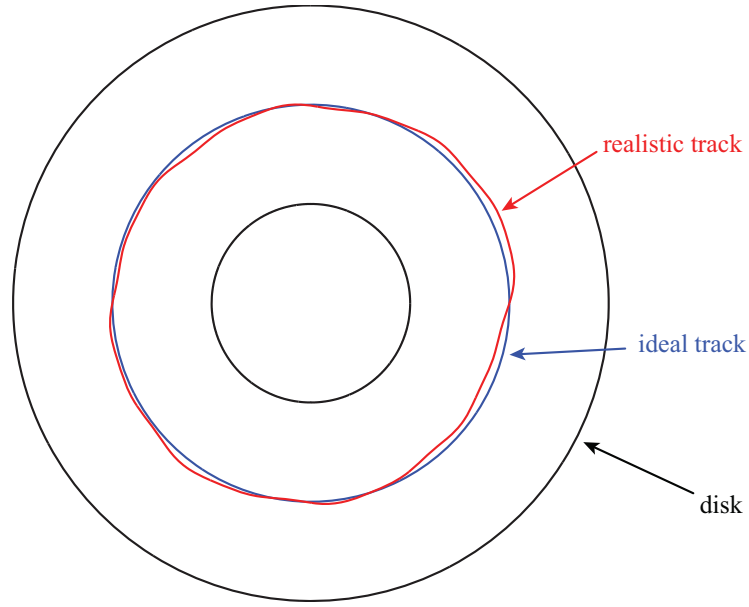


Figure 2.10: Ideal and realistic data tracks

The spindle motor bearing has a large contribution to the NRRO. Thus, more recently, fluid dynamic bearings (FDB) instead of ball bearings (BB) were introduced in spindle motors which significantly reduces the NRRO. In addition, FDB motors show larger damping, a reduced frequency resonance, a better non-operational shock resistance, and, FDB motors are less noisy compared to ball bearing motors [63]. A schematic of the cross-section of fluid dynamic bearings and ball bearings is shown in Fig. 2.11

Reliability is a key issue since HDDs are expected to run for years without being turned off. Small wear particles generated by the spindle motor could potentially cause damage to the head/disk interface and therefore result in decreased reliability. Thus, brushless direct current (BLDC) motors are typically used. They are not commutated mechanically as conventional DC motors (with brushes) but

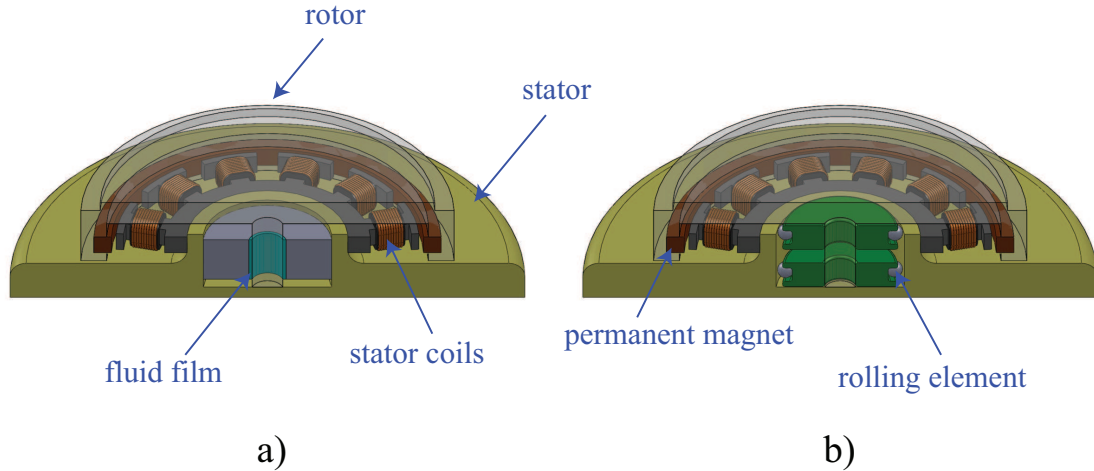


Figure 2.11: Schematic cross section view of a) fluid dynamic bearing and b) ball bearing in a spindle motor. The rotor is shown semi-transparent for clarity.

commutated electronically. A measurement of the back electromotive force (back emf) or an additional Hall sensor is used to determine the position of the rotor. A schematic of the main principle of a BLDC motor with two pole-pairs is shown in Fig. 2.12. The stator core consists of several electrically isolated ferromagnetic layers. The lamination is important to keep eddy currents at a minimum during operation. The rotating permanent magnet is oriented depending on the direction of the current in the coils and therefore magnetic polarity of the stator poles. Spindle motors in HDDs have typically several pole pairs and an upended build-up, i.e., the coils are facing outwards and the permanent magnet is orbiting around the stator (see Fig. 2.11).

The coils in spindle motors are either connected in a delta or a Y-connection (Fig. 2.13) where the Y-connection is favorable due to its lower cost [54].

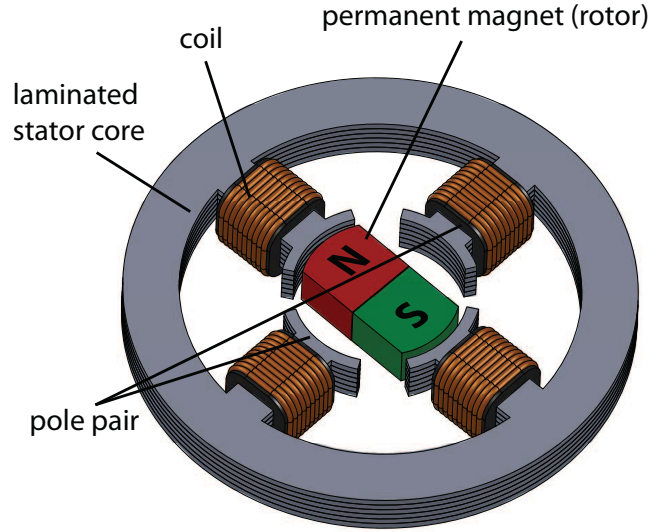


Figure 2.12: Main principle of inner rotor brushless DC motor

2.5.2 Voice coil motor

Voice coil motors (VCM) are electrodynamic actuators based on the "moving coil" principle. Since they function in the same way as loudspeakers, the term "voice coil motor" was established in the literature. The first hard disk drives used linear actuators and there is still research being performed on implementing linear actuators in disk drives [64]. However, rotatory actuators have been used predominantly since the 1980s. Figure 2.14 shows two 5.25" form factor drives from the mid 1980s, one with a linear actuator (Fig. 2.14a) and one with a rotary actuator (Fig. 2.14b).

The main functional principle of rotary VCM is illustrated in Fig. 2.15. The force F that is generated in one winding of the VCM is based on the Lorentz force

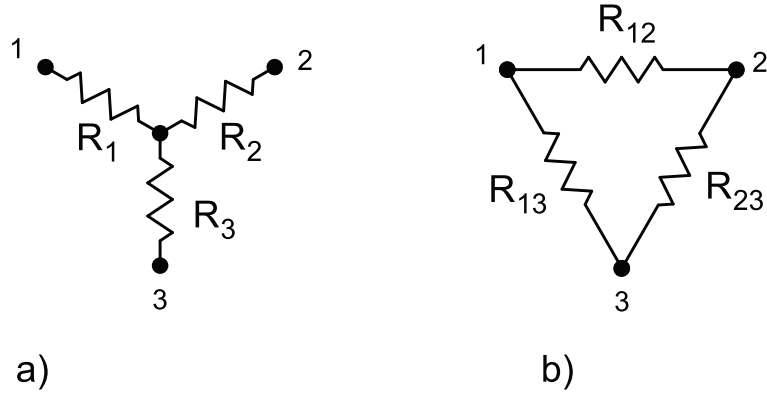


Figure 2.13: Spindle motor connection: a) Y and b) Δ

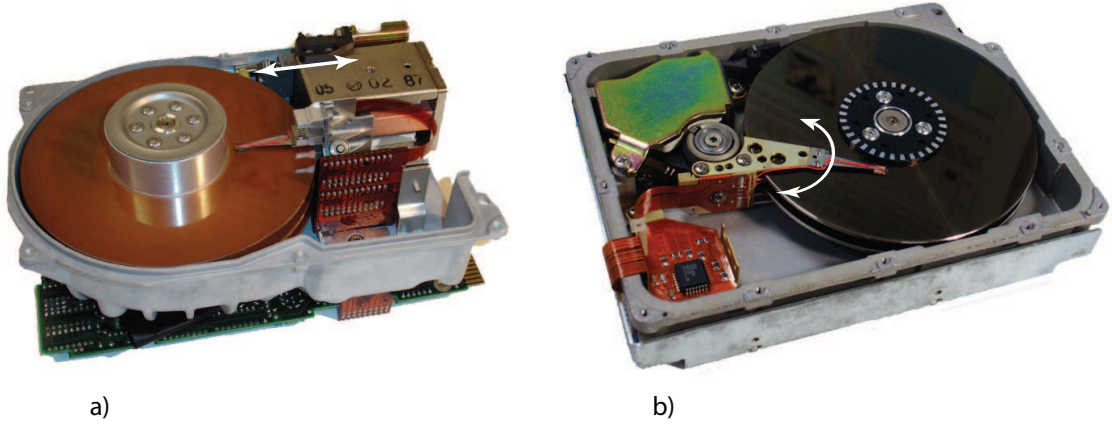


Figure 2.14: Two form factor 5.25" hard disk drives: a) MiniScribe-6053 44 MB from 1987 with linear actuator and b) Quantum Q250 53 MB from 1985 with rotary actuator

law given by

$$\vec{F} = I \cdot (\vec{l} \times \vec{B}) \quad (2.5)$$

where \vec{B} denotes the magnetic flux density generated by the permanent magnet, I is the input current and, \vec{l} is the vector of the coil wire exposed to the magnetic field of the permanent magnet. The polarity of I determines the direction of motion of the E-block with the suspensions and the sliders. As can be seen from Eq. (2.5),

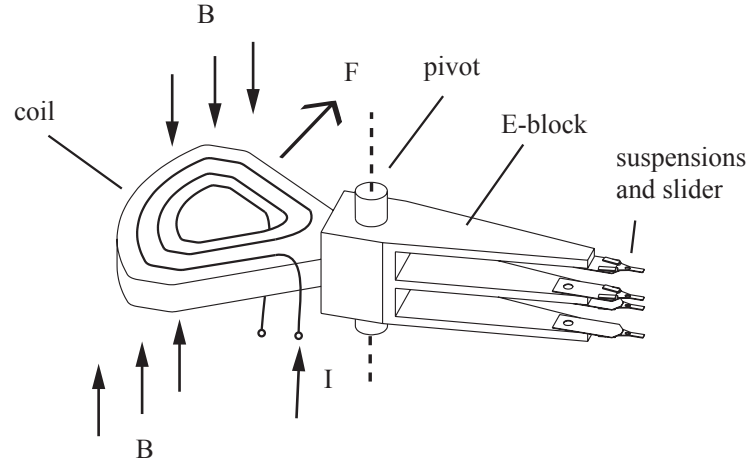


Figure 2.15: Main functional principle of rotary voice coil motor

the generated force is directly proportional to the applied current. According to Newton's second law of motion, the applied force is directly proportional to the resulting acceleration. Therefore, to get the output position, one needs to integrate twice. This yields the typical double integrator behavior (rigid body mode) of a voice coil motor. This simplification neglects any flexible modes and damping effects. To obtain a more accurate model of the actuator, one has to take flexible modes, the back EMF of the motor, effects of power amplifier [65], (non-linear) pivot friction [66] and damping into account. In this dissertation, data based actuator modeling will be performed rather than modeling based on first principles.

There exist two techniques to position the slider relative to the disk when the disk is at rest (Fig.2.16). One is to position the slider in a so-called landing zone close to the inner diameter of the disk. This zone is laser textured to lower the

adhesion forces between the slider and the disk. When the disk starts to rotate, the air bearing is established and the slider takes off. This method is often referred to as contact-start-stop (Fig. 2.16a). In recent years, a so-called load/unload mechanism (Fig. 2.16b) has been implemented which allows withdrawal of the slider when the disk is not spinning, i.e., the slider is "parked" on a ramp off the disk. This increases shock resistance and reliability of the disk drive [67].

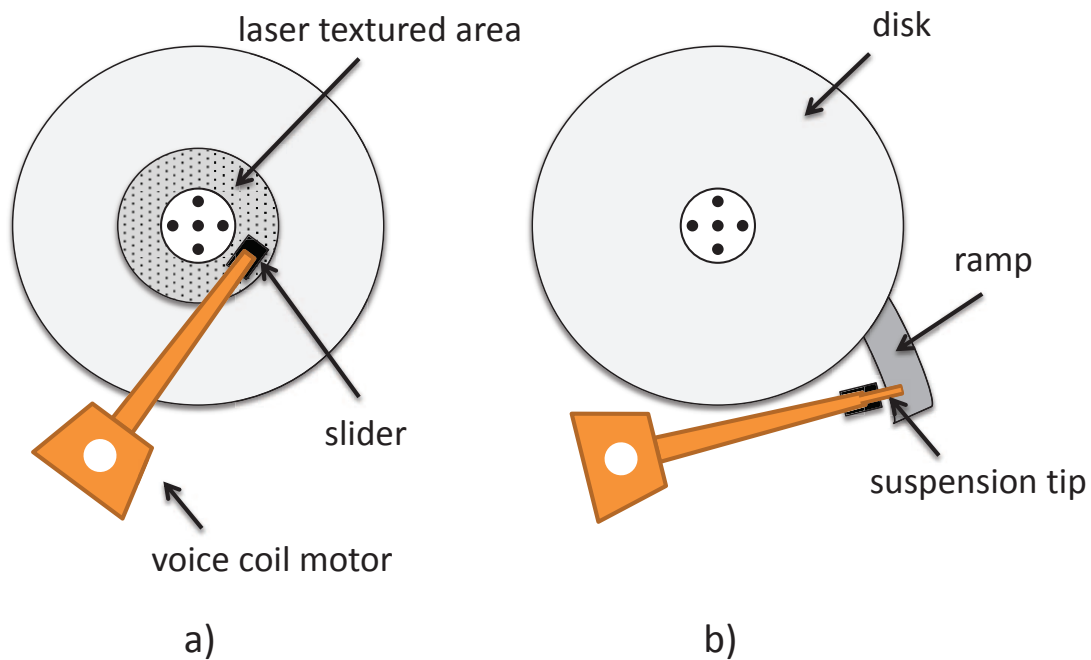


Figure 2.16: Methods for non-operational head positioning: a) contact-start-stop and b) load/unload

2.5.3 Micro-actuator

The VCM has a limited bandwidth due to its inertia and constrained control signals. Thus, high frequency disturbances cannot be rejected and track misreg-

istration (TMR) might occur. Furthermore, the increase in storage capacity and track density in disk drives requires a more accurate track seeking and track following servo mechanism.

Micro-actuators are believed to be one solution to overcome this problem and to meet higher accuracy and speed requirements of the servo mechanism [68] and during the process of servo writing [69]. One typically refers to this approach as dual-stage actuators considering the voice coil motor to be the first stage and the micro-actuator to be the second stage actuator. The VCM operates at low frequencies (typically below 1-2 kHz) with a relatively large stroke. The micro-actuator rejects high frequency disturbances (usually above 1kHz) with a stroke that is orders of magnitude smaller than the VCM stroke. The much smaller mass of the micro-actuator enables a higher bandwidth of the dual-stage actuator over conventional voice coil motor actuators.

The performance of a conventional VCM based servo mechanism has fundamental limits such as described by the Bode integral theorem. In continuous-time systems with relative actuator degree² greater or equal to 2, the following holds [70]

$$\int_0^{\infty} \ln |S(j\omega)| d\omega \quad (2.6)$$

where S is the sensitivity function of the stable feedback loop and ω is the angular frequency. This is known as the waterbed effect which states that the total area under the plot of the sensitivity function versus frequency remains constant. This

²difference between the denominator degree and the numerator degree in the transfer function

means that by improving the disturbance rejection in a certain frequency range, one worsens the disturbance rejection in another range. By considering dual-stage actuators, one can - depending on the micro-actuator design - bypass the waterbed effect.

A number of different approaches for second stage actuators in hard disk drives have been explored within the last few years. Some of these micro-actuators are MEMS-type devices (microelectromechanical systems) based on electrostatic or electromagnetic effects [71, 72, 73, 74, 75, 76, 77, 78]. Other micro-actuators are based on piezoelectric principles [79, 80, 81]. The actuators are either mounted on the suspension or on the slider. There are also approaches that have the micro-actuator integrated in the slider and allow a flying height adjustment in addition to off-track positioning [82]. An excellent overview of available second-stage actuators and control schemes is given in [83]. It was also proposed to use the second-stage actuator for active vibration damping using self sensing [84],[85], i.e., the actuator is used as a strain sensor to detect off-track vibrations and suppress them simultaneously.

The implementation of a dual-stage actuator in a HDD was proposed already 20 years ago [68]. Although their advantage over conventional servo mechanisms has been known for such a long time, dual-stage actuators have only been implemented in commercial products in the very recent past. One reason for this is increased production and implementation costs. In future hard disk drives with track densities exceeding 12,000 tracks per mm (300 ktpi), dual-stage actuators

are likely to be used.

A typical example of a commercially available suspension based piezo actuator is shown in Fig.2.17. The piezoelectric elements use a common electrical

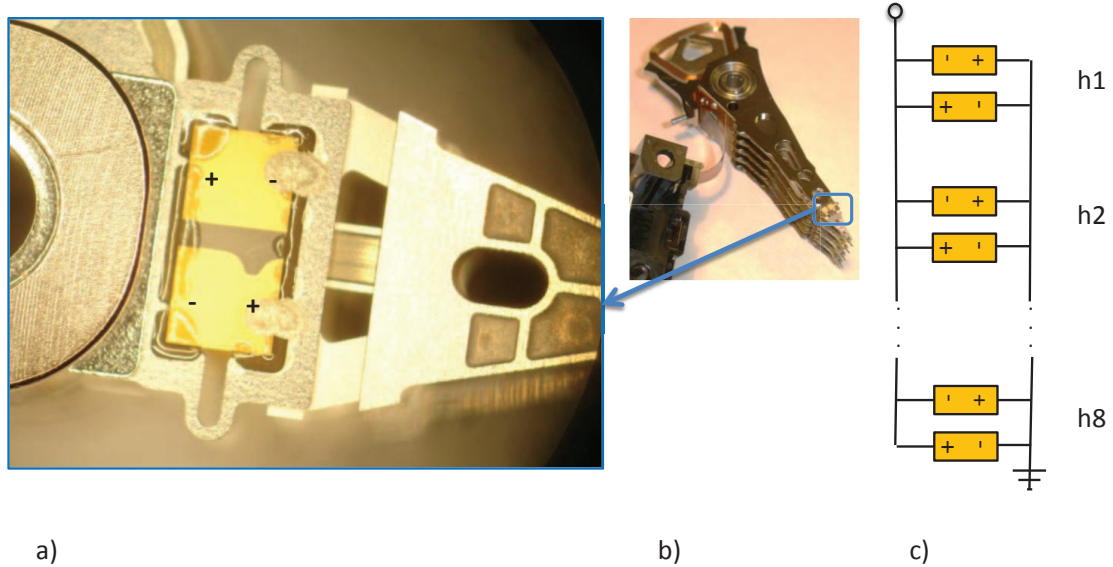


Figure 2.17: Piezo-electric push/pull actuated suspension in a commercial available hard disk drive: a) close-up b) E-block actuator arm with 8 suspensions and heads c) electrical schematic of connecting the 8 actuators

ground but are connected in the opposite way (Fig.2.17a and c). If a voltage is applied, one of the piezo elements contracts whereas the other one expands. Thus, a rotary motion is induced. The micro-actuator has a limited stroke, and, thus, it is more useful for track-following than for track-seeking [86]. However, it can be used for short distance seeks [86, 87].

2.5.4 Flying height actuator

Two of the key technologies in achieving higher storage density are the reduction of the clearance between the read/write element and the recording medium

and the minimization of flying height variations to maintain low bit error rates [88]. The flying height has decreased from initially about $20\text{ }\mu\text{m}$ [89] to a few nanometers in today's hard disk drives. The idea of actively controlling the flying height was introduced as early as 1990 [90]. The first design proposed was based on a piezo element. This approach was difficult to implement at a cost-efficient mass production level. Thin-film micro heaters for flying height control were later introduced by Meyer et al. [91] and Mächtle et al. [92]. The implementation of a resistance heater element became necessary at low flying heights for various reasons. First, the write head causes thermal deformation of the air bearing surface towards the disk during the write process which is referred to as pole tip protrusion [93]. This causes a different flying height during writing and reading, respectively, which is not desirable. To mitigate this effect and achieve the same flying height during reading and writing, heads were introduced that feature a resistance heater element that is positioned in close proximity to the read/write element. Figure 2.18 shows a side view of the slider and the disk for this case. As can be seen from Fig. 2.18, the read/write element and the resistance heater are positioned at the trailing edge of the slider. Activating the resistance heater, one finds that the head disk clearance can be reduced by Δd . Hence, write current induced pole tip protrusion can be compensated by activating the resistance heater during reading. A second reason for implementing micro heater elements in the slider is that tolerances during manufacturing of the head can be relaxed and flying height changes due to changes in environmental conditions during operation can be compensated.

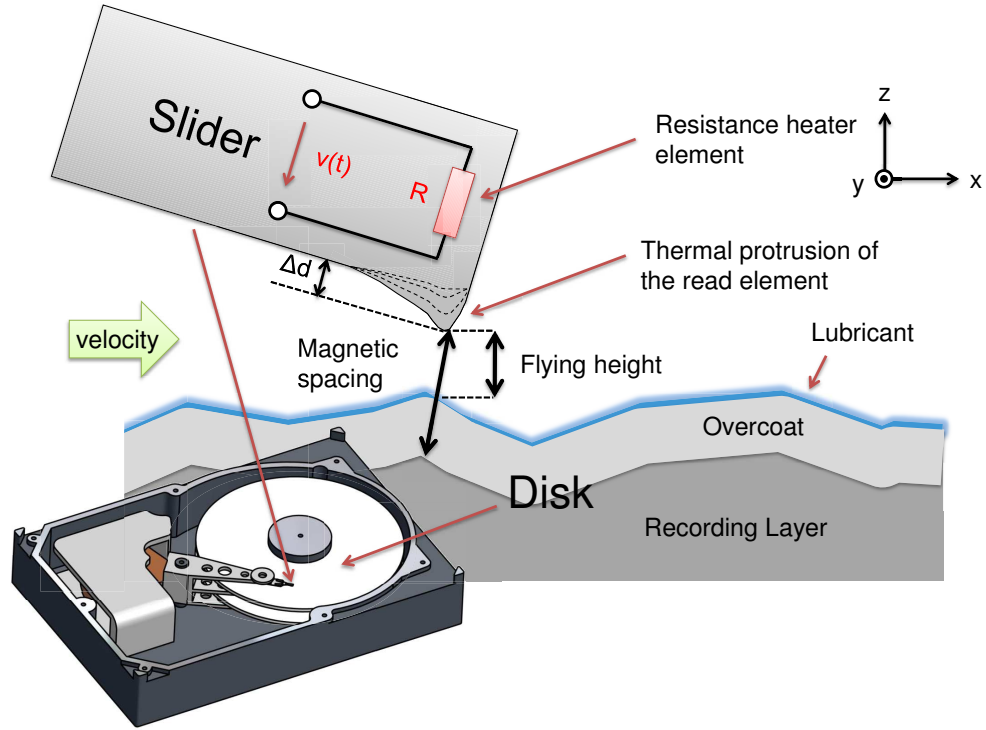


Figure 2.18: Hard disk drive and side view of trailing edge of the slider with resistance heater element for thermal flying height control

2.6 Control aspects

Hard disk drives are exposed to many different disturbances. As discussed in section 2.5.1, one can differentiate repeatable and non-repeatable disturbances. In addition to disturbances caused by misalignment of HDD components, one has to consider aerodynamic forces or external shocks and vibrations [54]. In order to accurately position the read/write head over a desired bit, a closed-loop servo controller as illustrated in Fig. 2.19 is needed. In disk drives, pre-written servo

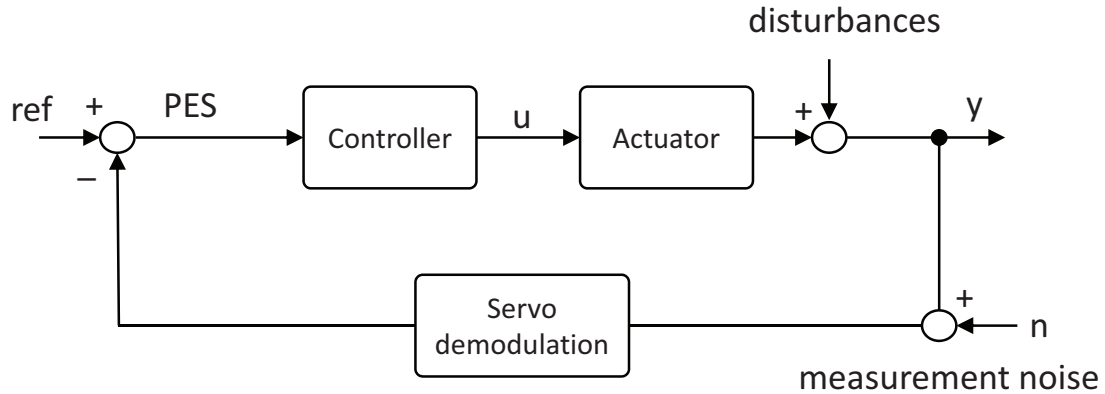


Figure 2.19: Common closed loop control structure

pattern allow to generate a position error signal (PES). The PES determines the lateral off-track position of the read/write head with respect to the track center. A so-called servo actuator, introduced in sections 2.5.2 and 2.5.3, adjusts the off-track position of the head. Three different operational situations occur in hard disk drives:

1. In the so-called "idle" or "rest" mode, the head is positioned on the ramp away from the disk (Fig. 2.16b)
2. In the so-called track seeking mode the head is moved from a given track to a desired track
3. In the track-following mode, the head is positioned on the same track so that data can be written or read back from the disk

The latter two situations will be explored in the next subsections. Before doing this, however, a short introduction is given on how to obtain the position feedback

for closed-loop control.

2.6.1 Servo sectors for position estimation

In the early years of hard disk drive technology, servo information was typically written on one disk surface only, i.e., one disk was dedicated to servo information and all other disk surfaces in the stack were used for data. This technique is referred to as *dedicated servo* where one head was responsible for the positioning of all other heads in the disk stack. However, this approach disregards dynamic effects between individual heads and the fact that disturbance characteristics are different for each head. Clearly, this approach is only viable at low track densities.

State-of-the-art hard disk drives use an *embedded servo* as indicated in Fig. 2.20. The data sectors are interrupted by servo sectors which contain a DC gap field, an automatic gain control field, a servo timing mark, a track identification number and a burst pattern for the position estimate [54]. The position estimate is available in each servo sector, i.e., it is available at discrete time intervals. The PES sampling frequency is determined by the rotational speed times the number of servo sectors. As the number of servo sectors increases, the servo overhead - or the percentage of area on the disk that cannot be used to store information - increases as well. Hence, a trade-off exists between storage capacity and PES sampling rate. The sampling rate should be chosen at least 10 times the bandwidth of the closed-loop system [94]. Typically, the number of servo sectors on the disk is on the order of 200, i.e., the sampling frequency is on the order of several tens of kHz. It should

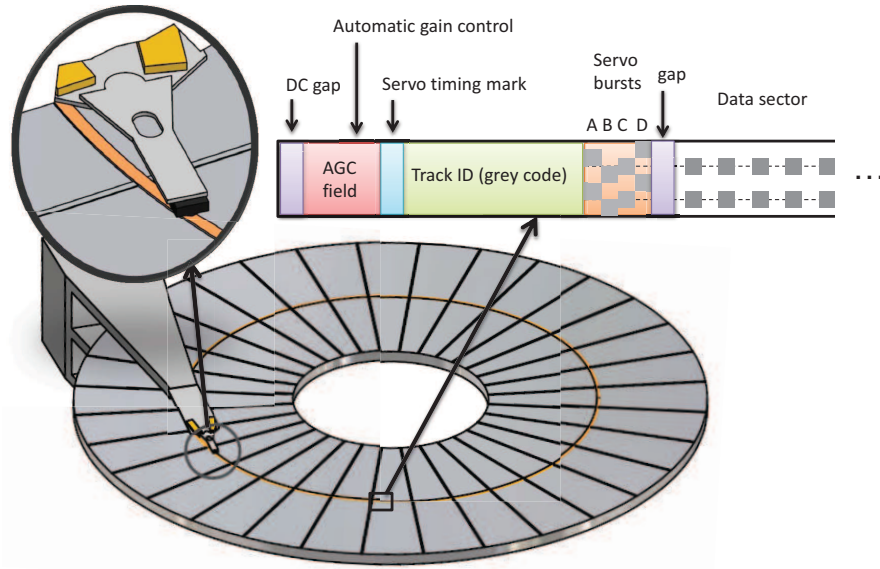


Figure 2.20: Disk with servo and data sectors

be noted that the embedded servo demands a significant amount of space on the disk and the overhead might exceed 15-20% [95]. The burst pattern is particularly important for the position estimate during the track-following mode. Figure 2.21 shows a typical arrangement of A,B,C and D burst pattern in an amplitude based servo. Bursts A, B, C and D are placed at different radial positions. In particular, Bursts A and B are off-set by one track from each other and Bursts C and D are also off-set by one track from each other, although they are off-set by one half of a track with respect to Burst A. Four different off-track positions of the head (1-4) are indicated in Fig. 2.21 by the dashed lines denoted by 1,2,3,4. The resulting in-phase and quadrature PES is shown on the right. The in-phase PES is zero at the track center and the quadrature PES is zero between two tracks. The corresponding

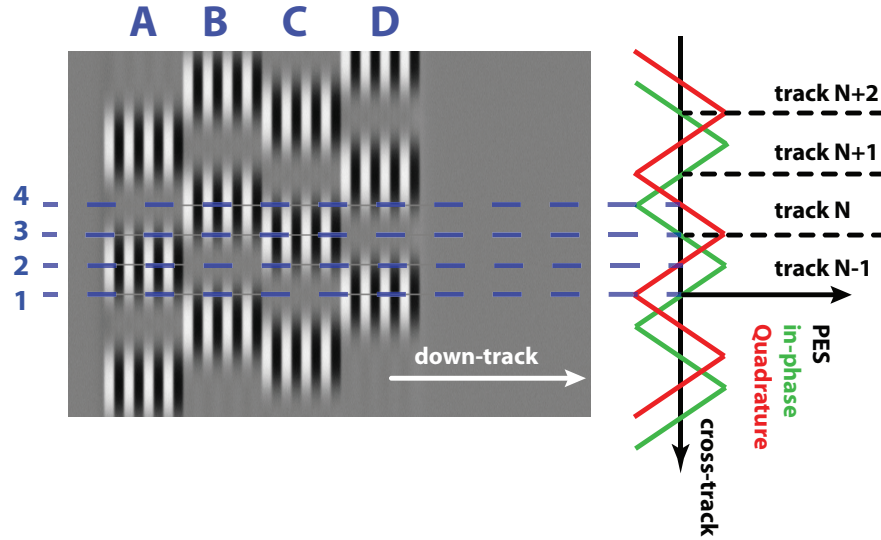


Figure 2.21: Typical amplitude based servo pattern (after [54])

readback signals for these four head positions are shown in Fig. 2.22. At position 1 (track N-1), the read head detects the same signal amplitude due to burst A (to the left) and due to burst B (to the right) as it moves along the track. Burst C is not detected while the full amplitude level of burst D is measured since it is centered on the track. At position 2, the head is located between track N and track N-1. As the head is moved from position 1 to position 2 the amplitude from burst A increases and the amplitude from burst B goes to zero. Now, burst C and D are detected with equal (but decreased) amplitude levels since the head is positioned at the centerline between the two bursts. The servo signals detected at head positions 3 and 4 are derived in a similar fashion. Based on the amplitude levels of A,B,C and D bursts that are detected (Fig. 2.22), the PES can be computed.

In recent years, more advanced servo pattern have been proposed such as

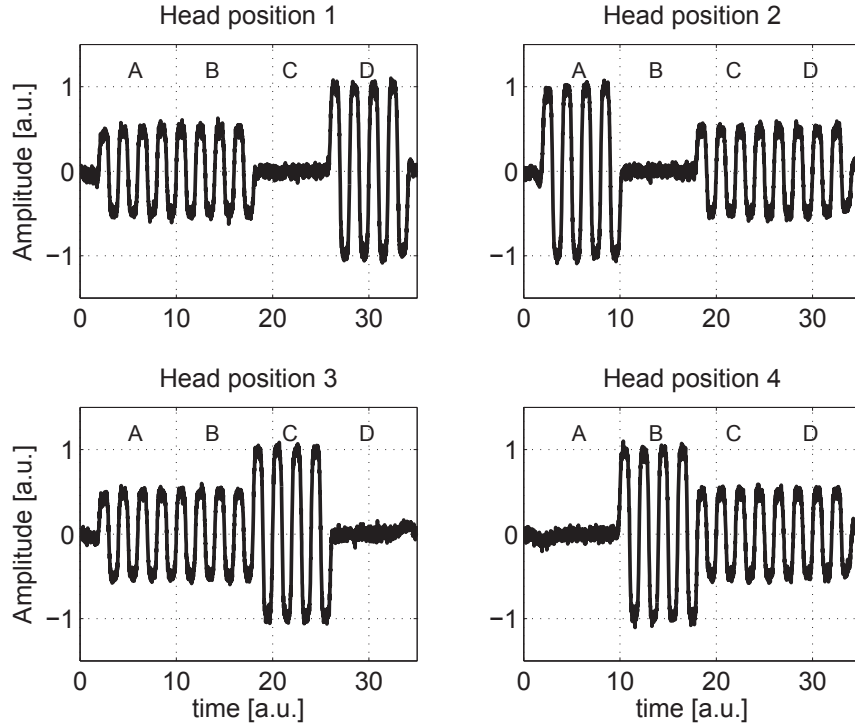


Figure 2.22: Readback signal for head position 1-4 from Fig. 2.21

the dual-frequency based servo pattern [96] that decreases the servo overhead. Also the use of timing-based instead of amplitude based pattern has been shown to increase the servo performance significantly [97].

2.6.2 Track following

It is generally acknowledged that measurable track-misregistration already occurs if the read head is 10% of the track pitch away from the track center [72]. This introduces tight constraints on the positioning accuracy of the head with respect to the track center. It is estimated that the TMR budget (3σ) will be as low

as 2.5 nm for future 40,000 tracks per mm (1,000 ktpi) drives [98]. This requires advanced control methods that compensate for repeatable run-out and significantly reduce non-repeatable run-out. Classic control design techniques such as PID-control combined with lead-lag compensators would yield sufficient tracking performance in older generation hard drives. Recently, more advanced techniques such as linear quadratic Gaussian (LQG) and/or linear loop-transfer recovery (LTR) [99], adaptive control [100], iterative learning control [101] and H_∞ -control [102] have been proposed to only name a few.

A different approach to increase the closed-loop servo bandwidth is the implementation of dual-stage actuators as discussed in section 2.5.3. In chapter 3, we will show in detail the design and implementation of a dual-stage track-following controller.

2.6.3 Track seeking

During the track seeking process, the head is moved from one track to another. The hard disk drive servo mechanism faces several non-linearities such as friction effects, or high frequency mechanical resonances [103]. However, the major non-linearity that becomes apparent during the track-seeking mode is actuator saturation, i.e., the VCM actuator has limits on its input and output. A number of different control schemes have been proposed to address this problem.

One very popular technique is the so-called proximate time-optimal servo mechanism (PTOS) [104] that was modified from conventional time-optimal con-

trol. The difference between both control methods is illustrated in Fig. 2.23 for the

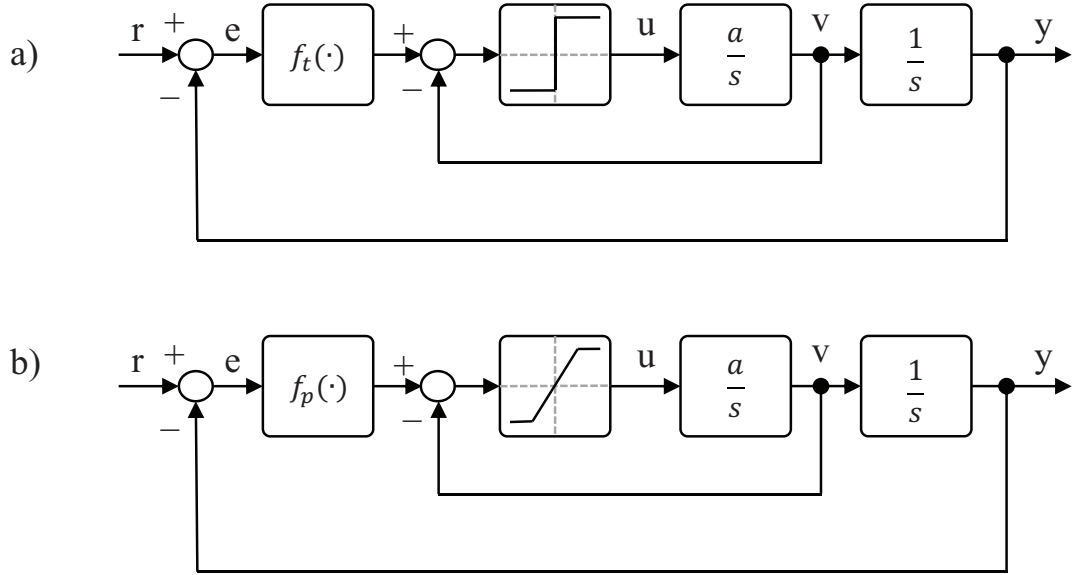


Figure 2.23: a) Time optimal control (TOC) scheme and b) proximate time-optimal control (PTOS)

continuous-time case where a is an acceleration constant of the voice coil motor and $f_{t,p}(\cdot)$ represents the switching function of the control law of TOC and PTOS, respectively. For the TOC scheme the switching function is defined as [103]

$$f_t(e) = \text{sgn}(e) \sqrt{2au_{\max}|a|} \quad (2.7)$$

which is very sensitive to noise. Hence, this scheme was improved by Workman [104] to include a saturation element instead of the signum function. A linear control law is applied for small errors e . The switching function of the PTOS becomes

$$f_p(e) = \begin{cases} k_1 e / k_2 & \text{for } |e| \leq y_l, \\ \text{sgn}(e) \left(\sqrt{2au_{\max}\alpha|e|} - \frac{u_{\max}}{k_2} \right) & \text{for } |e| > y_l. \end{cases} \quad (2.8)$$

where α is a constant between 0 and 1 and k_1 and k_2 are the feedback gains of position and velocity, respectively. The saturation element in Fig. 2.23b) is defined as

$$sat(x) = \begin{cases} +1 & \text{for } x > +y_l, \\ x & \text{for } -y_l \leq x \leq y_l, \\ -1 & \text{for } x < -y_l. \end{cases} \quad (2.9)$$

Workman proved that [104, 103]

$$y_l = \frac{u_{\max}}{k_1}, \quad k_2 = \sqrt{\frac{2k_1}{a\alpha}} \quad (2.10)$$

Another popular track-seeking control method is mode switching control with initial value compensation as proposed in the 1990s [105, 106]. Using this method, the transient behavior of the servo during the switching process between two controllers could be improved significantly. More recently, techniques such as composite nonlinear feedback (CNF) control [107] and shaped time-optimal servomechanism (STOS) [108] were proposed. The STOS technique is particularly interesting for the scope of this dissertation as it employs input shaping to deal with the actuator saturation effects. A schematic of the main working principle of STOS is shown in Fig. 2.24. The input to the closed-loop system is pre-shaped to suppress residual vibrations and achieve near time-optimal performance [108]. In chapter 4, we show how convex optimization techniques can be utilized to pre-shape reference signals for optimal seeking.

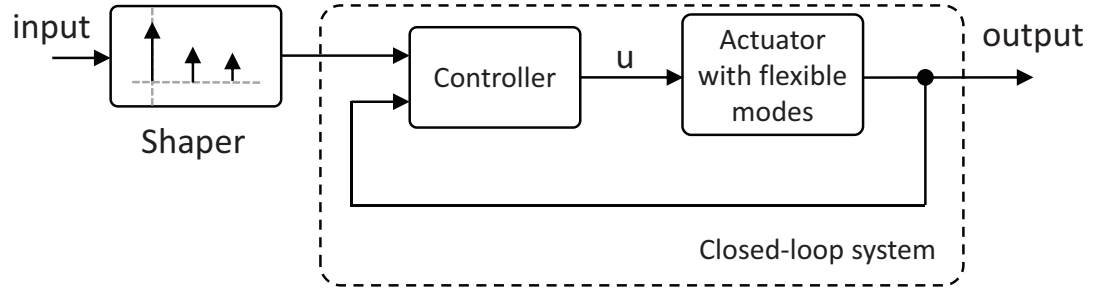


Figure 2.24: Schematic of shaped time-optimal servomechanism

2.7 Geometric aspects

2.7.1 Bit aspect ratio, linear density and areal density

The areal density in disk drives is defined by the track density times the linear density (Fig. 2.25). Here, the linear density is determined by the number of bits per unit and the track density by the number of tracks per unit length. The

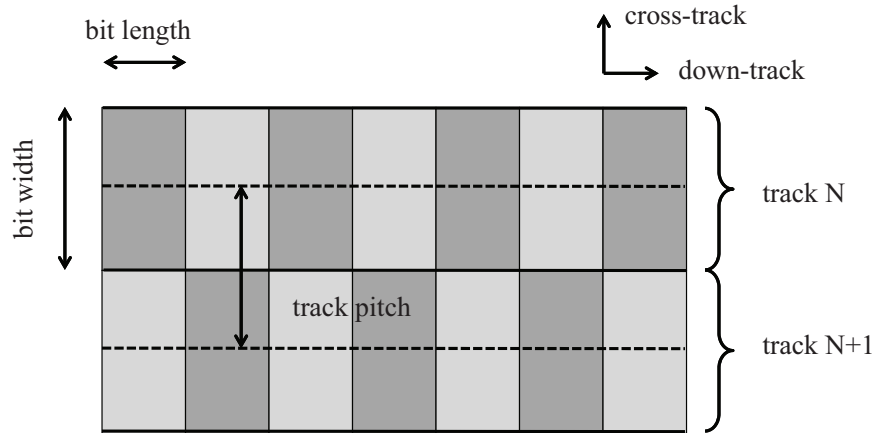


Figure 2.25: Bit geometry definition: simplified section of recorded bit pattern

bit aspect ratio (BAR) is defined by bit width over bit length. The BAR has been

decreasing as storage density increased. In today's drives the BAR is typically on the order of 6. It is likely that the BAR will be reduced to 4-5 as storage densities of 1.5 Gb/mm^2 (1 Tb/in^2) are approached [109].

2.7.2 Zone bit recording

One large benefit of storing data on a rotating disk versus e.g. (very long) tape is that the access time (latency) is comparably low. However, this introduces additional challenges that need to be addressed. If one would record data using a constant write frequency for the entire disk, one would be limited by the maximum linear bit density at the inner diameter of the disk. The bit length and data sector length would increase linearly towards the outer diameter of the disk. To compensate this effect, the disk is divided into several zones with different write frequencies. In Fig. 2.26, the schematic of the so-called zone bit recording [111] is illustrated. The disk model in Fig. 2.26 is divided into five different write frequency zones. The number of data sectors is increasing towards the outer diameter of the disk keeping the length of each sector approximately the same. This scheme allows to maintain a linear density in each zone that is close to its maximum.

2.7.3 Skew angle

The skew angle illustrated in Fig. 2.27 is a consequence of the use of rotational actuators rather than linear actuators for positioning the read/write element over a data track. There are several unwanted effects related to the skew angle in a

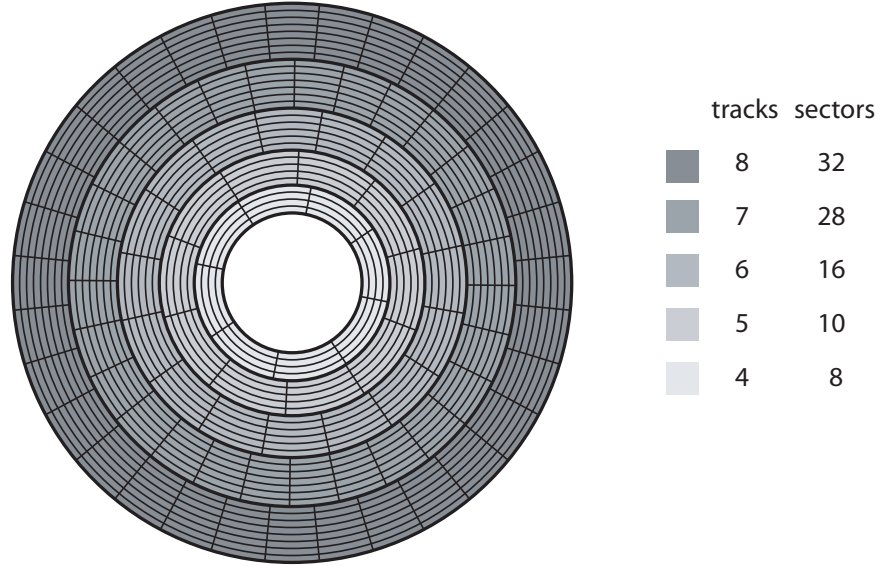


Figure 2.26: Schematic of zone bit recording with 5 different zones (after [110, 111])

hard disk drive. It causes a read/write offset as depicted in Fig. 2.27. It should be noted that the skew angle in Fig. 2.27 is shown exaggerated for clarity. In a hard disk drive, typically the skew profile is chosen (nearly) symmetrically to minimize the skew effect. The maximum skew angle is typically 15 degrees [113].

Tracks recorded at non-zero skew angle show side-track effects as depicted in Fig. 2.28. Close to the maximum linear recording density, the side-track effect is almost not detectable anymore as can be seen in [114]. It is also noted that the actual shape of a recorded bit pattern looks closer to the one shown in Fig. 2.28a) rather than the simplified geometry shown in Fig. 2.25 [114].

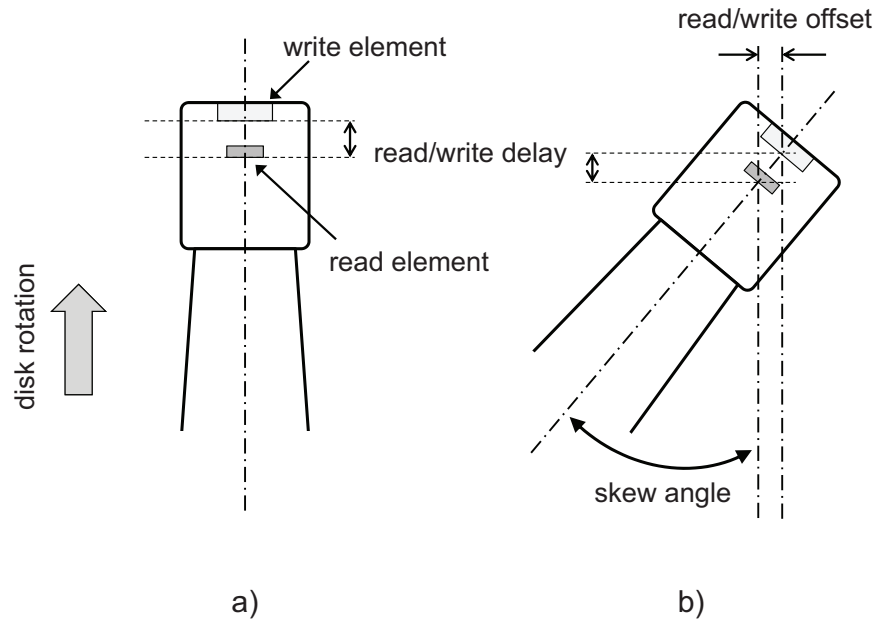


Figure 2.27: Effect of skew angle on read/write offset and read/write delay for a) zero skew (close to middle diameter of the disk) and b) at 15 degrees skew (close to outer diameter) - after [112]

2.8 Ongoing challenges and trends in hard disk drives

2.8.1 Miniaturization

Richard Feynman predicted in his famous paper "There is plenty of room at the bottom" already in 1960 [115] what tremendous progress in terms of miniaturization would be ahead. In hard drive technology that meant decreasing the size and number of disks in the drive. The progress went from 0.1 MB storage capacity on a single 24 inch disk in 1956 to a capacity exceeding 500 GB³ per 3.5 inch disk in 2011. The areal density in hard disk storage has increased over eight orders

³assumption based on 2 TB state of the art hard disk drive with a stack of 4 disks

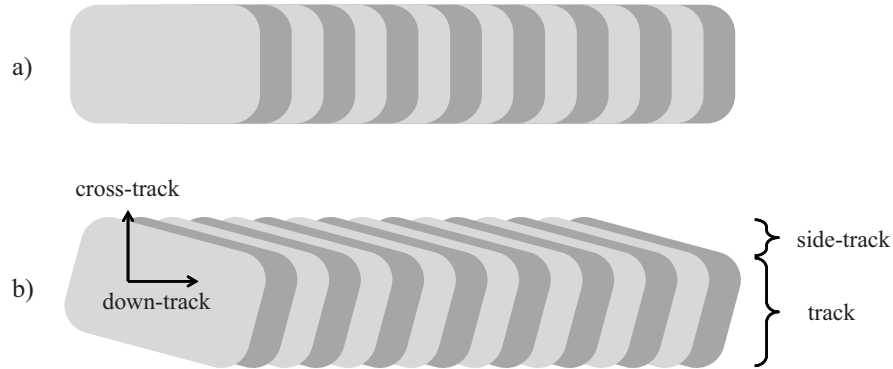


Figure 2.28: Bit shape recorded at a skew angle of a) 0° and b) 15° and skew related side-track effect.

of magnitude [116] since the IBM RAMAC of 1956. Figure 2.29 shows that the slope of the increase in storage density versus time has changed over the years. The "kink" in the curve in Fig. 2.29 that indicates a sharp rise in storage density in the 1990s is mostly attributed to the introduction of the magnetoresistive read elements as described in section 2.2.3. It can partially be attributed to the introduction of thin film disks and the substantial reduction in flying height. After reaching the limit of longitudinal magnetic recording about 10 years later in spite of switching to perpendicular recording the rise declined significantly. The limit of conventional perpendicular recording will be reached very soon and new emerging technologies such as shingle writing, bit patterned media or heat assisted magnetic recording are believed to overcome the existing limits. Those new technologies will be briefly introduced in section 2.9.

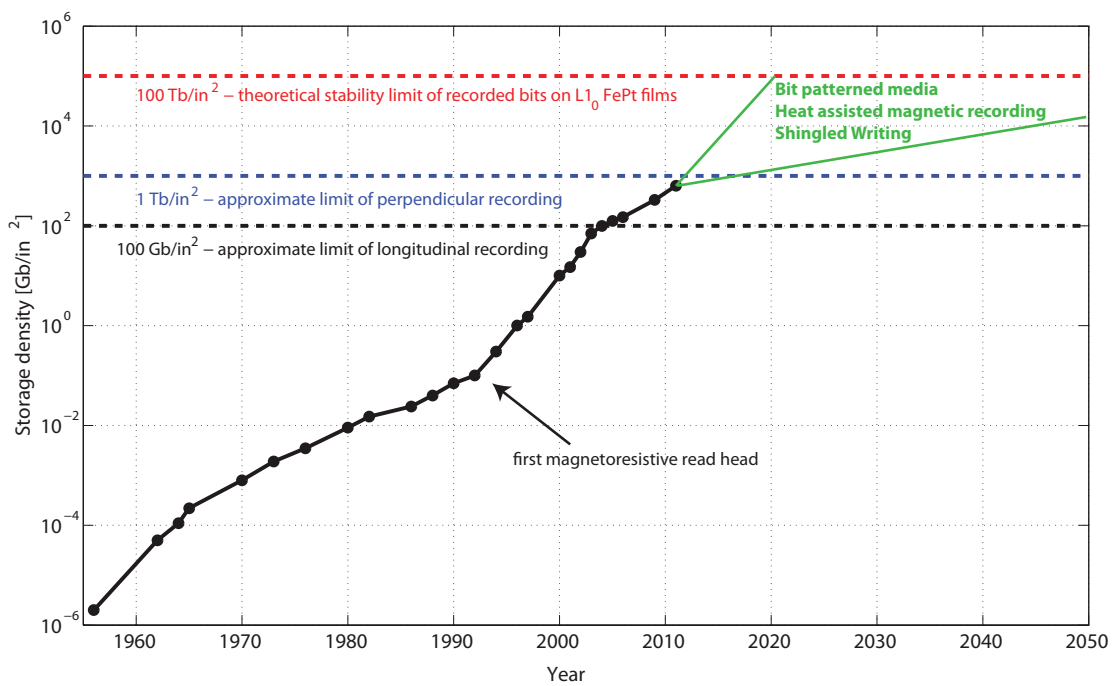


Figure 2.29: Areal density increase (data based on [117, 41, 29])

2.8.2 Form factors

The form factor of hard drives was reduced significantly over the years but reached its limit a few years ago. The smallest commercially available hard

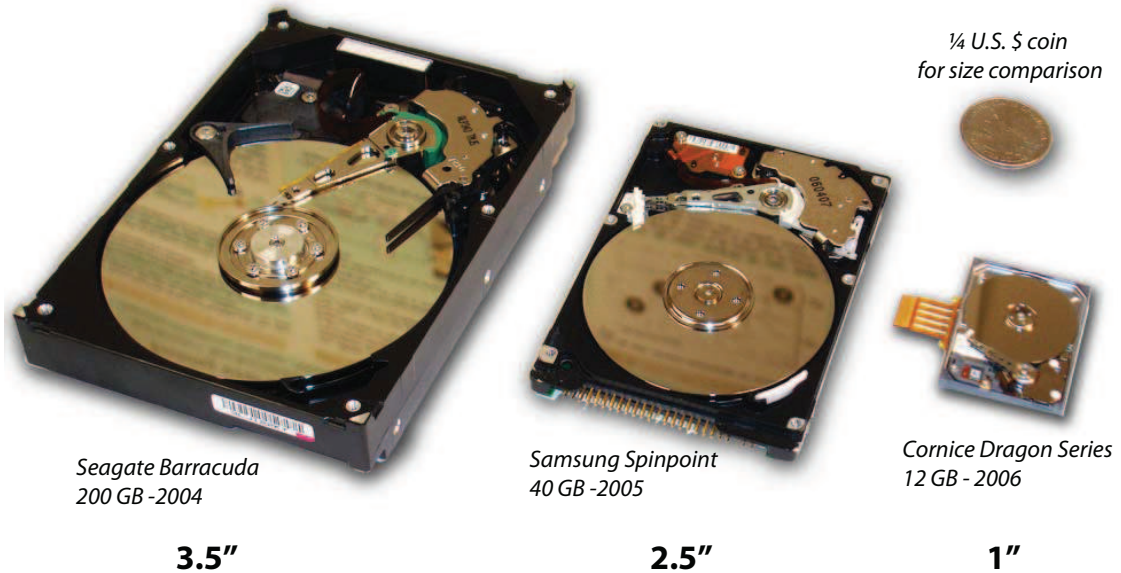


Figure 2.30: Different form factors of recent hard disk drives: 3.5", 2.5" and 1".

drive was presented in 2004 [118] as a 0.85" form factor drive. Figure 2.30 shows different form factor as they were available about 5 years ago. The so-called small form factor 1"-drive shown on the right in Fig. 2.30 lost its market share to solid state storage such as flash. Today, the most manufactured form factor is 2.5" for laptop applications and external storage devices followed by 3.5" form factor drives mostly for desktop and server applications. There are also 1.8" form factor drives on the market.

2.8.3 Economic challenges

As already indicated in chapter 1, the cost per storage in hard drives has decreased significantly over the past decades (Fig. 2.31). However, there has been

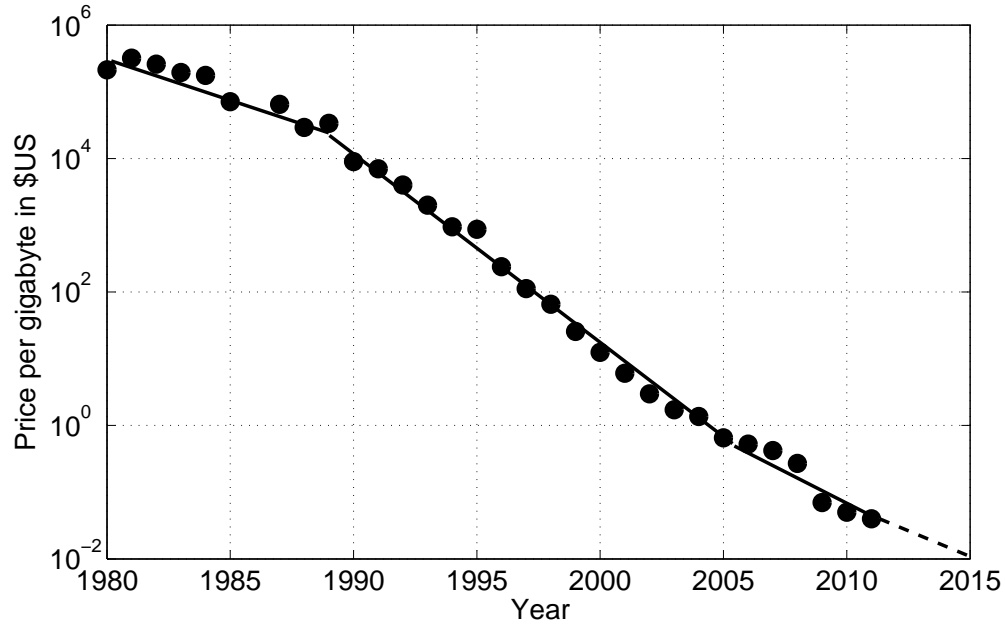


Figure 2.31: Evolution of price per gigabyte of hard drive storage since 1980. (Data based on [119, 120])

a growing threshold of storage capacity where competing solid state technology was able to replace hard disk drives. Currently, this threshold is on the order of 50 gigabytes of storage capacity. Clearly, scalability has its limits in hard disk drives since basic mechanical components add to a total cost, regardless of how few GB are needed in the capacity range below 50 GB.

2.9 Physical limits and possible solutions

2.9.1 Thermal stability and super paramagnetic limit

The long-term stability of the magnetically stored information is crucial in whether or not hard drive technology will survive. As the grain size gets smaller the thermal stability decreases [121, 35]. The energy barrier for re-magnetizing a magnetic grain must be much larger than its thermal energy. Considering an 8-year stability of stored information, the factor between thermal energy and switching barrier is estimated to be at least 40 [122]. Based on $L1_0$ FePt recording material there is a fundamental limit in theoretically achievable storage density which is reached at approximately 150 Gb/mm^2 (100 Tb/in^2) [29] which is also depicted in Fig. 2.29. This is still two orders of magnitude above today's storage densities. However, the practical limits of conventional media and perpendicular recording technology will soon be reached at approximately 1.5 Gb/mm^2 (1 Tb/in^2) [41]. Several new technology concepts that address this issue are currently under development and will be introduced in the following three subsections.

2.9.2 Patterned and discrete-track recording

Discrete-track recording and bit patterned recording significantly reduces magnetic "crosstalk" effects in high areal density recording compared to conventional perpendicular recording [123]. The main differences are illustrated in Fig. 2.32. In conventional granular media, several grains form one bit. The transi-

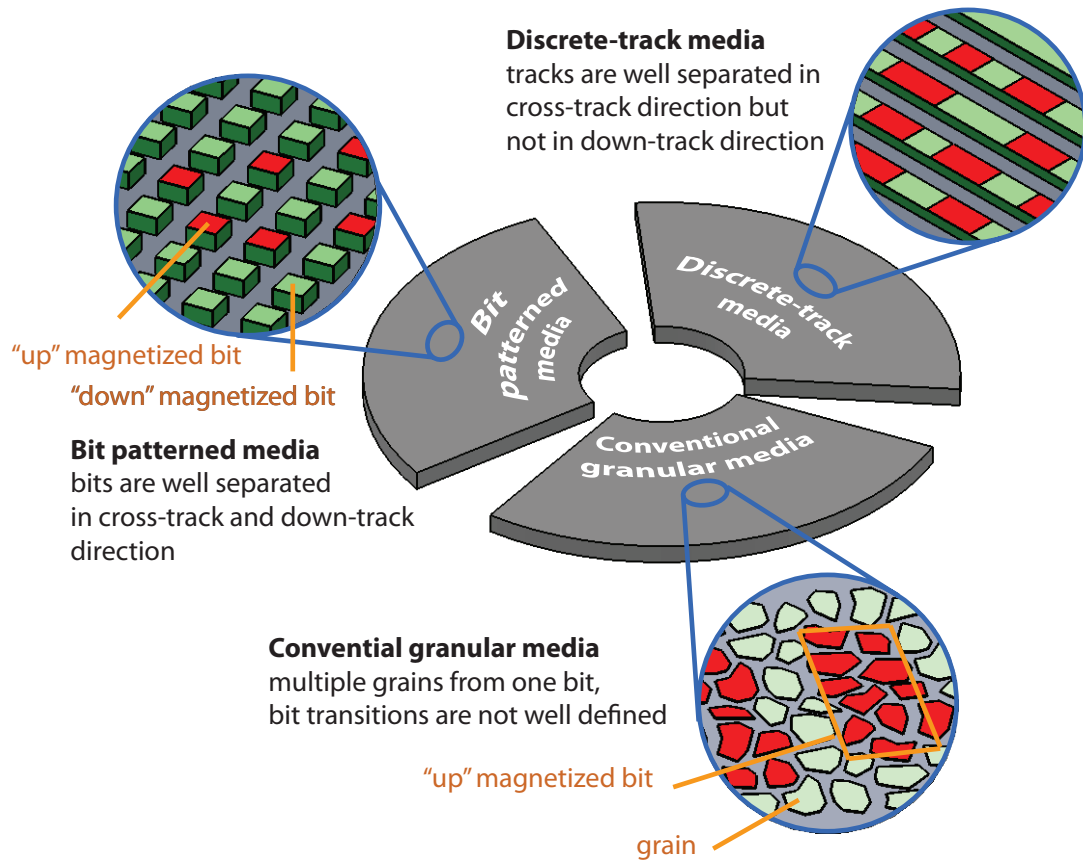


Figure 2.32: Patterned media, discrete-track media and conventional media

tions between the bits are not well defined which has a negative effect on the SNR. In discrete-track recording, the data tracks are magnetically separated in the radial (cross-track) direction. This reduces inter-track interference significantly. In bit patterned media, not only the tracks are magnetically separated in the radial direction but also the bits in the down-track direction. The thermal stability is much higher in discrete-track and bit patterned recording compared to conventional PMR. Therefore, much higher areal densities can be achieved. However, there are a number of problems related to flyability on patterned and discrete track media

[124]. It was suggested that the grooves would have to be filled and planarized to accomplish stable flying condition of the slider over the disk [125, 126]. In addition, a cost-efficient manufacturing process has to be developed to produce such media.

2.9.3 Energy assisted magnetic recording

Another approach to increase thermal stability is to use media with a higher coercivity and anisotropy than current media. This increases the energy barrier for bit reversal. However, additional local energy during the writing process is required. Different ideas have been proposed to address this. One interesting approach is microwave assisted recording. Simulations suggests that one could record with a write field that is $1/3$ of the coercivity of the media using ferromagnetic resonance effects and a localized AC field of tens of GHz frequency [127]. However, no working prototypes have been presented so far; thus, this technology is far from being implemented in a product.

A more promising approach seems to be the so-called heat (also thermally) assisted magnetic recording (HAMR/TAR) [128]. The main principle of HAMR is shown in Fig. 2.33. A laser is used to locally heat up the recording media which temporarily lowers the coercivity of the material. In this stage, a bit can be written and its magnetization remains "frozen" after cooling down. The required heat spot size is on the order of one magnitude smaller than the wavelength of the laser light. Therefore, a near-field optical transducer needs to be used and a complicated light delivering system. Several lab demos have experimentally verified the effectiveness

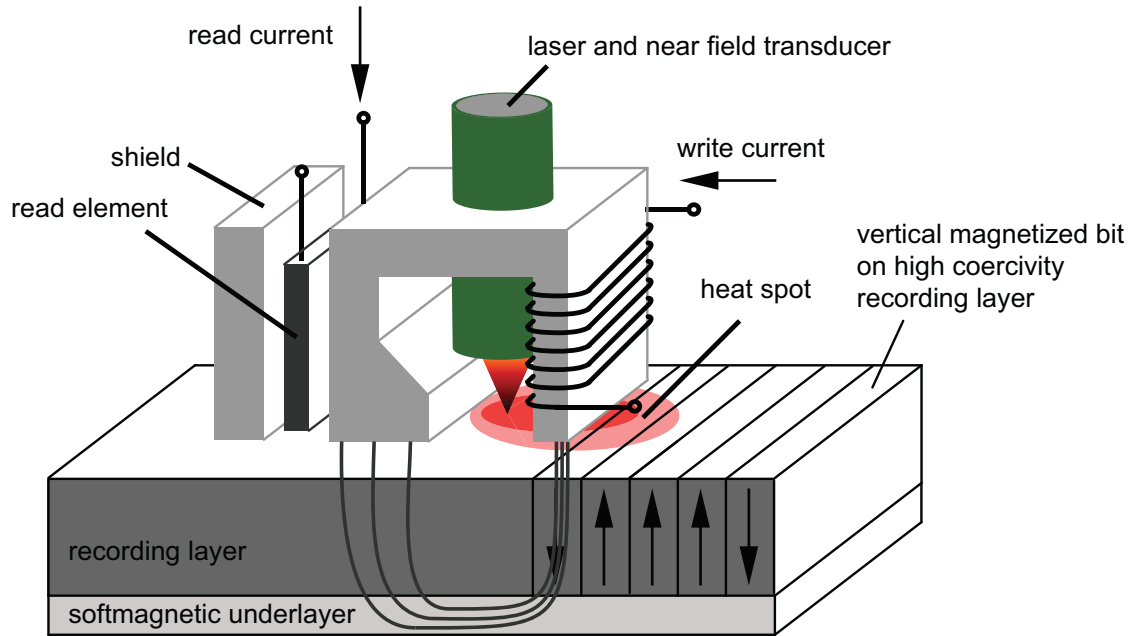


Figure 2.33: Principle of heat assisted magnetic recording

of HAMR [129, 130, 131].

2.9.4 Shingle recording

The implementation of BPM or HAMR will take a number of years (or it might never happen). However, as discussed earlier, conventional perpendicular recording will soon have reached its limits. Therefore, an intermediate solution is needed to increase storage density. Shingle recording is one possible option for future hard drives as only minor hardware and software modifications are needed. The main idea of shingle recording is shown in Fig. 2.34. The write pole has much larger width dimensions than the desired track width and a wide track is written in the first pass. In the second pass the first track is partially overwritten resulting

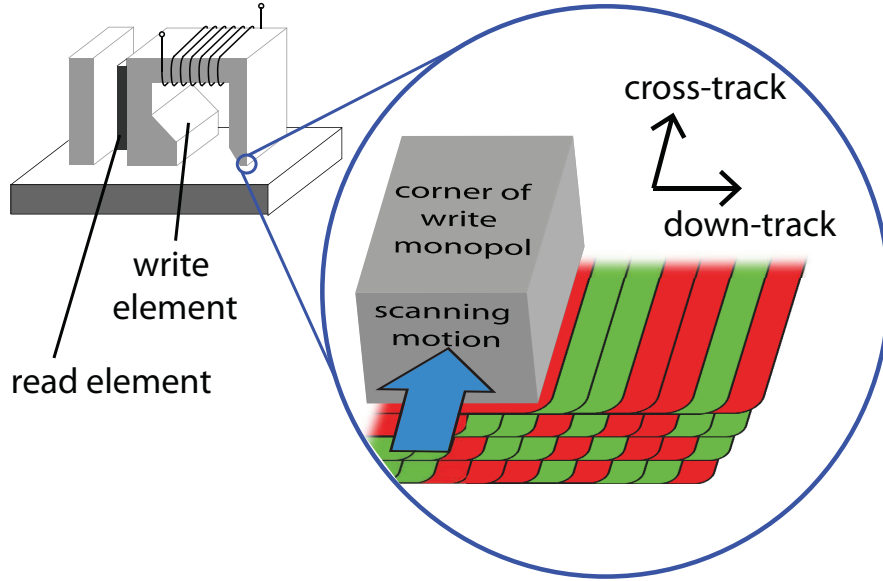


Figure 2.34: Principle of shingle magnetic recording

in a very narrow track. The tracks are written in a progressive scan as indicated in Fig. 2.34. One advantage of shingle recording over conventional PMR is that a higher write field can be applied. This increases the field gradient and results in a much more uniform magnetization through the recording layer [60]. The obvious disadvantage of shingle recording is a reduced speed in changing distinct bits or tracks. In that case, adjacent tracks would have to be re-written. However, improved data management [132] could make this problem insignificant.

2.10 Further reading

The first two chapters of this dissertation give a comprehensive introduction and motivation to magnetic recording technology. However, we only address key

issues that are important to understand subsequent chapters. There exist a large number of great textbooks on magnetic recording technology that include the various aspects discussed in chapter 1 and 2 in much more detail. The interested reader is referred to a reference book for magnetic recording by Bertram [133] and an extension to perpendicular technology by Khizroev and Litvinov [134].

A very detailed history of magnetic recording technology was given by Daniel, Mee and Clark [15] and Daniel and Mee authored another textbook a few years earlier that gives a good introduction to recording physics and media [135]. The latter issues are addressed in detail by Plumer, van Ek and Weller [136]. Concerning mechanical and control aspects there exist two excellent textbooks by Mamun, Guo and Bi [54] and by Chen, Lee, Peng and Venkataramanan [86]. The latter two books have particularly helped the author of this dissertation to learn about hard drive technology since 2007.

Tribology related issues are e.g. addressed by Bhushan [137]. Vasic and Kurtas [138] give a comprehensive overview of recording channels and signal processing aspects in magnetic recording.

2.11 Contribution and organization of this dissertation

This dissertation focuses on optimizing the positioning of the read/write head over the data track in hard disk drives. Cross-track positioning will be con-

sidered as well as vertical (flying height) adjustment.

In chapter 1, an introduction to the state-of-the-art in storage technology is given combined with a brief history. In addition, an outlook on emerging storage principles and future trends is presented.

Chapter 2 introduces hard drive technology with a particular focus on its multidisciplinary. A strong emphasis is given to electro-mechanical and control aspects since this lies within the main scope of this dissertation.

In chapter 3, we present the system identification and controller design for a dual-stage actuator hard disk drive. Two substantially different controller design methods, the sensitivity decoupling method and H_∞ -loop shaping, are applied to a dual-stage actuator servo system and compared. Both controllers are implemented in a hard drive.

Chapter 4 addresses the seeking process in hard disk drives. A framework for closed-loop input shaping based on convex optimization techniques is presented to achieve optimal performance and reduce residual vibrations of the closed-loop system. The theoretical framework is applied to a hard drive and experimental results are presented.

The second part of this dissertation deals with the positioning of the read/write element in the vertical direction. The main goal of this study is to minimize flying height variations using active thermal flying height control as introduced in section 2.5.4. The flying height change is measured using a pre-written servo pattern. We first develop a simplified analytical model of the readback process in chap-

ter 5. This model is straightforward to understand and is applicable to emerging technologies such as bit patterned recording as well as conventional recording.

In chapter 6, we develop a novel method of estimating the flying height change based on the servo pattern, in particular A and B burst. The technique relies on a modified Wallace spacing equation. Simulations and experimental results obtained on a spin stand show the effectiveness of the proposed method.

Chapter 7 shows how dynamic modeling of the thermal actuator can be performed using the measurement scheme developed in chapter 6. The modeling is based on a generalized realization algorithm. We employ a finite horizon framework similar to the one presented in chapter 4 to minimize circumferential flying height variations. The method is experimentally tested on a spin stand and a significant reduction in flying height variations is observed.

Finally, in chapter 8, a summary and concluding remarks are presented.

2.12 Acknowledgement

Chapter 2, in part, is a reprint of the material as it appears in "Modeling and Control of a Dual-Stage Actuator Hard Disk Drive", Boettcher U., de Callafon R.A., Talke F.E., *Journal of Advanced Mechanical Design, Systems, and Manufacturing*, Volume 4, Issue 1, pp. 107-118, 2010. The dissertation author was the primary investigator and author of this paper.

Chapter 2, in part, is a reprint of the material as it appears in "Servo Signal

Processing for Flying Height Control in Hard Disk Drives”, Boettcher U., Lacey C.A., Li H., Amemiya K., de Callafon R.A., Talke F.E., *Microsystem Technologies*, 2011. The dissertation author was the primary investigator and author of this paper.

Chapter 2, in part, is a reprint of the material as it appears in ”Dynamic Flying Height Adjustment in Hard Disk Drives through Feedforward Control”, Boettcher U., Li H., de Callafon R.A., Talke F.E., *IEEE, Transactions on Magnetics*, 2011. The dissertation author was the primary investigator and author of this paper.

In addition, chapter 2, in part, is a reprint of the material as it appears in the dissertation author’s ”Diplomarbeit” (Master’s thesis) at Dresden University of Technology. The Master’s thesis was done at UCSD/CMRR.

3 Modeling and control of a dual-stage actuator hard disk drive

3.1 Introduction

In section 2.5.3, we introduced dual-stage actuators and their ability to increase closed-loop servo performance in hard drives. In this chapter, we will investigate two different methods of dual-stage controller design: the sensitivity decoupling method and an H_∞ loop shaping method. First, data based modeling of both actuators is performed using frequency response function measurements and an impulse response based realization algorithm. Thereafter, two dual-stage controllers are designed and implemented in the drive. The dual-stage hard disk drive considered in this paper uses a push/pull actuator based on a piezoelectric transducer (PZT). A close-up of the slider with the suspension and the PZT elements is shown in Fig.3.1.

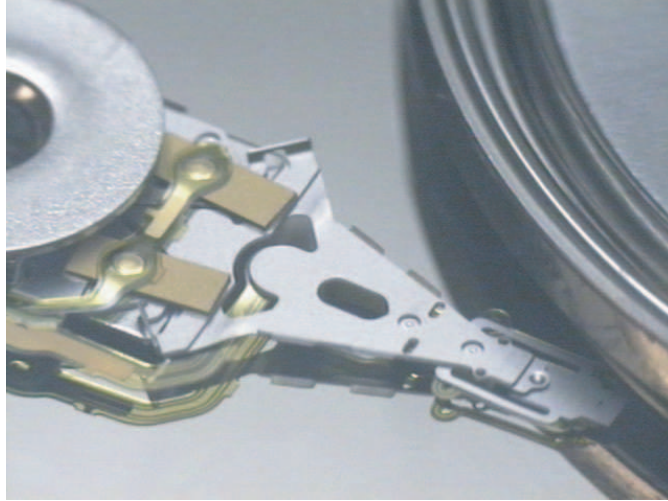


Figure 3.1: Close-up image of the piezoelectric microactuator considered in this study

3.2 Modeling and system identification

In order to be able to inject control signals, the hard disk drive servo controller was bypassed completely. The circuit board was disconnected from the HDD and all motor drivers were replaced. Since the position error signal (PES) of the servo mechanism was not directly available, a laser Doppler vibrometer (LDV) was used to measure the radial slider motion. To accomplish visual access to the slider the HDD had to be modified. The top cover was replaced with one made out of plexiglas and a mirror was used to deflect the laser beam onto the side of the slider. The experimental set-up illustrated in Fig. 3.2 was used to determine the frequency response function of both actuators.

Many modeling approaches yield a continuous time model of the actuator [139, 86]; however, we estimated directly a discrete-time model using a realization algorithm. It is noted that throughout this dissertation data based modeling is

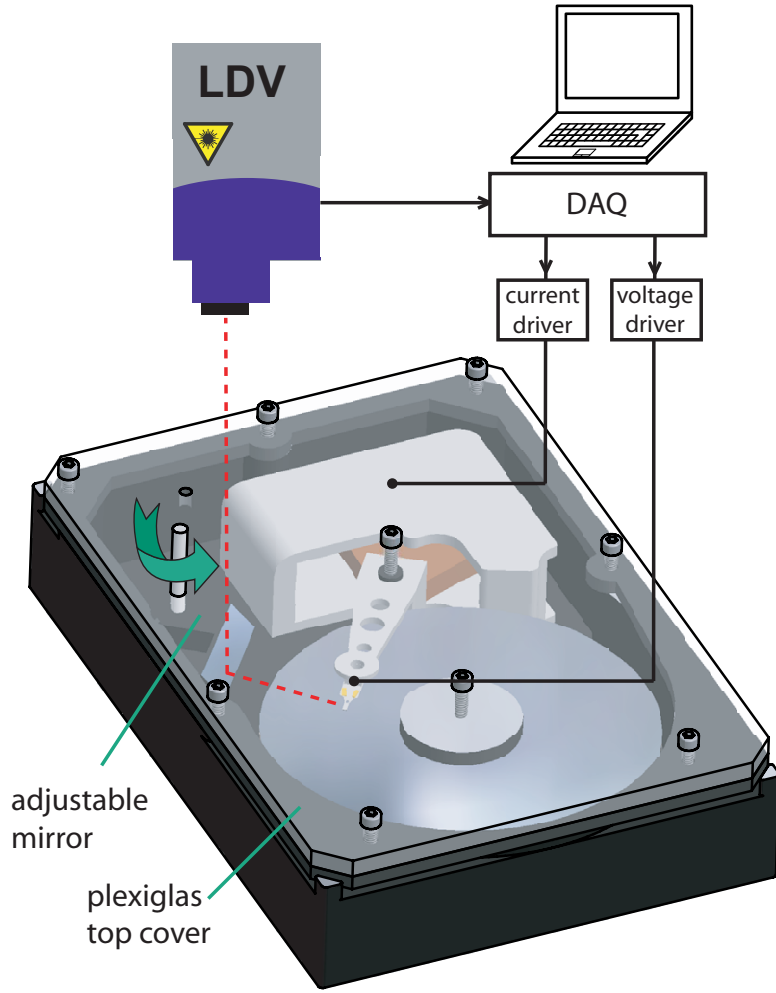


Figure 3.2: Schematic of the experimental set-up to determine the frequency response function of the dual-stage actuator.

obtained through realization algorithms. In chapter 4 and 7 we use step inputs and a generalized realization algorithm [140]. However, a step input is not a good choice for a voice coil motor since the actuator is only marginally stable in an open-loop configuration. This is due to a lack of an actual spring in the actuator design. Therefore, a step input would cause a loss in LDV signal and potentially move the head off the disk. Hence, we use frequency domain data instead that is converted into time domain data first by means of inverse discrete Fourier transform (IDFT).

And the modeling is performed using the eigensystem realization algorithm [141]. Additional frequency-dependent weighting functions are used to emphasize control relevant resonance modes of the actuator response. The inverse discrete Fourier transform (IDFT) of the frequency response function (FRF) measurement yields an estimate for the impulse response of the system. The impulse response coefficients (Markov parameters) are defined by

$$g_k = \frac{1}{2N} \sum_{l=0}^{2N-1} G_l e^{j\omega_k l}, \quad k = 0, 1, \dots, 2N-1 \quad (3.1)$$

where G_l contains the FRF data and ω_k is the frequency vector defined by

$$\omega_k = \frac{\pi k}{N}, \quad k = 0, 1, \dots, 2N-1 \quad (3.2)$$

N denotes the number of FFT lines (frequency points) in the FRF measurements. The measured data are stored in a Hankel matrix \mathbf{H} that contains the Markov parameter estimates defined in (3.1). By choosing m as the number of impulse response samples taken into account, one can define an $m \times m$ Hankel matrix by

$$\mathbf{H} = \begin{bmatrix} g_1 & g_2 & \cdots & g_m \\ g_2 & g_3 & \cdots & g_{m+1} \\ \vdots & \vdots & \vdots & \vdots \\ g_m & g_{m+1} & \cdots & g_{2m-1} \end{bmatrix} \quad (3.3)$$

The shifted version $\bar{\mathbf{H}}$ is defined by

$$\bar{\mathbf{H}} = \begin{bmatrix} g_2 & g_3 & \cdots & g_{m+1} \\ g_3 & g_4 & \cdots & g_{m+2} \\ \vdots & \vdots & \vdots & \vdots \\ g_{m+1} & g_{m+2} & \cdots & g_{2m} \end{bmatrix} \quad (3.4)$$

To perform a control oriented modeling by means of capturing relevant resonance modes only, an input weighting filter F_u was used. Performing an IDFT on F_u yields

$$g_{u_k} = \frac{1}{2N} \sum_{l=0}^{2N-1} F_{u_k} e^{j\omega_k l}, k = 0, 1, \dots, 2N-1 \quad (3.5)$$

The impulse response of the weighting filter g_{u_k} was stored in a $N \times N$ Toeplitz matrix defined by

$$\mathbf{\Gamma}_u = \begin{bmatrix} g_{u_0} & g_{u_1} & \cdots & g_{u_{N-1}} \\ 0 & g_{u_0} & \cdots & g_{u_{N-2}} \\ \vdots & \vdots & \vdots & \vdots \\ 0 & 0 & \cdots & g_{u_0} \end{bmatrix} \quad (3.6)$$

The procedure used in this study has been previously reported in [142] and [143].

The singular value decomposition (SVD) was applied to the weighted Hankel matrix \mathbf{H}_w defined by

$$\mathbf{H}_w = \mathbf{H}\mathbf{\Gamma}_u = \mathbf{U}\mathbf{\Sigma}\mathbf{V}^T \quad (3.7)$$

where \mathbf{V} , \mathbf{U} and $\mathbf{\Sigma}$ represent the unitary matrices and the singular value matrix of a standard SVD. The SVD is used to reduce \mathbf{H}_w to a matrix with rank n

$$\mathbf{H}_{wn} = \mathbf{H}_1\mathbf{H}_2 \quad (3.8)$$

where \mathbf{H}_1 and \mathbf{H}_2 are defined by

$$\mathbf{H}_1 = \mathbf{U}_n \Sigma_n^{1/2}, \quad \mathbf{H}_2 = \Sigma_n^{1/2} \mathbf{V}_n^T \quad (3.9)$$

An estimation for the state space matrix \mathbf{A} is

$$\mathbf{A} = \mathbf{H}_1^* \bar{\mathbf{H}}_w \mathbf{H}_2^* \quad (3.10)$$

where \mathbf{H}_1^* and \mathbf{H}_2^* denote the left and right inverse of \mathbf{H}_1 and \mathbf{H}_2 , respectively. The input matrix \mathbf{B} becomes the first column of $\mathbf{H}_2 \Gamma_u^{-1}$. The first row of \mathbf{H}_1 forms the output matrix \mathbf{C} . The feed-through term \mathbf{D} is estimated solving a least squares optimization [142]. For the VCM modeling, first an estimated second order model G_{2nd} representing the main actuator dynamics including the low frequency friction mode [54] at 17 Hz was removed from the FRF measurement and added back to the model after the estimation. The second order model (here given in continuous time) was parameterized by

$$G_{2nd} = \frac{K_v \omega_0^2}{s^2 + 2\delta \omega_0 s + \omega_0^2} \quad (3.11)$$

and the parameters are given by $K_v = 9750$, $\omega_0 = 17 \cdot 2\pi \frac{\text{rad}}{\text{s}}$, $\delta = 0.2$. The measurements and the estimated models of both actuators are depicted in Fig. 3.3 and Fig. 3.4, respectively.

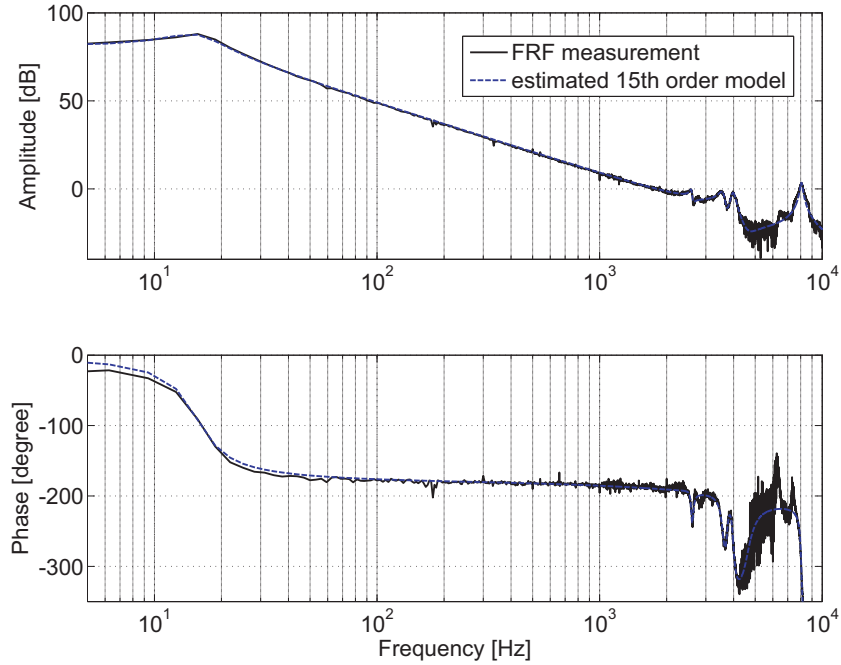


Figure 3.3: Comparison of FRF measurement and estimated 15th order VCM model

3.3 Controller design

3.3.1 General overview

One of the main characteristics of a dual-stage controller in HDDs is that there are two control outputs but there is only one position feed-back signal available that includes the contribution of both actuators. The relative displacement between the two actuators is not measured in an actual disk drive. Several different control design techniques for dual-stage actuators have been developed in recent years [72]. Some of those methods address the problem of actuator saturation [144], [145] and/or include feed-forward control in addition to feed-back control in order to accomplish combined track-following and track-seeking controllers [146]. In

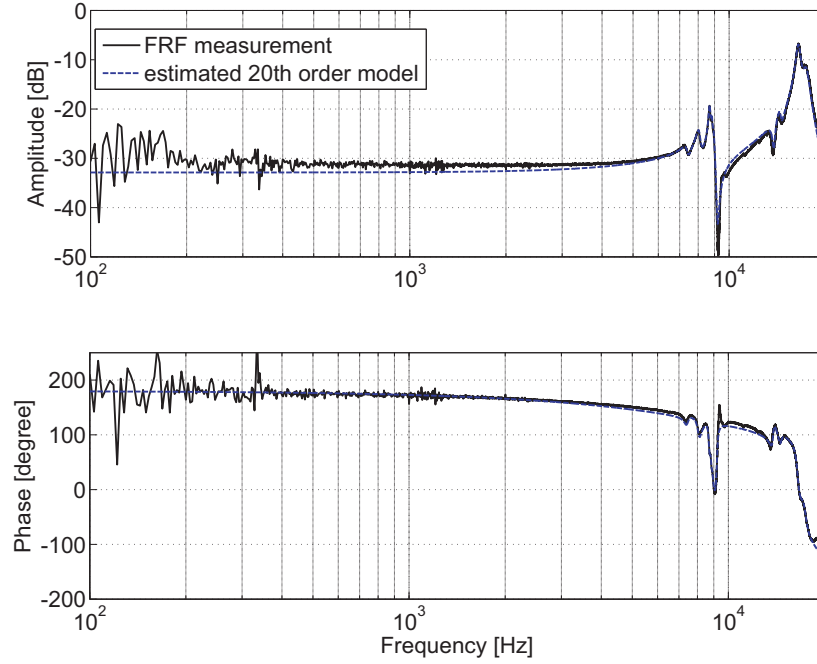


Figure 3.4: Comparison of FRF measurement and estimated 20th order PZT model

this study, we focus on feed-back controllers for track-following and short-distance seeks that do not exceed the stroke of the micro-actuator.

One dual-stage controller design technique is the PQ method [147, 148] that is based on loop shaping. It is shown in [147] that by placing the closed-loop zeros of the feed-back connection of plant P and compensator Q one can achieve frequency separation between both actuators. Here, P is defined as the ratio of the VCM and the PZT model and the compensator Q is defined in the same manner. We have recently applied the PQ method to a dual-stage tape head in [143]. However, in the present study, P yields a non-minimum phase system which limits bandwidth and makes it much more difficult to perform loop shaping based

where \hat{G}_{PZT} is a model of the PZT actuator. An obvious choice for \hat{G}_{PZT} would be the 20th order model depicted in Fig.3.4. However, to limit the complexity of the controller, \hat{G}_{PZT} is approximated by a simple DC gain g_{PZT} . The higher frequency resonance modes of the PZT do not have a significant impact on S_{VCM} because of a high frequency roll-off that is included in C_{VCM} . Hence, $K \approx 1$ and both control loops can be decoupled and designed separately.

C_{PZT} is designed as a band pass filter including a notch filter to suppress the micro-actuator (sway) mode [150] at 17 kHz. Thereafter C_{VCM} is designed containing a low pass filter approximating an integrator, a second order lead lag compensator and a high frequency roll-off. The actual dual-stage controller C_{DS} in a classical control loop definition yields

$$C_{DS} = \begin{bmatrix} (1 + g_{pzt}C_{PZT})C_{VCM} \\ C_{PZT} \end{bmatrix} \quad (3.14)$$

The dual-stage controller is depicted as the solid lines in Fig. 3.7 where the left plot shows the actual VCM controller $(1 + g_{pzt}C_{PZT})C_{VCM}$ and the right plot shows the micro-actuator controller C_{PZT} .

3.3.3 H_∞ loop shaping controller design

In addition to the sensitivity decoupling controller that is designed using loop shaping techniques only, a combined approach is applied that uses loop shaping and H_∞ optimal control design via H_∞ loop shaping [151], [152]. Figure 3.6 shows the main principle. The details on the H_∞ loop shaping algorithm are given

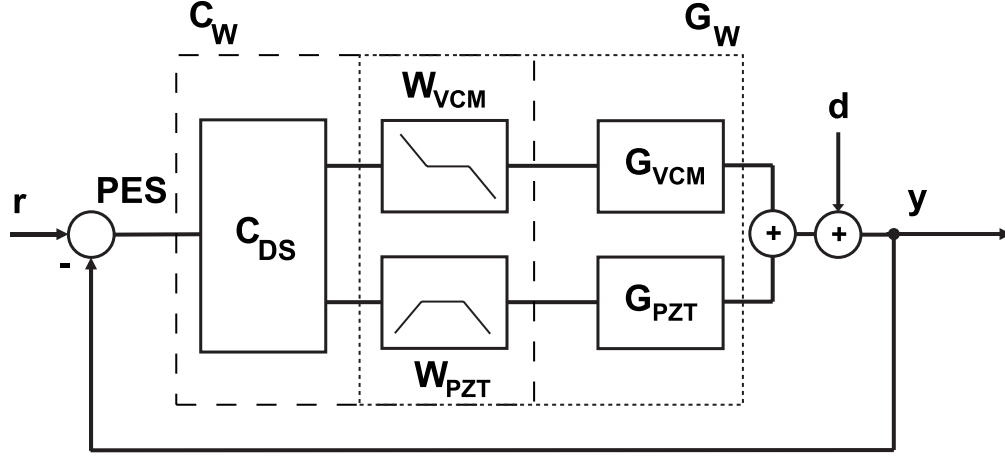


Figure 3.6: H_∞ loop shaping control structure

in [153]. The principle steps of the H_∞ loop shaping algorithm are:

First, weighting filters W_{VCM} and W_{PZT} are designed for both actuator models that represent the shape of the optimal controllers to be estimated. Then, a 4-block H_∞ control problem is formulated and used to minimize control signal peaking and error rejection peaking. Given the optimization constraints, an optimal controller C_{DS} is computed. Finally, the weighting filters are preserved in C_{DS} .

We define the weighted plant G_W (dotted box in Fig. 3.6) as

$$G_W = \begin{bmatrix} W_{VCM} & 0 \\ 0 & W_{PZT} \end{bmatrix} \begin{bmatrix} G_{VCM} \\ G_{PZT} \end{bmatrix} \quad (3.15)$$

The weighting functions are defined by

$$W_{VCM} = \frac{1}{K_{VCM}} \frac{\tau_1 s + 1}{\tau_2 s + 1} \frac{1}{\tau_3 s + 1} \quad (3.16)$$

$$W_{PZT} = \frac{R_g}{K_{PZT}} \frac{s}{\tau_4 s + 1} \frac{1}{\tau_5 s + 1}$$

where the design parameters are given by $\frac{1}{\tau_1} = 2\pi \cdot 200$, $\frac{1}{\tau_2} = 2\pi \cdot 1$, $\frac{1}{\tau_3} = 2\pi \cdot 5000$, $\frac{1}{\tau_4} = 2\pi \cdot 10$, $\frac{1}{\tau_5} = 2\pi \cdot 800 \frac{\text{rad}}{\text{s}}$ and $R_g = 5$. The gains K_{VCM} and K_{PZT} are adjusted in such a way that the 0-dB crossover frequency of the weighted plants are located at 500 Hz, respectively, and R_g is defined as the relative gain of the PZT with respect to the VCM at the crossover frequency. The H_∞ -norm of the closed-loop transfer function $T(G_W, C_{DS})$, defined by

$$T = \begin{bmatrix} G_W \\ I \end{bmatrix} [I + C_{DS}G_W]^{-1} \begin{bmatrix} C_{DS} & I \end{bmatrix}, \quad (3.17)$$

is analytically minimized using normalized coprime factorization and a Nehari extension [153]. Since the calculated controller is of high order (on the order of the plant), a closed-loop reduction routine that subdivides the high order controller into its low order components is applied. A 10th order stable approximation was obtained and is shown as the dashed lines in Fig. 3.7.

3.3.4 Controller evaluation

To evaluate the performance of the designed controllers, the closed loop feed-back connection was simulated. The sensitivity functions for both controllers are shown in Fig. 3.8. The cross-over frequency is nearly the same. However, the H_∞ controller shows a better disturbance rejection for lower frequencies than the SDM controller. Another common performance evaluation is a step function as an input representing either a high frequency disturbance or a short track seek. A step size of 100 nm relates to a track pitch of 250 ktpi in a hard disk drive. Figure

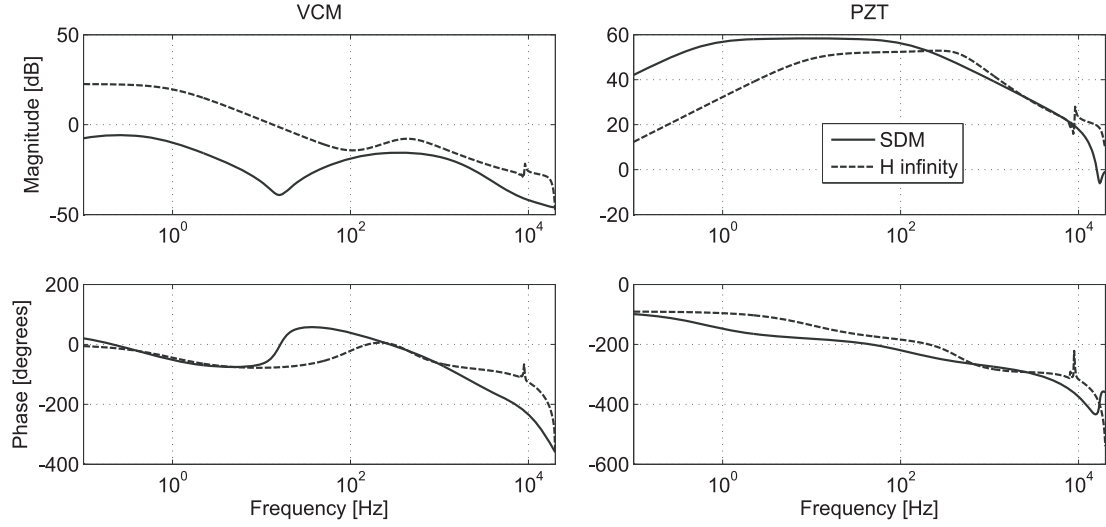


Figure 3.7: Comparison SDM and H_∞ loop shaping controller

3.9 shows the simulated response to a step input for both controllers, the control signal for the VCM and the PZT. Furthermore, the individual distribution of the VCM and the PZT to the total displacement is simulated and shown in Fig. 3.10.

We observe that the SDM controller settles slightly faster than the H_∞ controller. Also, the maximum value of the control signal and the overshoot are smaller for the SDM controller. Further performance measures are given in Table 3.1.

Table 3.1: Comparison sensitivity decoupling method (SDM) and H_∞ loop shaping control design

	SDM	H_∞ loop shaping
gain margin	6 dB	6 dB
phase margin	54 degrees	35 degrees
overshoot	22%	20%
10% settling time	0.175 ms	0.275 ms
crossover frequency	$\approx 2.37\text{kHz}$	$\approx 2.32\text{kHz}$
control signal level		
$\ u_{\text{VCM}}\ _\infty$	5 mV	10 mV
$\ u_{\text{PZT}}\ _\infty$	5.1 V	4.7 V

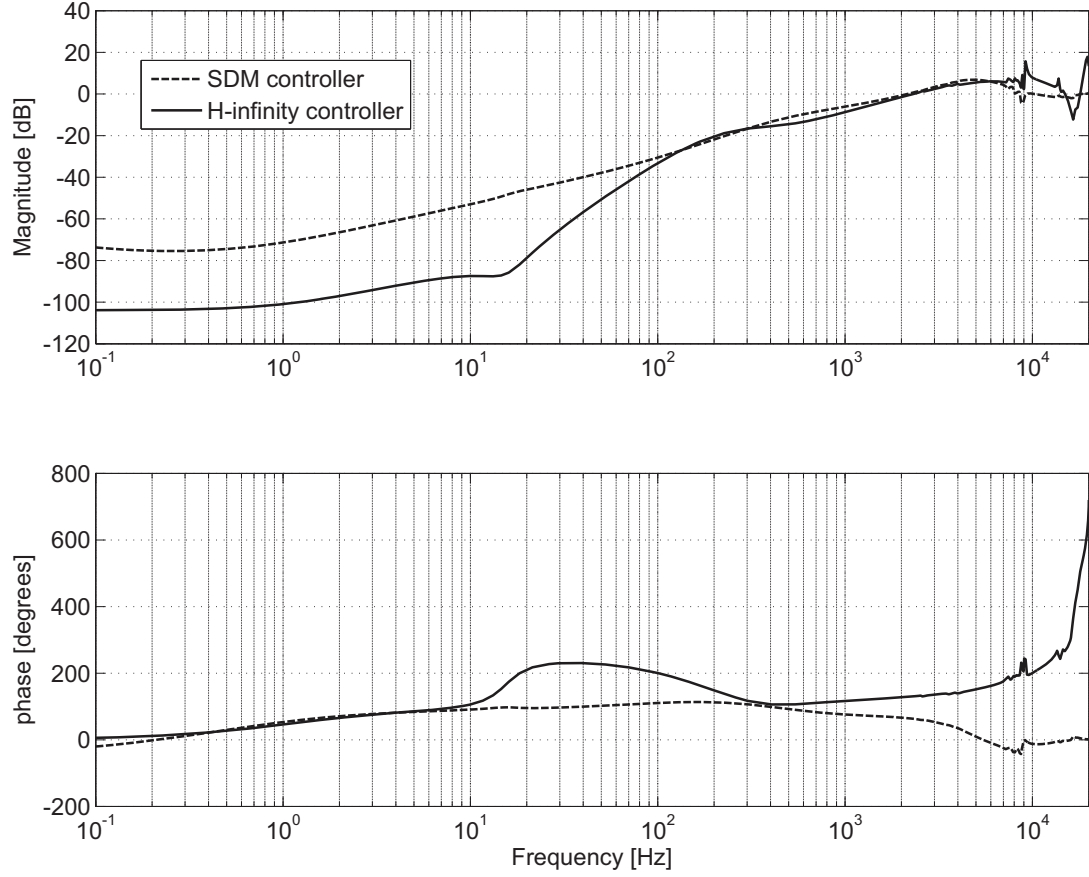


Figure 3.8: Comparison of closed loop error rejection (sensitivity function) - H_∞ loop shaping controller and sensitivity decoupling method controller

3.4 Controller implementation

The controller was implemented at a sampling frequency of 40 kHz. A 100 Hz square wave reference signal was applied representing a number of step functions. The measurement for the SDM controller is shown in Fig. 3.11. Each rise and fall in the reference signal (indicated by black arrows) is considered as a step and a trigger. Hence, time-based averaging can be applied (see Fig. 3.12). Numerous oscillations are observed in the averaged measurement. The unaveraged

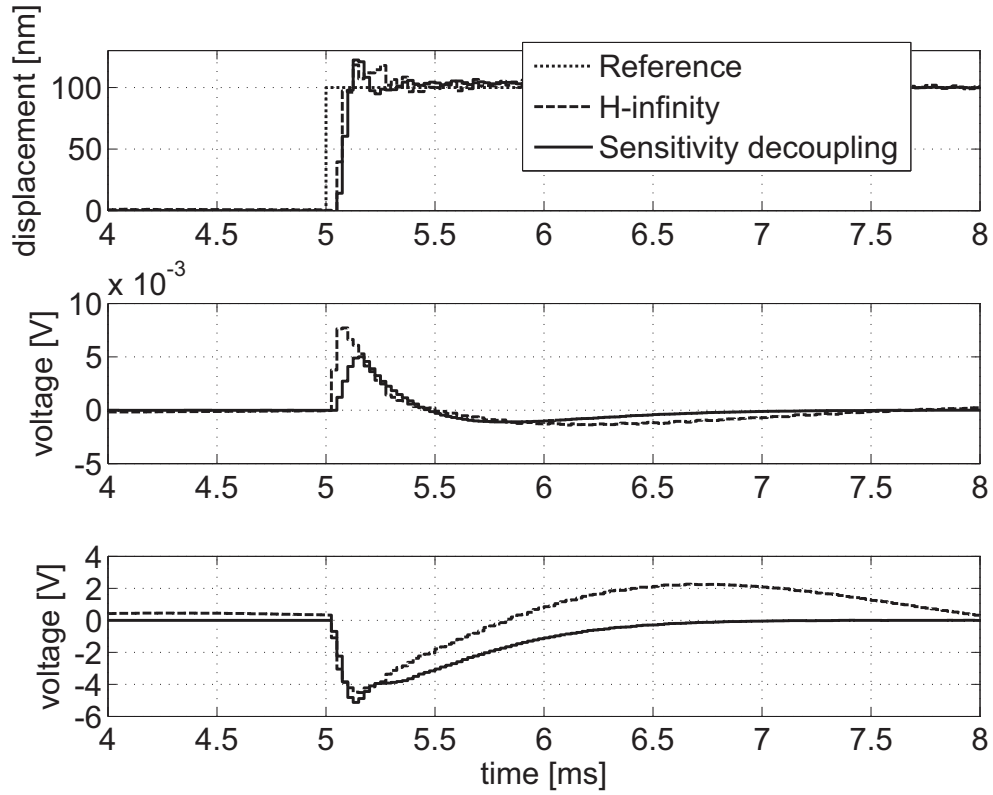


Figure 3.9: Simulation of step response - H_∞ loop shaping controller and sensitivity decoupling method controller

measurement of the H_∞ controller implementation is shown in Fig. 3.13. Looking at the averaged step response (Fig. 3.14), one can observe the same oscillations as in the SDM controller measurement.

The major oscillations in both controller implementations occur at about 2 kHz and 3.5 kHz. Furthermore, the control signals show the frequencies of the HDD spindle speed (167 Hz) and eigenfrequencies. It is conjectured that numerous repeatable (non-stochastic) disturbances that are not affected by time-based averaging cause the vibrations.

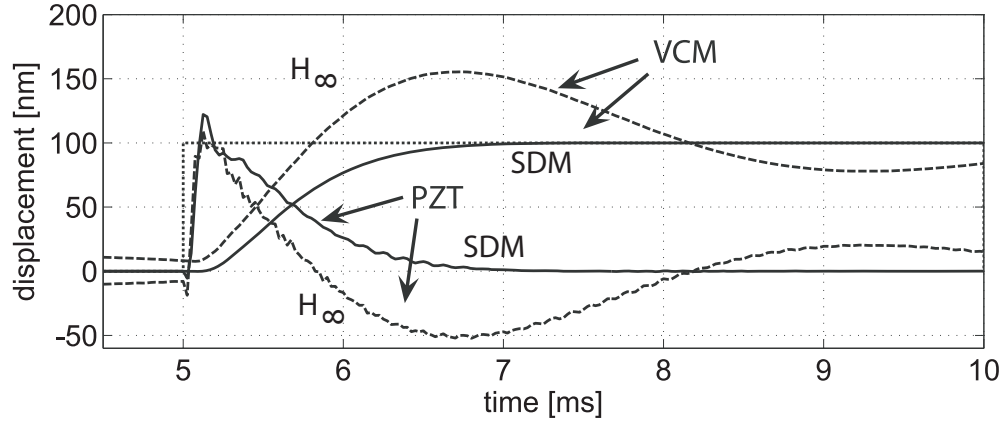


Figure 3.10: Simulated displacement for VCM and PZT

3.5 Conclusion

A hard disk drive with dual-stage-suspensions was modified to allow open loop FRF measurements of both servo actuators without having access to the PES. A discrete-time modeling algorithm based on frequency response function measurements was proposed. Two different dual-stage track-following controllers were designed using classic loop shaping techniques combined with modern H_∞ control problem algorithms. Both controllers show similar servo performance. However, the H_∞ controller shows a better disturbance rejection than the SDM controller for low frequencies which is due to a low gain in the VCM controller for low frequencies (see Fig.3.7). Also, the H_∞ approach does not use notch filters, and, thus, is more robust than the SDM controller. Since the optimization routine is constrained by the pre-defined parameters in the weighting functions different weighting functions might result in a better controller performance of the H_∞ controller.

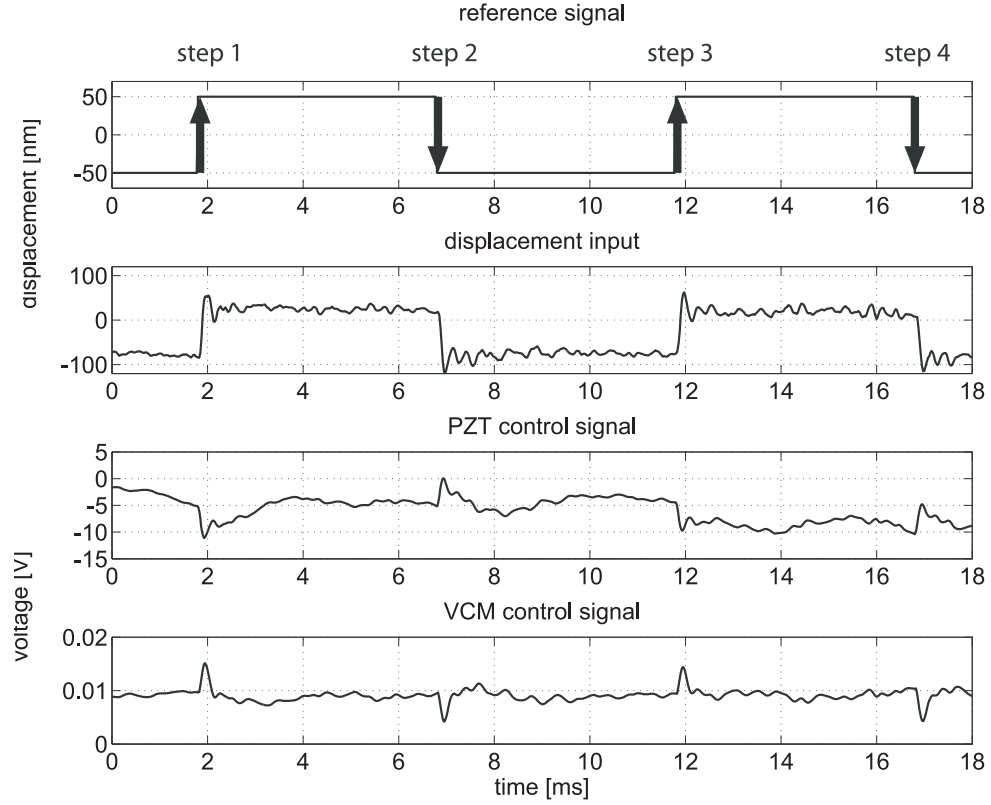


Figure 3.11: Implemented sensitivity decoupling method controller for a square wave reference input

Both, model estimation and optimized controller design based on predefined controller shape filters can be implemented in the hard disk drive firmware. Since actuator dynamics could be a function of tolerances during manufacturing, the drive could perform a controller calibration itself, and, thus, could improve the servo performance and the TMR budget.

The different controllers designed in this study were implemented in the HDD and showed a stable feed-back control. Small differences between measurement and simulation were observed that are caused by repeatable disturbances.

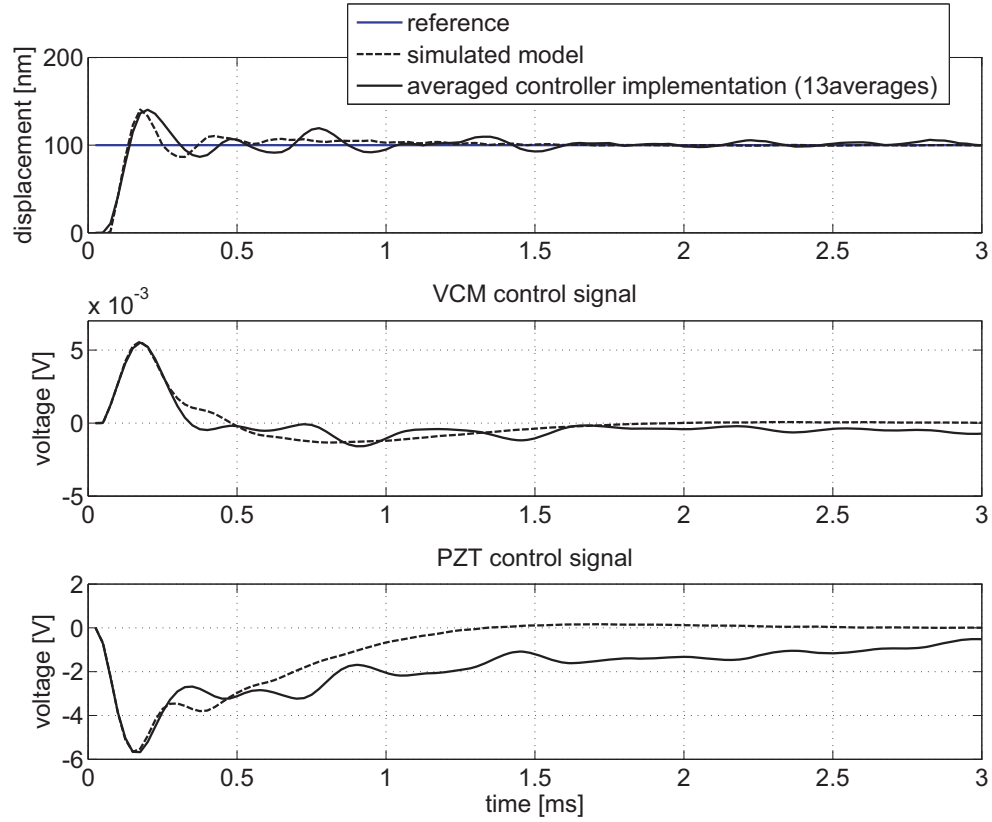


Figure 3.12: Head position and control signals for implemented SDM controller (averaged)

3.6 Acknowledgement

We would like to thank Seagate Technology, in particular, Alexei Sacks, for his interest in this work and for his help.

Chapter 3, in part, is a reprint of the material as it appears in "Modeling and Control of a Dual-Stage Actuator Hard Disk Drive", Boettcher U., de Callafon R.A., Talke F.E., *Journal of Advanced Mechanical Design, Systems, and Manufacturing*, Volume 4, Issue 1, pp. 107-118, 2010. The dissertation author was the primary investigator and author of this paper. In addition, chapter 3, in part, is

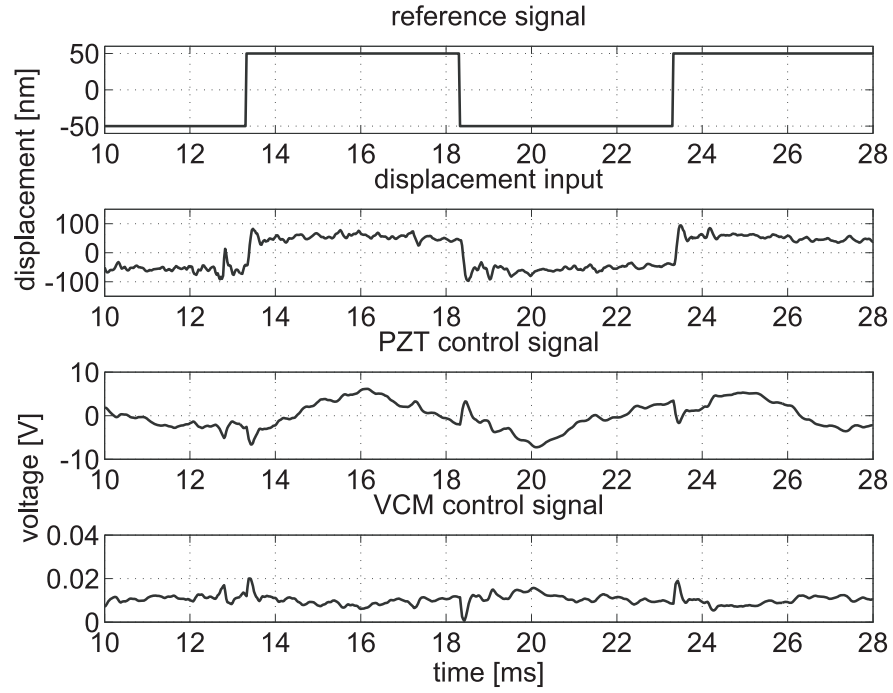


Figure 3.13: Implemented H_∞ loop shaping controller for a square wave reference input

a reprint of the material as it appears in the dissertation author's "Diplomarbeit" (Master's thesis) at Dresden University of Technology. The Master's thesis was done at UCSD/CMRR.

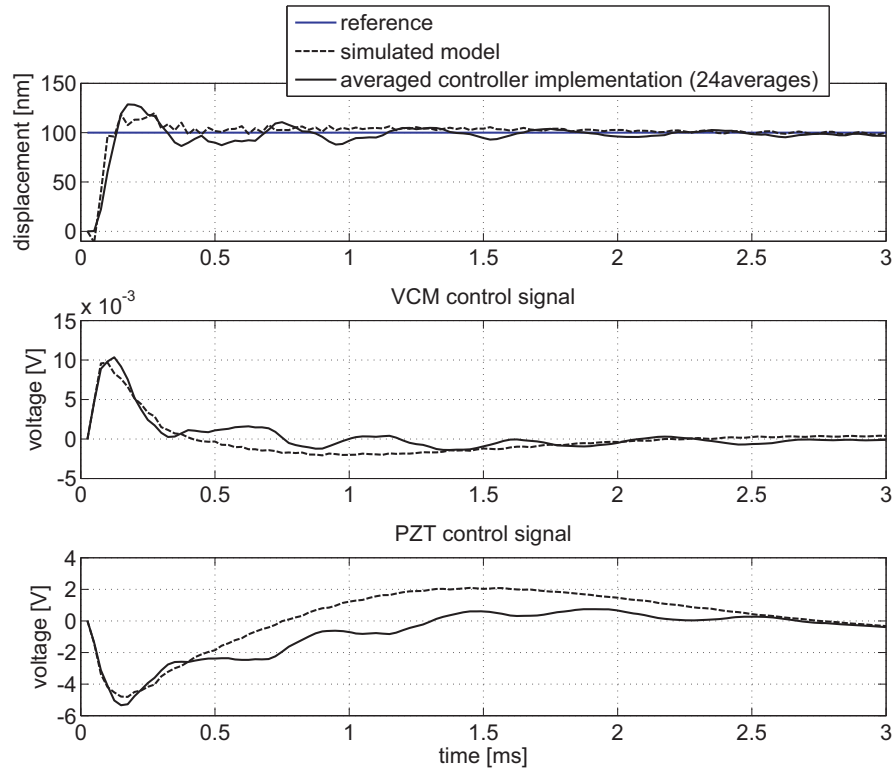


Figure 3.14: Head position and control signals for implemented H_∞ loop shaping controller (averaged)

4 Reference signal shaping for seeking in hard disk drives

4.1 Introduction

For linear time-invariant (LTI) systems that are subject to a change from an initial state to a target state, input shaping is a powerful technique to reduce residual vibrations [154]. To understand the main principle of input shaping and see its benefits, we first analytically derive the shaped input signal for a straightforward introductory example. We consider a spring-mass-damper system as shown in Fig. 4.1. The system is governed by the 2nd order differential equation

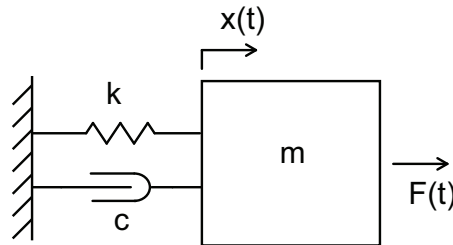


Figure 4.1: Mass-spring-damper system

$$m\ddot{x}(t) + c\dot{x}(t) + kx(t) = F(t) \quad (4.1)$$

where m is the mass, c is the damping coefficient and k is the spring constant. Two different force inputs are applied to this mechanical system and the simulated response is shown in Fig. 4.2 for $m = 1$ kg, $c = 0.5$ kg/s and $k = 1$ N/m. We observe

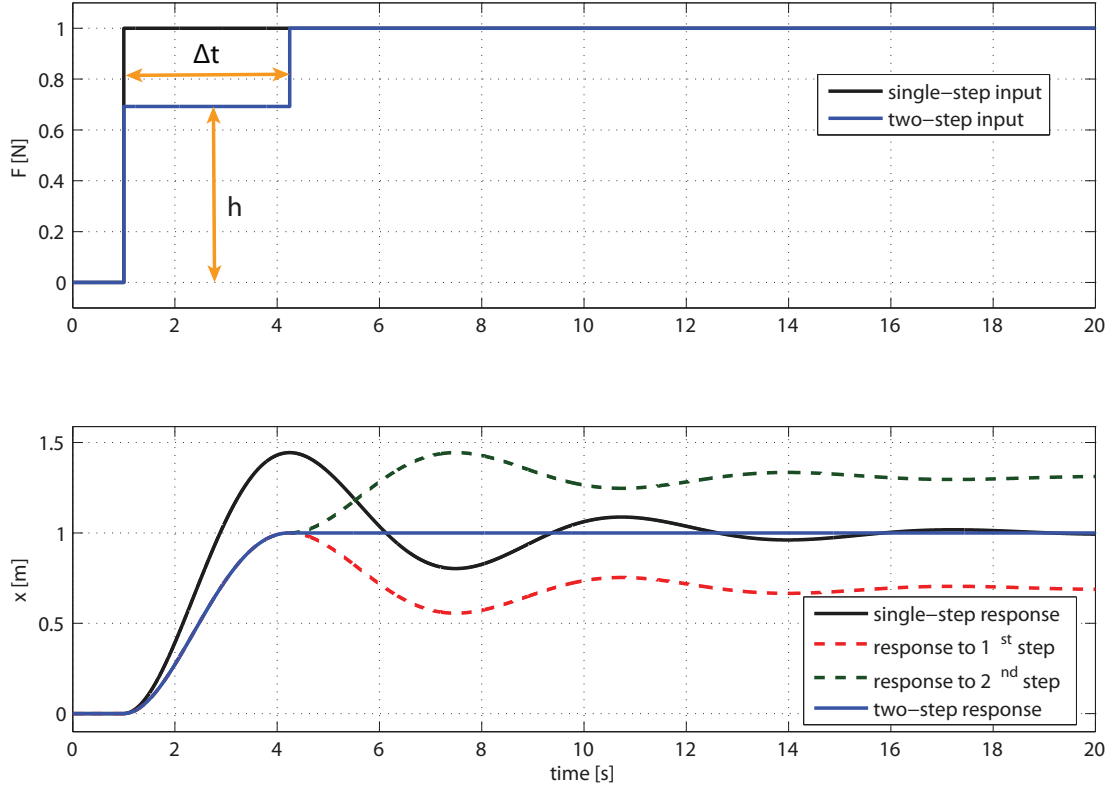


Figure 4.2: Input shaping example: force input and displacement output

that the response to a single-step input is highly under-damped and oscillations occur. However, applying a two-step input signal, the residual vibrations of the two steps (dashed lines in Fig. 4.2) cancel each other out and one obtains very fast settling at the cost of reduced rise time. This simple procedure needs only two parameters: the modified relative step height h and the time delay Δt as indicated

in Fig. 4.2. We will now show how we can analytically obtain these two parameters for this straightforward mechanical structure.

First, we define the dimensionless damping ratio $\delta = \frac{c}{2\sqrt{km}}$ and the angular natural frequency $\omega_0 = \sqrt{\frac{k}{m}}$ for better manageability during the derivation. The single-step input is defined by

$$F(t) = \begin{cases} F & \text{if } t \geq 0. \\ 0 & \text{otherwise.} \end{cases} \quad (4.2)$$

Considering this input step, we can find the analytical solution of (4.1) for the under-damped case ($0 \leq \delta < 1$) as

$$x(t) = \frac{F}{k} \left[1 - e^{-\delta\omega_0 t} \left(\cos(\omega_d t) + \delta \frac{\omega_0}{\omega_d} \sin(\omega_d t) \right) \right] \quad (4.3)$$

where the initial conditions are $x(0) = 0$ and $\dot{x}(0) = 0$ and $\omega_d = \omega_0 \sqrt{1 - \delta^2}$ denotes the damped natural angular frequency. It should be noted that the under-damped case is more interesting for this type of input shaping. The main idea is to compensate for the occurring overshoot and scaling the initial step F down to h times its original size. We can find the first maximum of the step response by taking the derivative of (4.3)

$$\dot{x}(t) = \frac{F}{k} e^{-\delta\omega_0 t} \frac{1}{\delta\sqrt{1 - \delta^2}} \sin(\omega_d t) \quad (4.4)$$

and setting it to zero. This yields the first maximum at

$$t = \Delta t = \frac{\pi}{\omega_d} \quad (4.5)$$

Thus, the first maximum in the output response of a lightly damped system occurs at one half of the cycle duration. We can now calculate the relative step height h by substituting (4.5) into (4.3) and dividing by the steady state value F/k to obtain

$$h = \frac{1}{1 + e^{-\delta\pi\frac{\omega_0}{\omega_d}}} \quad (4.6)$$

With (4.5) and (4.6), the shaped input command is fully defined. This straightforward approach can be extended to higher-order systems and can be used to design pre-shaping input filters as shown in [154, 155].

In this chapter, we focus on reference signal input shaping for closed-loop systems with saturation constraints on the control output as indicated in Fig. 4.3. The targeting trajectory can be further optimized by minimizing targeting time, energy consumption or other system parameters, through convex optimization techniques. Those techniques have been widely applied to these problems since they guaranty convergence to a global optimum. In addition, recent increases in computational power in control systems justify their increasing complexity. A broad overview of real-time or nearly real-time applications has been given in [156].

Input shaping is usually formulated as an open-loop problem where linear constraints on input and output signals are imposed to formulate a convex optimization problem to find optimal input profiles. In general, finite impulse response (FIR) filters are used to pre-filter input signals such as shown for multi-input multi-output (MIMO) systems in continuous time in [157] and for discrete time systems

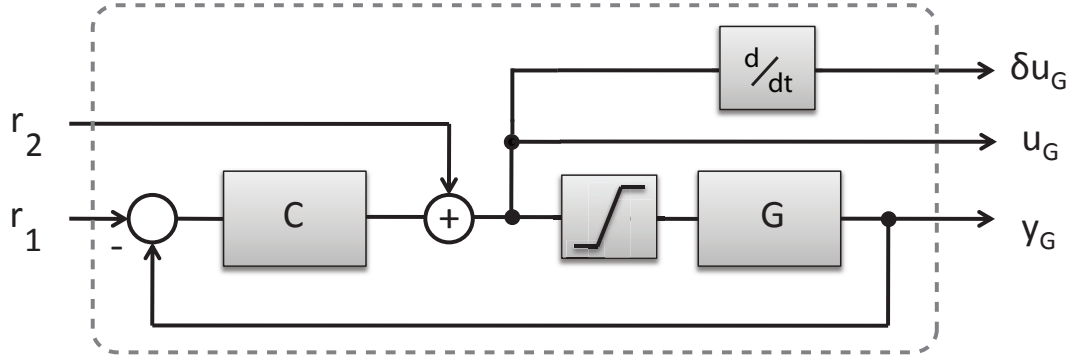


Figure 4.3: Closed loop LTI system with constraints on closed-loop signals

in [158].

Some closed-loop approaches are given in [159] where input shaping based on FIR filters is also applied to closed-loop systems. Another approach to closed-loop input shaping is the shaped time-optimal servo mechanism (STOS) approach that has been developed in [108] for continuous time systems. The STOS was briefly introduced in section 2.6.3 and is illustrated in Fig. 2.24 on page 52. Here, mode switching control turns off the feedback during the targeting stage. In [160], the reference signal generation is shown for constrained closed-loop systems based on piecewise affine functions of state and reference. The conventionally shaped input signal tends to be longer than the non-shaped input signal as addressed in [161] where a solution to this problem is proposed. Another interesting approach to open-loop input shaping has been proposed in [162] where a graphical representation of the phase portrait is used to derive the input shaper. A low quantization level of the actuator signals (finite-state input) reduces the effectiveness of input

shaping [163]. In [164, 165, 166], the reference signal generation is shown for a closed-loop system although time-minimal control is not addressed. It has been shown recently in [167] how an online optimization can yield improved performance compared to conventional input shapers.

Limited results are available on performing input shaping on closed-loop systems where reference and feedforward signals are computed in the presence of constraints on control and output signals. The here presented computational scheme is motivated by previous work [168] where optimal input and reference signals were computed and simulation results were shown for a hard drive seeking process. In this chapter, we present a general framework for a multi-input multi-output system that is subjected to amplitude and rate constraints of reference signals, closed-loop signals and outputs.

The computation of optimal reference profiles in closed-loop systems has direct application to high performance servo systems where short-time tracking of set-point values is required in the presence of saturation limits on control signals. A relevant application example is the servo mechanism in a hard disk drive (HDD) as introduced in section 2.6 of this dissertation. On the other hand, since the algorithm is applicable to a broad field of applications, we develop here a general input shaping technique for closed-loop MIMO linear time-invariant systems with actuator saturation that use full degree-of-freedom control such as the one shown in Fig. 4.3. The algorithm computes the optimal reference signals r_1 and r_2 given linear constraints on the output signal y_G , the plant control signal u_G and the

reference signals r_1 and r_2 . The simulated and experimentally verified results of the algorithm are applied in section 4.4 to the seeking process in a hard disk drive.

4.2 Defining the system

4.2.1 Specifications of closed-loop signals

We consider a linear time-invariant model of the plant G in Fig. 4.3 with p inputs and m outputs of order n_G and an LTI model of the controller C with p outputs and m inputs of order n_C . The state space model of G is given by

$$\begin{aligned} x_G(k+1) &= A_G x_G(k) + B_G(r_2(k) + y_C(k)) \\ y_G(k) &= C_G x_G(k) + D_G(r_2(k) + y_C(k)) \end{aligned} \quad (4.7)$$

and the feedback connection is given by

$$\begin{aligned} x_C(k+1) &= A_C x_C(k) + B_C(r_1(k) - y_G(k)) \\ y_C(k) &= C_C x_C(k) + D_C(r_1(k) - y_G(k)) \end{aligned} \quad (4.8)$$

In order to specify constraints to the plant input, u_G and the rate of change δu_G must be available as outputs of the closed-loop state-space system as indicated in Fig. 4.3. Therefore, we add p states to the closed-loop model and define a measurement state vector x_M

$$x_M(k+1) = u_G(k) = y_C(k) + r_2(k) \quad (4.9)$$

and

$$u_G(k-1) = x_M(k) \quad (4.10)$$

We can now define the two additional outputs of our closed-loop system

$$\begin{aligned} u_G(k) &= y_C(k) + r_2(k) \\ \delta u_G(k) &= u_G(k) - u_G(k-1) \end{aligned} \tag{4.11}$$

Furthermore, we define the reference vector $r(k) \in \mathbb{R}^{(m+p) \times 1}$, the output vector $y(k) \in \mathbb{R}^{(m+2p) \times 1}$ and the state space vector $x(k) \in \mathbb{R}^{(n_C+n_G+p) \times 1}$ as

$$\begin{aligned} r(k) &= \begin{pmatrix} r_1 \\ r_2 \end{pmatrix} \\ y(k) &= \begin{pmatrix} y_G \\ u_G \\ \delta u_G \end{pmatrix} \quad x(k) = \begin{pmatrix} x_C \\ x_G \\ x_M \end{pmatrix} \end{aligned} \tag{4.12}$$

Here, $r_1(k)$ and $r_2(k)$ are the computed reference signals.

Using (4.7)-(4.12) we can define the state space system of the closed loop system as

$$\begin{aligned} x(k+1) &= Ax(k) + Br(k) \\ y(k) &= Cx(k) + Dr(k) \end{aligned} \tag{4.13}$$

where the state space matrices are calculated by

$$\begin{aligned}
 A &= \begin{bmatrix} A_C - B_C M D_G C_C & -B_C M C_G & 0 \\ B_G C_C - B_G D_C M D_G C_C & A_G - B_G D_C M C_G & 0 \\ C_C - D_C M D_G C_C & -D_C M C_G & 0 \end{bmatrix} \\
 B &= \begin{bmatrix} B_C - B_C M D_G D_C & -B_C M D_G \\ B_G D_C - B_G D_C M D_G D_C & B_G - B_G D_C M D_G \\ D_C - D_C M D_G D_C & -D_C M D_G + I \end{bmatrix} \\
 C &= \begin{bmatrix} M D_G C_C & M C_G & 0 \\ C_C - D_C M D_G C_C & -D_C M C_G & 0 \\ C_C - D_C M D_G C_C & -D_C M C_G & -I \end{bmatrix} \\
 D &= \begin{bmatrix} M D_G D_C & M D_G \\ D_C - D_C M D_G D_C & I - D_C M D_G \\ D_C - D_C M D_G D_C & I - D_C M D_G \end{bmatrix}
 \end{aligned} \tag{4.14}$$

In (4.14), M is defined as

$$M = (I + D_G D_C)^{-1} \tag{4.15}$$

The inverse in (4.15) can be calculated for a well-defined closed-loop system with $D_G D_C \neq -I$. In practical applications most plants will have at least one sample time delay with $D_G = 0$ making $M = I$.

4.2.2 Explicit solution of the closed-loop system

The output y combines the plant output y_G , the plant input u_G and its rate of change δu_G on which constraints will be imposed. For the formulation of the linear constraints we use (4.13) and follow [169, 168] to write the output equations recursively as

$$\begin{aligned}
 y(0) &= Cx(0) + Dr(0) \\
 y(1) &= CAx(0) + CBr(0) + Dr(1) \\
 y(2) &= CA^2x(0) + CABr(0) + CBr(1) + Dr(2) \\
 &\vdots \\
 y(M) &= CA^Mx(0) + \sum_{i=1}^M CA^{M-i}Br(i-1) + Dr_s
 \end{aligned} \tag{4.16}$$

$$\begin{aligned}
 y(M+1) &= CA^{M+1}x(0) + \sum_{i=1}^M CA^{M+1-i}Br(i-1) + Dr_s + CBr_s \\
 &\vdots \\
 y(N-1) &= CA^{N-1}x(0) + \sum_{i=1}^M CA^{N-i-1}Br(i-1) + Dr_s \\
 &\quad + \sum_{i=1}^{N-M-1} CA^{i-1}Br_s
 \end{aligned}$$

where M is the control horizon and N is the optimization horizon. Here, r_s defines the residual reference signal after the control horizon which in our work is set to a constant desired value. An obvious choice is $r_1 = y_t$ and $r_2 = 0$ for $k \geq M$ where y_t represents the target value of the output.

We can now rewrite (4.16) conveniently in matrix notation by defining Ψ

as

$$\Psi = \begin{bmatrix} D & 0 & 0 & \cdots & 0 \\ CB & D & 0 & \cdots & 0 \\ CAB & CB & D & \cdots & 0 \\ \vdots & \vdots & \vdots & \ddots & \vdots \\ CA^{M-2}B & CA^{M-3}B & \cdots & D \\ CA^{M-1}B & CA^{M-2}B & \cdots & CB \\ CA^M B & CA^{M-1}B & \cdots & CAB \\ \vdots & \vdots & \ddots & \vdots \\ CA^{N-2}B & CA^{N-3}B & \cdots & CA^{N-M-1}B \end{bmatrix} \quad (4.17)$$

Furthermore, we define $\mathbf{\Omega}$, \mathbf{y} as

$$\mathbf{\Omega} = \begin{bmatrix} C \\ CA \\ CA^2 \\ \vdots \\ CA^{N-1} \end{bmatrix}, \mathbf{y} = \begin{bmatrix} y(0) \\ y(1) \\ y(2) \\ \vdots \\ y(N-1) \end{bmatrix} \quad (4.18)$$

and Δ as

$$\Delta = \begin{bmatrix} 0 \\ \vdots \\ 0 \\ Dr_s \\ Dr_s + CBr_s \\ \vdots \\ Dr_s + \sum_{i=1}^{N-M-1} CA^{i-1}Br_s \end{bmatrix} \quad (4.19)$$

With this definition we can rewrite (4.16) as

$$\mathbf{y} = \Psi \mathbf{r} + \underbrace{\Omega x(0) + \Delta}_{\mathbf{q}} \quad (4.20)$$

where the vector \mathbf{r} contains the reference signals

$$\mathbf{r} = \begin{bmatrix} r(0), & \dots, & r(M-1) \end{bmatrix}^T \quad (4.21)$$

and the vector \mathbf{y} contains the output signals

$$\mathbf{y} = \begin{bmatrix} y(0), & \dots, & y(N-1) \end{bmatrix}^T \quad (4.22)$$

for each time step k . In (4.20), we also introduce \mathbf{q} that captures the residual and initial condition. Each element in (4.21) is a vector of size $(m+p) \times 1$, and, each element in (4.22) is a vector of size $(m+2p) \times 1$. In (4.20), the explicit input-output relation is linear in \mathbf{r} . We shall now proceed to specify the constraints and the optimization routine for reference signal shaping.

4.3 Convex optimization

For a comprehensive overview of convex optimization techniques the reader is referred to [170]. In this study a specific solution to the closed-loop problem will be given for designing the reference signal \mathbf{r} subjected to constraints on the closed-loop signals and the reference signals (4.12).

4.3.1 Constraints on the closed-loop signals

As indicated in Fig. 4.3, the output y captures all of the relevant closed-loop signals. It contains not only the output of the plant y_G but also the plant input u_G and its rate of change δu_G . In defining constraints on closed-loop signals we refer to the constraints on the output $y = (y_G, u_G, \delta u_G)^T$ in which we distinguish between different signals. The plant output y_G is subject to two different amplitude constraints as indicated in Fig. 4.4. One constraint is a large amplitude constraint during the targeting stage. We define the maximum and minimum constraints by $\overline{y_1}$ and $\underline{y_1}$, respectively. Once the target is reached, a tolerance ϵ of the output from the desired target is specified by

$$\underline{y_2} = y_t - \epsilon \leq y_G \leq \overline{y_2} = y_t + \epsilon \quad (4.23)$$

creating a tight amplitude constraint during the settling stage. In Fig. 4.4, k^* denotes the number of samples to reach the target. For all sample numbers $k < k^*$ the targeting output constraints apply, while for all sample numbers $k \geq k^*$ the settling stage (and finally steady state) output constraints apply. Choosing a

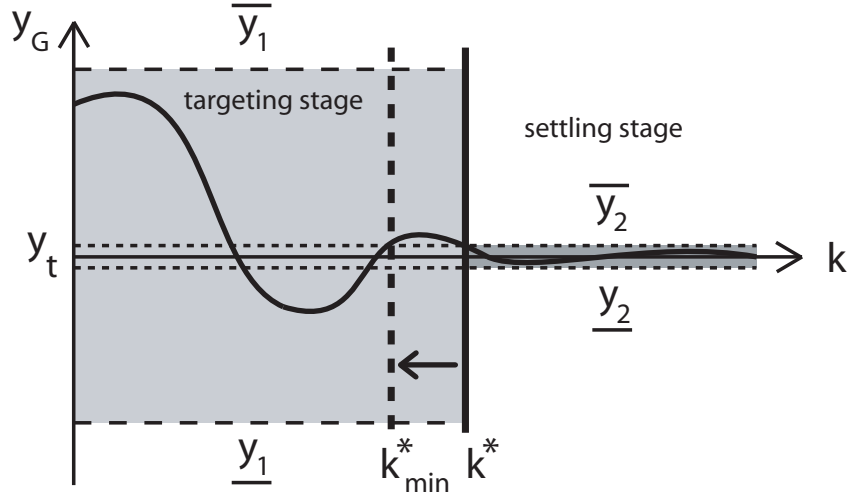


Figure 4.4: Definition of the output constraints

minimal value for k^* would amount to finding a minimal time solution. We will later use a line search over k^* to find the minimal time solution. For now, k^* is assumed to be given.

Furthermore, we specify constraints on the plant input u_G . We consider amplitude constraints on the input. In addition, the maximum rate of change of the input signal is limited which is commonly introduced through rate limitations in digital-to-analog conversion. We define amplitude and rate constraints as

$$u_G \leq \overline{u_G} \quad \delta u_G \leq \overline{\delta u_G} \quad (4.24)$$

and similarly

$$\begin{aligned} u_G &\geq \underline{u_G} \Leftrightarrow -u_G \leq -\underline{u_G} \\ \delta u_G &\geq \underline{\delta u_G} \Leftrightarrow -\delta u_G \leq -\underline{\delta u_G} \end{aligned} \quad (4.25)$$

In matrix notation the output constraints can be written as

$$\Psi \mathbf{r} + \mathbf{q} \leq \bar{\mathbf{y}}(k^*) \quad (4.26)$$

and

$$\Psi \mathbf{r} + \mathbf{q} \geq \underline{\mathbf{y}}(k^*) \quad (4.27)$$

where \mathbf{q} is given in (4.20) and $\bar{\mathbf{y}}$ and $\underline{\mathbf{y}}$ are defined by

$$\bar{\mathbf{y}}(k^*) = \begin{bmatrix} \bar{y}_1 \\ \bar{u}_G \\ \bar{\delta u}_G \\ \vdots \\ \bar{y}_2 \\ \bar{u}_G \\ \bar{\delta u}_G \end{bmatrix}, \quad \underline{\mathbf{y}}(k^*) = \begin{bmatrix} \underline{y}_1 \\ \underline{u}_G \\ \underline{\delta u}_G \\ \vdots \\ \underline{y}_2 \\ \underline{u}_G \\ \underline{\delta u}_G \end{bmatrix} \quad (4.28)$$

4.3.2 Constraints on reference signals

The reference signals r_1 and r_2 in Fig.4.3 are captured in the signal \mathbf{r} in (4.13) and (4.21). By imposing constraints on \mathbf{r} we are now referring to the constraints on the reference inputs r_1 and r_2 . The reference signals are limited by an amplitude constraint

$$\underline{\mathbf{r}} \leq \mathbf{r} \leq \bar{\mathbf{r}} \quad (4.29)$$

whereas a rate of change constraint

$$\underline{\delta \mathbf{r}} \leq \delta \mathbf{r} \leq \bar{\delta \mathbf{r}} \quad (4.30)$$

with

$$\bar{\mathbf{r}} = \begin{bmatrix} \bar{r}, & \cdots, & \bar{r} \end{bmatrix}^T \quad (4.31)$$

$$\overline{\delta\mathbf{r}} = \begin{bmatrix} \overline{\delta r}, & \cdots, & \overline{\delta r} \end{bmatrix}^T \quad (4.32)$$

can also be included in our approach. We note that $\underline{\mathbf{r}}$ and $\underline{\delta\mathbf{r}}$ are defined similarly.

A reference change is defined by

$$\delta r(k) = r(k) - r(k-1) \quad (4.33)$$

for each $k \in [0, \cdots, M-1]$. In matrix notation we calculate $\delta\mathbf{r}$ by

$$\delta\mathbf{r} = \mathbf{E}\mathbf{r} \quad (4.34)$$

where \mathbf{E} is given by

$$\mathbf{E} = \begin{bmatrix} I_{m+p} & 0 & \cdots & 0 \\ -I_{m+p} & I_{m+p} & \cdots & 0 \\ & \ddots & \ddots & \\ 0 & \cdots & -I_{m+p} & I_{m+p} \end{bmatrix} \quad (4.35)$$

and I_{m+p} represents a $(m+p) \times (m+p)$ identity matrix.

4.3.3 Combined constraints in linear form

All the constraints in (4.26), (4.27), (4.29), (4.30) and (4.34) can be combined in one single linear matrix inequality (LMI):

$$\begin{bmatrix} \mathbf{I} \\ -\mathbf{I} \\ \mathbf{E} \\ -\mathbf{E} \\ \mathbf{\Psi} \\ -\mathbf{\Psi} \end{bmatrix} \begin{bmatrix} r(0) \\ \vdots \\ r(M-1) \end{bmatrix} \leq \begin{bmatrix} \bar{\mathbf{r}} \\ -\underline{\mathbf{r}} \\ \overline{\delta \mathbf{r}} \\ -\underline{\delta \mathbf{r}} \\ \bar{\mathbf{y}}(k^*) \\ -\underline{\mathbf{y}}(k^*) \end{bmatrix} - \begin{bmatrix} 0 \\ 0 \\ 0 \\ 0 \\ \mathbf{q} \\ -\mathbf{q} \end{bmatrix} \quad (4.36)$$

or short

$$\mathbf{L}\mathbf{r} \leq \mathbf{W}(\mathbf{k}^*) - \mathbf{Q} \quad (4.37)$$

In (4.36), \mathbf{I} is an $(m+p)M \times (m+p)M$ identity matrix, and $\mathbf{\Psi}$ is given in (4.17).

In (4.36) and (4.37) the term \mathbf{Q} with $\mathbf{q} = \mathbf{\Omega}\mathbf{x}(0) + \mathbf{\Delta}$ represents the effect of initial and residual conditions. It should be noted that \mathbf{W} depends on the choice of k^* in Fig. 4.4. The additional freedom in k^* will be used to check for a feasible solution of the input shaping problem and to formulate a minimal time solution for settling.

4.3.4 Feasibility check for time-optimal solution

We can check whether or not the constraints are feasible for a given k^* by solving a relatively simple linear program (LP) [171, 172]:

$$\begin{aligned}
& \min_{r, z} \quad \mathbf{1}^T \mathbf{z} \\
& \text{subject to} \quad \mathbf{Lr} - \mathbf{z} \leq \mathbf{W}(\mathbf{k}^*) - \mathbf{Q} \\
& \quad \mathbf{z} \geq 0
\end{aligned} \tag{4.38}$$

If $\mathbf{z} = 0$ is the optimal solution then the inequality (4.37) is feasible, otherwise infeasible. In (4.38), $\mathbf{1} = [1, \dots, 1]^T$ is a column vector of ones.

In order to obtain the time-optimal solution we solve the LP in (4.38) several times for different values of k^* . We use a bisection method [170] that results in quadratic convergence to find the minimum sample number k_{min}^* (where $1 \leq k_{min}^* \leq M$) for a feasible set of constraints. The pseudo code of the bisection algorithm is listed in Tab. 4.1.

Table 4.1: Bisection algorithm

```

 $k_{upper}^* = M$ 
 $k_{lower}^* = 1$ 
while ( $k_{upper}^* - k_{lower}^* > 1$ )
     $k^* = \frac{k_{upper}^* + k_{lower}^*}{2}$ 
    solve LP in (4.38) with  $k^*$ 
    if LP feasible
         $k_{upper}^* = k^*$ 
    else
         $k_{lower}^* = k^*$ 
    end if
end
 $k_{min}^* = k_{upper}^*$ 

```

The bisection algorithm to find k_{min}^* leads also to a computed reference signal \mathbf{r} that satisfies all imposed constraints. The LP in (4.38) is used only to check the feasibility of the proposed reference signal shaping under the given

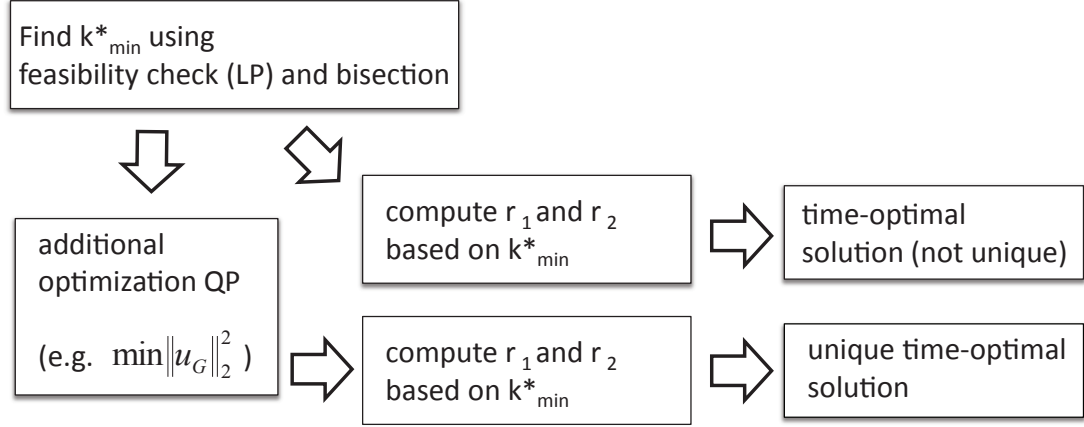


Figure 4.5: Optimization algorithm

constraints. The additional bisection in table 4.1 will also allow us to find the minimal time solution that is still feasible.

It should be noted that the solution for \mathbf{r} found by (4.38) is not unique and most likely will not be a desired reference signal. Moreover, in many applications a minimum time solution might not be required. Given the feasibility check from the LP problem we now design a unique reference signal by posing a quadratic programming (QP) problem as indicated in Fig. 4.5 that aims at minimizing the (weighted) energy level of the signals, leading to a unique solution of the reference signal \mathbf{r} .

4.3.5 Quadratic programming

To further improve the energy properties of the signals in the input shaping problem, one can pose a quadratic criterion involving both \mathbf{y} and \mathbf{r} given the

constraints in (4.36) and (4.37). A particular value for k^* can give a feasible solution from the LP problem in (4.38) and a further refinement of this solution can be found by solving the quadratic programming (QP) problem

$$\begin{aligned}
 \min_{r, y'} \quad & \mathbf{y}'^T \mathbf{P}_1 \mathbf{y}' + \mathbf{r}^T \mathbf{P}_2 \mathbf{r} \\
 \text{subject to} \quad & \mathbf{Lr} \leq \mathbf{W}(\mathbf{k}^*) - \mathbf{Q} \\
 & \mathbf{y}' = \mathbf{\Psi r} + \mathbf{q} - \mathbf{y}_t^*
 \end{aligned} \tag{4.39}$$

where \mathbf{y}_t^* is defined by

$$\mathbf{y}_t^* = \begin{bmatrix} y_t & 0 & 0 & \cdots & y_t & 0 & 0 \end{bmatrix}^T \tag{4.40}$$

In (4.39), \mathbf{P}_1 and \mathbf{P}_2 are semi-positive definite matrices with dimensions of \mathbf{y}' and \mathbf{r} , respectively. With $\mathbf{P}_1 \geq 0$ and $\mathbf{P}_2 \geq 0$, the QP problem is convex. The QP in (4.39) consists of a quadratic cost function, an inequality constraint linear in \mathbf{r} and an equality constraint linear in \mathbf{r} and \mathbf{y}' .

The introduction of the additional variable \mathbf{y}' and the equality constraint is necessary in order to perform optimization on y_G , u_G and δu_G .

The QP in (4.39) represents only one possible optimization objective but there are many other possible objectives. The weighting matrices \mathbf{P}_1 and \mathbf{P}_2 allow an accurate tuning according to the desired closed-loop response also depending on k . If only some of the constraints in (4.36) are in use, the problem size should be reduced in favor of shorter computational time.

4.3.6 Semidefinite programming

The quadratic programming problem in (4.39) can be reformulated as a semidefinite programming (SDP) problem that can be considered as an extension of linear programming [173]. First, the equality constraint is incorporated in the cost function J which yields the QP

$$\min_{\mathbf{r}} J \quad (4.41)$$

$$\text{subject to } \mathbf{L}\mathbf{r} \leq \mathbf{W}(\mathbf{k}^*) - \mathbf{Q}$$

where J is defined by

$$\begin{aligned} J = & \mathbf{r}^T \underbrace{(\Psi^T \mathbf{P}_1 \Psi + \mathbf{P}_2)}_{\Theta_1} \mathbf{r} + \underbrace{(\mathbf{q}^T - \mathbf{y}_t^{*T}) \mathbf{P}_1 \Psi}_{\Theta_3} \mathbf{r} \\ & + \mathbf{r}^T \underbrace{\Psi^T \mathbf{P}_1 (\mathbf{q} - \mathbf{y}_t^*)}_{\Theta_3^T} + \underbrace{(\mathbf{q}^T - \mathbf{y}_t^{*T}) \mathbf{P}_1 (\mathbf{q} - \mathbf{y}_t^*)}_{\Theta_2} \end{aligned} \quad (4.42)$$

Suppose γ is the upper bound on J we can rewrite (4.41) as

$$\min_{\mathbf{r}, \gamma} \gamma \quad (4.43)$$

$$\text{subject to } \gamma - J \geq 0$$

$$\mathbf{L}\mathbf{r} \leq \mathbf{W}(\mathbf{k}^*) - \mathbf{Q}$$

If $P_1 \succ 0$ and/or $P_2 \succ 0$ holds, the inverse of Θ_1 in (4.42) is defined and we can apply the Schur complement to reformulate the first inequality constraint in (4.43) as

$$\mathbf{M}_{\text{opt}} = \begin{bmatrix} \gamma - \Theta_3 \mathbf{r} - \mathbf{r}^T \Theta_3^T - \Theta_2 & \mathbf{r}^T \\ \mathbf{r} & \Theta_1^{-1} \end{bmatrix} \succeq 0 \quad (4.44)$$

where \mathbf{M}_{opt} is denoted as the optimization matrix that minimizes the cost function for the minimal value of γ . It should be noted that \mathbf{M}_{opt} is linear in \mathbf{r} and γ .

The second inequality constraint that incorporates the constraints on the closed-loop signals can be rewritten as

$$\mathbf{M}_{\text{constr}} = \text{diag}(\mathbf{W}(\mathbf{k}^*) - \mathbf{Q} - \mathbf{L}\mathbf{r}) \succeq 0 \quad (4.45)$$

where $\text{diag}(\cdot)$ denotes a diagonal matrix that has the elements of the argument vector in its main diagonal. Finally, the resulting SDP yields

$$\begin{aligned} & \min_{\mathbf{r}, \gamma} \quad \gamma \\ & \text{subject to} \quad \begin{bmatrix} \mathbf{M}_{\text{opt}} & 0 \\ 0 & \mathbf{M}_{\text{constr}} \end{bmatrix} \succeq 0 \end{aligned} \quad (4.46)$$

4.3.7 Solution to LP, QP and SDP problems

A number of numerical techniques are available that solve LPs, QPs and SDPs. Very efficient ways to solving those problems are based on primal-dual interior-point methods as shown in [174]. There it is noted that it is more efficient to solve the second-order cone programming problem which is a generalization of LP or QP rather than solving the more general SDP.

We will now show the effectiveness of the optimization routine proposed in section 4.3.1 through 4.3.5 by means of an illustrative application example: the seeking process in a hard disk drive. Both simulation and experimental results are presented that illustrate the effectiveness of closed-loop reference input shaping. To

solve such optimization problems, commonly used tools are the open source LMI parser YALMIP [175] and solver SeDuMi [176]. Our computations presented in the next subsection were carried out using Matlab and the CVX software package [177].

4.4 Experimental verification: seeking in a hard disk drive

4.4.1 Experimental set-up

We consider an experimental set-up depicted in Fig.4.6 and Fig.4.7. A modified 3.5 inch form factor HDD spinning at 7200 rpm was used to experimentally verify the proposed optimization algorithm. As indicated in Fig.4.6, a digital signal processing (DSP) board is connected to the HDD and a computer. The DSP board allows to gain access to HDD internal signals such as gray code and position error signal (PES) in the drive. It also allows to inject pre-defined reference signals for seeking. The steps to obtain the experimental data are listed and indicated in Fig.4.6. The HDD used for this study has 180 servo sectors which yields a PES/gray code sampling frequency of 21.6 kHz. We consider a servo loop according to Fig.4.3 where the dynamics of the HDD servo actuator - the voice coil motor (VCM) - are represented by G . Furthermore, a low bandwidth PID controller C is implemented for track-following. In order to compute optimized reference

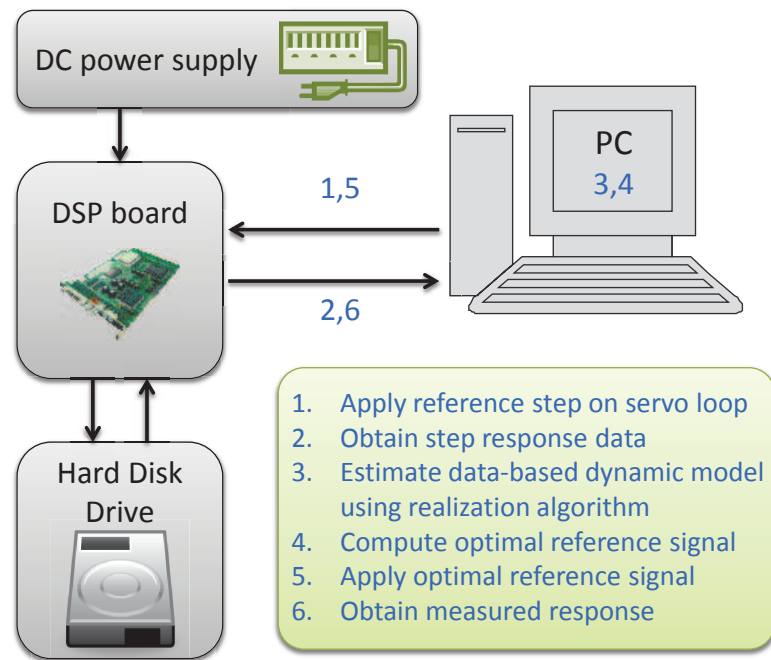


Figure 4.6: Computational steps and scheme of the experimental set-up

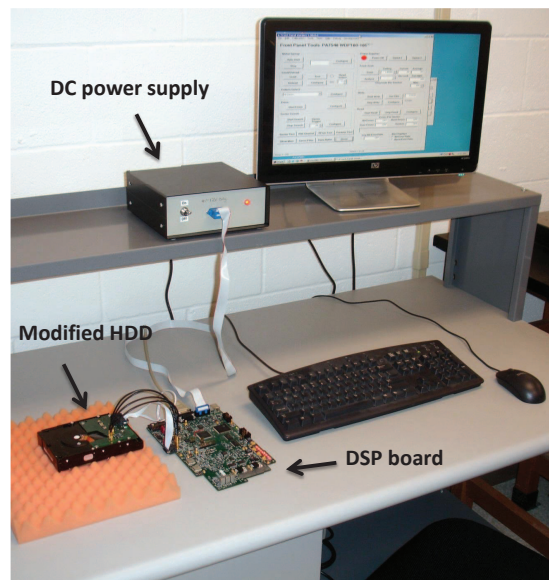


Figure 4.7: Experimental set-up: Modified HDD, DSP board, DC power supply and computer

signals, the dynamic response of the servo loop needs to be identified. This was accomplished through step experiments described in the following subsection.

4.4.2 Closed-loop dynamic modeling of the servo mechanism

The state space matrices A, B, C and D in (4.14) can be formulated using explicit information of actuator and controller dynamics. Alternatively, since we are dealing with a closed-loop system, the matrices can also be formulated by directly studying the dynamics from reference signals to actuator output y_G and controller output y_C . For that purpose, a 10-track step on the reference signal r_1 was used to identify the dynamic behavior of the closed-loop system. For simplification, we neither consider r_2 nor constraints on δu_G in this study. Therefore, the estimation problem reduces to a single-input (r_1) dual-output (y_G and $y_C = u_G$) system. A generalized realization algorithm (GRA) [140] was used to identify a discrete-time model based on the time-domain step response data. This algorithm will be explained more in detail in section 7.3.2 of this dissertation. The step response measurement for both outputs is shown in Fig.4.8. Based on the step data and the GRA a 12^{th} order closed-loop model was estimated. The simulated step response based on this model is also shown in Fig.4.8 (solid lines). It can be observed that the estimated model captures the response of the system very well. Furthermore, a frequency domain comparison of the estimated model and a

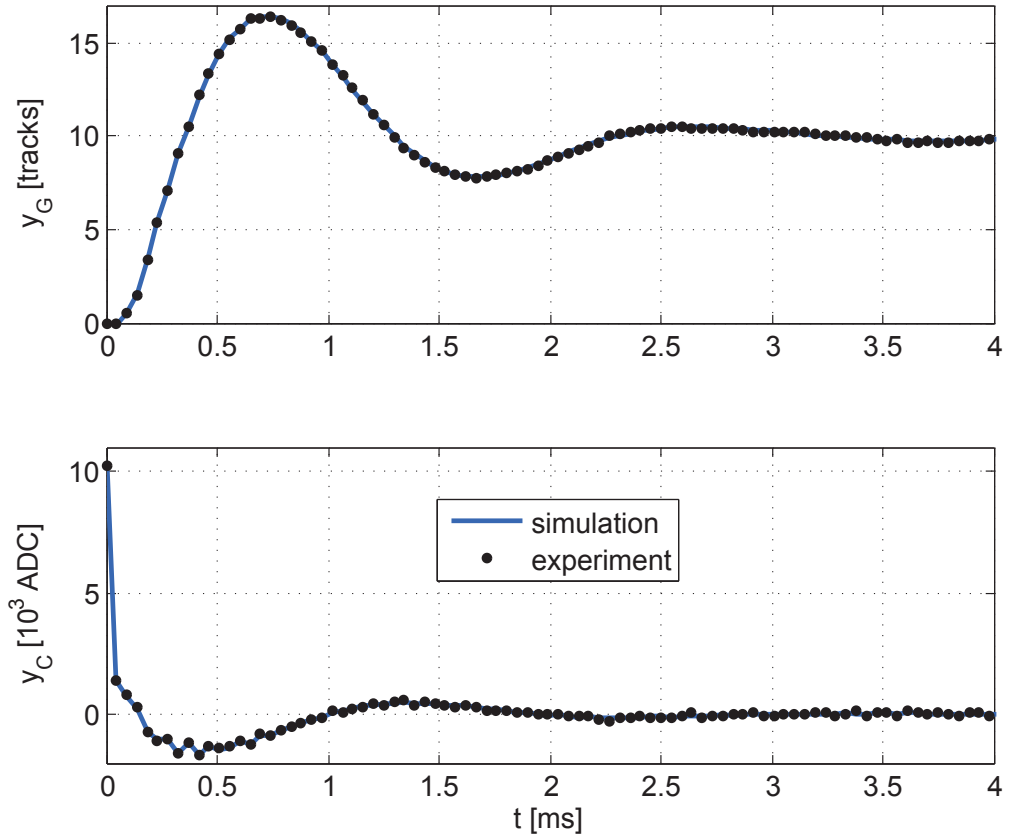


Figure 4.8: Measured and simulated actuator (top) and controller (bottom) outputs for a closed-loop step of 10 tracks on r_1 .

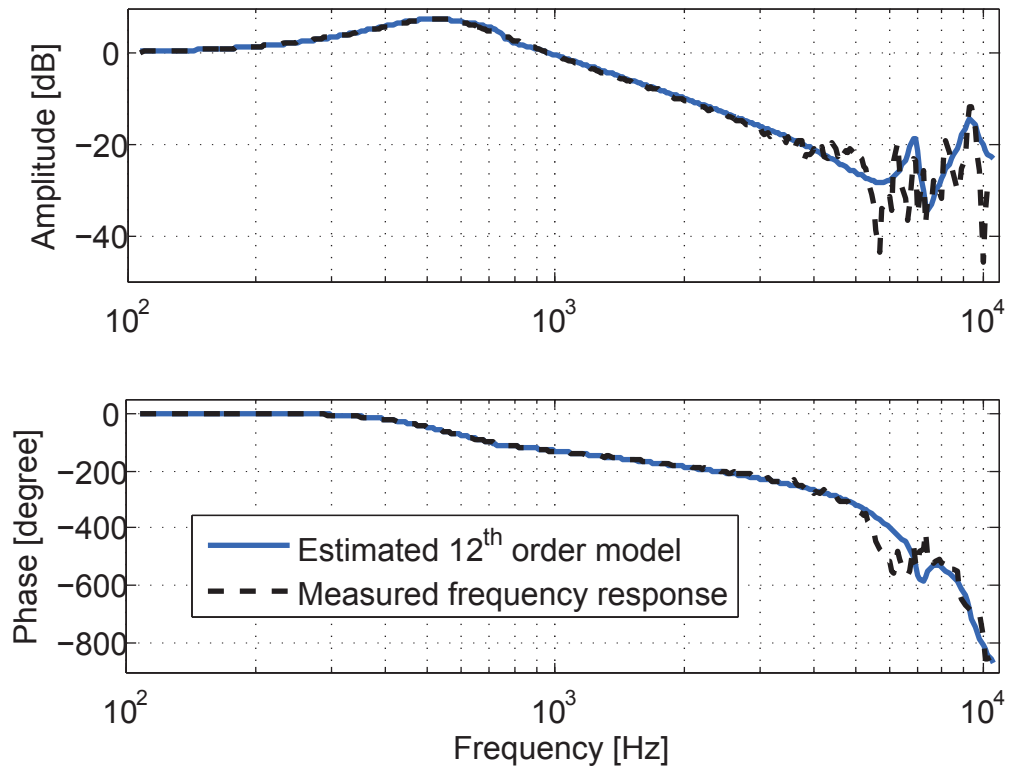


Figure 4.9: Bode plot of estimated 12th order model of the closed-loop transfer function and the measured frequency response function from the HDD set-up.

frequency response function measurement of the closed-loop transfer function (r_1 to y_G) based on sine sweep measurements was performed. The results are shown in Fig. 4.9. It can be seen that for low frequencies there is a strong agreement between measured and modeled response. However, high frequency resonance modes are not captured very well by the model. This is mainly due to the fact that the step input based modeling emphasises on low frequency and most dominant resonance modes. We will see later that this does not have a large effect on the performance of the shaping algorithm as those high frequencies will not be excited by the shaped reference signal profile in closed-loop. In Fig. 4.9, the mismatch at higher frequencies between the frequency response function measurement and the step input based model might also be caused by the different input signals. The frequency response measurement is based on a sine sweep input. In addition, the measurement could potentially be aliased.

4.4.3 Results

For our experimental studies we consider the reference signal r_1 and amplitude constraints on the control signal y_C which was set to a maximum absolute value of 3000 units. The value ϵ was set to 10% of the track pitch which is a generally accepted limit in HDD technology as discussed in section 2.6.2. The difference between the output y_G and the target y_t was minimized along with the control signal $y_C = u_G$. No explicit constraints on the reference signal were considered by setting \mathbf{P}_2 in (4.39) to zero. The experimental results are based on 5 averages of

the measured signal. We will investigate the following four different cases:

1. A fixed step size of 10 tracks and various settling times
2. A variable step size combined with a fixed settling time of 10 samples
3. Tight versus loose amplitude constraints on y_G for 10 track step
4. Time-minimum solution versus a fixed settling time for a 100 track seek

Fixed step size and various settling times

In Fig. 4.10 (rotated), the results for a fixed target track number of 10 tracks are shown. Each column in Fig.4.10 represents a desired seek time ranging from 20 to 10 samples. It can be observed that the output y_G reaches the target much faster compared to the standard step input results in Fig. 4.8 and has no residual vibrations. It can also be observed that as the desired seek time approaches the time-minimum solution of 10 samples, the shape of the control output y_C looks very similar to "bang-bang" control which has been shown to be the time-optimal solution for an ideal double integrator actuator [178]. The additional flexibilities in the actuator require the control signal y_C to be slightly different than bang-bang and we accomplish this automatically by actual input shaping of the reference signal as plotted in the top row of Fig. 4.10. The zoom-in of the output y_G is shown in the third row of Fig. 4.10. One can observe that the experimentally obtained data follow the shaped output signal y_G of the actuator very closely. The violation of the imposed boundaries in the experimental data is due to repeatable

and non-repeatable run-out errors (disturbances) that are poorly suppressed by the low bandwidth PID controller used in our experiments.

Variable step size combined with a fixed settling time

In a second experiment, the settling time was set to the time-optimal solution of the 10 track step at 10 samples and the step size was varied from 1 to 10 tracks. The results are shown in Fig. 4.11. It is interesting to observe that the output y_G for each step height is just a scaled version of a different step height whereas y_C and r_1 are shaped accordingly.

Tight versus loose amplitude constraints on y_G

We also investigated the difference between tight amplitude constraints on y_G (ϵ equals 10% of the track pitch) and loose constraints on y_G (ϵ equals 10% of the step height). The results in Fig. 4.12 show the time-optimal solution for both cases. Clearly, one can observe much smoother and less "aggressive" reference and control signals for the case of the loose constraint compared to the tight constraint.

Time-minimum solution versus a fixed settling time

The final example shown in Fig 4.13 considers a 100 track seek where the time-optimal solution is desired. Given the constraints on y_C , the target is reached within 24 samples. However, this yields large control signals that are saturated at the upper and lower boundaries for a significant amount of time. In addition, a

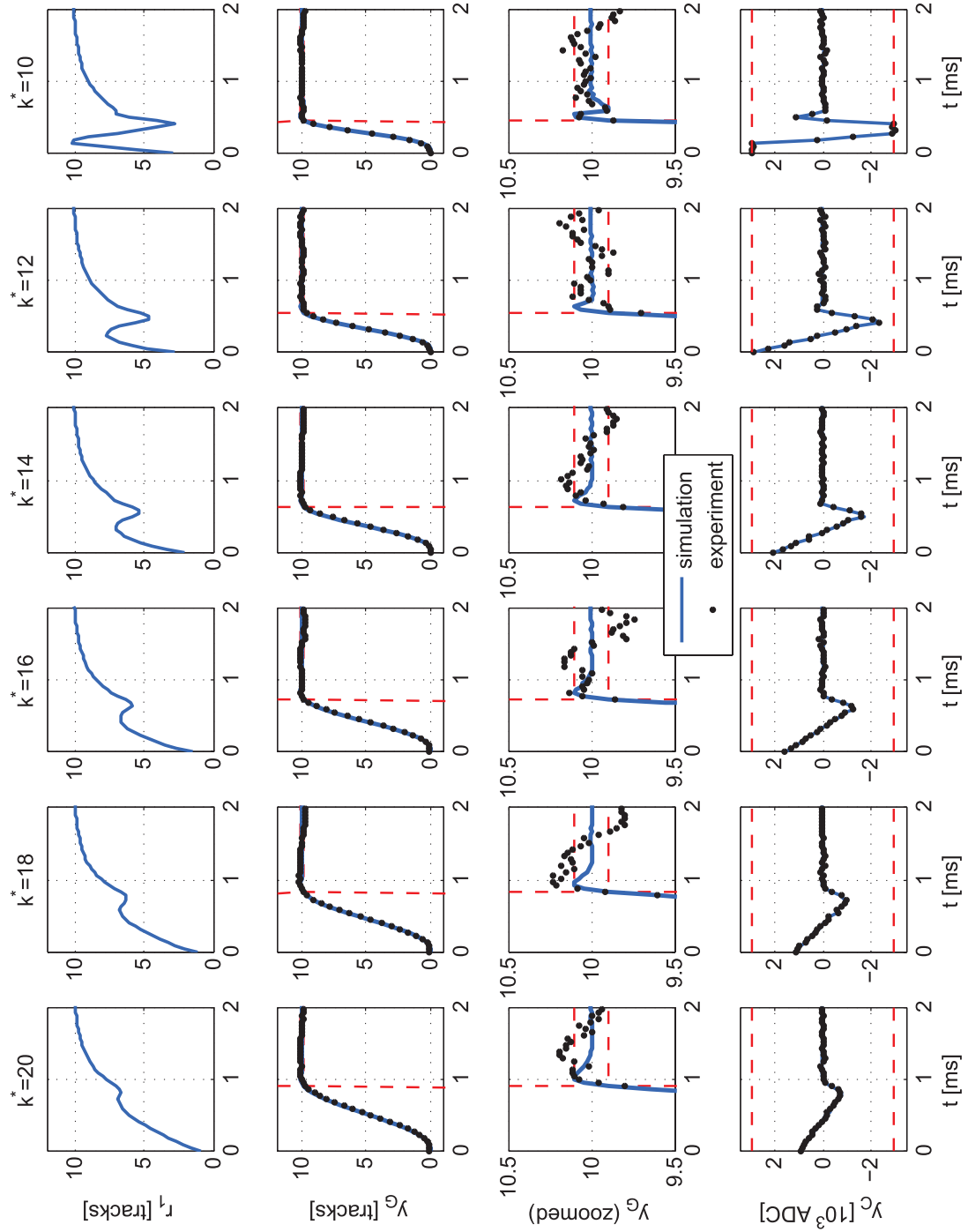


Figure 4.10: [Rotated 90 degrees] Optimized reference signal r_1 (top row), output y_G (middle rows) and control signal y_C (bottom row) for 6 different sample numbers for k^* in simulation and actual experiment for a 10 track step. $k^* = 10$ samples represents the minimal time solution given the imposed constraints on y_C depicted by the dashed lines in the bottom row.

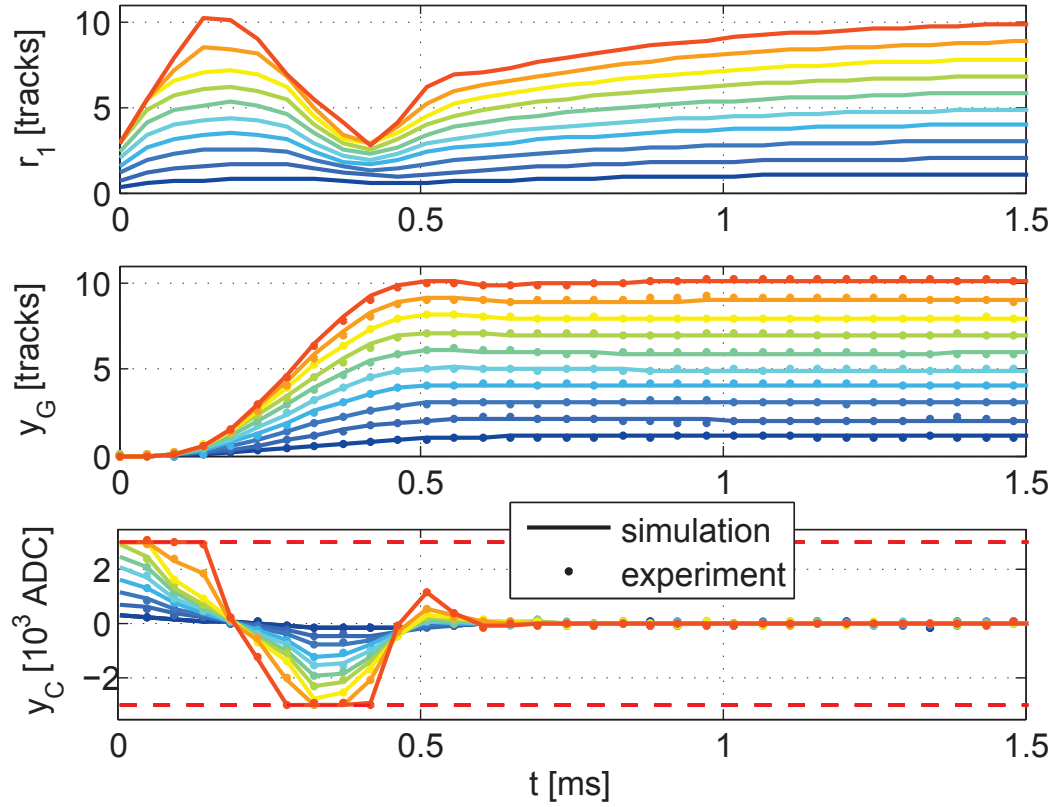


Figure 4.11: Optimized reference signal r_1 (top), output y_G (middle) and control signal y_C (bottom) for different step sizes (1 to 10 tracks) at a fixed sample number of $k^* = 10$ in simulation and actual experiment

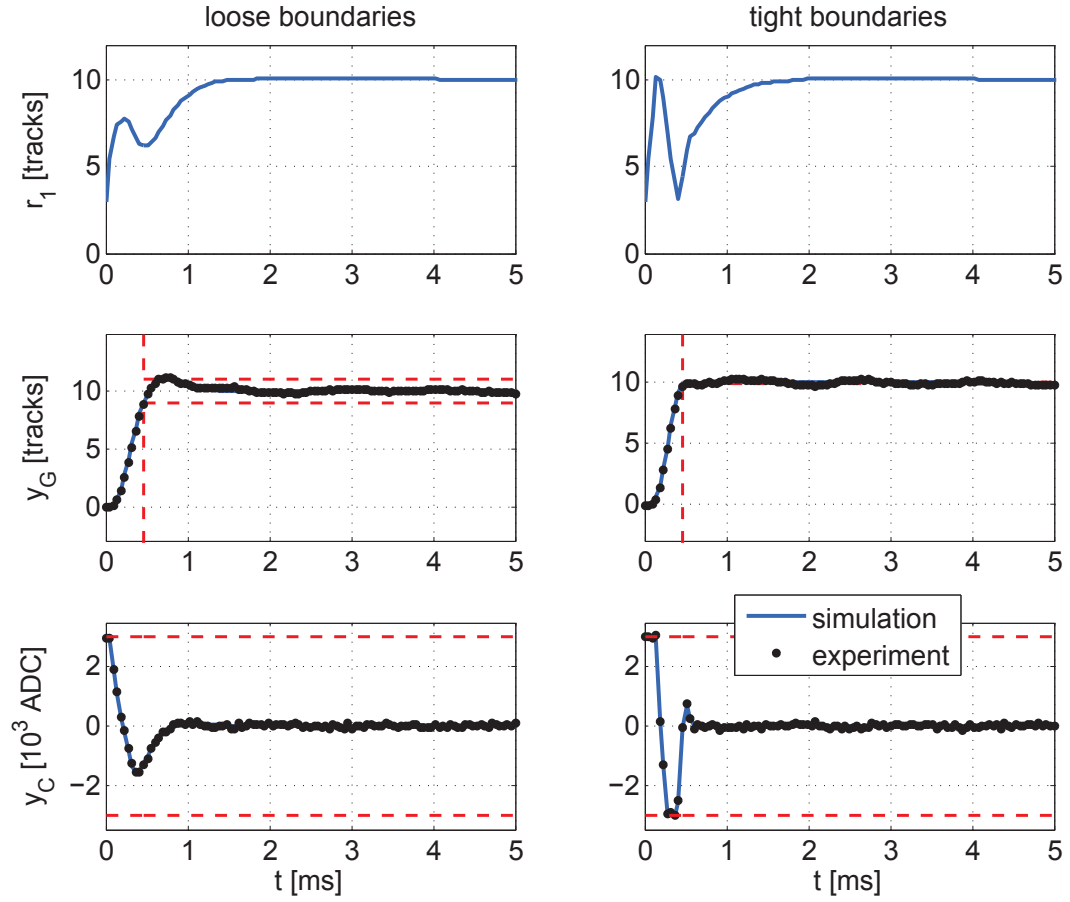


Figure 4.12: Loose and tight output boundaries for a 10 track seek and $k^* = 10$ samples in simulation and experiment

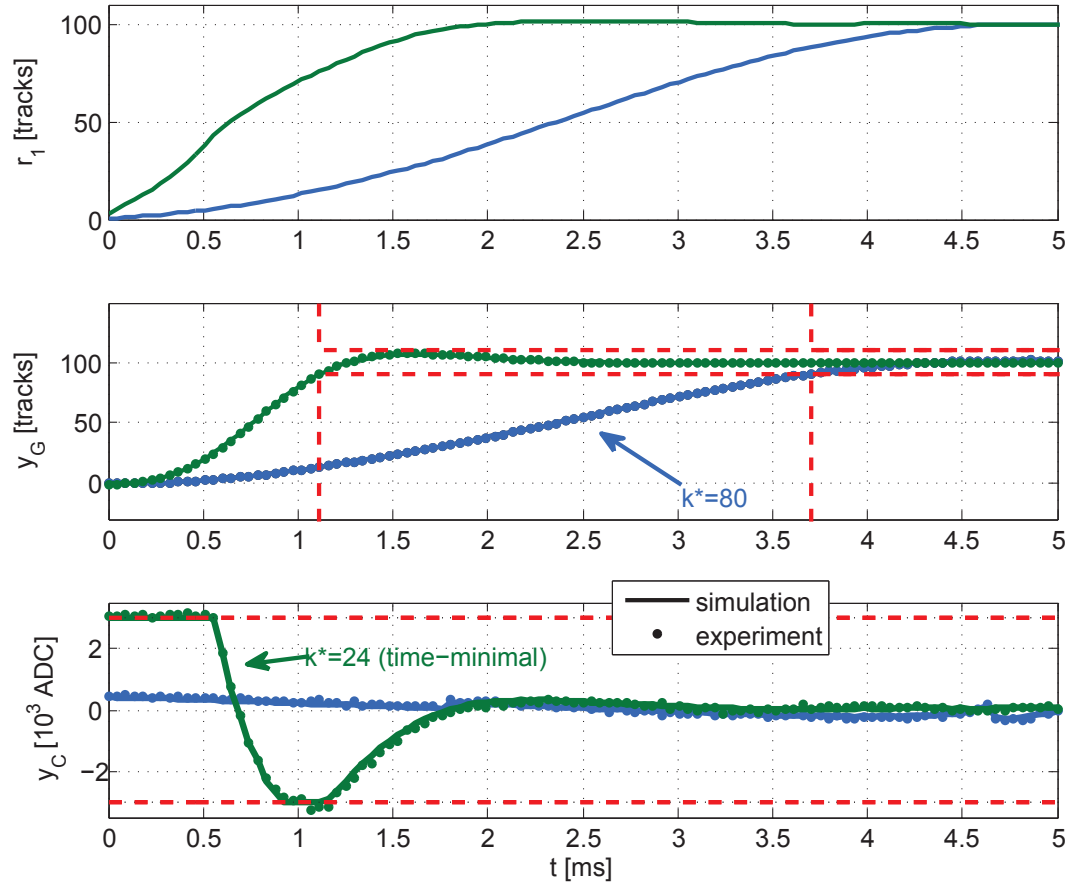


Figure 4.13: 100 track step for loose boundaries and $k^* = 24$ (time-optimal) and $k^* = 80$ samples in simulation and experiment

slow seek to the same target was considered and a fixed settling time of 80 samples was assumed. One can observe in Fig 4.13 that in this case the control signal is much smaller than for the time minimal seek which is expected. This might be of particular interest in a HDD as not always the time-minimum solution is desired. Moving the read/write head from one data sector to the next might yield a fixed idle time due to the limited rotational speed of the disk. Since the idle time is known, one can compute an optimized control signal that minimizes the control energy and residual vibrations.

4.5 Conclusions

An input shaping algorithm for closed-loop discrete-time LTI systems has been described in this chapter. The algorithm was experimentally verified in a modified HDD set-up showing excellent agreement between theoretical (simulation) and actual experimental results. It was shown that input shaping significantly reduces targeting time and residual vibrations compared to an output response obtained using standard reference signals such as steps. It was also shown that input shaping improves the response of systems whether or not plant saturation is present. The method is computational inexpensive and could be implemented in the firmware of a hard disk drive which might significantly reduce seek-time, energy consumption and system vibrations during the seeking process in a HDD.

4.6 Appendix - selected matrix dimensions

Symbol	row dimensions	column dimensions
A	$n_C + n_G + p$	
B	$n_C + n_G + p$	$m + p$
C	$m + 2p$	$n_C + n_G + p$
D	$m + 2p$	$m + p$
L	$4M(m + p) + 2N(m + 2p)$	$M(m + p)$
M	m	
M_{opt}	$M(m + p) + 1$	
M_{constr}	$4M(m + p) + 2N(m + 2p)$	
P₁	$N(m + 2p)$	
P₂	$M(m + p)$	
Ψ	$N(m + 2p)$	$M(m + p)$
Q, W	$4M(m + p) + 2N(m + 2p)$	1
q	$N(m + 2p)$	1
Θ₁	$M(m + p)$	
Θ₂	1	
Θ₃	1	$M(m + p)$
u	$M(m + p)$	1

4.7 Acknowledgment

The authors would like to thank Headway Technologies Inc for providing the experimental set-up.

Chapter 4, in part, is a reprint of the material as it appears in "Reference Signal Shaping for Closed-loop Systems with Application to Seeking in Hard Disk Drives", Boettcher U., Fetzer D., Li H., de Callafon R.A., Talke F.E., submitted to *IEEE, Transactions on Control Systems Technology*. The dissertation author was the primary investigator and author of this paper.

5 Analytical read back signal modeling in magnetic recording

5.1 Introduction

A large number of analytical models for the magnetic read back signal have been developed in the past for longitudinal and perpendicular magnetic recording [179, 180, 181, 182, 183, 184, 185, 186, 187, 188, 133, 134, 189, 190, 191, 192, 193]. Initially, the "on-track" response was approximated in 2-D by neglecting off-track effects and approximating an isolated bit transition which yields a bell-shaped curve for longitudinal recording and a di-bit curve for perpendicular recording [189]. With increasing storage density and decreasing bit aspect ratio there was a need to switch from initial 2-D models to 3-D models [182]. Many of the models developed consider isolated magnetic bit transitions [179, 182, 184]. A commonly used technique is based on the principle of reciprocity as applied in [180, 181, 184, 190, 191] or Fourier components [183, 185, 192, 193]. An excellent overview of previously developed models is given in [186]. In [186], the read back signal is

approximated by considering various magnetic potentials.

In this chapter, we follow a different approach for an analytical approximation of the read back signal which is motivated by the evolution in read head technology described in section 2.2.3 of this dissertation. Previously, inductive recording heads were used that measured the transition (derivative) of the magnetization pattern on the disk. Today, giant/ tunnel magneto-resistance (G/TMR) heads are in use that change their resistance in the presence of a magnetic field. Furthermore, one of the possible future technologies in hard disk drives might be bit patterned media (BPM) as discussed in section 2.9.2 of this dissertation. G/TMR and BPM will intuitively require a read back signal model that considers the measured response of the bit rather than the bit transition as the transition parameter might not be described correctly with current analytical models. Furthermore, servo designs in bit patterned media that incorporate either only "up" or only "down" magnetized bits could be captured by the model. Track edge effects and written transitions that are sometimes modeled by an ellipse [182] would be decreased as the bits on patterned media would potentially have a well defined shape. More complicated shapes could be investigated by using the model developed and a so-called micro grid approach [184] that is very accurate and considerably faster than finite element solutions.

The objective of this study is to propose a 3D analytical model of the read back signal that allows the investigation of any recorded bit pattern separated from the various different types of head sensitivity functions. This chapter is organized

as follows. Section 5.2 shows how the 3D distribution of the magnetic field can be approximated for longitudinal and perpendicular magnetic recording using the law of Biot-Savart. Thereafter, in section 5.3, a simple model of head sensitivity is given which will be used to calculate the read back signal. Finally, in section 5.4, the read signal for longitudinal and perpendicular recording is simulated for an example pattern.

5.2 Media contribution

The media magnetization is modeled considering a single point of measurement. The coordinate system is defined according to Fig. 5.1 which corresponds to longitudinal magnetic recording (LMR). It will be shown later that the results of the LMR system can be simply modified to perpendicular magnetic recording (PMR) through a rotation by $\frac{\pi}{2}$ and adding a soft magnetic underlayer (SUL).

For a simple analytic approach continuity of space is assumed. Therefore, it is necessary to assume that the relative permeability of the recording layer is unity for both perpendicular and longitudinal recording [194]. As indicated in Fig. 5.1, each bit is assumed to have a cuboidal shape with length L , width W and recording layer thickness T . Other shapes such as cylindrical shapes could also be of interest for bit patterned media but are beyond the scope of this study. Each bit can be modeled as a permanent magnet which itself can be modeled by placing equivalent currents on its surface. As indicated in Fig. 5.1, an infinite number of equidistant

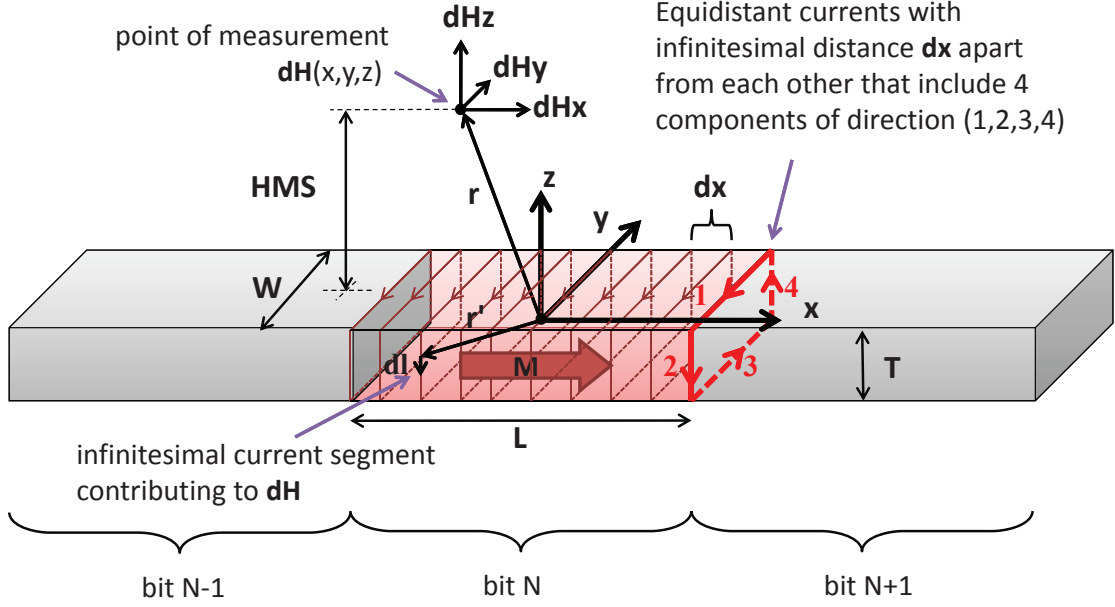


Figure 5.1: Defining the coordinate system

currents with infinitesimal distance dx apart from each other are placed on the bit. The origin of the coordinate system is defined in the center of the bit. Using the law of Biot-Savart [195], which can be derived from Maxwell's equations, one can calculate the differential magnetic field $d\vec{H}(\vec{r})$ caused by each surface current segment as

$$d\vec{H}(\vec{r}) = \frac{I}{4\pi} \frac{d\vec{l} \times (\vec{r}' - \vec{r})}{|\vec{r}' - \vec{r}|^3} \quad (5.1)$$

where \vec{r} is the vector to the measurement point, \vec{r}' is the vector to the contributing surface current segment and $d\vec{l}$ is the vector of the contributing surface current segment (Fig. 5.1). The value of each surface current equals

$$I = H_C dx \quad (5.2)$$

where H_C is the coercivity of the magnetic recording layer. The currents that are

indicated in Fig. 5.1 have four main components of direction (1,2,3,4). The vector \vec{r}' to each current segment \vec{dl} can be parameterized for the four components of direction as

$$\vec{r}'_1(x, t) = \begin{pmatrix} x \\ W/2 \\ T/2 \end{pmatrix} + t \begin{pmatrix} 0 \\ -W \\ 0 \end{pmatrix} \quad (5.3)$$

$$\vec{r}'_2(x, t) = \begin{pmatrix} x \\ -W/2 \\ T/2 \end{pmatrix} + t \begin{pmatrix} 0 \\ 0 \\ -T \end{pmatrix} \quad (5.4)$$

$$\vec{r}'_3(x, t) = \begin{pmatrix} x \\ -W/2 \\ -T/2 \end{pmatrix} + t \begin{pmatrix} 0 \\ W \\ 0 \end{pmatrix} \quad (5.5)$$

$$\vec{r}'_4(x, t) = \begin{pmatrix} x \\ W/2 \\ -T/2 \end{pmatrix} + t \begin{pmatrix} 0 \\ 0 \\ T \end{pmatrix} \quad (5.6)$$

Here, t ranges from 0 to 1 and x ranges from $-\frac{L}{2}$ to $\frac{L}{2}$. The vectors \vec{r}'_i are given in (5.3)-(5.6) and each current segment \vec{dl}_i is defined as

$$\vec{dl}_i = \frac{\partial \vec{r}'_i}{\partial t} dt \quad (5.7)$$

We can now compute the total magnetic field as

$$\vec{H}(\vec{r}) = \sum_{i=1}^4 \int_{-\frac{L}{2}}^{\frac{L}{2}} \int_0^1 \frac{\mu_0}{4\pi} \frac{\frac{\partial \vec{r}'_i}{\partial t} \times (\vec{r}'_i - \vec{r})}{|\vec{r}'_i - \vec{r}|^3} dt dx \quad (5.8)$$

Each of the two integrals in (5.8) yields two components in the analytical solution of (5.8) and since there are four main current directions we obtain $4 \times 2 \times 2 = 16$ components for the solution of (5.8). We can solve this integral analytically. For clarity, we write the x-,y- and z-components of the measured magnetic field at point $\vec{r} = (x_m, y_m, z_m)^T$ separately in (5.9)-(5.11) as

$$H_x = \frac{H_C}{4\pi} \sum_{i=1}^{16} S_i \arctan \left(\frac{\left(\frac{L}{2} + a_{xi}x\right) \left(\frac{\frac{T}{2} + a_{zi}z}{\left|\frac{W}{2} + a_{yi}y\right|}\right)^{a_{ei}}}{R_i} \right) \quad (5.9)$$

$$H_y = \frac{H_C}{4\pi} \sum_{i=1}^{16} \frac{a_{ei}}{2} \ln \left[a_{zi} \left(a_{yi} \left(\frac{T}{2} + a_{zi}z \right) + a_{xi}a_{ei}R_i \right) \right] \quad (5.10)$$

$$H_z = \frac{H_C}{4\pi} \sum_{i=1}^{16} \frac{a_{ei}}{2} \ln \left[a_{yi} \left(a_{zi} \left(\frac{W}{2} + a_{yi}y \right) + a_{xi}a_{ei}R_i \right) \right] \quad (5.11)$$

where R_i and S_i are defined by

$$R_i = \sqrt{\left(\frac{L}{2} + a_{xi}x\right)^2 + \left(\frac{W}{2} + a_{yi}y\right)^2 + \left(\frac{T}{2} + a_{zi}z\right)^2} \quad (5.12)$$

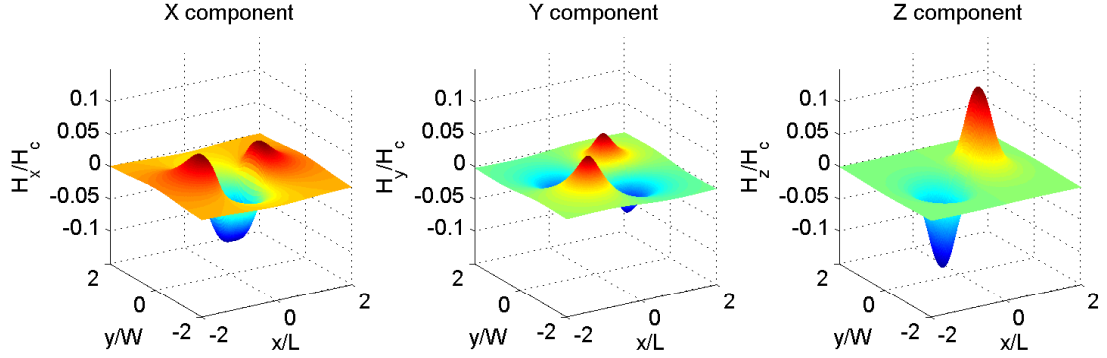
and

$$S_i = \text{sign} \left(\left(\frac{W}{2} + a_{yi}y \right) \left(\frac{T}{2} + a_{zi}z \right) \right) \quad (5.13)$$

respectively. The coefficients $a_{xi} \in \{-1, 1\}$, $a_{yi} \in \{-1, 1\}$, $a_{zi} \in \{-1, 1\}$ and $a_{ei} \in \{-1, 1\}$ (x-, y-, z-direction and exponent) occur in all possible perturbations and are listed in Tab 5.1. For a simple numerical example with parameters: head-medium spacing (HMS)=10, W=50, W=50, T=20 nm, the normalized media magnetization in longitudinal recording is plotted in Fig. 5.2. As indicated earlier, this result can be modified to obtain the solution for perpendicular magnetic recording. Figure 5.3a shows the cuboidal shaped bit from Fig. 5.1 rotated by $\frac{\pi}{2}$ around the

Table 5.1: Coefficients

i	1	2	3	4	5	6	7	8	9	10	11	12	13	14	15	16
a_{xi}	1	1	1	1	1	1	1	1	-1	-1	-1	-1	-1	-1	-1	-1
a_{yi}	1	1	1	1	-1	-1	-1	-1	1	1	1	1	-1	-1	-1	-1
a_{zi}	1	1	-1	-1	1	1	-1	-1	1	1	-1	-1	1	1	-1	-1
a_{ei}	1	-1	1	-1	1	-1	1	-1	1	-1	1	-1	1	-1	1	-1

**Figure 5.2:** Normalized magnetic field components for longitudinal magnetic recording measured at HMS=10 for W=50,L=50,T=20 nm

y-axis. The contribution of the soft magnetic underlayer (SUL) to the magnetic field measured at $\vec{r} = (x_m, y_m, z_m)^T$ has to be taken into account. The SUL has a relative permeability that is much larger than 1 (on the order of 100). For the analytical approximation it is assumed to be infinity. Therefore, an image source is placed below the bit (Fig. 5.3 a). It can also be modeled by a mirror head [134] as shown in Fig. 5.3 b). Fig. 5.3 a) (one head and two bits) represents the equivalent numerical problem as Fig. 5.3 b) (one bit and two heads) where the magnetic field is computed for two different points yielding the contribution of the real head H^{real} and the contribution of the image head H^{img} . An adjustment parameter $\sigma \geq 0$ is introduced that depends on the thickness and the relative permeability of the

soft magnetic underlayer and the thickness of the intermediate layer. It is obvious that placing the soft magnetic layer further away from the recording layer will decrease the effect of the underlayer on the read back signal. By switching x- and

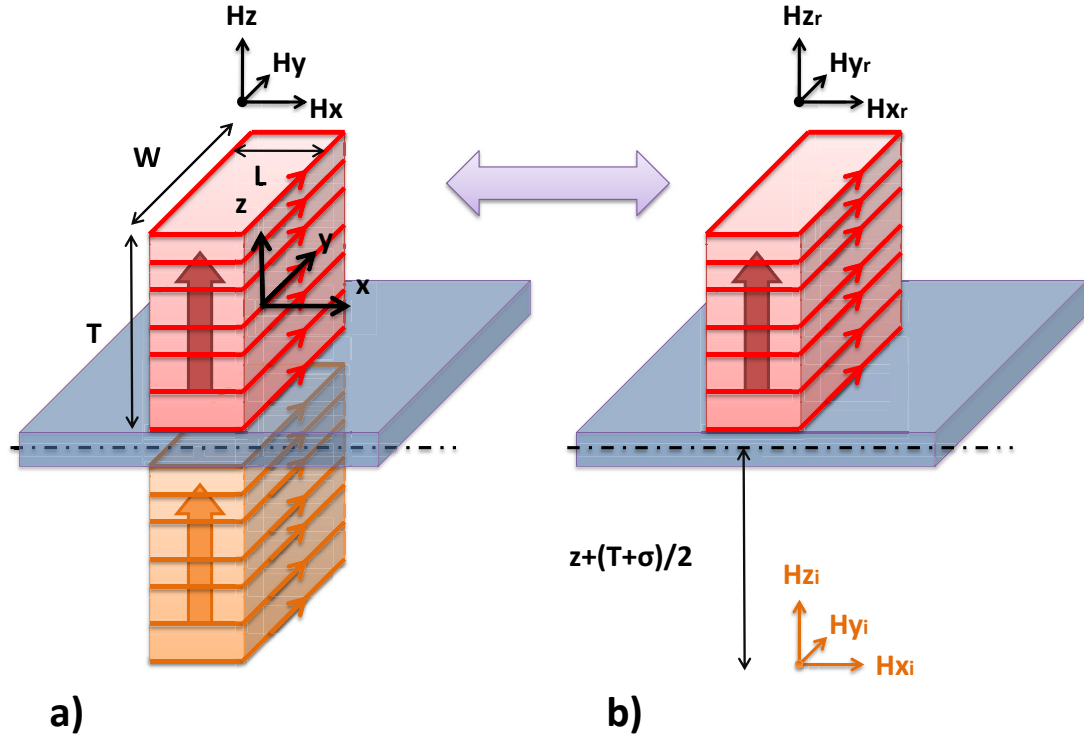


Figure 5.3: Modeling perpendicular recording

z-components in the coordinate system definitions, (5.9)-(5.11) can be rewritten. The shielded tunnel magneto resistance (TMR) head is mainly sensitive to the z-component of the magnetic field [182]. Hence, only the z-component is considered here. However, depending on the head design, the x- and y-components could be considered as well. H_z can be written as the superposition of the contribution of the "real" head and the "image" head as indicated in Fig. 5.3 b). Thus, the new

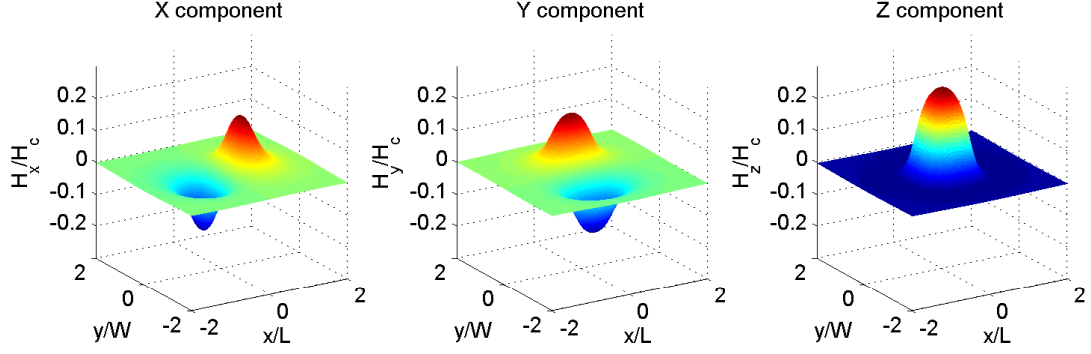


Figure 5.4: Normalized magnetic field components for perpendicular magnetic recording measured at HMS=10 for W=50,L=50,T=20 nm

z-component of the magnetic field for perpendicular recording yields

$$H_z = \frac{H_C}{4\pi} \sum_{i=1}^{16} S_i \left(H_i^{\text{real}} + H_i^{\text{img}} \right) \quad (5.14)$$

where

$$H_i^{\text{real}} = \arctan \left(\frac{\left(\frac{T}{2} + a_{zi}z \right) \left(\frac{\frac{L}{2} + a_{xi}x}{\left| \frac{W}{2} + a_{yi}y \right|} \right)^{a_{ei}}}{R_i} \right) \quad (5.15)$$

and

$$H_i^{\text{img}} = \arctan \left(\frac{\left(\frac{T}{2} + a_{zi}(z + T + \sigma) \right) \left(\frac{\frac{L}{2} + a_{xi}x}{\left| \frac{W}{2} + a_{yi}y \right|} \right)^{a_{ei}}}{R'_i} \right) \quad (5.16)$$

where

$$R'_i = R'_i(x, y, z) = R_i(x, y, z + T + \sigma) \quad (5.17)$$

The normalized contribution of the three components to the magnetic field are plotted in Fig.5.4. One can clearly see the similarities by comparing the x-component and z-component in Fig.5.2 to the z-component and x-component in Fig. 5.4.

5.3 Head sensitivity

The sensitivity of the read head is defined in a similar way in [190] as shown in Fig.5.5. The shields are assumed to have infinite width and the read element

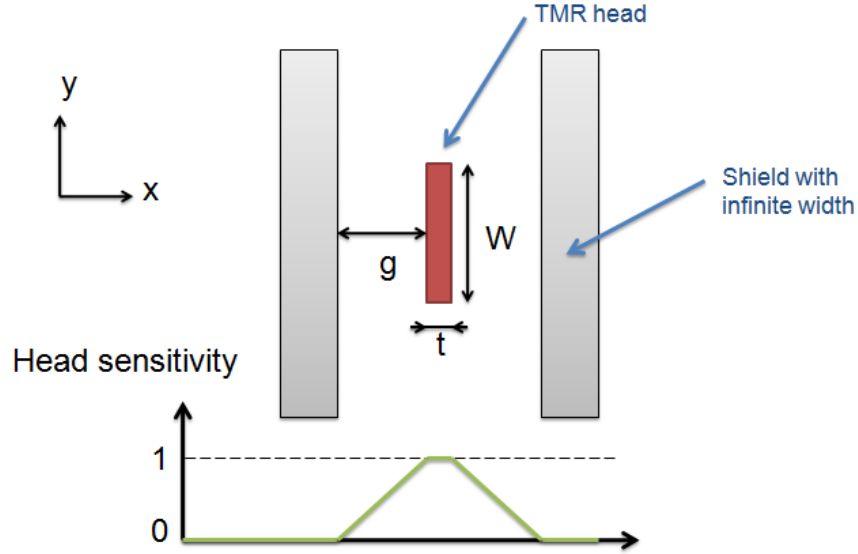


Figure 5.5: Assumed TMR head sensitivity function

has a finite width w and thickness t . The gap between the read element and the shield is defined as g . The sensitivity function is unique to the head design. In simulations in this chapter a sensitivity as indicated in Fig.5.5 is assumed. The TMR element reads 100% of the signal and the sensitivity decreases towards the edges of the shield. At the shield, no signal is detected by the read element. Different sensitivity functions are conceivable, such as a Gaussian shaped read sensitivity function [196].

The read back signal is approximated by the convolution of media magneti-

zation and read element sensitivity function. Using superposition and the analytic model for one single bit allows the computation of the x-y distribution of the read back signal for different flying heights and for arbitrary bit pattern.

5.4 Simulation example

As a simulation example, three different head-medium spacings are computed for longitudinal and perpendicular magnetic recording. Fig. 5.7 shows the computed read back signal for the following assumed parameters: The bit dimensions were defined as $L = 170 \text{ nm}$, $W = 80 \text{ nm}$, $T = 20 \text{ nm}$, $\sigma = 0 \text{ nm}$ and reader parameter were assumed as $w = 60 \text{ nm}$, $g = 30 \text{ nm}$, $t = 10 \text{ nm}$. Figure 5.6 shows the simulated read back signal based on the above parameters for a "16T"-type pattern that is used in section 6.3. The 16T pattern consists of 8 "up"-magnetized bits followed by 8 "down"-magnetized bits. Three different head-medium spacings are shown in Fig. 5.6: 18, 10 and 2 nm. The left column shows the time domain signal (normalized by the maximum signal at 2 nm HMS) at track center ($y=0$); the second column shows the corresponding single sided amplitude of the frequency spectrum and the third column shows the read back signal distribution for one single bit in down-track (x) and off-track (y) direction. In a similar fashion, the read back signal for perpendicular magnetic recording is shown in Fig. 5.7. Here, the same bit pattern and bit and head parameters were used and a typical shape for a PMR signal can be observed.

For further verification, the "16T"-type pattern was written at 450 MHz onto a disk using a commercially available spinstand (Microphysics Inc.). The raw read back signal is shown in Fig. 5.8. We observe the typical U-shape of perpendicular recording signals when written at relatively low linear densities. Furthermore, a good qualitative agreement between Fig. 5.8 and Fig. 5.7 (bottom left) can be observed. A quantitative comparison could not be performed since exact media and read element parameters are unknown.

5.5 Conclusions

The significance of the mathematical model derived in this chapter is due to its simplicity. In particular, the magnetic field is computed directly instead of using the transition (derivative) of the magnetization in the read back signal. This allows a very fast simulation, without compromising accuracy. The model is applicable to continuous and bit patterned media. The media magnetization model is separated from the reader sensitivity function. The simulated (perpendicular) read signal is in qualitative agreement with experimentally obtained read back signals.

5.6 Acknowledgement

We would like to acknowledge Dr. Neil Bertram and Dr. Gordon Hughes for the valuable discussions related to the read back signal modeling.

Chapter 5, in part, is a reprint of the material as it appears in "Analytical Read Back Signal Modeling in Magnetic Recording", Boettcher U., Lacey C.A., Li H., Amemiya K., de Callafon R.A., Talke F.E., *Microsystem Technologies*, 2011. The dissertation author was the primary investigator and author of this paper.

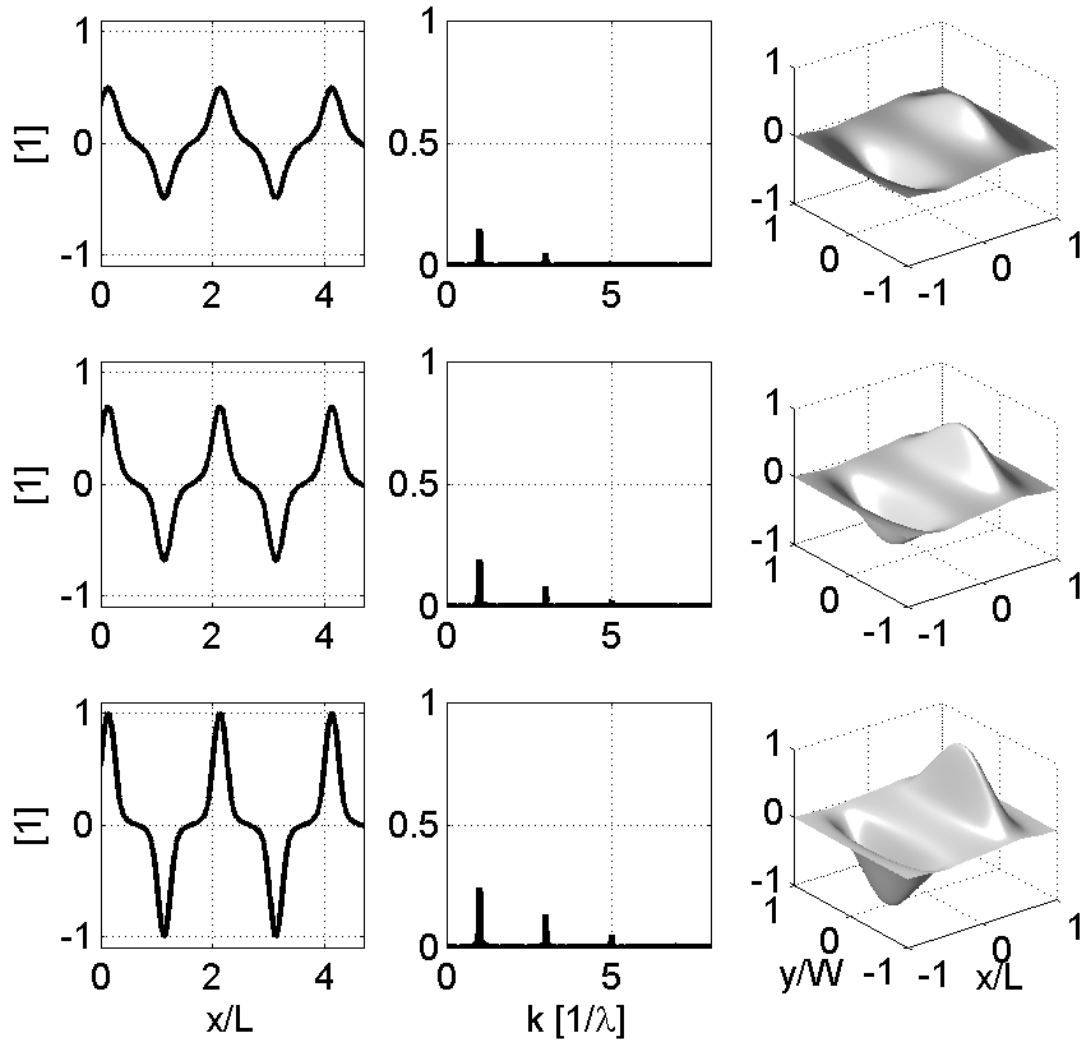


Figure 5.6: Normalized LMR read back signal for a head-medium-spacing of 18, 10 and 2 nm. First column: time/spacial domain, second column: frequency domain, third column: read back signal of 1 single bit (normalized by bit length and bit width)

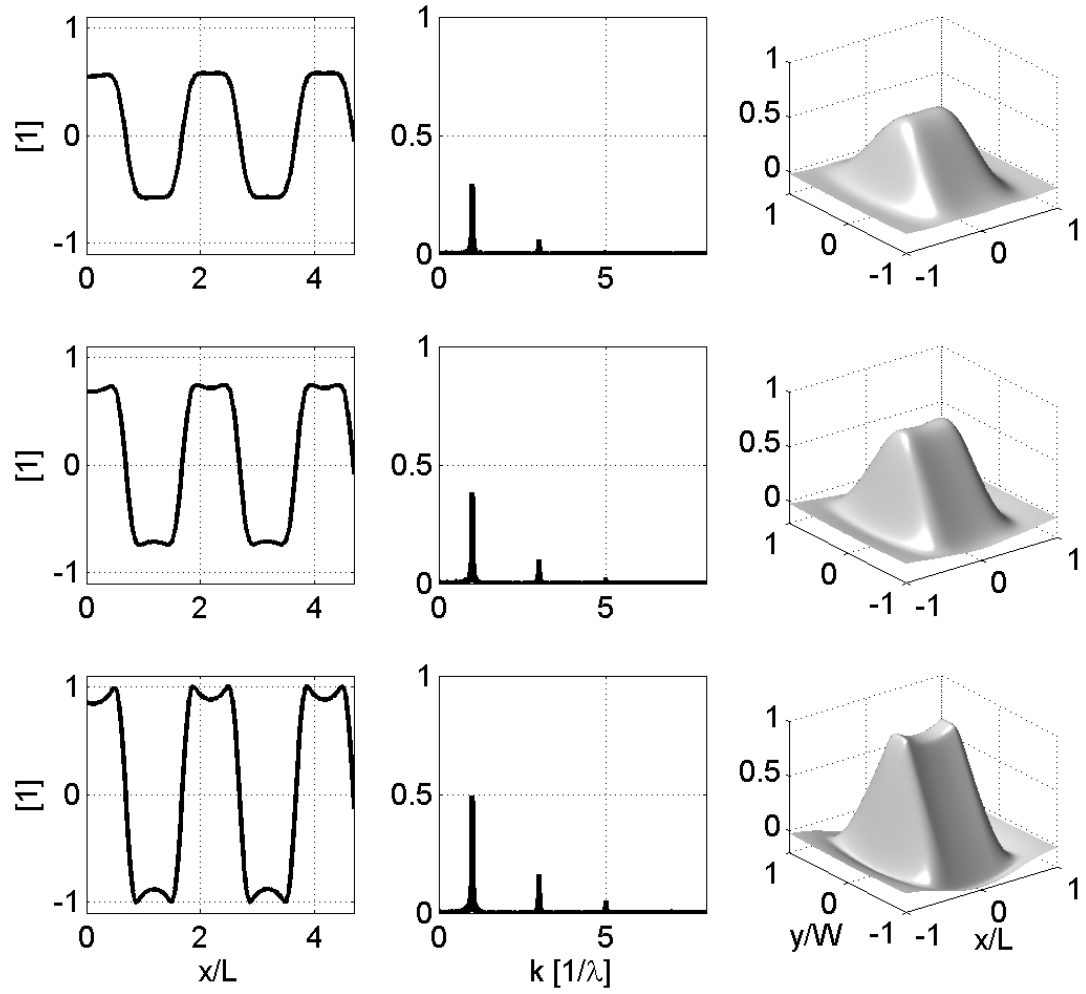


Figure 5.7: Normalized PMR read back signal for a head-medium-spacing of 18,10 and 2 nm. First column: time/spacial domain, second column: frequency domain, third column: read back signal of 1 single bit (normalized by bit length and bit width)

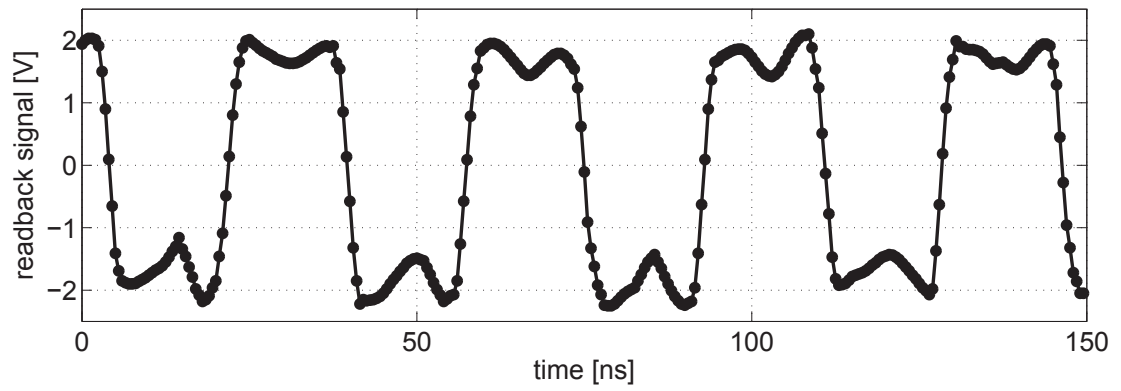


Figure 5.8: Raw read back signal of a 16T pattern at approximately 2 nm head-medium-spacing measured on Microphysics spinstand at a write frequency of 450 MHz sampled at 2 GHz.

6 Servo signal processing for flying height control in hard disk drives

6.1 Introduction

The objective of this chapter is to propose a method for accurately measuring flying height variations based on servo sector measurements. The method is based on an amplitude based servo pattern for off-track position estimation as introduced in chapter 2.6.1. After a brief review of existing flying height estimation schemes we will utilize the readback signal model developed in chapter 5 to simulate off-track characteristics of the proposed method. An experimental verification of the measurement method is given in 6.3.

6.2 Flying height estimation

6.2.1 Available techniques

Most of the reported algorithms on in-situ flying height estimation are based on a specific data pattern that is written onto the disk, thereby resulting in certain harmonics in the frequency spectrum of the read signal. The Wallace spacing formula translates the decay of the signal to spacing change and has been shown to be applicable to longitudinal magnetic recording as well as perpendicular magnetic recording [197]. Commonly used is the triple harmonics method [198, 199, 200] that uses a "111100" data pattern to create a large first and third harmonic. The logarithm of the ratio of the third over the first harmonic is proportional to the flying height modulation. Ratios of different harmonics other than the third and the first have also been used and servo pattern might be taken into account [201]. Approaches have also been implemented based on maximum or average amplitudes [202] rather than harmonics amplitudes. Also, approaches that employ random data instead of a fixed data pattern were proposed [203]. A technique that extracts both the position error signal (PES) and the flying height information is reported in [204] where radially adjacent and circumferentially aligned servo bursts are generated with different frequency contributions to generate position error and flying height signals. Other techniques are the pulse width method [205], the spectral fitting method [206] and methods that estimate the flying height based on the slope of isolated pulses of the read back signal [207]. Some of those estimation

algorithms are only applicable to longitudinal magnetic recording (LMR) technology and some are developed for (or are extendable to) perpendicular magnetic recording (PMR) technology. Some embody the following disadvantages:

- Cross-track-motion might wrongfully be detected as a change in flying height
- The measurement can strongly depend on the radial position of the read element over the disk (skew angle)
- A particular data pattern and/or the data sector is necessary, and, thus, storage space is lost.
- The method may not be capable for perpendicular magnetic recording

6.2.2 Servo signal based flying height estimation

As described in section 2.6.1, the servo sectors on the disk are used to determine the off-track position of the read/write head with respect to the track center. The estimation scheme for the measurement of the variation of flying height proposed in this chapter is based on the servo pattern written in the servo sectors on the disk. Using the servo pattern for the estimation of flying height has a number of advantages. At every servo sector the off-track position is known. Hence, the effect of cross-track motion of the head on the flying height signal can be eliminated. The estimation of flying height variation using a conventional amplitude based servo pattern as shown in Fig.2.21 on page 47 will be shown in this chapter. The following assumptions are made:

1. The change in magnetic spacing corresponds to a change in flying height which requires a constant overcoat and lubricant thickness (Fig. 2.18 on p. 43)
2. The flying height variation of adjacent servo bursts within the same servo sector is small compared to the flying height variation between adjacent servo sectors.
3. The writing process is less sensitive to flying height variations than the reading process [200]

Based on those assumptions the change in flying height can be computed from the Wallace equation. The Fourier transform of the read back signal decays exponentially with increasing distance from the magnetic medium [133]. For simplicity, only A and B bursts are considered here. The read back signal voltage is measured at a specific frequency in the frequency domain of two subsequent servo bursts, i.e., Φ_A and Φ_B

$$\Phi_A(k, z) + \Phi_B(k, z) = (\Phi_A(k, 0) + \Phi_B(k, 0)) e^{-kz} \quad (6.1)$$

where $k = \frac{2\pi}{\lambda}$ is the wave number. The flying height change $\Delta z = z - z_0$ can be calculated from

$$\Delta z = -\frac{\lambda}{2\pi} \ln \left(\frac{\Phi_A(\lambda, z) + \Phi_B(\lambda, z)}{\Phi_A(\lambda, z_0) + \Phi_B(\lambda, z_0)} \right) \quad (6.2)$$

where z_0 is the reference flying height. The fluctuation of the product of the recording layer thickness and the remanent magnetization (M_r) of the recording media [200] causes read back signal modulation, and, therefore modulations in the

measured flying height. The harmonics ratio method referred to earlier decreases this effect. Two different approaches are proposed here, both based on the first and the third harmonic of the read back signal in the servo sector. We can modify (6.1) to compute the first harmonic corresponding to the wavelength λ_1

$$\ln(\Phi_{A1} + \Phi_{B1}) = \ln(\Phi_{0,A1} + \Phi_{0,B1}) - \frac{2\pi}{\lambda_1}z \quad (6.3)$$

and the third harmonic corresponding to the wavelength

$$\ln(\Phi_{A3} + \Phi_{B3}) = \ln(\Phi_{0,A3} + \Phi_{0,B3}) - \frac{6\pi}{\lambda_1}z \quad (6.4)$$

Now, (6.4) can be subtracted from (6.3) and the change in flying height can be computed via

$$\Delta z_{1-3} = +\frac{\lambda_1}{4\pi} (\ln(\Phi_{A1} + \Phi_{B1}) - \ln(\Phi_{A3} + \Phi_{B3})) \quad (6.5)$$

which is similar to the known triple harmonics formula except that the sum of servo burst harmonics are considered. The subscript "1-3" indicates that the difference between the first and third harmonic was taken into account for the computation of Δz . Alternatively, the sum of (6.4) and (6.3) can be used to calculate

$$\Delta z_{1+3} = -\frac{\lambda_1}{8\pi} (\ln(\Phi_{A1} + \Phi_{B1}) + \ln(\Phi_{A3} + \Phi_{B3})) \quad (6.6)$$

6.2.3 Simulated off-track characteristics

The cross-track characteristics of the flying height change estimate were simulated using the same model and parameters as in chapter 5 for three cases

(18,10 and 2nm) for LMR and PMR, respectively. Two different servo burst spacing values were simulated. The definition of burst spacing is illustrated in Fig. 6.1. A servo burst spacing of 0.5 (Fig. 6.2a and b) corresponds to a shift of $0.5W$ from

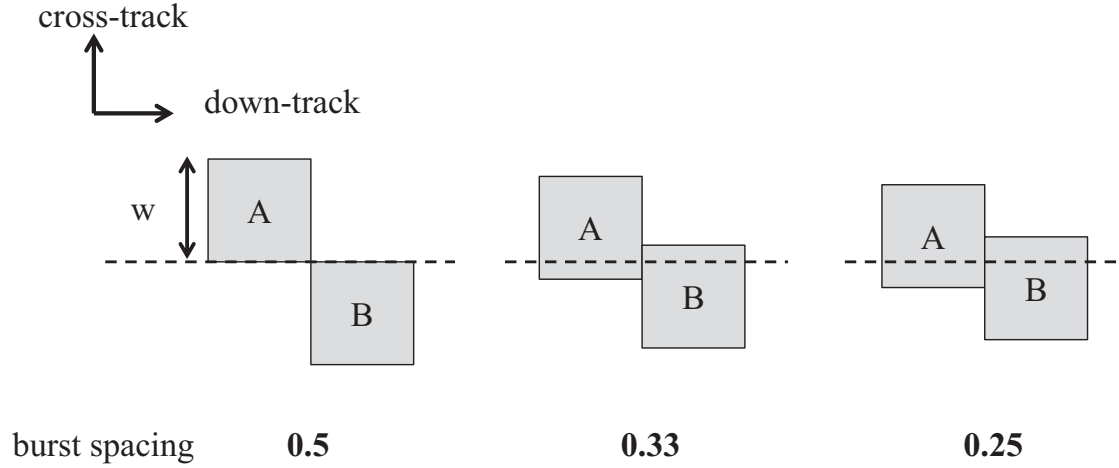


Figure 6.1: Illustrative definition of burst spacing for a dual servo pattern consisting of A and B bursts.

the track center for each burst. The resulting total radial distance between A and B burst would yield $0.5W + 0.5W = 1W$ which equals the bit width. A servo burst spacing of 0.25 (Fig. 6.2c) indicates a 50% overlap of the servo bursts.

The flying height change in Fig. 6.2 was estimated based on (6.5) and (6.6) as given by the dash-dot line and the dashed line, respectively. Since the measurement is relative, it was shifted in the z direction to the 2nm track center value. The magnetic spacings at 10 and 18nm were computed using the relative knowledge of the 2nm value. It can be seen that the 0.5 burst spacing case has a very small sensitivity to off-track variations for both LMR and PMR (Fig. 6.2a and b). The two proposed methods measure almost the same value close to the track center.

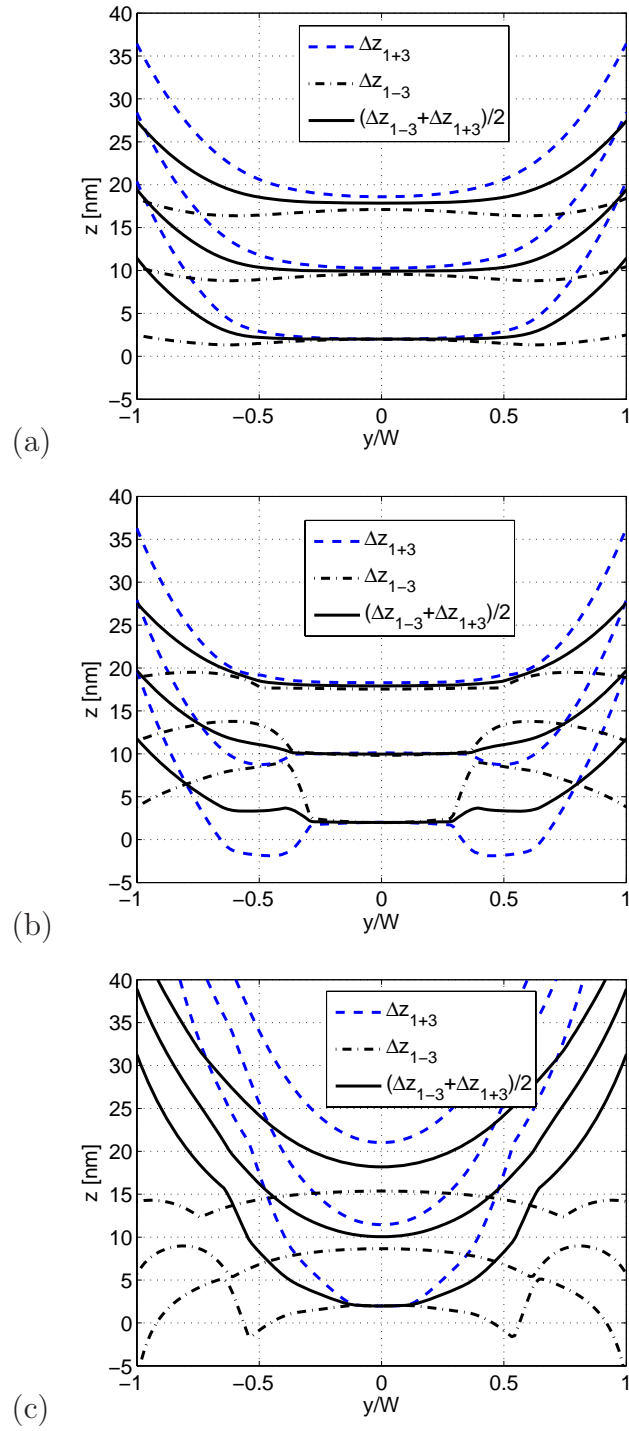


Figure 6.2: Off-track dependence of measurement technique: computed head-medium-spacing z for 18,10 and 2 nm and burst spacing of a) 0.5 and longitudinal recording b) 0.5 and perpendicular recording c) 0.25 and perpendicular recording as a function of the normalized off-track position y

However, the values of Δz_{1-3} and Δz_{1+3} differ slightly but the arithmetic mean (solid line) of both yields the correct values (10 and 18nm) close to the track center. This effect becomes more obvious for a burst spacing of 0.25 as shown in Fig. 6.2c. The arithmetic mean of (6.6) and (6.5) simply yields

$$\Delta z_{\text{mean}} = \frac{\lambda_1}{16\pi} (\ln(\Phi_{A1} + \Phi_{B1}) - 3 \ln(\Phi_{A3} + \Phi_{B3})) \quad (6.7)$$

Based on the performed simulations, the relative flying height change computed by (6.7) is relatively insensitive to off-track motion for $|\Delta y| < 0.3W$ and a burst spacing of 0.5. For a burst spacing of 0.25 it is still relatively insensitive to off-track motion for $|\Delta y| < 0.1W$ which is the generally accepted positioning requirement in magnetic recording technology in order to avoid track misregistration. A sudden increase in difference between Δz_{1-3} and Δz_{1+3} might indicate large off-track motion. However, Δz_{mean} shows small off-track sensitivity compared to Δz_{1-3} and Δz_{1+3} within a much larger range.

6.3 Experimental results

6.3.1 Experimental set-up and methodology

A number of flying height modulation measurements have been performed using a disk head tester (MicroPhysics). The experimental set-up is shown in Fig.6.3. Perpendicular magnetic recording disks and matching head/gimbal assemblies (HGA) were employed. The disk was spun at 7200 rpm and a simple dual

servo pattern with A and B bursts only was written onto the disk using a 16T pattern. A write frequency of 900 MHz was used with the first harmonic of the servo occurring at 56.25 MHz. The read back signal was captured using a 2GS/s digitizer. All measurements were performed at 2 degrees skew angle and at a radius $r = 25$ mm. The disk was divided into 128 servo sectors which yields a sampling frequency of position error signal and flying height measurement of 15.36 kHz. As indicated in Fig. 6.3, an arbitrary waveform generator was used to apply a voltage to the thermal actuator and a spindle index signal was used as a trigger for the waveform generator.

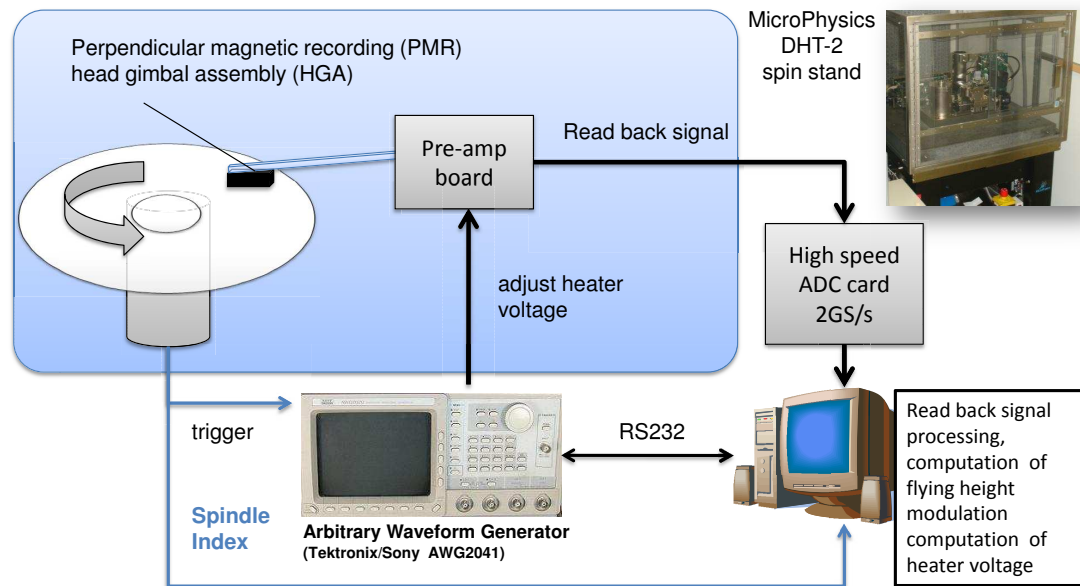


Figure 6.3: Experimental set-up

6.3.2 Verification of proposed flying height estimation scheme

The proposed estimation method from section 6.2 was used to calculate the flying height modulation based on the measured read back signal. First, the dynamic flying height modulation was measured for constant (but gradually increased) power levels. Figure 6.4 shows 15 different heater power levels P_{in} and the flying height modulations were computed based on (6.5) and (6.6), respectively. The PES was computed by

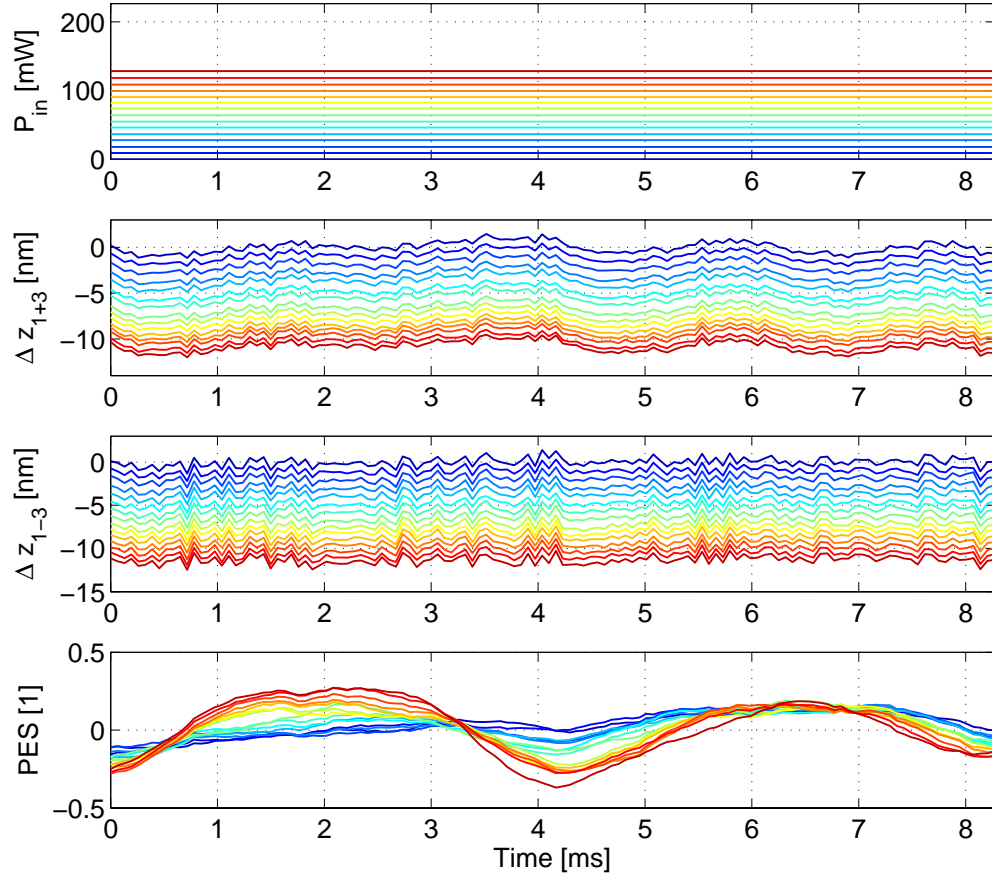


Figure 6.4: Averaged flying height modulation for 15 different constant power inputs to the heater element and position error signal over one revolution

$$\text{PES} = \frac{A - B}{A + B} \quad (6.8)$$

where A and B represents the track averaged amplitude (TAA) of the A and B burst, respectively. In Fig. 6.4, averaged values of 20 measurements are shown. It should be noted that a voltage v was applied to the heater element and the resulting input power P_{in} was computed by $P_{in} = v^2/R$ assuming a fixed value of the heater resistance R . Subsequently, we investigate the effect of resistance change in the DC gain of the model. P_{in} was varied from 0 mW to approximately 130 mW. From Fig. 6.4 it can be observed that the measured relative flying height decreases as the heater power increases. It is furthermore observed that the dynamic variation of Δz is very repeatable and very similar for different bias power level except for a DC offset. The difference between the static flying height variation Δz_{1+3} and Δz_{1-3} is very small. However, in terms of dynamic behavior, Δz_{1+3} looks slightly different from Δz_{1-3} at some angular positions. In general, Δz_{1+3} shows more low frequency flying height variations compared to Δz_{1-3} .

6.3.3 Off-track characteristics

A single (non-averaged) off-track measurement is shown in Fig 6.5. Here, Fig 6.5a) shows the track averaged amplitude of the A and B burst and the computed PES according to (6.8). On a large scale (Fig 6.5b)) Δz_{1-3} appears less sensitive to off-track motion than Δz_{1+3} . However, on a smaller scale (Fig 6.5c)) it can be observed that Δz_{1+3} is quite insensitive to off-track motion close to the track center. As predicted by the simulation results in section 6.2, an increase in measured flying height can be observed for increasing off-track motion for Δz_{1+3}

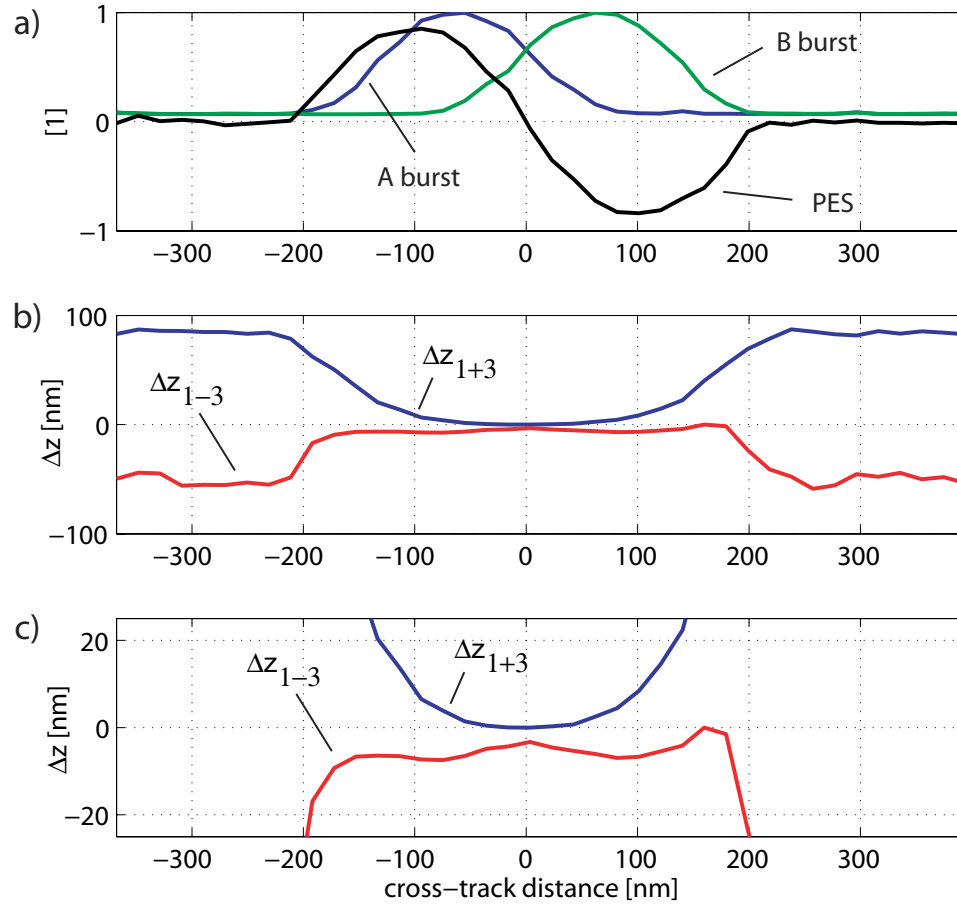


Figure 6.5: Measured cross-track behavior at 10mW heater input. a) track averaged amplitude (TAA) for A burst and B burst, b) measured flying height modulation, c) zoomed version of b)

where Δz_{1-3} decreases for increasing off-track motion.

6.3.4 Voltage step measurements

In order to identify a dynamic model of the heater actuator, a step input was applied. The results are shown in Fig. 6.6. The step height of the input voltage was kept constant and only the bias voltage was increased yielding a linearly increasing power step height with increasing bias voltage. As in the static case, an average

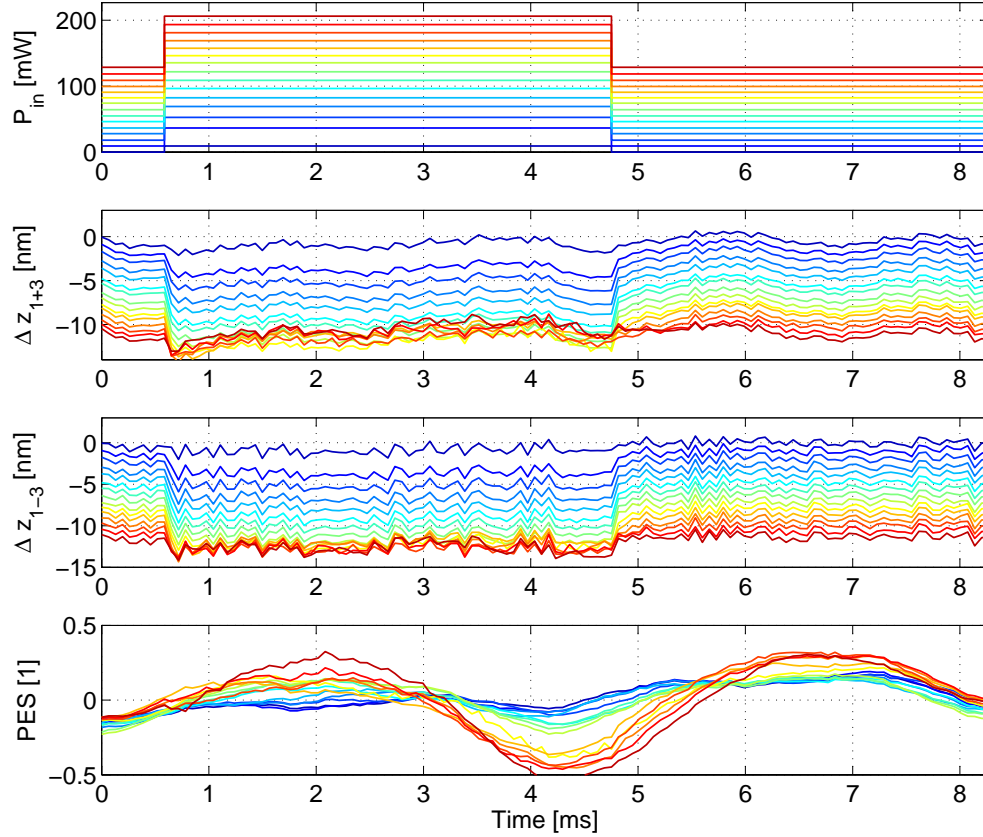


Figure 6.6: Averaged flying height modulation for 15 different step power inputs to the heater element and position error signal over one revolution

over 20 measurements was calculated. Figure 6.6 shows that the response of the actuator is very fast and that there is a minimum flying height around 12 nm below the initial flying height. The flying height does not go below this limit which is likely the result of head/disk contact. For heater power values above approximately 80 mW a sudden increase in position error signal and variance in flying height modulation (Fig. 6.8) can be observed which might indicate head disk contact.

6.3.5 Data based dynamic modeling of the heater response

The heater response was identified based on the relative spacing between the reference measurement (Fig. 6.4) and the step measurement (Fig. 6.6). The relative spacing measurements for the 15 different input steps are shown in Fig. 6.7. The two different estimation methods are in excellent agreement. The heater response was modeled using a standard least-squares estimation and a first order model. A significant time-delay could not be measured since the sampling time of the flying height modulation measurement was $65.1\mu\text{s}$ which is on the order of the determined time constant τ . It is obvious that this results in a decreased accuracy of the estimation of τ compared to the estimation accuracy of the steady-state gain K based on the least-squares solution. Time constant τ and gain K were estimated

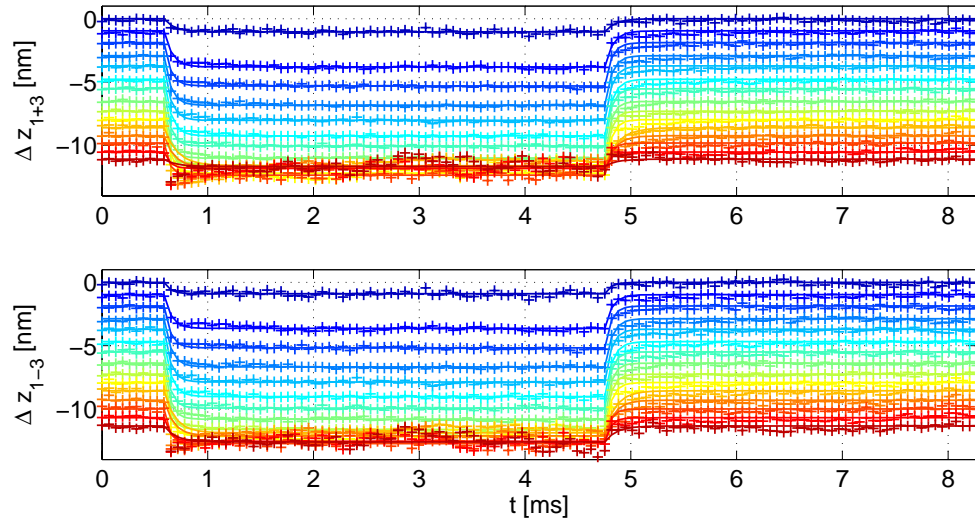


Figure 6.7: Relative steps (Fig. 6.6-Fig. 6.4) and identified first order models

for both proposed relative flying height estimation methods and Fig. 6.9 shows the

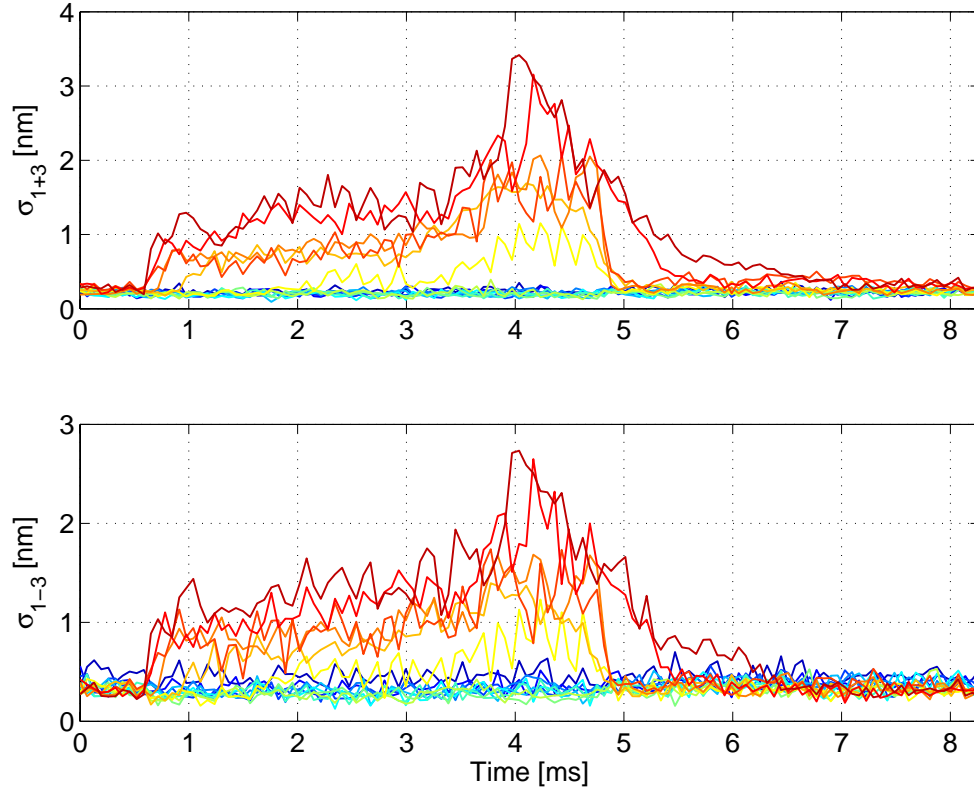


Figure 6.8: Variance in relative flying height

results as a function of the power step size P_{step} . The average time constant for the measurements up to 80 mW bias power P_{in} is on the order of the PES sampling time ($65 \mu\text{s}$). The absolute value of the gain K decreases from about 0.1 nm/mW gradually to almost zero as the bias heater power P_{in} and step size P_{step} increases. This is likely due to contact with the disk at approximately -12 nm where a further head-disk-distance decrease is not possible. The static flying height change as a function of heater input power P_{in} is shown in Fig. 6.10. The relationship seems nearly linear, although the slope of the curve (which corresponds to the static gain) is slowly decreasing as P_{in} increases. This could be due to the air bearing cooling

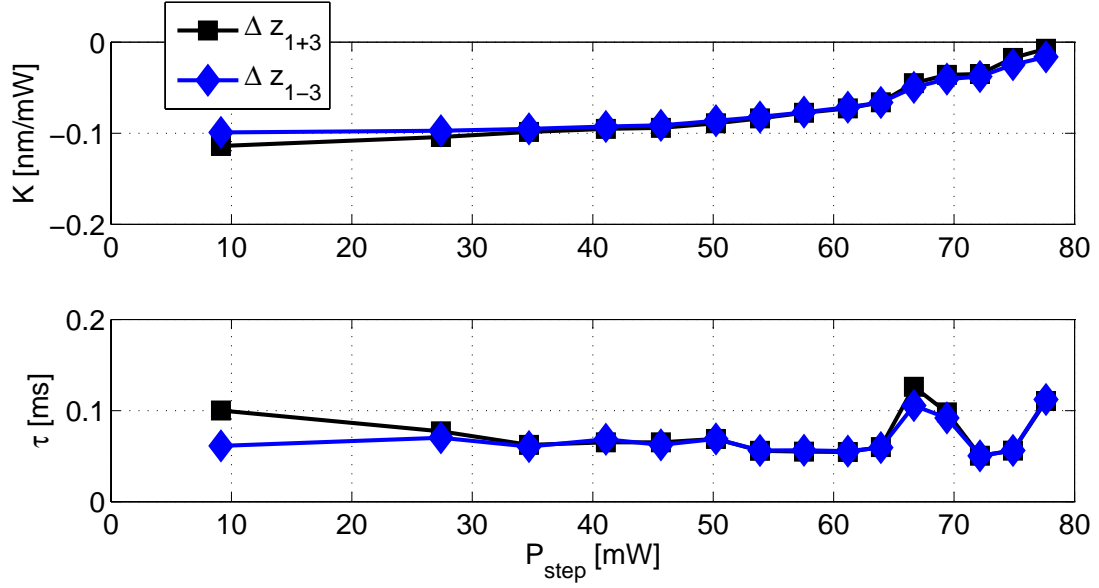


Figure 6.9: Estimated gain K and time constant τ from Fig. 6.7 based on a least squares estimate

effect (increased thermal conductivity between head and disk as local air bearing pressure increases and flying height decreases) [208] and/or the so-called push-back effect (due to higher air bearing pressure at lower flying heights) [209]. Another explanation would be an increasing heater resistance with increasing heater voltage yielding an actual lower heater power compared to the computed heater power assuming a constant resistance.

6.4 Conclusions

A flying height measurement scheme based on the servo pattern recorded in the servo sectors was developed and simulated using a read back signal model. The two proposed flying height measurement methods show excellent agreement

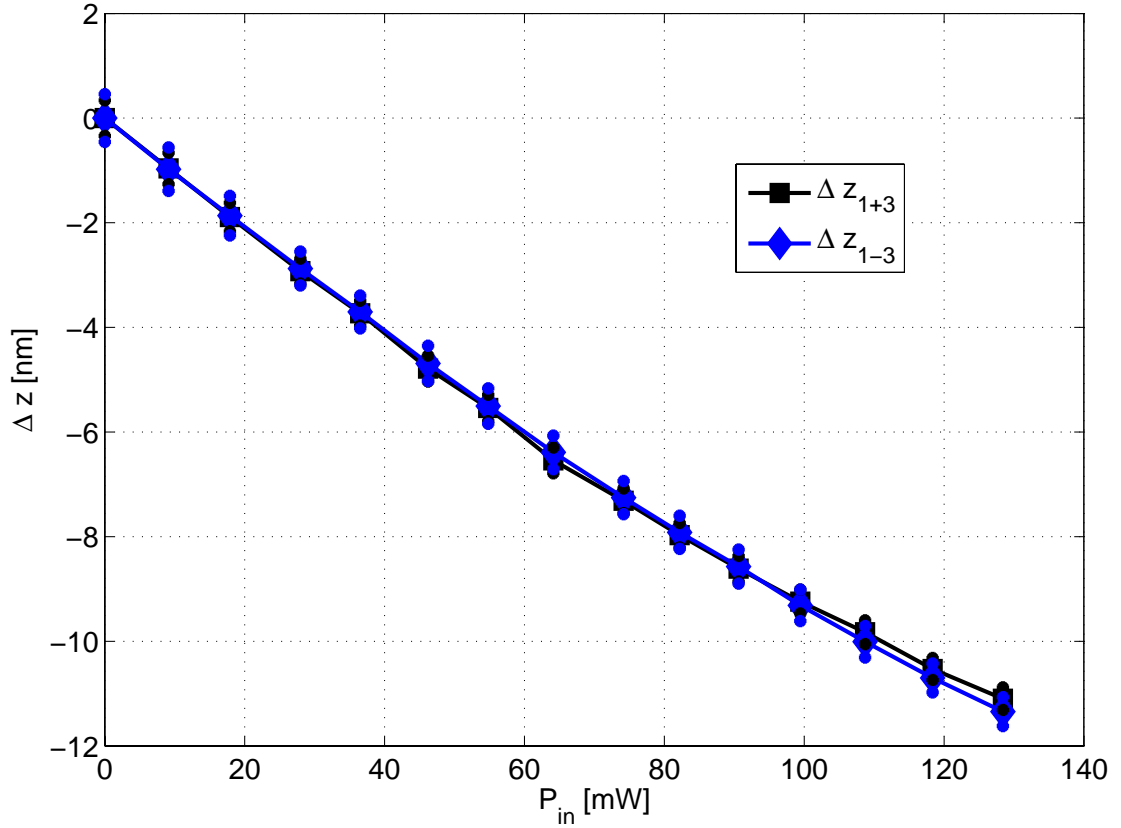


Figure 6.10: Static flying height change for different heater input power levels

within a large flying height range while being insensitive to off-track motion of the read write head. In the proposed method, the off-track sensitivity is a function of the radial servo burst spacing, i.e., the cross-track spacing between the A and B burst in each servo sector. The proposed method was tested experimentally to identify the dynamics of a resistance heater element capable of modifying the flying height at the read/write element. Based on the current data that uses a servo sector-based signal at a sampling rate of approximately 15.36 kHz it is suggested that the response of the thermal actuator can be approximated by a first order

system with a time-delay. It was found that the time delay was negligible and the time constant was found to be very small at around $65\mu s$. Chapter 7 will show that a second order model of the actuator is more suitable for dynamic control. The fast actuator response promises feasible solutions to real-time flying height adjustment up the kHz-regime. The gain or actuator efficiency (input power vs. flying height reduction) decreases as the flying height decreases which might be due to the so-called push-back effect or the air-bearing cooling effect, both of which will be further explained in section 7.3.1 of this dissertation.

6.5 Acknowledgement

We would like to thank Gregory Kimball of Texas Instruments, John Contreras of Hitachi Global Storage Technologies, Alexei Sacks of Seagate Technology and Tom Crittenden of Microphysics for their interest in this work and for their help with the experimental set-up.

Chapter 6, in part, is a reprint of the material as it appears in "Servo Signal Processing for Flying Height Control in Hard Disk Drives", Boettcher U., Lacey C.A., Li H., Amemiya K., de Callafon R.A., Talke F.E., *Microsystem Technologies*, 2011. The dissertation author was the primary investigator and author of this paper.

7 Dynamic flying height adjustment in hard disk drives through feedforward control

7.1 Introduction

Thermal flying height control is used in a 'static manner' in today's disk drives, i.e., the power level applied to the heater is independent of the circumferential position of the slider on the disk. The power level is adjusted only depending on the radial position of the slider on the disk, whether writing or reading operation are performed and on the environmental conditions. However, the flying height in a disk drive varies in a dynamic manner [198]. Dynamic flying height variations of a slider over a disk are composed of repeatable and non-repeatable contributions. As the name suggests, repeatable variations of flying height occur at the same angular and radial position of the slider above the disk at each revolution [198]. Thus, the question arises as to whether a thermal flying height control

slider can be used to dynamically control the repeatable flying height variations between slider and disk. It is likely that contact between slider and disk occurs at the same position on the disk as the flying height is decreased. Therefore, thermal flying height control could also be used to dynamically increase the flying height in those regions where contact occurs. This would allow a decrease in the overall flying height without slider/disk contacts.

Limited results are available on dynamically adjusting the TFC power to minimize flying height variations that occur along the circumference. One approach for dynamic flying height control has been shown by Shiramatsu et al. [210] who used a feed forward methodology without giving details on the control law that they used. An adaptive regulator scheme was proposed and simulated by Wu et al. [211] and experimental results using a piezo-electric actuator were recently given [212]. In this chapter, a different method of flying height control based on convex optimization is presented to solve the flying height variation minimization problem. Efficient solvers for those type of problems have been developed recently, which make real-time or nearly real-time applications feasible as shown in [156]. Hence, the optimal power profile to the heater element can be computed that minimizes repeatable circumferential variations of flying height. It should be noted that the computational effort of our approach is much larger compared to look-up tables that are pre-computed during manufacturing calibration. However, this study indicates how optimal profiles can be obtained and stored in look-up tables. In addition, considering the increasing complexity and computational power in micro-

controllers, one could utilize this additional degree of freedom to be able to adapt to changes in operational and/or environmental conditions.

The problem of dynamically adjusting the flying height can be divided into three main steps:

1. Measurement of flying height variation
2. Data based estimation of dynamic heater response
3. Computation of optimal input profile to the heater based on estimated model

The first task was addressed in chapter 6. Steps 2 and 3 will be discussed in detail in the following sections.

7.2 Experimental set-up

The same set-up as in chapter 6 (Fig. 6.3 on p. 149) is employed for experimental verification of dynamic flying height adjustment. The measurements were performed at a radius of 28 mm, a skew angle of 1.3 degrees and a rotational speed of 7200 rpm. The relative magnetic spacing was computed in two different ways.

First, the approach presented in chapter 6 was utilized and the flying height change Δz was computed from (Eq. 6.7 from p. 148 repeated)

$$\Delta z = \frac{\lambda_1}{16\pi} (\ln(\Phi_{A1} + \Phi_{B1}) - 3 \ln(\Phi_{A3} + \Phi_{B3})) \quad (7.1)$$

where $\Phi_{A,Bi}$ is the amplitude of the i^{th} harmonic of the A and B burst, respectively,

and λ_1 is the wavelength of the first harmonic. The same "16T" pattern from section 6.3.1 are considered in this chapter.

The second method employs the conventional triple harmonics method [200, 199] to measure the flying height change based on data written in the servo sectors. The approach resulted in a higher sampling rate compared to the servo sector measurements. For this method, the flying height change was computed as

$$\Delta z = \frac{\lambda_1}{4\pi} (\ln(\Phi_1) - \ln(\Phi_3)) \quad (7.2)$$

where Φ_1 and Φ_3 represent the first and third harmonic of the read back signal, respectively. The read back signals in the servo and data sectors were sampled at 2 GHz. The total number of 128 servo sectors corresponds to a sampling frequency of the flying height modulation of 15.36 kHz for the first method. The resolution of the data sector based method contains a trade-off between time-domain and frequency-domain accuracy. A number of 20 flying height measurements per data sector was chosen yielding an effective sampling rate of 380 kHz which is significantly higher than the sampling rate of the servo sector based method. A waveform generator was used to apply the power profile to the heater. The spindle index signal was used as a trigger.

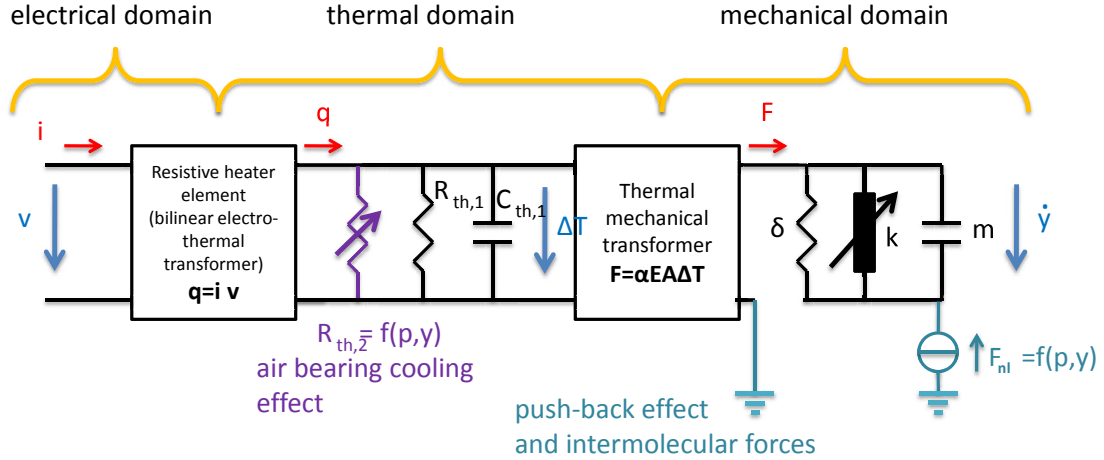


Figure 7.1: Simplified network model of the resistance heater element including non-linear effects such as air-bearing cooling effect and push-back effect

7.3 Dynamic modeling of the heater response

7.3.1 Modeling based on physical principles

To model the flying height variation induced by the thermal actuator based on physical principles is complicated and contains several interrelated effects that have been reported in the literature; a short overview is given in the following. As can be seen from Fig. 7.1, the system ranges over three physical domains, i.e., electrical, thermal and mechanical. The power applied to the heater causes a resistive heating (Joule heating) of the heater element and its surrounding materials. This, in turn, causes a thermal deformation of the air bearing surface which positions the read/write element closer to the disk as indicated in Fig. 2.18 on page 43. There are several effects that counteract the thermally induced flying height reduction:

1. Electrical domain: The resistance of the heater element changes as the tem-

perature increases which changes the Joule heating effect (Fig. 7.3)

2. Thermal domain: It was found in [208] that the main heat exchange between the head and the disk is through heat conduction. As the distance between the thermal protrusion and the disk is reduced, the conductive heat exchange between the head and disk is affected by the local air bearing pressure and the decrease in the mean free path of the air in the gap between thermal protrusion and disk. This is known as the air bearing cooling effect [213, 214].
3. Mechanical domain: A local increase in air bearing pressure causes a so-called push-back effect which is indicated in Fig.7.1 by the non-linear force F_{nl} acting on the output. Furthermore, in the close-contact regime, intermolecular and electrostatic forces will play a role as has been shown in [215].

7.3.2 Data-based modeling approach

A data-based (black-box) modeling approach seems more feasible than a model derivation based on physical principles considering the presence of numerous parameter uncertainties. A schematic of the actuator and measurement system is shown in Fig.7.2. Here, u represents the input power applied to the thermal actuator G . The flying height variation d is considered an unknown disturbance to be rejected by the thermal actuator. In the experimental set-up, the absolute spacing z is not measurable. However, the spacing variation relative to an initially

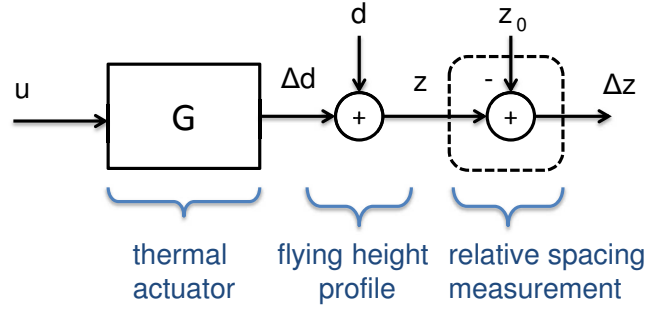


Figure 7.2: Schematic of thermal actuator and flying height sensor

unknown flying height z_0 can be measured where

$$\Delta z = z - z_0 \quad (7.3)$$

The contribution of the actuator to the flying height change can be estimated by performing two experiments: one without a dynamic input signal as a reference measurement and a second experiment using an input signal which is "persistently exciting". A good choice is a step input signal. The step data can then be used to identify a discrete-time model of the actuator using the generalized realization algorithm (GRA) as presented in [140, 143]. The algorithm has some similarities to the Hankel matrix based estimation method described in section 3.2. However, the GRA considers a step input rather than an impuls and the estimation is based on time-domain data only. The algorithm will be briefly reviewed below.

The GRA computes the state space matrices **A**, **B** and **C** of a discrete-time model of the thermal actuator, illustrated in Fig.7.2. The input/output

relationship of the heater system shown in Fig. 7.2 can be written as

$$\Delta \mathbf{D} = \mathbf{H}\mathbf{U} + \mathbf{E} \quad (7.4)$$

where $\Delta \mathbf{D}$ is a Hankel matrix of the output signals defined in (7.9), \mathbf{U} is the input matrix (upper triangular matrix with only ones) and \mathbf{H} is a Hankel matrix that contains the Markov parameters $g(k)$ that are defined by

$$g(k) = \begin{cases} \mathbf{D} & \text{for } k = 0 \\ \mathbf{C}\mathbf{A}^{k-1}\mathbf{B} & \text{for } k \geq 1 \end{cases} \quad (7.5)$$

This forms the matrix

$$\mathbf{H} = \mathbf{\Gamma}\mathbf{\Omega} \quad (7.6)$$

In (7.6), $\mathbf{\Gamma}$ and $\mathbf{\Omega}$ are the observability and controllability matrix, respectively, defined by

$$\mathbf{\Gamma} = \begin{bmatrix} \mathbf{C} \\ \mathbf{C}\mathbf{A} \\ \vdots \\ \mathbf{C}\mathbf{A}^{k-1} \end{bmatrix}, \mathbf{\Omega} = \begin{bmatrix} \mathbf{B} & \mathbf{A}\mathbf{B} & \dots & \mathbf{A}^{k-1}\mathbf{B} \end{bmatrix} \quad (7.7)$$

The matrix \mathbf{E} in (7.4) contains the effect of past input signals multiplied by the Markov parameters of the system. For a step-function as an input, \mathbf{E} is a row-wise listing of past output signals [216] and yields

$$\mathbf{E} = \begin{bmatrix} \Delta d(0) & \dots & \Delta d(0) \\ \vdots & \vdots & \vdots \\ \Delta d(N-1) & \dots & \Delta d(N-1) \end{bmatrix} \quad (7.8)$$

A realization is performed based on the weighted Hankel matrix

$$\mathbf{R} = \mathbf{\Delta D} - \mathbf{E}$$

allowing the use of step function input signals instead of impulse response measurements.

The measured step data are stored in a $N \times N$ Hankel matrix

$$\mathbf{\Delta D} = \begin{bmatrix} \Delta d(1) & \Delta d(2) & \cdots & \Delta d(N) \\ \Delta d(2) & \Delta d(3) & \cdots & \Delta d(N+1) \\ \vdots & \vdots & \vdots & \vdots \\ \Delta d(N) & \Delta d(N+1) & \cdots & \Delta d(2N-1) \end{bmatrix} \quad (7.9)$$

where N denotes the number of data points for each measurement. The vector Δd denotes the measured step response. The weighted Hankel matrix \mathbf{R} is defined as

$$\mathbf{R} = \mathbf{\Delta D} - \mathbf{E} = \mathbf{H}\mathbf{U} \quad (7.10)$$

and has the same rank as \mathbf{H} . The matrix \mathbf{R} is decomposed into an $N \times n$ matrix \mathbf{R}_1 and an $n \times N$ matrix \mathbf{R}_2 , by using singular value decomposition. This decomposition allows choosing the rank n of the matrix, and, thus, the order of the estimated model. The singular value decomposition applied to \mathbf{R} yields

$$\mathbf{R} = \mathbf{U}\mathbf{\Sigma}\mathbf{V}^T = \begin{bmatrix} U_n & U_s \end{bmatrix} \begin{bmatrix} \Sigma_n & 0 \\ 0 & \Sigma_s \end{bmatrix} \begin{bmatrix} V_n^T \\ V_s^T \end{bmatrix} \quad (7.11)$$

where \mathbf{V} and \mathbf{U} are unitary matrices, and $\mathbf{\Sigma}$ is a diagonal matrix that contains the singular values of the original matrix. In (7.11), Σ_n stores the n largest singular

values and Σ_s contains the remaining smaller part. The unitary matrices are divided in a similar fashion into $U_{n,s}$ and $V_{n,s}$, respectively. Using the singular value decomposition \mathbf{R} is reduced to a rank n matrix

$$\mathbf{R}_n = \mathbf{R}_1 \mathbf{R}_2 \quad (7.12)$$

where

$$\mathbf{R}_1 = \mathbf{U}_n \Sigma_n^{1/2}, \quad \mathbf{R}_2 = \Sigma_n^{1/2} \mathbf{V}_n^T \quad (7.13)$$

With (7.7) we have $\mathbf{R}_1 = \mathbf{\Gamma}$ and $\mathbf{R}_2 = \mathbf{\Omega} \mathbf{U}$ where \mathbf{U} has full rank. A shifted version of \mathbf{R} is defined by

$$\bar{\mathbf{R}} = \Delta \bar{\mathbf{D}} - \bar{\mathbf{E}} \quad (7.14)$$

where each element is shifted one sample forward in time. Hence, $\Delta \bar{\mathbf{D}}$ becomes

$$\Delta \bar{\mathbf{D}} = \begin{bmatrix} \Delta d(2) & \Delta d(3) & \cdots & \Delta d(N+1) \\ \Delta d(3) & \Delta d(4) & \cdots & \Delta d(N+2) \\ \vdots & \vdots & \vdots & \vdots \\ \Delta d(N+1) & \Delta d(N+2) & \cdots & \Delta d(2N) \end{bmatrix} \quad (7.15)$$

and $\bar{\mathbf{E}}$ is defined in a similar fashion.

From (7.5) and (7.7) it can be shown that

$$\bar{\mathbf{R}} = \mathbf{\Gamma} \mathbf{A} \mathbf{\Omega} \mathbf{U} = \mathbf{R}_1 \mathbf{A} \mathbf{R}_2 \quad (7.16)$$

\mathbf{R}_1 , \mathbf{R}_2 and $\bar{\mathbf{R}}$ in (7.16) are computed in previous steps. Hence, the state matrix \mathbf{A} can be estimated by

$$\mathbf{A} = \mathbf{R}_1^* \bar{\mathbf{R}} \mathbf{R}_2^* \quad (7.17)$$

where

$$\mathbf{R}_1^* = \Sigma_n^{-1/2} \mathbf{U}_n^T, \quad \mathbf{R}_2^* = \mathbf{V}_n \Sigma_n^{-1/2} \quad (7.18)$$

denote the left and right inverse of (7.13), respectively.

From (7.7) it can be observed that the input matrix \mathbf{B} is the first column of \mathbf{R}_2 and that the first row of \mathbf{R}_1 forms the output matrix \mathbf{C} .

The feed-through term \mathbf{D} contains only the first data point of the output signal after an input step, i.e., $\mathbf{D} = \Delta d(0)$. The \mathbf{D} matrix could also be estimated by solving a least-square problem but in the present case it can also be set to zero as one sample time-delay can be assumed for the thermal actuator.

7.3.3 Modeling algorithm applied to experimental data

The described modeling procedure was applied to the heater element in the TFC slider. As in chapter 6, voltage steps v were applied to the heater element and the input power P was computed using $P = v^2/R$ assuming a fixed value for the heater resistance R . This assumption is reasonable since it was found experimentally that the resistance of the heater element is not a strong function of the applied voltage. Fig. 7.3 shows the change in resistance based on different input power levels for the case that the head is flying on the disk (loaded) and the case that the head is stationary away from the disk without an air bearing present (unloaded). The unloaded case shows a much higher increase in heater resistance compared to the loaded case which is likely related to the heat transfer from the head to the disk [213]. The dynamic response to a 2V-step input for three different

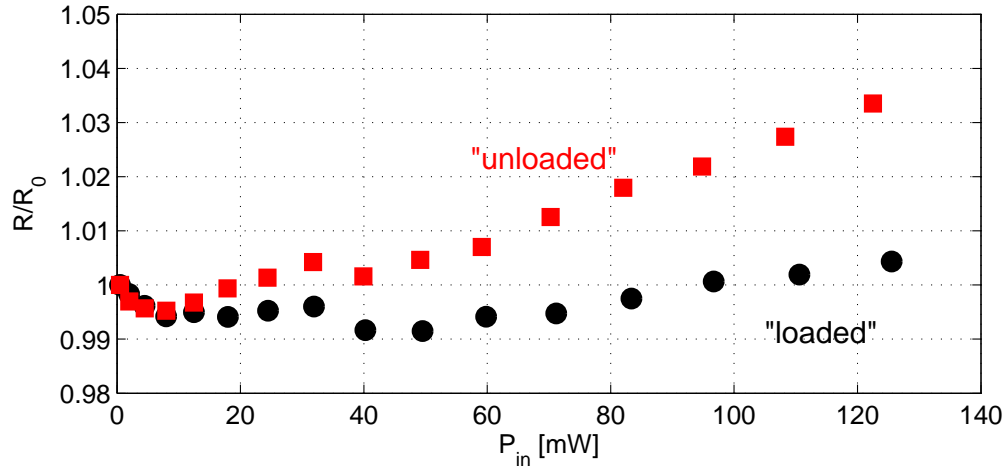


Figure 7.3: Dependence of the heater resistance on the input power level for a loaded and unloaded head

bias voltages (3.5, 4.0 and 4.5 V) is measured. The results are shown in Fig. 7.4 and Fig. 7.5, respectively. In Fig. 7.4 the flying height change is determined using the servo sector approach that was presented in chapter 6 and in Fig. 7.5 the flying height change is estimated based on data sector measurements. The simulated response using estimated 2nd order models can be seen in Fig. 7.4 and 7.5 as the solid lines. We observe that the estimated models are in excellent agreement with the measurements. By estimating only a first order model of the heater response, one would observe a significant modeling error. It is also noted that the response is in qualitative agreement with recent numerical studies [217]. The Bode plots of the resulting 2nd order continuous-time models assuming zero-order-hold for the 380 kHz sampling frequency case are shown in Fig. 7.6. One can observe the presence of two time constants in the Bode plot. The estimated second order

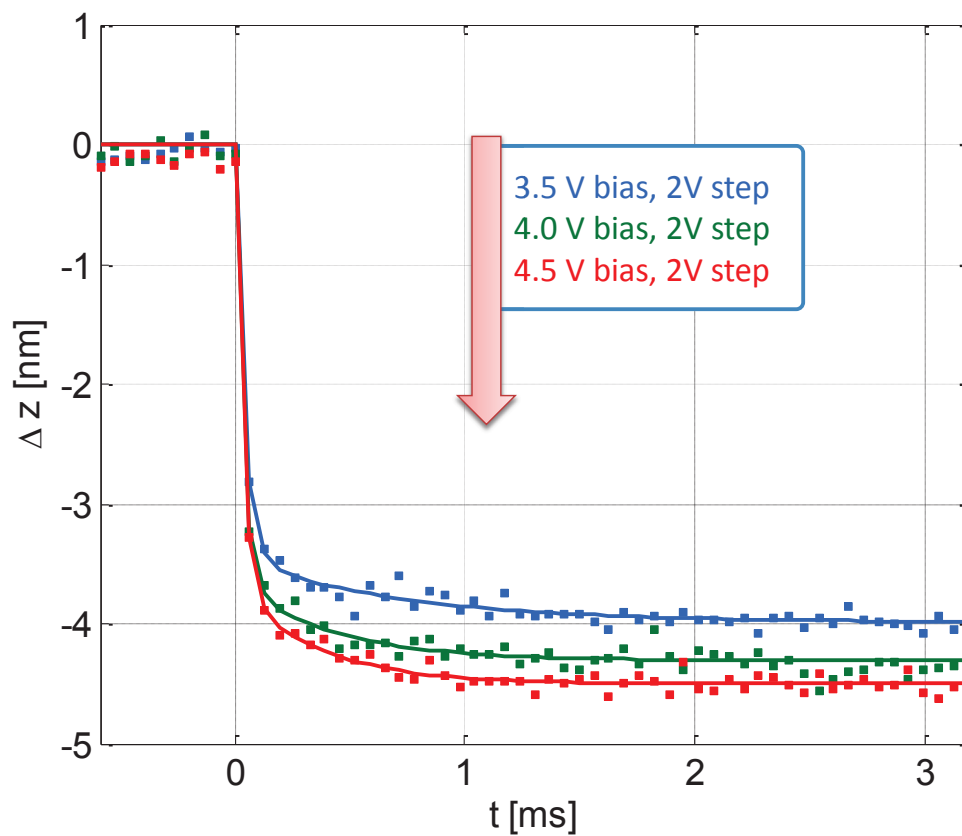


Figure 7.4: Dynamic response of the relative flying height to voltage step inputs measured using the servo sectors at a sampling rate of 15.36 kHz and estimated 2nd order model (solid lines).

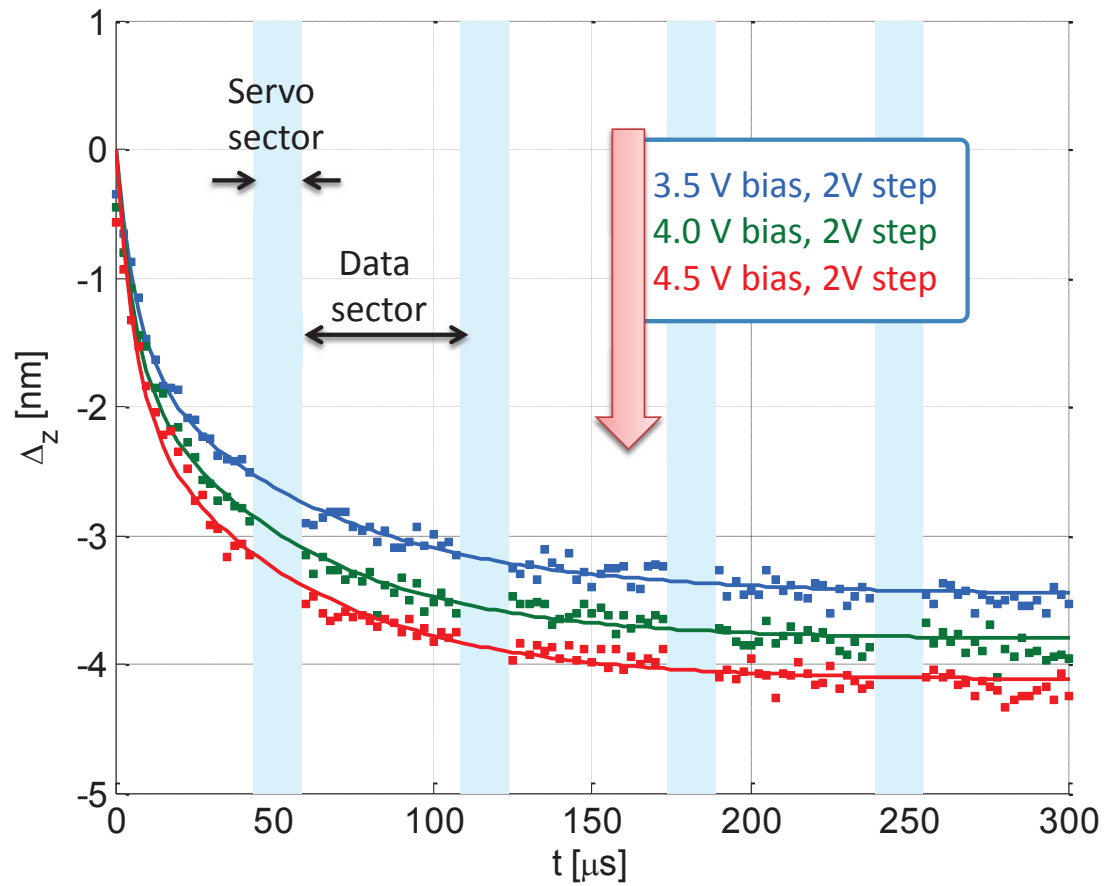


Figure 7.5: Dynamic response of the relative flying height to voltage step inputs measured using the data sectors at an effective sampling rate of 380 kHz and estimated 2nd order models (solid lines).

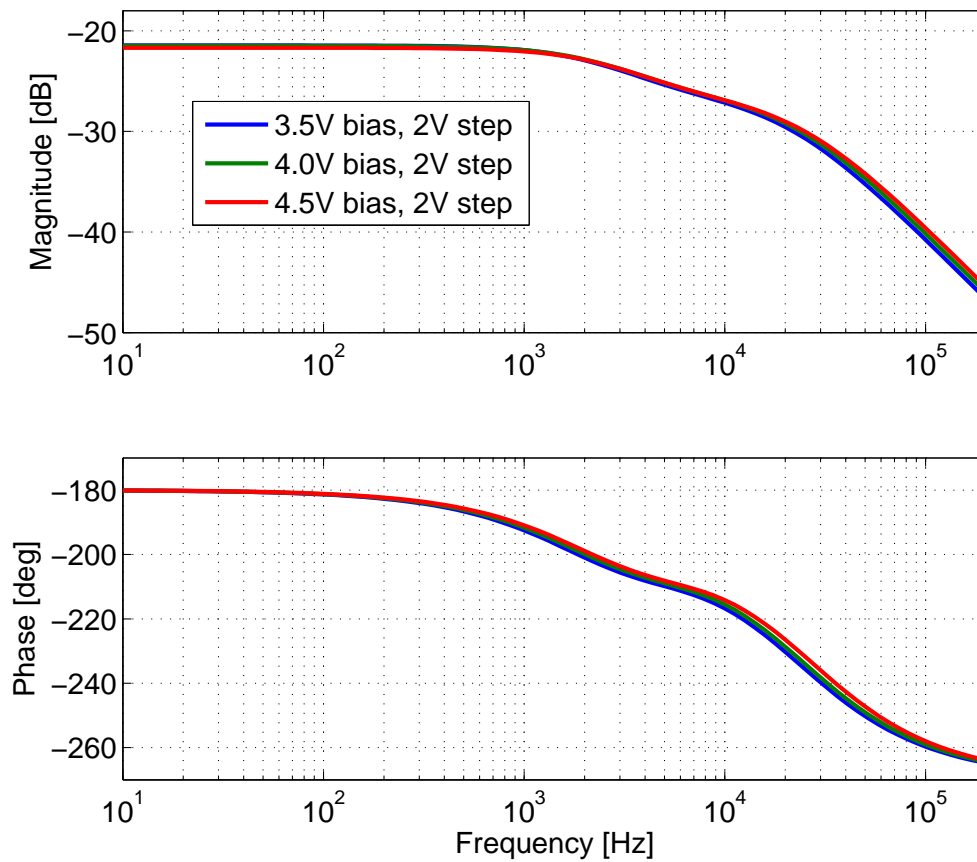


Figure 7.6: Bode response of zero-order-hold equivalent continuous-time models estimated from discrete-time models at 380 kHz.

Table 7.1: Parameter of 2nd order discrete-time models

Bias	sampling rate	a	b	c	d
3.5 V	15.35 kHz	-0.06847	0.06162	-1.108	0.1789
4.0 V	15.35 kHz	-0.07005	0.05851	-1.005	0.1277
4.5 V	15.35 kHz	-0.06536	0.05299	-0.9887	0.1266
3.5 V	380 kHz	-0.01333	0.01237	-1.674	0.6858
4.0 V	380 kHz	-0.01418	0.01311	-1.657	0.6699
4.5 V	380 kHz	-0.01499	0.01378	-1.631	0.6454

models can be parameterized in the discrete-time transfer function form

$$G(z) = \frac{az + b}{z^2 + cz + d} \quad (7.19)$$

where the model parameters a, b, c and d are given in Tab. 7.1 for the 6 identified models.

In the remainder of this chapter we consider only the flying height change measurements based on the servo sector approach since this is the more practical approach in an HDD application. The step experiments were performed approximately 3 nm below the initial flying height (without power input to the heater) after applying a bias voltage. Figure 7.7 shows the change in average flying height Δz versus heater power. We observe that the flying height decreases almost linearly as the heater power increases. In the close-contact regime, at the far right of the figure, the flying height change stops to decrease and the variance of the averaged signal increases. At this "critical" flying height, slider vibrations at the air bearing frequency near 300 kHz can be observed in the read back signal (Fig. 7.8). It should be noted that the dynamic and static behavior of the thermal actuator is inherently non-linear in extremely close proximity to the disk and highly depen-

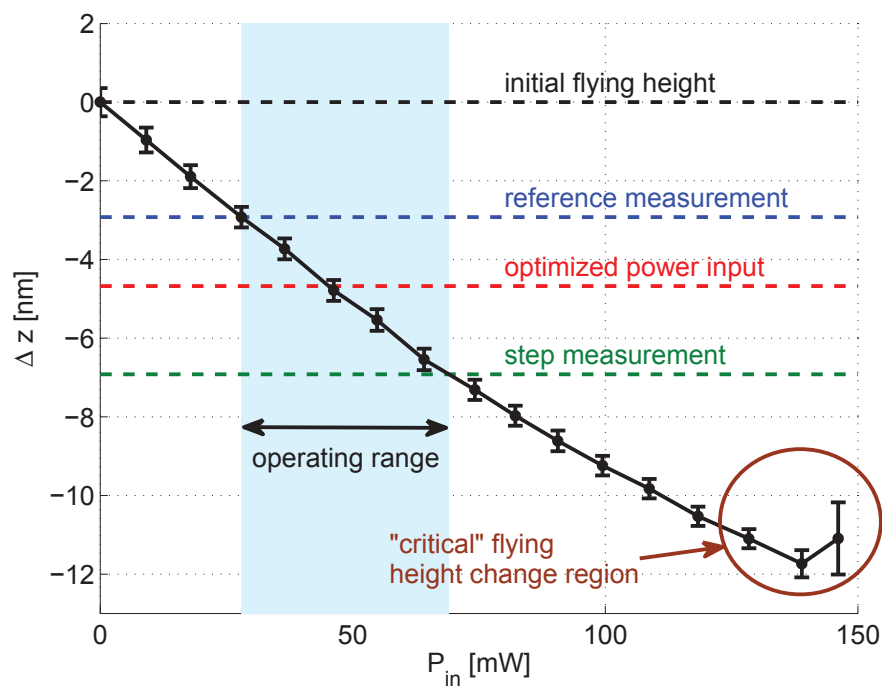


Figure 7.7: Touch down experiment showing the mean value of the flying height change over the circumference for the averaged (20 averages) flying height measurements and the variance.

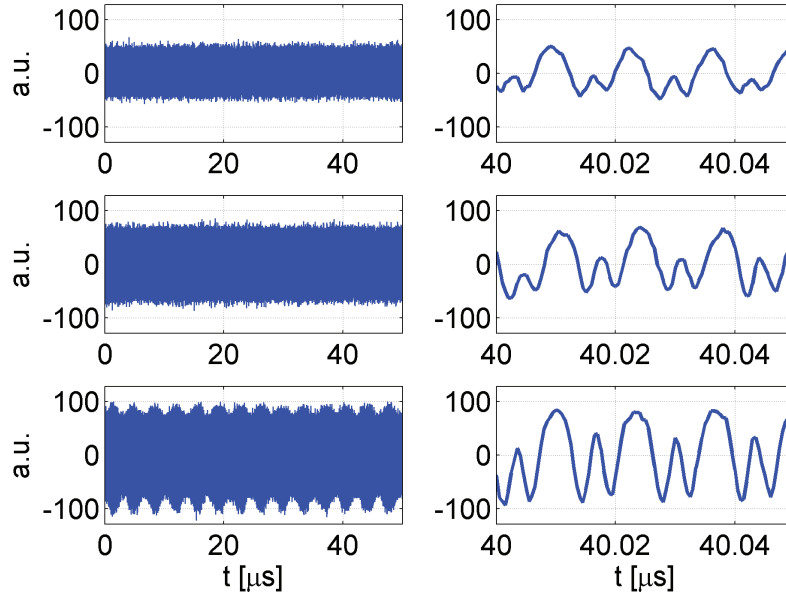


Figure 7.8: Measured read back signal of the data sector for three different flying heights: a) initial b) -8nm c) -12nm

dent on the absolute spacing of the head over the disk as indicated in section 7.3.1. Therefore, for our dynamic flying height control studies, we restrict our attention to the range depicted as "operating range" in Fig. 7.7. The initial flying height (0 mW heater input) in our experiment is around 11-12 nm and the operating range is 3 to 7 nm below the initial flying height.

In order to compute the optimal feedforward profile in the given operating range (Fig. 7.7), we estimate a dynamic model of the thermal actuator within that range. The results are shown in Fig. 7.9 where Fig. 7.9a) shows the reference input power and the step input power. The flying height change Δz (response) can be seen in Fig. 7.9b). The squares in Fig. 7.9b) represent the averaged values (20 averages) obtained at each of the 128 servo sectors and the lines in the neighbor-

hood of the squares represent the standard deviation. The flying height change due to the thermal actuator is the difference between the two flying height change measurements in Fig. 7.9b) and is shown in Fig. 7.9c). The simulated flying height change of the estimated 2nd order model is plotted in Fig. 7.9c) as well.

A plot of the singular values of the weighted Hankel matrix \mathbf{R} in (7.10) is shown in Fig. 7.10. From Fig. 7.10 it can be observed that although the second singular value is much less significant than the first one, there is considerable difference between the second and third singular value. Thus, this plot suggests the choice of a second order model.

For maximum read back performance, the operating flying height range of the read/write element should be as close as possible to the disk. The flying height in an HDD needs to be reduced to approximately 1 nm as the storage density approaches 1 Tb/in² [218]. As seen in Fig. 7.7, this introduces non-linear effects for the head gimbal assembly used in this study. These non-linear effects are beyond the scope of this paper but will be of interest for future work. Here, we restrict ourselves to show how repeatable flying height variations can be minimized for the operational range depicted in Fig. 7.7.

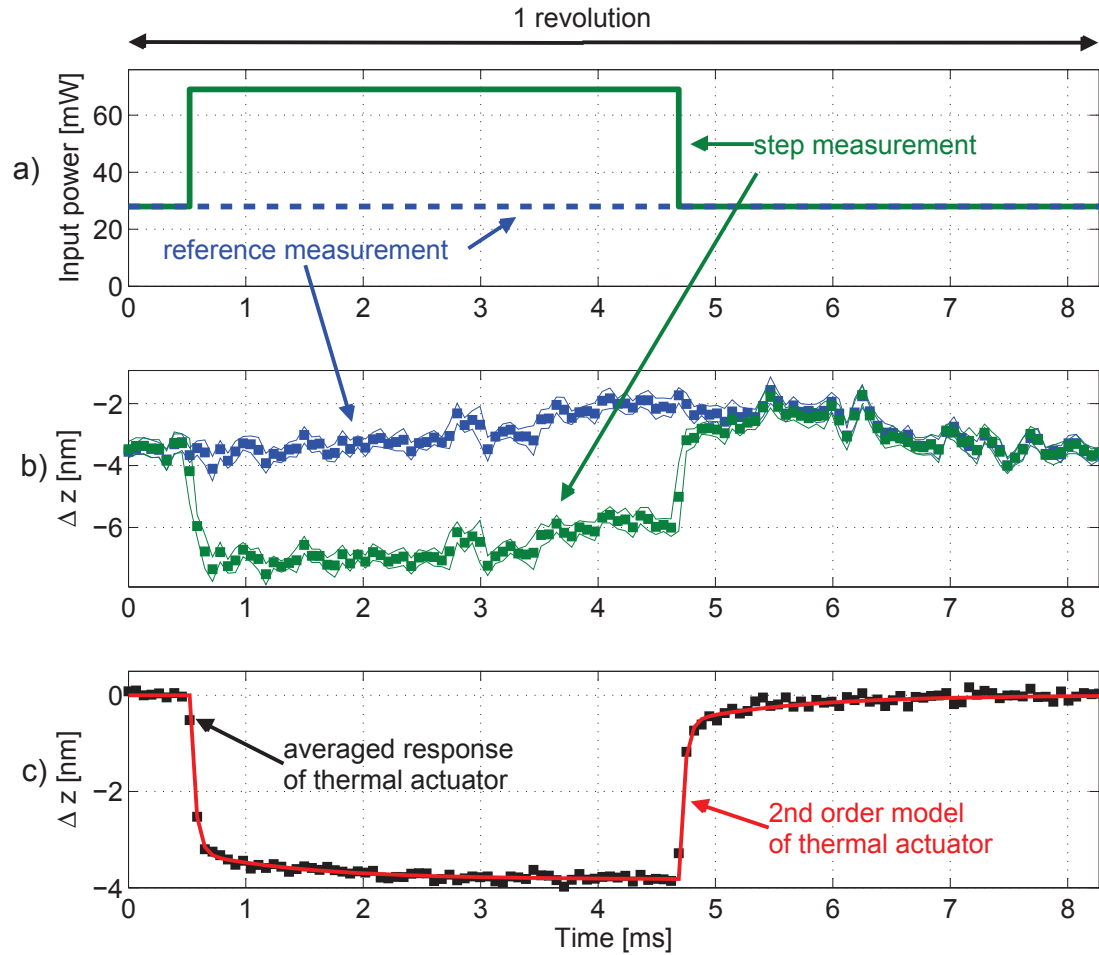


Figure 7.9: Averaged spin stand measurement (20 averages): a) power input: reference and step power. b) corresponding measured flying height variation (averaged values and standard derivation) c) identified 2nd order model and relative averaged spacing measurement

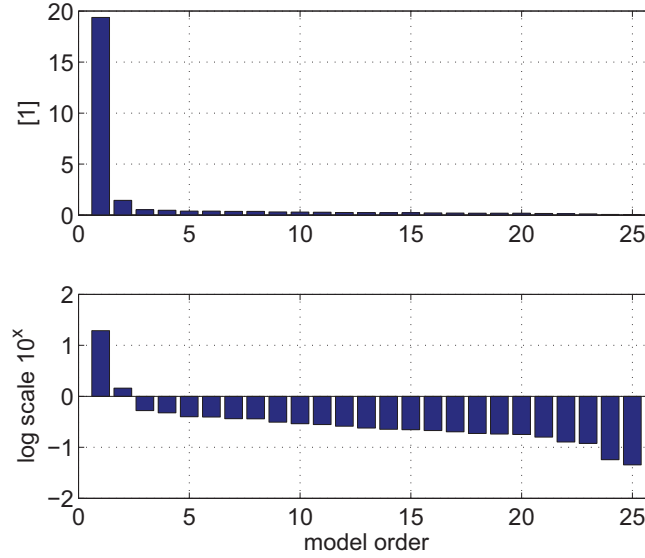


Figure 7.10: Singular values of the weighted Hankel matrix

7.4 Computing optimal power profile

7.4.1 Development of the optimization algorithm

If the flying height change generated by the thermal actuator matches the inverse of the flying height modulation, a constant flying height is obtained. The computation of the power profile based on the inverse of the flying height modulation is not trivial as the inverse of the actuator model is not necessarily stable and, in addition, non-causal. Furthermore, the fact that the control energy is limited should be taken into account. The problem at hand can be formulated as a convex optimization problem where the flying height modulation is minimized in a 2-norm sense. The direct computation of a feed forward profile makes the design of a feed

forward filter redundant.

The second order model of the identified heater actuator is written in state space form as

$$\begin{aligned} x(k+1) &= \mathbf{A}x(k) + \mathbf{B}u(k) \\ \Delta d(k) &= \mathbf{C}x(k) \end{aligned} \quad (7.20)$$

where \mathbf{A} , \mathbf{B} and \mathbf{C} follow from the identification procedure described in section 7.3.

Following [169], we can recursively re-write the actuator output Δd as

$$\begin{aligned} \Delta d(0) &= Cx(0) \\ \Delta d(1) &= CAx(0) + CBu(0) \\ \Delta d(2) &= CA^2x(0) + CABu(0) + CBu(1) \\ &\vdots \\ \Delta d(N-1) &= CA^{N-1}x(0) + \sum_{i=1}^{N-1} CA^{N-i}Bu(i-1) \end{aligned} \quad (7.21)$$

or in matrix form

$$\Delta \mathbf{d} = \Psi \mathbf{u} \quad (7.22)$$

where

$$\Psi = \begin{bmatrix} 0 & 0 & 0 & \cdots & 0 \\ CB & 0 & 0 & \cdots & 0 \\ CAB & CB & 0 & \cdots & 0 \\ \vdots & \vdots & \vdots & \ddots & \vdots \\ CA^{N-2}B & CA^{N-3}B & \cdots & 0 \\ CA^{N-1}B & CA^{N-2}B & \cdots & CB \end{bmatrix} \quad (7.23)$$

The initial value of the state $x(0)$ is set to zero. Based on this definition, the following optimization problem can be stated:

$$\begin{aligned}
 \min_{\mathbf{u}} \quad & \|\Psi\mathbf{u} + \mathbf{d} - \inf(\mathbf{d}) - \Delta z_0\|_2 \\
 \text{subject to} \quad & \mathbf{u} \leq \mathbf{u}_{\max} \\
 & \mathbf{u} \geq \mathbf{u}_{\min}
 \end{aligned} \tag{7.24}$$

The motivation to pose the optimization problem as shown in (7.24) is as follows. A flying height lower than the infimum (in this case minimum) of the flying height modulation d is desired since no negative power can be applied to the heater. An additional spacing parameter $\Delta z_0 > 0$ is required to reduce the flying height. Linear constraints on the input power u are imposed through energy and design limitations on the thermal actuator reflected by \mathbf{u}_{\max} and \mathbf{u}_{\min} . In a hard disk drive application, Δz_0 could be increased until the minimum stable flying height is reached. Minimizing the Euclidean norm as in (7.24) is equivalent to minimizing the Euclidean norm squared [170]. Thus, the problem can be reformulated as a quadratic programming problem or a semidefinite programming problem. For no or very loose constraints on the actuator signal, the problem can be reduced to a conventional non-constrained least-squares optimization problem which may be sufficient in an actual hard disk drive.

7.4.2 Optimization algorithm applied to experimental set-up

The model of the heater element estimated in section 7.3 and (7.24) was used to compute an optimized power input signal. The CVX software package [177] was used to solve the optimization problem. Δz_0 was chosen to be 0.5 nm because a bias voltage was already applied to the heater. For our experimental conditions, this yields an approximate absolute flying height of 7 – 8 nm. The measurements are shown in Fig. 7.11. We characterize the flying height variation by the difference between maximum and minimum value due to repeatable (averaged) variations (dots in Fig. 7.11b) and the variance due to non-periodic variations (solid lines in Fig. 7.11b). It is clear from Fig. 7.11 that our feedforward compensation targets the repeatable variations by minimizing the difference between maximum and minimum averaged value, creating an almost flat averaged profile of flying height variations. For comparison purposes, the dashed line in Fig. 7.11b indicates the prediction of the feedforward compensation based on our linear model. The good agreement between experiments and simulation indicates a) validation of our model and b) successful computation of the optimized feedforward profile. The variance due to non-periodic variations remains almost the same.

The measured optimized flying height profile depicted in Fig. 7.11b shows much smaller flying height variations than the reference measurement where no optimization was performed. We note, in particular, that the difference between

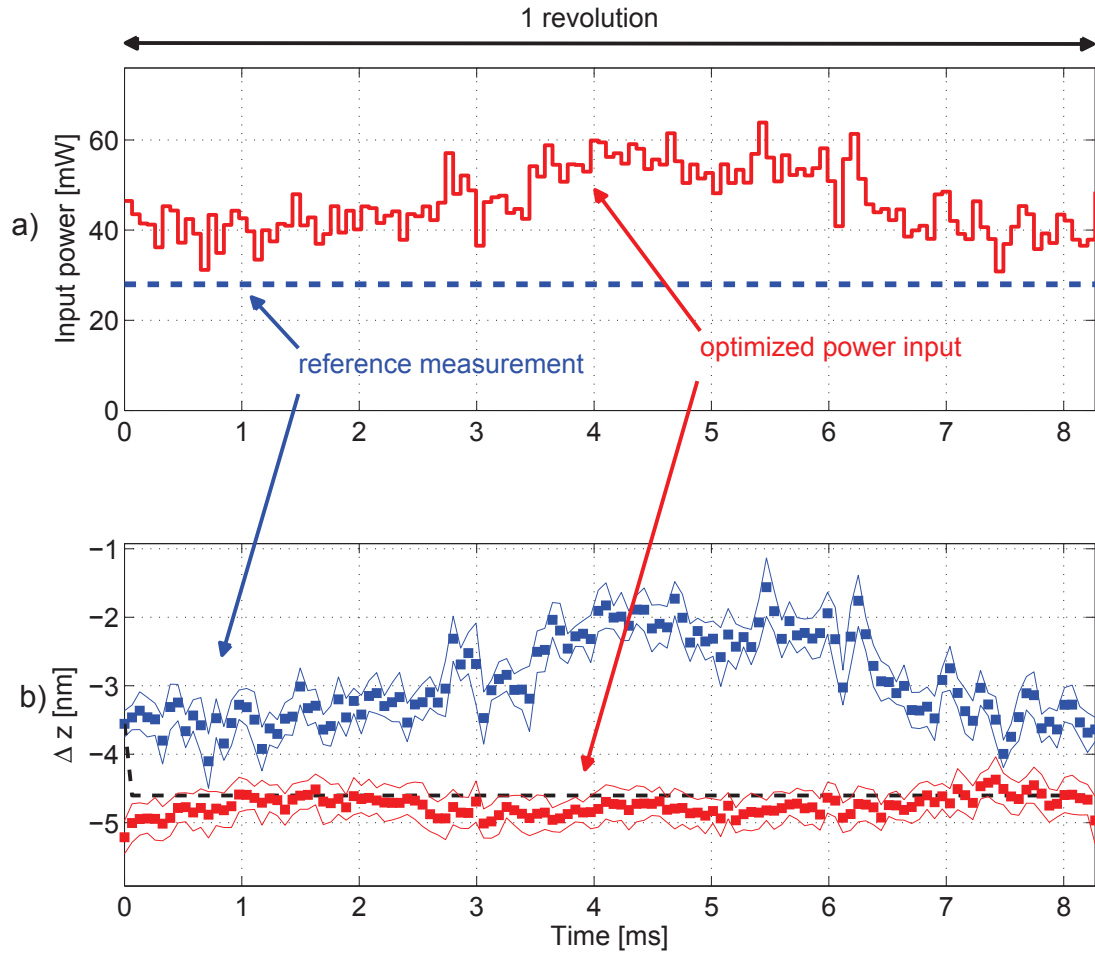


Figure 7.11: Averaged spin stand measurement (20 averages): a) power input: reference signal, optimized signal. b) corresponding measured flying height variation (averaged values and standard derivation)

maximum and minimum value is reduced from 2.54 nm to 0.84 nm. These results show that the technique used is very promising and potentially of great use in future disk drives.

7.5 Conclusions

A discrete-time dynamic model of a thermal flying height actuator in a hard disk drive was identified using step experiments and a generalized realization algorithm. The flying height change measurements used in this study were based on two different measurement techniques with sampling rates of 15.36 kHz and 380 kHz, respectively. It was found that the heater response can be modeled sufficiently well with a second order model that captures both a fast and a slow time constant observed in the heater step response. The resistance change of the thermal actuator was measured as a function of the input power and found to be within a few percent of the case of a flying slider (loaded). It was shown that convex optimization techniques can be used to significantly minimize circumferential flying height variations in a disk drive based on the identified heater actuator model. Spin stand experiments showed that the maximum-minimum value difference of the averaged flying height variations was reduced to about one third compared to the initial reference measurement where no power optimization was performed. Since the proposed method is a true feed forward technique it can only compensate repeatable flying height variations. Both the simulated step response and

the simulated response to the optimized input signal are in good agreement with experimentally obtained results. Small variations can be explained with modeling and measurement errors. The presented algorithms on heater dynamics modeling and input power optimization are not computationally expensive and could be implemented in the firmware of the hard disk drive. This might enable an increase in durability and reliability of the drive while decreasing flying height and bit error rate. The identified linear model of the heater becomes invalid in the close-contact regime due to non-linearities. Future work should involve non-linear modeling approaches and adaptive feed forward approaches to minimize the flying height while maintaining a minimum in flying height variations. A final point is related to the response time of the thermal actuator. Even though thermal equilibrium is only reached after a few milliseconds, the second (fast) time constant of the thermal actuator enables flying height adjustment up to several kHz.

Acknowledgment

The authors would like to thank Tom Crittenden and Christopher Lacey of Microphysics, Inc., Gregory Kimball of Texas Instruments and John Contreras of Hitachi Global Storage Technologies, Ltd. for their help with the experimental set-up.

Chapter 7, in part, is a reprint of the material as it appears in "Dynamic Flying Height Adjustment in Hard Disk Drives through Feedforward Control",

Boettcher U., Li H., de Callafon R.A., Talke F.E., *IEEE, Transactions on Magnetics*, 2011. The dissertation author was the primary investigator and author of this paper.

8 Summary

In this dissertation, the optimization of positioning the read/write element over the data track in a hard disk drive was studied. The first focus was on increasing the performance of the track-following servo mechanism using dual-stage actuators. A state-of-the-art dual-stage hard drive was modified to allow open loop frequency response function measurements of the voice coil motor and the piezo-based micro-actuator. A discrete-time modeling algorithm based on frequency response function measurements was proposed that allowed control relevant system identification. Based on the estimated models, two different dual-stage track-following controllers were designed. One was derived using classic loop shaping techniques, the so-called sensitivity decoupling method. The second method utilized modern H_∞ loop shaping algorithms. Both controllers showed similar servo performance. However, the H_∞ controller shows a better disturbance rejection than the sensitivity decoupling controller for low frequencies. The H_∞ approach does not use notch filters, and, thus, is more robust against model variations. The H_∞ optimization routine is constrained by pre-defined parameters in form of weighting functions. Hence, the choice of this weighting function is crucial to controller performance.

The clear advantage of the H_∞ framework is that automated controller design can be performed.

Furthermore, a track-seeking scheme was proposed that is based on convex optimization techniques. The reference signal of the servo loop is shaped to obtain time-optimal performance and/or to optimize the energy properties of the closed-loop signals. The algorithm was experimentally verified in a modified hard disk drive set-up showing excellent agreement between theoretical (simulation) and actual experimental results. It was shown that the reference signal shaping significantly reduces targeting time and residual vibrations compared to an output response obtained using step inputs. It was also shown that the shaping algorithm improves the response of systems whether or not the actuator is saturated. Above and beyond all other consideration, the shaping algorithm is applicable to any linear time-invariant system with an arbitrary number of inputs and outputs.

The second focus of this dissertation is on dynamic flying height control. We first studied the effect of cross-track and vertical motion of the read element on the readback signal. A straightforward mathematical model for the read signal was derived. We compute the magnetic field of a contributing bit directly instead of modeling the bit transition (derivative) of the magnetization in the read back signal. This allows a very fast simulation without compromising accuracy. The model is applicable to continuous and bit patterned media and allows also the investigation of read signals of pattern that only consist of "up" or "down" magnetized bits such as some novel servo pattern that were proposed for patterned

recording.

Furthermore, a flying height measurement scheme based on the servo pattern was developed and simulated using the derived readback signal model. The flying height measurement method shows very small sensitivity to cross-track motion of the read write head. In the proposed method, the off-track sensitivity is a function of the radial servo burst spacing, i.e., the cross-track spacing between the A and B burst in each servo sector. The estimation scheme was tested experimentally on a spin stand to identify the dynamics of a resistance heater element capable of modifying the flying height at the read/write element. It was found that the gain or actuator efficiency (input power vs. flying height reduction) decreases as the flying height decreases which might be due to the push-back effect or the air-bearing cooling effect.

In the final part of this dissertation we estimated a discrete-time dynamic model of a thermal flying height actuator using step excitation and a generalized realization algorithm. The flying height change was measured using two different techniques with sampling rates of 15.36 kHz and 380 kHz, respectively. It was found that the heater response can be modeled sufficiently well with a second order model that captures both a fast and a slow time constant observed in the heater step response. The resistance change of the thermal actuator was measured as a function of the input power and found to be within a few percent of the case of a flying slider (loaded); therefore, it was neglected in the algorithm. It was shown that convex optimization techniques can be used to significantly minimize circumferen-

tial flying height variations in a disk drive based on the identified heater actuator model. Spin stand experiments showed that the maximum-minimum value difference of the flying height variation was reduced to about one third compared to the initial reference measurement where no power optimization was performed. Since the proposed method is a true feed forward technique it can only compensate repeatable flying height variations. The prediction is in good agreement with experimental results. Even though thermal equilibrium is only reached after a few milliseconds, the second (fast) time-constant of the thermal actuator enables flying height adjustment up to several kHz.

All presented algorithms on dynamic modeling, convex optimization and computation of optimal feedforward signals throughout this dissertation are computational inexpensive and could be implemented in the firmware of a hard disk drive. This might significantly reduce seek-time, energy consumption and system vibrations during the seeking process. In addition, it might enable an increase in durability and reliability and reduce bit errors rates due to reduced flying height variations. Such advanced high-precision positioning methods are required in future hard disk drive servo mechanisms as the storage density increases. Both the vertical and cross-track direction need to be considered.

In conclusion, hard disk drives are extraordinary multi-disciplinary products that deliver high-end technology at low cost. It is particularly astonishing that a device that relies on moving parts has been able to keep up with alternative solid-state technology for such a long time. The growing demand in storage space will

enable hard drives to keep their number one position in terms of storage capacity market share for years to come. The continuing decrease in bit aspect ratio and increase in track density imposes unprecedented challenges on servo performance in vertical and cross-track direction which encourages academic research on this topic.

Bibliography

- [1] Paul Rincon. Earliest writing found in china. *BBC Science*, 2003. [Online; accessed 17-January-2011]. Available from: <http://news.bbc.co.uk/2/hi/science/nature/2956925.stm>.
- [2] W.J. Duiker and J.J. Spielvogel. *The Essential World History*. Cengage Learning, 2010.
- [3] John R. Rachal. Gutenberg, literacy, and the ancient arts of memory. *Adult Education Quarterly*, 38(3):125–135, 1988. doi:10.1177/0001848188038003001.
- [4] Wikimedia commons. Available from: <http://commons.wikimedia.org>.
- [5] R. Hirsch. *Printing, selling and reading 1450-1550*. Otto Harrassovitz, Wiesbaden, 1967.
- [6] E.L. Eisenstein. Some conjectures about the impact of printing on western society and thought: A preliminary report. *Journal of Modern History*, 40:1–56, 1968.
- [7] Steven Shapin. *The scientific revolution*. The University of Chicago Press, 1996.
- [8] Robert Hirsch. *Seizing the light: a history of photography*. McGraw-Hill, 2000.
- [9] Thomas A. Edison. Us patent number: 227679. 1880.
- [10] L. Heide. *Punched-card systems and the early information explosion, 1880-1945*. Studies in industry and society. Johns Hopkins University Press, 2009.
- [11] Oberlin Smith. Some possible forms of phonograph. *The Electrical World*, 12:116–117, 1888.
- [12] Valdemar Poulsen. Us patent number: 822222. 1899.

- [13] Mark Clark and Henry Nielsen. Crossed wires and missing connections: Valdemar poulsen, the american telegraphone company, and the failure to commercialize magnetic recording. *The Business History Review*, 69(1):pp. 1–41, 1995.
- [14] Robert von Lieben. Us patent number: 1169082. 1912.
- [15] E.D. Daniel, C.D. Mee, and M.H. Clark. *Magnetic recording: the first 100 years*. IEEE Press, 1999.
- [16] Wikipedia. Univac 1 — wikipedia, the free encyclopedia. 2011. [Online; accessed 17-January-2011]. Available from: http://en.wikipedia.org/w/index.php?title=UNIVAC_I&oldid=405752177.
- [17] Ibm 726 - magnetic tape reader/recorder. IBM Archive [Online; accessed 17-January-2011]. Available from: http://www-03.ibm.com/ibm/history/exhibits/701/701_1415bx26.html.
- [18] Computer History Museum. [Online; accessed 17-January-2011]. Available from: <http://www.computerhistory.org/timeline/?year=1952>.
- [19] E. R. Childers, W. Imaino, J. H. Eaton, G. A. Jaquette, P. V. Koeppe, and D. J. Hellman. Six orders of magnitude in linear tape technology: The one-terabyte project. *IBM Journal of Research and Development*, 47(4):471–482, 2003. doi:10.1147/rd.474.0471.
- [20] R.C. Barrett, E.H. Klaassen, T.R. Albrecht, G.A. Jaquette, and J.H. Eaton. Timing-based track-following servo for linear tape systems. *Magnetics, IEEE Transactions on*, 34(4):1872–1877, July 1998. doi:10.1109/20.706730.
- [21] G. Cherubini, R. D. Cideciyan, L. Dellmann, E. Eleftheriou, W. Haeberle, J. Jelitto, V. Kartik, M. A. Lantz, S. Olcer, A. Pantazi, H. E. Rothuizen, D. Berman, W. Imaino, P.-O. Jubert, G. McClelland, P. V. Koeppe, K. Tsuruta, T. Harasawa, Y. Murata, A. Musha, H. Noguchi, H. Ohtsu, O. Shimizu, and R. Suzuki. 29.5- gb/in² recording areal density on barium ferrite tape. *Magnetics, IEEE Transactions on*, 47(1):137–147, 2011. doi:10.1109/TMAG.2010.2076797.
- [22] D. J. Hellman, R. Yardy, and P. E. Abbott. Innovations in tape storage automation at ibm. *IBM Journal of Research and Development*, 47(4):445–452, 2003. doi:10.1147/rd.474.0445.
- [23] Yu Junjie, Zhou Changhe, Wang Wei, and Jia Wei. Red-light high density optical pickup employing annular binary phase filter. In *Lasers Electro Optics The Pacific Rim Conference on Lasers and Electro-Optics, 2009. CLEO/PACIFIC RIM '09. Conference on*, pages 1–2, 2009. doi:10.1109/CLEOPR.2009.5292281.

- [24] Matteo Meneghini, Nicola Trivellin, Kenji Orita, Masaaki Yuri, Tsuyoshi Tanaka, Daisuke Ueda, Enrico Zanoni, and Gaudenzio Meneghesso. Reliability evaluation for blu-ray laser diodes. *Microelectronics Reliability*, 50(4):467 – 470, 2010. International Symposium on Reliability of Optoelectronics for Space / Advances in Wafer Level Packaging. doi:10.1016/j.microrel.2010.01.034.
- [25] Simona Boboila and Peter Desnoyers. Write endurance in flash drives: measurements and analysis. In *Proceedings of the 8th USENIX conference on File and storage technologies*, FAST’10, pages 9–9, Berkeley, CA, USA, 2010. USENIX Association.
- [26] Magnetic ram. [Online; accessed 5-March-2011]. Available from: http://www.pctechguide.com/14Memory_Magnetic_RAM.htm.
- [27] Johan Akerman. Toward a Universal Memory. *Science*, 308(5721):508–510, 2005. doi:10.1126/science.1110549.
- [28] S. Raoux, G. W. Burr, M. J. Breitwisch, C. T. Rettner, Y.-C. Chen, R. M. Shelby, M. Salinga, D. Krebs, S.-H. Chen, H.-L. Lung, and C. H. Lam. Phase-change random access memory: A scalable technology. *IBM Journal of Research and Development*, 52(4.5):465 –479, 2008. doi:10.1147/rd.524.0465.
- [29] M.H. Kryder and Chang Soo Kim. After hard drives: What comes next? *Magnetics, IEEE Transactions on*, 45(10):3406 –3413, 2009. doi:10.1109/TMAG.2009.2024163.
- [30] The digital universe. *International Data Corporation*, 2007. [Online; accessed 21-January-2011]. Available from: <http://www.emc.com/collateral/analyst-reports/diverse-exploding-digital-universe.pdf>.
- [31] John Gantz and David Reinsel. The digital universe decade are you ready? *International Data Corporation*, 2010. [Online; accessed 23-January-2011]. Available from: <http://idcdocserv.com/925>.
- [32] T.M. Coughlin. Virtualization of consumer storage. In *Consumer Electronics (ISCE), 2010 IEEE 14th International Symposium on*, pages 1 –4, 2010. doi:10.1109/ISCE.2010.5523736.
- [33] John Rydning. Worldwide hard disk drive 2010-2014 forecast: Sowing seeds of change for enterprise applications. *International Data Corporation*, 2010.
- [34] Home and portable - total consumer storage usage: Optical disc, hard drive, and flash. *Coughlin Associates - Digital Storage in Consumer Electronics*, 2008.

- [35] R. Wood. The feasibility of magnetic recording at 1 terabit per square inch. *Magnetics, IEEE Transactions on*, 36(1):36–42, 2000. doi:10.1109/20.824422.
- [36] Harold Hamilton. Status report: perpendicular contact recording on rigid media. *Journal of the Magnetic Society of Japan*, 18(S1):171–178, 1994.
- [37] Toshiba leads industry in bringing perpendicular data recording to hdd-sets new record for storage capacity with two new hdds. [Online; accessed 21-January-2011], 2004. Available from: http://www.toshiba.co.jp/about/press/2004_12/pr1401.htm.
- [38] A. S. Hoagland. High-resolution magnetic recording structures. *IBM Journal of Research and Development*, 2(2):90–104, 1958. doi:10.1147/rd.22.0090.
- [39] S. Iwasaki and Y. Nakamura. An analysis for the magnetization mode for high density magnetic recording. *Magnetics, IEEE Transactions on*, 13(5):1272–1277, September 1977. doi:10.1109/TMAG.1977.1059695.
- [40] R.H. Victora, Jianhua Xue, and M. Patwari. Areal density limits for perpendicular magnetic recording. *Magnetics, IEEE Transactions on*, 38(5):1886–1891, September 2002. doi:10.1109/TMAG.2002.802791.
- [41] M. Mallery, A. Torabi, and M. Benakli. One terabit per square inch perpendicular recording conceptual design. *Magnetics, IEEE Transactions on*, 38(4):1719–1724, July 2002. doi:10.1109/TMAG.2002.1017762.
- [42] Dmitri Litvinov, Mark H. Kryder, and Sakhrat Khizroev. Recording physics of perpendicular media: soft underlayers. *Journal of Magnetism and Magnetic Materials*, 232(1-2):84–90, 2001. doi:10.1016/S0304-8853(01)00216-5.
- [43] Thin film recording head copper coil. IBM Archive [Online; accessed 26-January-2011]. Available from: http://www-03.ibm.com/ibm/history/exhibits/storage/storage_PH12-60.html.
- [44] Jim Fitch. Interview with luminary professor h. peter jost - the man who gave birth to the word "tribology". *Machinery Lubrication*, 2006. [Online; accessed 30-March-2011]. Available from: <http://www.machinerylubrication.com/Read/834/tribology-jost>.
- [45] K. Miyoshi and Y. Chung. *Surface diagnostics in tribology: fundamental principles and applications*. Series in modern tribology. World Scientific, 1993.

- [46] Sung-Chang Lee and Andreas A. Polycarpou. Effect of hard-disk drive spindle motor vibration on dynamic microwaviness and flying-height modulation. *Tribology International*, 38(6-7):665 – 674, 2005. Tribology of Information Storage Devices, TISD 2003. doi:10.1016/j.triboint.2005.01.002.
- [47] Maik Duwensee. Numerical and experimental investigations of the head/disk interface. *Dissertation, University of California, San Diego*, 2007.
- [48] Eric M. Jayson, J. Murphy, P. W. Smith, and Frank E. Talke. Effects of air bearing stiffness on a hard disk drive subject to shock and vibration. *Journal of Tribology*, 125(2):343–349, 2003. doi:10.1115/1.1509770.
- [49] Sha Lu, Yong Hu, M. O’Hara, D.B. Bogy, C. Singh Bhatia, and Yiao-Tee Hsia. Air bearing design, optimization, stability analysis and verification for sub-25 nm flying. *Magnetics, IEEE Transactions on*, 32(1):103 –109, January 1996. doi:10.1109/20.477558.
- [50] B.H. Thornton and D.B. Bogy. Head-disk interface dynamic instability due to intermolecular forces. *Magnetics, IEEE Transactions on*, 39(5):2420 – 2422, 2003. doi:10.1109/TMAG.2003.816424.
- [51] Bo Liu, Jin Liu, and Tow-Chong Chong. Slider design for sub-3-nm flying height head-disk systems. *Journal of Magnetism and Magnetic Materials*, 287:339 – 345, 2005. Selected papers from the seventh Perpendicular Magnetic Recording Conference (PMRC 2004). doi:10.1016/j.jmmm.2004.10.055.
- [52] Q. H. Zeng and D. B. Bogy. Numerical simulation of shock response of disk-suspension-slider air bearing systems in hard disk drives. *Microsystem Technologies*, 8:289–296, 2002. 10.1007/s00542-002-0186-6. Available from: <http://dx.doi.org/10.1007/s00542-002-0186-6>.
- [53] John Best, Sandy Bolasna, Lee Dorius, Yasuhiro Iihara, John Kotla, Tsuyoshi Matsumoto, Randy Simmons, Atsushi Tobari, and Hiroyasu Tsuchida. The femto slider in hitachi hard disk drives. *Hitachi Global Storage Technologies White Paper*, 2007.
- [54] A.A. Mamun, G. Guo, and C. Bi. *Hard disk drive: mechatronics and control*. Automation and control engineering. CRC Press, 2007.
- [55] Lee Dorius, S. Bolasna, J. Kotla, R. Simmons, Y. Iihara, T. Matsumoto, A. Tobari, and H. Tsuchida. Introduction of femto slider in mobile disk drives. *Magnetics, IEEE Transactions on*, 40(1):349 – 352, 2004. doi:10.1109/TMAG.2003.821153.

- [56] Seyhan Karakulak. From channel modeling to signal processing for bit patterned media recording. *Ph.D. dissertation, University of California, San Diego*, 2010.
- [57] Martin Hassner and Ed Grochowski. 4k byte-sector hdd-data format standard. *online available at www.idema.org.*, 2011. [Online; accessed 17-January-2011].
- [58] D.J.C. MacKay and R.M. Neal. Near shannon limit performance of low density parity check codes. *Electronics Letters*, 33(6):457–458, March 1997. doi:10.1049/el:19970362.
- [59] J.S. Chitode. *Digital Communication*. Technical Publications, 2009.
- [60] R. Wood, M. Williams, A. Kavcic, and J. Miles. The feasibility of magnetic recording at 10 terabits per square inch on conventional media. *Magnetics, IEEE Transactions on*, 45(2):917–923, 2009. doi:10.1109/TMAG.2008.2010676.
- [61] T. F. Ying, C. M. Chen, C. P. Liao, M. D. Wu, and D. R. Huang. An efficient design to reduce the flux leakage of a spindle motor. *Journal of Applied Physics*, 79(8):5557–5559, April 1996. doi:10.1063/1.362241.
- [62] G. Bouchard and F. Talke. Non-repeatable flutter of magnetic recording disks. *IEEE Transactions on Magnetics*, 22:1019–1021, September 1986. doi:10.1109/TMAG.1986.1064437.
- [63] Walker C. Blount. Fluid dynamic bearing spindle motors: Their future in hard disk drives. *Hitachi Global Storage Technologies White Paper*, 2007.
- [64] Shigeki Mori, Takayuki Hoshino, Hirohiko Tada, Goro Obinata, and Kazuhiro Ouchi. Linear actuator for precise track following. *Microsystem Technologies*, 11:718–727, 2005. doi:10.1007/s00542-005-0551-3.
- [65] G.F. Franklin, J.D. Powell, and M.L. Workman. *Digital control of dynamic systems*. Addison-Wesley world student series. Addison-Wesley, 1998.
- [66] Chunling Du, Lihua Xie, and Jingliang Zhang. Compensation of vcm actuator pivot friction based on an operator modeling method. *Control Systems Technology, IEEE Transactions on*, 18(4):918–926, 2010. doi:10.1109/TCST.2009.2027430.
- [67] Mike Suk Patricia Kim. Ramp load/unload technology in hard disk drives. *Hitachi Global Storage Technologies White Paper*, 2007.

- [68] K. Mori, T. Munemoto, H. Otsuki, Y. Yamaguchi, and K. Akagi. A dual-stage magnetic disk drive actuator using a piezoelectric device for a high track density. *Magnetics, IEEE Transactions on*, 27(6):5298 –5300, November 1991. doi:10.1109/20.278818.
- [69] Chin Kwan Thum, Chunling Du, Jingliang Zhang, Kim Piew Tan, B.M. Chen, and Eng Hong Ong. Servo control design for a high tpi servo track writer with microactuators. *Magnetics, IEEE Transactions on*, 44(9):2227 –2234, 2008. doi:10.1109/TMAG.2008.2000507.
- [70] Chee Pang, Daowei Wu, Guoxiao Guo, Tow Chong, and Youyi Wang. Suppressing sensitivity hump in hdd dual-stage servo systems. *Microsystem Technologies*, 11:653–662, 2005. 10.1007/s00542-005-0535-3. Available from: <http://dx.doi.org/10.1007/s00542-005-0535-3>.
- [71] Nitin Afzulpurkar and Yossawee Weerakamhaeng. Precision positioning using mems based microactuator. *Mechatronics*, 12(9-10):1213 – 1223, 2002. doi:10.1016/S0957-4158(02)00025-9.
- [72] Roberto Horowitz, Yunfeng Li, Kenn Oldham, Stanley Kon, and Xinghui Huang. Dual-stage servo systems and vibration compensation in computer hard disk drives. *Control Engineering Practice*, 15(3):291 – 305, 2007. Selected Papers Presented at the Third IFAC Symposium on Mechatronic Systems (2004), Third IFAC Symposium on Mechatronic Systems. doi:10.1016/j.conengprac.2006.09.003.
- [73] Xinghui Huang, Roberto Horowitz, and Yunfeng Li. Track-following control with active vibration damping and compensation of a dual-stage servo system. *Microsyst. Technol.*, 11:1276–1286, November 2005. doi:10.1007/s00542-005-0594-5.
- [74] T. Hirano, Long-Sheng Fan, Wen Y. Lee, J. Hong, W. Imaino, S. Patanaik, S. Chan, P. Webb, R. Horowitz, S. Aggarwal, and D.A. Horsley. High-bandwidth high-accuracy rotary microactuators for magnetic hard disk drive tracking servos. *Mechatronics, IEEE/ASME Transactions on*, 3(3):156 –165, September 1998. doi:10.1109/3516.712111.
- [75] Long-Sheng Fan, H.H. Ottesen, T.C. Reiley, and R.W. Wood. Magnetic recording-head positioning at very high track densities using a microactuator-based, two-stage servo system. *Industrial Electronics, IEEE Transactions on*, 42(3):222 –233, June 1995. doi:10.1109/41.382132.
- [76] D.A. Horsley, N. Wongkomet, R. Horowitz, and A.P. Pisano. Precision positioning using a microfabricated electrostatic actuator. *Magnetics, IEEE Transactions on*, 35(2):993 –999, March 1999. doi:10.1109/20.753822.

- [77] T. Semba, T. Hirano, J. Hong, and L.-S. Fan. Dual-stage servo controller for hdd using mems microactuator. *Magnetics, IEEE Transactions on*, 35(5):2271–2273, September 1999. doi:10.1109/20.800796.
- [78] Chung Choo Chung, Chin Won Seo, and Seung-Hi Lee. Two degree-of-freedom dual-stage actuator controller design for hard disk drives. *Magnetics, IEEE Transactions on*, 36(5):2255–2257, September 2000. doi:10.1109/20.908384.
- [79] Yunfeng Li, Federico Marcassa, Roberto Horowitz, Roberto Oboe, and Robert Evans. Track-following control with active vibration damping of a pzt-actuated suspension dual-stage servo system. *Journal of Dynamic Systems, Measurement, and Control*, 128(3):568–576, 2006. doi:10.1115/1.2229257.
- [80] S. Nakamura, H. Numasato, K. Sato, M. Kobayashi, and I. Naniwa. A pushpull multi-layered piggyback pzt actuator. *Microsystem Technologies*, 8:149–154, 2002. doi:10.1007/s00542-002-0180-z.
- [81] R.B. Evans, J.S. Griesbach, and W.C. Messner. Piezoelectric microactuator for dual stage control. *Magnetics, IEEE Transactions on*, 35(2):977–982, March 1999. doi:10.1109/20.753819.
- [82] H.H. Gatzen, P. Freitas, E. Obermeier, and J. Robertson. A slider with an integrated microactuator (slim) for second stage actuation in hard disc drives. *Magnetics, IEEE Transactions on*, 44(11):3726–3729, 2008. doi:10.1109/TMAG.2008.2002592.
- [83] S. Devasia, E. Eleftheriou, and S.O.R. Moheimani. A survey of control issues in nanopositioning. *Control Systems Technology, IEEE Transactions on*, 15(5):802–823, 2007. doi:10.1109/TCST.2007.903345.
- [84] Chee Khiang Pang, F.L. Lewis, S.S. Ge, Guoxiao Guo, B.M. Chen, and Tong Heng Lee. Singular perturbation control for vibration rejection in hdds using the pzt active suspension as fast subsystem observer. *Industrial Electronics, IEEE Transactions on*, 54(3):1375–1386, 2007. doi:10.1109/TIE.2007.893074.
- [85] Chee Khiang Pang, Guoxiao Guo, B.M. Chen, and Tong Heng Lee. Self-sensing actuation for nanopositioning and active-mode damping in dual-stage hdds. *Mechatronics, IEEE/ASME Transactions on*, 11(3):328–338, 2006. doi:10.1109/TMECH.2006.875560.
- [86] B.M. Chen, T.H. Lee, K. Peng, and V. Venkataramanan. *Hard Disk Drive Servo Systems*. Springer-Verlag, second edition, 2006.

- [87] B. Hredzak, G. Herrmann, and G. Guo. A proximate-time-optimal-control design and its application to a hard disk drive dual-stage actuator system. *Magnetics, IEEE Transactions on*, 42(6):1708 –1715, 2006. doi:10.1109/TMAG.2006.872003.
- [88] Y. Tang, S.-Y. Hong, N.-Y. Kim, and X. Che. Overview of fly height control applications in perpendicular magnetic recording. *Magnetics, IEEE Transactions on*, 43(2):709 –714, feb. 2007. doi:10.1109/TMAG.2006.888363.
- [89] J. M. Harker, D. W. Brede, R. E. Pattison, G. R. Santana, and L. G. Taft. A quarter century of disk file innovation. *IBM Journal of Research and Development*, 25(5):677 –690, sep. 1981. doi:10.1147/rd.255.0677.
- [90] C.E. Yeack-Scranton, V.D. Khanna, K.F. Etzold, and A.P. Praino. An active slider for practical contact recording. *Magnetics, IEEE Transactions on*, 26(5):2478 –2483, sep. 1990. doi:10.1109/20.104770.
- [91] Dallas W. Meyer, Paul E. Kupinski, and Joseph C. Liu. Slider with temperature responsive transducer positioning. *U.S. Patent 5991113*, 1999.
- [92] P. Machtle, R. Berger, A. Dietzel, M. Despont, W. Haberle, R. Stutz, G.K. Binnig, and P. Vettiger. Integrated microheaters for in-situ flying-height control of sliders used in hard-disk drives. *Micro Electro Mechanical Systems, 2001. MEMS 2001. The 14th IEEE International Conference on*, pages 196 –199, 2001. doi:10.1109/MEMSYS.2001.906512.
- [93] Zhong-Qing Gong and Jia Jay Liu. Pole-tip protrusion effect on head-disk interface at low flying clearance. *Magnetics, IEEE Transactions on*, 41(10):3019 – 3021, oct. 2005. doi:10.1109/TMAG.2005.855245.
- [94] *Digital control and state variable methods: conventional and neural-fuzzy control systems*. McGraw-Hill Education (India) Pvt Ltd, 2008.
- [95] G.J. Tarnopolsky. Hard disk drive capacity at high magnetic areal density. *Magnetics, IEEE Transactions on*, 40(1):301 – 306, 2004. doi:10.1109/TMAG.2003.821169.
- [96] A.A. Mamun, T.H. Lee, G.X. Guo, W.E. Wong, and W.C. Ye. Measurement of position offset in hard disk drive using dual frequency servo bursts. *Instrumentation and Measurement, IEEE Transactions on*, 52(6):1870 – 1880, 2003. doi:10.1109/TIM.2003.820473.
- [97] Younghee Han and R.A. de Callafon. Evaluating track-following servo performance of high-density hard disk drives using patterned media. *Magnetics, IEEE Transactions on*, 45(12):5352 –5359, dec. 2009. doi:10.1109/TMAG.2009.2025035.

- [98] R. Conway, Jongeun Choi, R. Nagamune, and R. Horowitz. Robust track-following controller design in hard disk drives based on parameter dependent lyapunov functions. *Magnetics, IEEE Transactions on*, 46(4):1060 –1068, 2010. doi:10.1109/TMAG.2009.2037952.
- [99] Chen Lin, Guoxiao Guo, Ben M. Chen, and Chi-Chung Ko. Optimal track following control for hard disk drives. *Advanced Motion Control, 2000. Proceedings. 6th International Workshop on*, 2000.
- [100] K.P. Tee, S.S. Ge, and E.H. Tay. Adaptive resonance compensation for hard disk drive servo systems. In *Decision and Control, 2007 46th IEEE Conference on*, pages 3567 –3572, 2007. doi:10.1109/CDC.2007.4434104.
- [101] M.R. Graham and R.A. de Callafon. An iterative learning design for repeatable runout cancellation in disk drives. *Control Systems Technology, IEEE Transactions on*, 14(3):474 – 482, May 2006. doi:10.1109/TCST.2006.872531.
- [102] M. Hirata and Y. Hasegawa. High bandwidth design of track-following control system of hard disk drive using h-infinity control theory. In *Control Applications, 2007. CCA 2007. IEEE International Conference on*, pages 114 –117, 2007. doi:10.1109/CCA.2007.4389215.
- [103] B.M. Chen, T.H. Lee, and V. Venkatakrishnan. *Hard disk drive servo systems*. Advances in industrial control. Springer, 2002.
- [104] M. L. Workman, R. L. Kosut, and G. F. Franklin. Adaptive proximate time-optimal servomechanisms: Continuous time case. In *American Control Conference, 1987*, pages 589 –594, 1987.
- [105] T. Yamaguchi, K. Shishida, S. Tohyama, and H. Hirai. Mode switching control design with initial value compensation and its application to head positioning control on magnetic disk drives. *Industrial Electronics, IEEE Transactions on*, 43(1):65 –73, February 1996. doi:10.1109/41.481409.
- [106] T. Yamaguchi, H. Numasato, and H. Hirai. A mode-switching control for motion control and its application to disk drives: design of optimal mode-switching conditions. *Mechatronics, IEEE/ASME Transactions on*, 3(3):202 –209, September 1998. doi:10.1109/3516.712116.
- [107] B.M. Chen, T.H. Lee, Kemao Peng, and V. Venkataramanan. Composite nonlinear feedback control for linear systems with input saturation: theory and an application. *Automatic Control, IEEE Transactions on*, 48(3):427 – 439, March 2003. doi:10.1109/TAC.2003.809148.

- [108] Lucy Y. Pao and Chanat La-orpacharapan. Shaped time-optimal feedback controllers for flexible structures. *Journal of Dynamic Systems, Measurement, and Control*, 126(1):173–186, 2004. doi:10.1115/1.1637639.
- [109] R.E. Fontana, N. Robertson, and S.R. Hetzler. Thin-film processing realities for 1tbit/in² recording. *Magnetics, IEEE Transactions on*, 44(11):3617 – 3620, 2008. doi:10.1109/TMAG.2008.2002532.
- [110] Charles M. Kozierok. Zoned bit recording. [Online; accessed 3-March-2011]. Available from: http://www.pcguide.com/ref/hdd/geom/tracks_ZBR.htm.
- [111] Zoned bit recording. [Online; accessed 3-March-2011]. Available from: <http://www.storagereview.com/guide/tracksZBR.html>.
- [112] Artem Rubtsov. Hdd from inside: Tracks and zones. how hard it can be? *HDDScan*, 2009. [Online; accessed 23-January-2011]. Available from: http://hddscan.com/doc/HDD_Tracks_and_Zones.html.
- [113] Zhihao Li, Mike Schaff, Rolf Munson, Mark Jurisch, Ted Noonon, Shaoping Li, and Yuming Zhou. Adjacent track encroachment analysis at high track density. *Journal of Applied Physics*, 93(10):6456 –6458, May 2003. doi:10.1063/1.1557651.
- [114] E. B. Svedberg, D. Litvinov, R. Gustafson, C. H. Chang, and S. Khizroev. Magnetic force microscopy of skew angle dependencies in perpendicular magnetic recording. *Journal of Applied Physics*, 93(5):2828 –2833, March 2003. doi:10.1063/1.1544069.
- [115] Richard P. Feynman. There is plenty of room at the bottom. 1960. Available from: http://media.wiley.com/product_data/excerpt/53/07803108/0780310853.pdf.
- [116] Yiao-Tee Hsia. The ever shrinking hard disk drive and its components: What are the challenges? *Micro-NanoMechatronics and Human Science, 2006 International Symposium on*, pages 1 –2, nov. 2006. doi:10.1109/MHS.2006.320313.
- [117] A brief history of areal density. Available from: <http://www.ibm.com>.
- [118] Toshiba enters guinness world records book with the world’s smallest hard disk drive. 2004. [Online; accessed 27-February-2011]. Available from: http://www.toshiba.co.jp/about/press/2004_03/pr1601.htm.
- [119] Matthew Komorowski. A history of storage cost. 2009. [Online; accessed 27-February-2011]. Available from: <http://www.mkomo.com/cost-per-gigabyte>.

- [120] Ivan Smith. Cost of hard drive storage space. 2004. [Online; accessed 27-February-2011]. Available from: <http://ns1758.ca/winch/winchest.html>.
- [121] D. Weller and A. Moser. Thermal effect limits in ultrahigh-density magnetic recording. *Magnetics, IEEE Transactions on*, 35(6):4423–4439, November 1999. doi:10.1109/20.809134.
- [122] S.H. Charap, Pu-Ling Lu, and Yanjun He. Thermal stability of recorded information at high densities. *Magnetics, IEEE Transactions on*, 33(1):978–983, January 1997. doi:10.1109/20.560142.
- [123] Y. Soeno, M. Moriya, K. Ito, K. Hattori, T. Aoyama, M. Matsuzaki, and H. Sakai. Feasibility of discrete track perpendicular media for high track density recording. In *Joint NAPMRC 2003. Digest of Technical Papers [Perpendicular Magnetic Recording Conference 2003]*, page 64, 2003. doi:10.1109/NAPMRC.2003.1177068.
- [124] Maik Duwensee, D. Lee, Y. Yoon, F. Talke, S. Suzuki, and J. Lin. Tribological testing of sliders on discrete track media and verification with numerical predictions. *Microsystem Technologies*, 15:1597–1603, 2009. doi:10.1007/s00542-009-0816-3.
- [125] S.N. Piramanayagam, R. Sbiaa, Ei-Leen Tan, A. Poh, Hang Khume Tan, Kyaw Oo Aung, Jinmin Zhao, and Seng Kai Wong. Planarization of patterned recording media. *Magnetics, IEEE Transactions on*, 46(3):758–763, 2010. doi:10.1109/TMAG.2009.2039018.
- [126] Chulmin Choi, Yeoungchin Yoon, Daehoon Hong, Young Oh, Frank Talke, and Sungho Jin. Planarization of patterned magnetic recording media to enable head flyability. *Microsystem Technologies*, pages 1–8, 2011. doi:10.1007/s00542-011-1222-1.
- [127] Jian-Gang Zhu, Xiaochun Zhu, and Yuhui Tang. Microwave assisted magnetic recording. *Magnetics, IEEE Transactions on*, 44(1):125–131, 2008. doi:10.1109/TMAG.2007.911031.
- [128] M.H. Kryder, E.C. Gage, T.W. McDaniel, W.A. Challener, R.E. Rottmayer, Ganping Ju, Yiao-Tee Hsia, and M.F. Erden. Heat assisted magnetic recording. *Proceedings of the IEEE*, 96(11):1810–1835, 2008. doi:10.1109/JPROC.2008.2004315.
- [129] W. A. Challener, C. Peng, A. V. Itagi, D. Karns, W. Peng, Y. Peng, X. Yang, X. Zhu, N. J. Gokemeijer, Y.-T. Hsia, G. Ju, R. E. Rottmayer, M. A. Seigler, and E. C. Gage. Heat-assisted magnetic recording by a near-field transducer with efficient optical energy transfer. *Nature Photonics*, 3:220–224, April 2009. doi:10.1038/nphoton.2009.26.

- [130] M.A. Seigler, W.A. Challener, E. Gage, N. Gokemeijer, Ganping Ju, Bin Lu, K. Pelhos, Chubing Peng, R.E. Rottmayer, Xiaomin Yang, Hua Zhou, and T. Rausch. Integrated heat assisted magnetic recording head: Design and recording demonstration. *Magnetics, IEEE Transactions on*, 44(1):119–124, 2008. doi:10.1109/TMAG.2007.911029.
- [131] M. A. Seigler, W. A. Challener, E. Gage, N. Gokemeijer, B. Lu, K. Pelhos, C. Peng, R. E. Rottmayer, X. Yang, H. Zhou, X. Zhu, and T. Rausch. Heat assisted magnetic recording with a fully integrated recording head. In *Society of Photo-Optical Instrumentation Engineers (SPIE) Conference Series*, volume 6620 of *Presented at the Society of Photo-Optical Instrumentation Engineers (SPIE) Conference*, July 2007. doi:10.1117/12.738903.
- [132] P. Kasiraj and M. Williams. System and method for writing hard disk drive depending on head skew. *U.S. Patent 6967810B2*, 2005.
- [133] N. Bertram. *Theory of Magnetic Recording*. Cambridge University Press, 1994.
- [134] S. Khizroev and D. Litvinov. *Perpendicular Magnetic Recording*. Kluwer Academic Publishers, 2004.
- [135] C.D. Mee and E.D. Daniel. *Magnetic recording technology*. McGraw-Hill, 1996.
- [136] M.L. Plumer, J.V. Ek, and D. Weller. *The physics of ultra-high-density magnetic recording*. Springer series in surface sciences. Springer, 2001.
- [137] B. Bhushan. *Tribology and Mechanics of Magnetic Storage Devices*. IEEE, 1996.
- [138] B. Vasic and E. Kurtas. *Coding and signal processing for magnetic recording systems*. Computer engineering. CRC Press, 2005.
- [139] P.A. Ioannou, Haojian Xu, and B. Fidan. Identification and high bandwidth control of hard disk drive servo systems based on sampled data measurements. *Control Systems Technology, IEEE Transactions on*, 15(6):1089–1095, 2007. doi:10.1109/TCST.2006.890296.
- [140] R. A. de Callafon, B. Moaveni, J. P. Conte, X. He, and E. Udd. General realization algorithm for modal identification of linear dynamic systems. *Journal of Engineering Mechanics*, 134(9):712–722, 2008. doi:10.1061/(ASCE)0733-9399(2008)134:9(712).
- [141] J.N. Juang and R.S. Pappa. An eigensystem realization algorithm for modal parameter identification and model reduction. *Journal of guidance, control, and dynamics*, 8(5):620–627, 1985.

- [142] Michel Claes, Matthew Graham, and Raymond de Callafon. Frequency domain subspace identification of a tape servo system. *Microsystem Technologies*, 13:1439–1447, 2007. 10.1007/s00542-007-0389-y. Available from: <http://dx.doi.org/10.1007/s00542-007-0389-y>.
- [143] U. Boettcher, B. Raeymaekers, R.A. de Callafon, and F.E. Talke. Dynamic modeling and control of a piezo-electric dual-stage tape servo actuator. *Magnetics, IEEE Transactions on*, 45(7):3017 –3024, 2009. doi:10.1109/TMAG.2009.2015050.
- [144] G. Herrmann, B. Hredzak, M.C. Turner, I. Postlethwaite, and Guoxiao Guo. Discrete robust anti-windup to improve a novel dual-stage large-span track-seek/following method. *Control Systems Technology, IEEE Transactions on*, 16(6):1342 –1351, 2008. doi:10.1109/TCST.2008.917876.
- [145] D. Wu, G. Guo, and Y. Wang. Reset integral-derivative control for hdd servo systems. *Control Systems Technology, IEEE Transactions on*, 15(1):161 –167, 2007. doi:10.1109/TCST.2006.883230.
- [146] J. Zhang, C. Du, and S.S. Ge. A novel settling controller for dual-stage servo systems. *Magnetics, IEEE Transactions on*, 44(11):3757 –3760, 2008. doi:10.1109/TMAG.2008.2002610.
- [147] S.J. Schroeck and W.C. Messner. On controller design for linear time-invariant dual-input single-output systems. In *American Control Conference, 1999. Proceedings of the 1999*, volume 6, pages 4122–4126, 1999. doi:10.1109/ACC.1999.786322.
- [148] M. Graham, R.J.M. Oosterbosch, and R.A. de Callafon. Fixed order pq-control design method for dual stage instrumented suspension. IFAC Congress, Praha, Czech Republic, 2005.
- [149] M. Kobayashi and R. Horowitz. Track seek control for hard disk dual-stage servo systems. *Magnetics, IEEE Transactions on*, 37(2):949 –954, March 2001. doi:10.1109/20.917648.
- [150] N.F. Gunderson, K.J. Schulz, and T.A. Bordson. Component development and product integration of secondary piezoelectric actuator for disc drives. ASME/JSME Joint Conference on Micromechatronics for Information and Precision Equipment, Santa Clara, CA, U.S.A., 2006.
- [151] D. McFarlane and K. Glover. A loop-shaping design procedure using h_∞ synthesis. *Automatic Control, IEEE Transactions on*, 37(6):759 –769, June 1992. doi:10.1109/9.256330.

- [152] K. Glover and D. McFarlane. Robust stabilization of normalized coprime factor plant descriptions with h_∞ -bounded uncertainty. *Automatic Control, IEEE Transactions on*, 34(8):821–830, August 1989. doi:10.1109/9.29424.
- [153] P.M.M. Bongers and O.H. Bosgra. Low order robust h_∞ controller synthesis. In *Decision and Control, 1990., Proceedings of the 29th IEEE Conference on*, pages 194–199 vol.1, December 1990. doi:10.1109/CDC.1990.203575.
- [154] N. C. Singer and W. P. Seering. Preshaping command inputs to reduce system vibration. *Journal of Dynamic Systems, Measurement, and Control*, 112(1):76–82, 1990.
- [155] R.D. Robinett. *Flexible robot dynamics and controls*. IFSR international series on systems science and engineering. Kluwer Academic/Plenum Publishers, 2002.
- [156] J. Mattingley and S. Boyd. Real-time convex optimization in signal processing. *Signal Processing Magazine, IEEE*, 27(3):50–61, may. 2010. doi:10.1109/MSP.2010.936020.
- [157] Lucy Y. Pao. Multi-input shaping design for vibration reduction. *Automatica*, 35(1):81–89, 1999. doi:10.1016/S0005-1098(98)00124-1.
- [158] Matthew D. Baumgart and Lucy Y. Pao. Discrete time-optimal command shaping. *Automatica*, 43(8):1403–1409, 2007. doi:10.1016/j.automatica.2007.01.003.
- [159] Vikram Kapila, Anthony Tzes, and Qiguo Yan. Closed-loop input shaping for flexible structures using time-delay control. *Journal of Dynamic Systems, Measurement, and Control*, 122(3):454–460, 2000. doi:10.1115/1.1286269.
- [160] Kiminao Kogiso and Kenji Hirata. Reference governor for constrained systems with time-varying references. *Robot. Auton. Syst.*, 57:289–295, March 2009. doi:10.1016/j.robot.2008.10.015.
- [161] C.F. Cutforth and L.Y. Pao. Control using equal length shaped commands to reduce vibration. *Control Systems Technology, IEEE Transactions on*, 11(1):62–72, January 2003. doi:10.1109/TCST.2002.806460.
- [162] Z.N. Masoud and M.F. Daqaq. A graphical approach to input-shaping control design for container cranes with hoist. *Control Systems Technology, IEEE Transactions on*, 14(6):1070–1077, 2006. doi:10.1109/TCST.2006.883194.
- [163] K.L. Sorensen, K. Hekman, and W.E. Singhose. Finite-state input shaping. *Control Systems Technology, IEEE Transactions on*, 18(3):664–672, May 2010. doi:10.1109/TCST.2009.2027428.

- [164] T. Sugie and H. Yamamoto. Reference management for closed loop systems with state and control constraints. In *American Control Conference, 2001. Proceedings of the 2001*, 2001.
- [165] H. Suzuki and T. Sugie. Off-line reference shaping of periodic trajectories for constrained systems with uncertainties. *Automatic Control, IEEE Transactions on*, 53(6):1531–1535, 2008. doi:10.1109/TAC.2008.928310.
- [166] T. Sugie and H. Suzuki. Reference shaping of periodic trajectory for systems having constraints. In *American Control Conference, 2004. Proceedings of the 2004*, volume 5, pages 4657 – 4662, june-2 july 2004.
- [167] L. Van den Broeck, M. Diehl, and J. Swevers. Embedded optimization for input shaping. *Control Systems Technology, IEEE Transactions on*, 18(5):1146–1154, 2010. doi:10.1109/TCST.2009.2032165.
- [168] O. N. Starnes. Numerical time-optimal reference signal generation for hard disk drive servo systems. *Project Report - University of California, San Diego*, 2007.
- [169] G.C. Goodwin, M.M. Seron, and J.A. de Dona. *Constrained Control and Estimation: An Optimization Approach*. Springer Verlag, London, 2005. doi:10.1007/b138145.
- [170] Stephen Boyd and Lieven Vandenberghe. *Convex Optimization*. Cambridge University Press, New York, 2004. Available from: <http://www.stanford.edu/~boyd/cvxbook/>.
- [171] Jorge Nocedal and Stephen J. Wright. *Numerical Optimization*. Springer-Verlag, New York, 1999.
- [172] O. N. Starnes and R. A. de Callafon. Time-optimal input shaping for discrete-time lti systems with application to seek profiles of a hdd system. *Proc. ASME ISPS Conference, Santa Clara, CA, USA*, 2007.
- [173] Lieven Vandenberghe and Stephen Boyd. Semidefinite programming. *Society for Industrial and Applied Mathematics Review*, 38(1):49–95, 1996. Available from: <http://www.jstor.org/stable/2132974>.
- [174] Miguel Soma Lobo, Lieven Vandenberghe, Stephen Boyd, and Herve Lebret. Applications of second-order cone programming. *Linear Algebra and its Applications*, 284(1):193–228, 1998. Available from: <http://stanford.edu/~boyd/papers/pdf/socp.pdf>.
- [175] J. Lofberg. Yalmip : a toolbox for modeling and optimization in matlab. In *Computer Aided Control Systems Design, 2004 IEEE International Symposium on*, pages 284 –289, 2004. doi:10.1109/CACSD.2004.1393890.

- [176] Jos F. Sturm. Using sedumi 1.02, a matlab toolbox for optimization over symmetric cones, 1999.
- [177] M. Grant and S. Boyd. CVX: Matlab software for disciplined convex programming, version 1.21. <http://cvxr.com/cvx>, September 2010.
- [178] Abdullah Al Mamun. *Hard Disk Drive: Mechatronics and Control; electronic version*. CRC Press, Hoboken, NJ, 2006.
- [179] B. Valcu and H.N. Bertram. 3-d analysis of the playback signal in perpendicular recording for an off-centered gmr element. *Magnetics, IEEE Transactions on*, 38(5):2081 – 2083, sep. 2002. doi:10.1109/TMAG.2002.801838.
- [180] T. A. Roscamp, E. D. Boerner, and G. J. Parker. Three-dimensional modeling of perpendicular reading with a soft underlayer. *Journal of Applied Physics*, 91(10):8366 – 8368, may. 2002. doi:10.1063/1.1452281.
- [181] N. Smith. Reciprocity principles for magnetoresistive heads. *Magnetics, IEEE Transactions on*, 29(5):2279 – 2285, sep. 1993. doi:10.1109/20.231633.
- [182] R.W. Wood and D.T. Wilton. Readback responses in three dimensions for multilayered recording media configurations. *Magnetics, IEEE Transactions on*, 44(7):1874 – 1890, jul. 2008. doi:10.1109/TMAG.2008.920525.
- [183] H.A. Shute, D.T. Wilton, D.Mc.A. McKirdy, P.M. Jerney, and J.C. Mallinson. Analytic three-dimensional response function of a double-shielded magnetoresistive or giant magnetoresistive perpendicular head. *Magnetics, IEEE Transactions on*, 42(5):1611 – 1619, may. 2006. doi:10.1109/TMAG.2005.861829.
- [184] K.S. Chai, Z.J. Liu, J.T. Li, and H.H. Long. 3d analysis of medium field with consideration of perpendicular head-medium combinations. pages 1 – 2, nov. 2006. doi:10.1109/APMRC.2006.365937.
- [185] Y. Suzuki, H. Aoi, H. Muraoka, and Y. Nakamura. Fast calculation of read field from perpendicular recording medium using head characteristic matrix. pages 798 – 798, may. 2006. doi:10.1109/INTMAG.2006.376522.
- [186] D.T. Wilton, D.Mc.A. McKirdy, H.A. Shute, J.J. Miles, and D.J. Mapps. Approximate three-dimensional head fields for perpendicular magnetic recording. *Magnetics, IEEE Transactions on*, 40(1):148 – 156, jan. 2004. doi:10.1109/TMAG.2003.821132.
- [187] J. Mallinson and H. Bertram. On the characteristics of pole-keeper head fields. *Magnetics, IEEE Transactions on*, 20(5):721 – 723, sep. 1984. doi:10.1109/TMAG.1984.1063385.

- [188] R. Radhakrishnan, M.F. Erden, Ching He, and B. Vasic. Transition response characteristics of heat-assisted magnetic recording and their performance with mtr codes. *Magnetics, IEEE Transactions on*, 43(6):2298 –2300, jun. 2007. doi:10.1109/TMAG.2007.892334.
- [189] Hans Jürgen Richter. Recent advances in the recording physics of thin-film media. *Journal of Physics D: Applied Physics*, 32(21):R147, 1999. doi:10.1088/0022-3727/32/21/201.
- [190] S.W. Yuan and H.N. Bertram. Off-track spacing loss of shielded mr heads. *Magnetics, IEEE Transactions on*, 30(3):1267 –1273, may. 1994. doi:10.1109/20.297764.
- [191] S.W. Yuan and H.N. Bertram. Correction to "off-track spacing loss of shielded mr heads". *Magnetics, IEEE Transactions on*, 32(4):3334, jul. 1996. doi:10.1109/TMAG.1996.508399.
- [192] Y. Suzuki and Y. Nishida. Calculation method of gmr head response for double layered perpendicular medium. *Magnetics, IEEE Transactions on*, 37(4):1337 –1339, jul. 2001. doi:10.1109/20.950834.
- [193] Y. Suzuki and Y. Nishida. Exact calculation method for medium field from a perpendicular medium. *Magnetics, IEEE Transactions on*, 39(5):2633 –2635, sep. 2003. doi:10.1109/TMAG.2003.815534.
- [194] S. Takahashi, K. Yamakawa, and K. Ouchi. Design of multisurface single pole head for high-density recording. *Journal of Applied Physics*, 93(10):6546 –6548, may. 2003. doi:10.1063/1.1561793.
- [195] N.A. Spaldin. *Magnetic materials: fundamentals and device applications*. Cambridge University Press, 2003.
- [196] D. Wachenschwanz, Wen Jiang, E. Roddick, A. Homola, P. Dorsey, B. Harper, D. Treves, and C. Bajorek. Design of a manufacturable discrete track recording medium. *Magnetics, IEEE Transactions on*, 41(2):670 –675, feb. 2005. doi:10.1109/TMAG.2004.838049.
- [197] Davide Guarisco, Zhaohui Li, Bill E. Higgins, Kaz Saito, Yan Wu, and Andrew LeFebvre. Drive integration in perpendicular recording (invited). *Journal of Applied Physics*, 99(8):08Q908 –08Q908–5, apr. 2006. doi:10.1063/1.2175821.
- [198] J. Xu, Y. Shimizu, and L. Su. Drive level measurement of flying height modulation and control of slider disk contact. *Tribology Letters*, 24:159–162, 2006. doi:10.1007/s11249-006-9153-1.

- [199] Bo Liu and Zhimin Yuan. Tribo-magnetics and nanometer spaced head-disk systems. In *Asia-Pacific Magnetic Recording Conference, 2000. APMRC 2000*, pages TB5/1 –TB5/2, December 2000. doi:10.1109/APMRC.2000.898927.
- [200] Zhi-Min Yuan, Bo Liu, Wei Zhang, and Sheng-Bin Hu. Engineering study of triple-harmonic method for in situ characterization of head-disk spacing. *Journal of Magnetism and Magnetic Materials*, 239(1-3):367 – 370, 2002. doi:10.1016/S0304-8853(01)00604-7.
- [201] Timothy Francis Ellis. Us patent application 20,090,153,996. 2009.
- [202] Toru Yokohata Takahiro Imamura. Us patent 7,522,360. 2009.
- [203] Qing-Hua Zeng and M. Chen. Flying height modulation estimation from pseudorandom readback signal in disk drives. *Magnetics, IEEE Transactions on*, 39(5):2417 – 2419, sep. 2003. doi:10.1109/TMAG.2003.816423.
- [204] Seungwoo Jung Ashish Manjrekar Rajkumar Jayaraman, Taras Dudar. Us patent #7,253,984. 2010.
- [205] K.B. Klaassen and J.C.L. van Peppen. Slider-disk clearance measurements in magnetic disk drives using the readback transducer. *Instrumentation and Measurement, IEEE Transactions on*, 43(2):121 –126, apr. 1994. doi:10.1109/19.293407.
- [206] Chengjiang Fu, Akihiko Takeo, and H. Neal Bertram. Technique to obtain head-medium magnetic spacing in a disk drive. *Journal of Applied Physics*, 97(10):10P107 –10P107–3, may. 2005. doi:10.1063/1.1853251.
- [207] Hal Hjalmar Ottesen and Gordon James Smith. Us patent 6,288,856. 2001.
- [208] Du Chen and David Bogy. Simulation of static flying attitudes with different heat transfer models for a flying-height control slider with thermal protrusion. *Tribology Letters*, 40:31–39, 2010. doi:10.1007/s11249-009-9551-2.
- [209] Weidong Zhou, Bo Liu, Shengkai Yu, Wei Hua, and Chee Wong. Effects of environmental temperature and humidity on thermal flying height adjustment. *Microsystem Technologies*, 16:49–55, 2010. doi:10.1007/s00542-008-0748-3.
- [210] T. Shiramatsu, T. Atsumi, M. Kurita, Y. Shimizu, and H. Tanaka. Dynamically controlled thermal flying-height control slider. *Magnetics, IEEE Transactions on*, 44(11):3695 –3697, nov. 2008. doi:10.1109/TMAG.2008.2002626.

- [211] Zhizheng Wu and F.B. Amara. Adaptive regulation of the flying height in hard disk drives. In *Control Applications, 2005. CCA 2005. Proceedings of 2005 IEEE Conference on*, pages 1146 –1151, 2005. doi:10.1109/CCA.2005.1507285.
- [212] Zhizheng Wu and F. Ben Amara. Adaptive regulation in switched bimodal systems: An experimental evaluation. *Control Systems Technology, IEEE Transactions on*, 18(4):885 –895, 2010. doi:10.1109/TCST.2009.2030789.
- [213] Jia-Yang Juang and David B. Bogy. Air-bearing effects on actuated thermal pole-tip protrusion for hard disk drives. *Journal of Tribology*, 129(3):570–578, 2007. doi:10.1115/1.2736456.
- [214] Joerg Fritzsche, Hui Li, Hao Zheng, Kensuke Amemiya, and Frank E. Talke. The effect of air bearing contour design on thermal pole-tip protrusion. In *ASME Information Storage and Processing Systems Conference, Santa Clara, CA*, 2010.
- [215] V. Gupta and D.B. Bogy. Dynamics of sub-5-nm air-bearing sliders in the presence of electrostatic and intermolecular forces at the head-disk interface. *Magnetics, IEEE Transactions on*, 41(2):610 – 615, feb. 2005. doi:10.1109/TMAG.2004.838062.
- [216] R.A. de Callafon. Estimating parameters in a lumped parameter system with first principle modeling and dynamic experiments. *Proceedings of 13th IFAC Symposium on System Identification, Rotterdam, the Netherlands*, pages 1613 – 1618, 2003.
- [217] Hui Li, Hao Zheng, J. Fritzsche, K. Amemiya, and F.E. Talke. Simulation of flying height and response time of thermal flying height control sliders with thermal insulators. *Magnetics, IEEE Transactions on*, 46(6):1292 –1294, 2010. doi:10.1109/TMAG.2010.2040025.
- [218] Satoru OOKUBO, Toshiya SHIRAMATSU, Masayuki KURITA, Hidekazu KOHIRA, and Yoshinori TAKEUCHI. Investigation of mechanical clearance change with thermal flying-height control slider at high altitude. *Journal of Advanced Mechanical Design, Systems, and Manufacturing*, 4(1):32–41, 2010. doi:10.1299/jamdsm.4.32.